Imaging of In-Vivo Pressure using Ultrasound

Olesen, Jacob Bjerring; Jensen, Jørgen Arendt; Traberg, Marie Sand

Publication date:
2016

Document Version
Publisher's PDF, also known as Version of record

Citation (APA):
Olesen, J. B., Jensen, J. A., & Traberg, M. S. (2016). Imaging of In-Vivo Pressure using Ultrasound. Technical University of Denmark, Department of Electrical Engineering.

PhD Thesis

Imaging of In-Vivo Pressure using Ultrasound

Jacob Bjerring Olesen

Supervised by: Prof. Jørgen Arendt Jensen, PhD, Dr. Techn.

Co-supervised by: Marie Sand Traberg, PhD

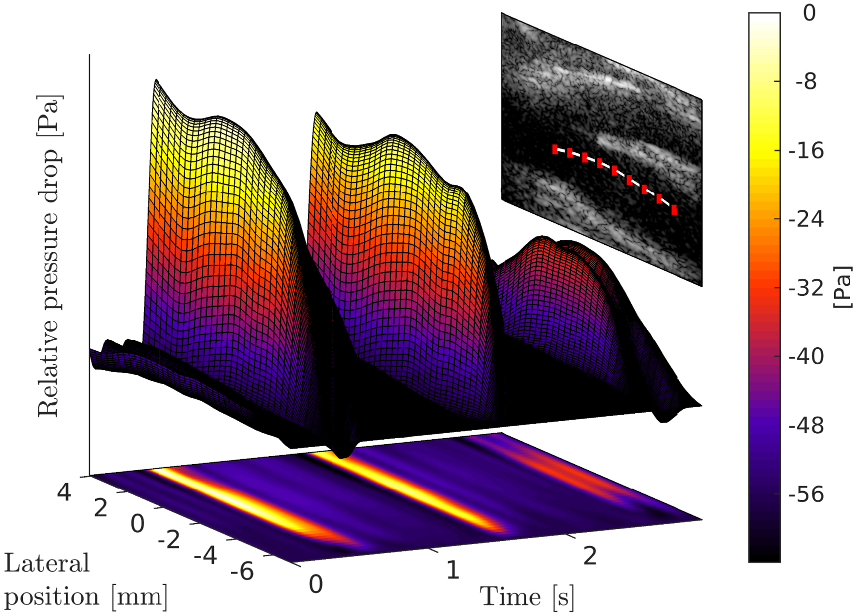

Technical University of Denmark
Kgs. Lyngby, Denmark 2016

Cover image: Pressure changes measured in the carotid bifurcation using non-invasive medical ultrasound.

Technical University of Denmark
Department of Electrical Engineering
Center for Fast Ultrasound Imaging (CFU)
Ørsteds Plads 349
2800 Kgs. Lyngby
DENMARK
Tel: (+45) 4525 5832
Web: www.bme.elektro.dtu.dk
Author e-mail: jbjol@elektro.dtu.dk

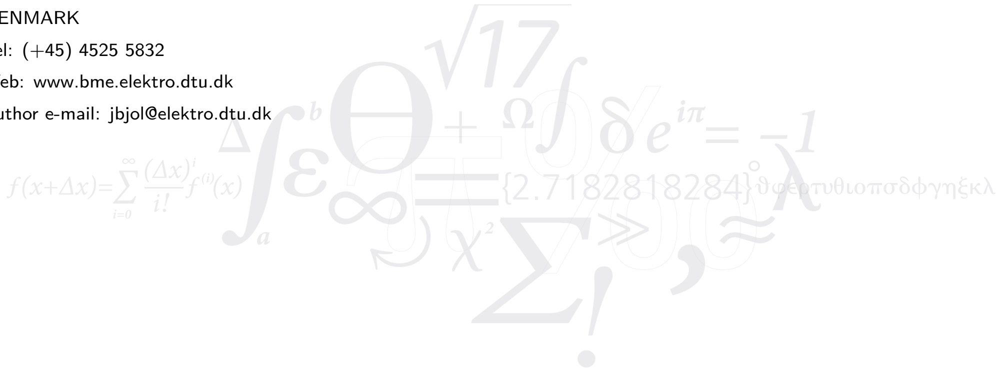

Contents

Preface

This PhD thesis has been submitted to the Department of Electrical Engineering at the Technical University of Denmark in partial fulfillment of the requirements for acquiring the PhD degree. The research providing the foundation for the thesis has been conducted over a period of three years from December 1st, 2012, to November 30th, 2015 at the Center for Fast Ultrasound Imaging (CFU), Department of Electrical Engineering. The project has been supervised by Prof. Jørgen Arendt Jensen, PhD, Dr. Techn, and co-supervised by Marie Sand Traberg, PhD. The project was financially supported by grant 024-2008-3 from the Danish Advanced Technology Foundation, BK Medical Aps, Denmark and by Radiometer A/S, Denmark.

In the spring of 2015 I had the privilege of spending a two-month external stay in Hong Kong as a visiting researcher in Prof. Alfred Yu's group at the University of Hong Kong, Pokfulam, Hong Kong. In addition to this, I have had the opportunity to meet fellow researchers at conferences in Dredsen, Orlando, Toronto, Prague, Tel Aviv, Chicago, and Taipei. Travelling to these places to present my research has truly helped in developing the competences I hold today; both technically and theoretically.

During the project period, I have had the pleasure of co-supervising three engineering students in one master's project and one bachelor's project. Furthermore, I have enjoyed the experience of teaching and tutoring students for three semesters on an medical imaging systems course.

Jacob Bjerring Olesen
Kgs. Lyngby, Denmark
November 2015

Summary

The main purpose of this PhD project was to develop an ultrasonic method capable of determining intravascular pressure changes non-invasively. Measuring pressure variations is used clinically as a diagnostic marker for the physiological state of a cardiovascular region. Current clinical procedures for assessing pressure changes are by means of invasive devices such as pressure sensing catheters. Such devices suffer severe limitations as they are invasive and require the use of ionizing radiation for guidance and positioning. To overcome the concerns related to the use of invasive pressure catheters this project introduces a method that derives pressure changes from 2-D vector velocity flow data acquired non-invasively. The method is based on the Navier-Stokes equations and is tested on fabricated flow models. Results from the flow models are compared with simulations from finite element modeling. The developed technique showed a standard deviation and bias across constricted flow domains of 9 % and 8 %, respectively. Finally, the first in-vivo examples of deriving pressure changes from 2-D vector velocity ultrasound data is presented.

Based on the presented results it is concluded that non-invasive determination of pressure changes from 2-D flow data is feasible. However, when transferring the method into clinical practice, where blood vessels follow more complex flow geometries, the influence of out-of-plane flow movement becomes increasingly more important. Therefore, for scans using a 1-D transducer it is crucial that the out-of-plane flow component is negligible.

Resumé

(Summary in Danish)

Kraftige ændringer i det intravaskulære blodtryk er en indikation på et forsnævret blodkar. Trykmålinger bruges derfor klinisk som et diagnostisk redskab til at vurdere tilstanden af sygdomsramte kar. I dag udføres trykmålinger ved indførelse af invasive trykkatetre i lysken, før de føres til det forsnævrede kar. Udover at være en invasiv operation, kræver brugen af katetre også ioniserende stråling for at guide dem igennem kroppens blodkar. I dette projekt foreslås en ny teknik, der ved hjælp af ultralyd, måler det intravaskulære trykfald uden brug af invasive redskaber eller røntgenstråling. Teknikken muliggøres af state-of-the-art ultralydsskannere, der er i stand til at måle blodstrømninger i både 2- og 3-D. Fra blodstømningerne kan det intravaskulære tryk udledes på baggrund af Navier-Stokes ligning – en ligning der relaterer ændringer i flowhastigheder til det trykfelt, som presser flowet igennem blodkarrene. Ved at udlede acceleration fra målt hastighedsdata, kan trykket bestemmes via ikke-invasive ultralydsteknikker.

Metoden er testet på fabrikerede flow fantomer, og resultaterne sammenholdt med simulationsmodeller, hvis geometri er identisk med de konstruerede modeller. I det eksperimentelle set-up, viste den foreslåede metode en standard afvigelse på 9 % og en bias på 8 %. Ydermere blev teknikken for første gang afprøvet in-vivo på raske forsøgspersoner.

Med indførelsen af et ikke-invasivt alternativ til registrering af tryk, får klinikeren et værktøj, der viser det vaskulære tryk ved flere hundrede billeder i sekundet uden brug af ioniserende stråling eller indgribende operationer. Den præsenterede metode vil derfor muliggøre follow-up studier undervejs i et sygdomsforløb, da ubehaget og de tekniske forhindringer forbundet med invasive operationer undgås.

Acknowledgements

First and foremost I would like to extent my sincere thanks to my supervisor, Prof. Jørgen Arendt Jensen, and my co-supervisor, Ass. Prof. Marie Sand Traberg for their commitment and guidance throughout the project. Without their experience and expertise this project would never have made it as far as it has. Thank you for giving me the freedom to explore my own ideas, but at the same time keeping me focused on the end goal. A special thanks goes to Prof. Alfred Yu from the University of Hong Kong for letting me join his research group for two month in the spring of 2015. This lab gave me the best possible experience, and I am thankful for all the great stuff you taught me on the fabrication process of flow phantoms. On that note, I would also like to thank the Technical University of Denmark, Oticon, and the Augustinus Foundation for supporting me financially on my external research stay.

My warmest thanks goes to all of my colleagues at the Center for Fast Ultrasound Imaging, and the guys at DTU Nanotech. Thank you for creating an environment that holds both work and the best social activities. You are the primary reason for why I have enjoyed working at DTU over the past three years. I would like to extent a great thank you to Morten Fisher Rasmussen and Michael Johannes Pihl for the many great hours we have spent together, and for being a great source of inspiration in every aspect of this project. To Carlos Armando Villagómez-Hoyos, I owe you the biggest thanks for always being there when I needed technical guidance. Without all the hard work you have put into improving the velocity estimators, which I benefited so much from, this project would never have shown the good results it has. I am truly grateful for the collaboration we have established. A special thank to my office mate Simon Holbek for always providing a pleasant atmosphere in the office. Further, I would like to thanks Nina Kjærgaard for proof-reading the thesis.

Finally, I huge thanks goes to my family for their great support throughout the project and for always taking time to listen to my complains when things at work didn't go as I wanted. Last, but definitely not least, I would like to thank you, Josefine Fauerholdt, for your love and support throughout the final stages of this project. Being with you is the greatest pleasure of all.

Abbreviations

2-D	Two-Dimensional
3-D	Three-Dimensional
CFM	Color flow map
DTU	Danmarks Tekniske Universitet (Technical University of Denmark)
$F_{\#}$	f-number, equal to the focal length divided by the aperture diameter
FDA	Food and Drug Administration
FE	Finite element
FOV	Field of view
MRI	Magnetic Resonance Imaging
NRMSE	Normalized root-mean-square-error
PIV	Particle Imaging Velocimetry
PRF	Pulse Repetition Frequency
RF	Radio frequency
Rx	Receive
SAFI	Synthetic aperture flow imaging
SAI	Synthetic aperture imaging
SARUS	Synthetic aperture real-time ultrasound system
SNR	Signal to Noise Ratio
Std	Standard deviation
TO	Transverse oscillation
Tx	Transmit
US	Ultrasound
VFM	Vector flow map

CHAPTER 1

Introduction

Cardiovascular diseases remain some of the most potent killers in western countries, many of which are related to the process of atherosclerosis (Naghavi et al. 2003; World Health Organization 2014). The microscopic alterations that occur in the vessel wall already present themselves during early youth, but usually remain latent until pass the age of fifty (Kavey et al. 2003). As the disease advances, more plaque is build up, which essentially narrows the lumen of the vessels creating a stenosis, as depicted in Fig. 1.1. The narrowing makes it harder for blood to flow, potentially leading to thrombus formation or embolism that prevents oxygenated blood to reach the vascular beds. Without treatment the blood deprived cells quickly become damaged resulting in heart or brain injury, serious disability, or death.

1.1 Today's severity-assessment of a stenotic vessel

Today, the degree of luminal narrowing is used as a diagnostic marker in assessing the severity of the atherosclerosis advancement (Osarumwense et al. 2005; Wardlaw et al. 2006). This assessment is usually obtained by angiography using either ultrasound imaging, X-ray imaging, computed tomography, magnetic resonance imaging (MRI), or a combination of these to image the vessel's anatomic shape. However, several angiographic studies made over the coronary and the carotid arteries have demonstrated that even low-

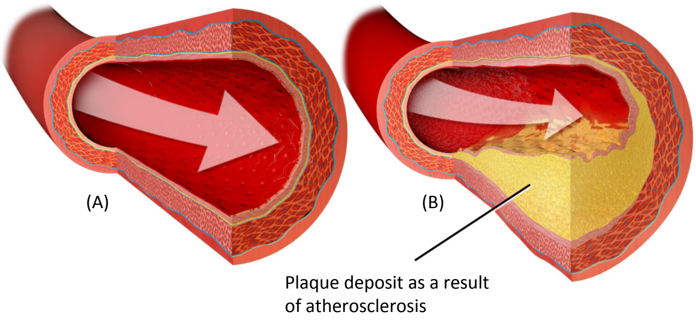

Figure 1.1: Cross-sectional view of a healthy vessel (A), and a vessel suffering from artheriosclerosis (B). The figure is modified from (Blausen 2014)

grade stenosis is capable of creating acute myocardial infarction and cerebrovascular events, suggesting that the severity of a stenosis not only is based on its geometry but also the vulnerability of the plaque constituting the stenosis (Ambrose et al. 1988; Little et al. 1988; Lovett et al. 2004; Saba et al. 2012; Wasserman et al. 2005). To better understand the mechanism that causes vulnerable plaque to rupture a series of both invasive and non-invasive techniques has been introduced to the clinic (Bruyne et al. 1994; Gould 1985; N. H. Pijls et al. 2000; Strauss, F. J. Roth, and Rieger 1993; Stroud, Berger, and Saloner 2002; Taylor, Fonte, and Min 2013). Among the more popular approaches are pressure catheters used in conjunction with a bolus injection of a vasodilating substance to measure the drop in pressure that exists across a stenotic region (Donohue et al. 1993; Tonino, Bruyne, et al. 2009; Young, Cholvin, and A. C. Roth 1975). Extensive studies by Tonino *et al.* (Tonino, Fearon, et al. 2010) confirm that pressure catheters are less inter-operator dependent when assessing the severity of a stenosis, and they further yield a more functional assessment of the stenotic significance seen in comparison to conventional angiography techniques.

1.1.1 How does transstenotic pressure estimation improve the severity-assessment

Abnormal changes in intravascular blood pressure arise from abrupt alterations in blood flow, typically, seen in the presence of a stenosis. As flow passes through a stenotic vessel it experiences a pressure drop caused by the dissipation of energy that goes into forming localized flow jets, eddies, and overcoming the viscous drag met by the blood cells (Young, Cholvin, and A. C. Roth 1975). From a physics point-of-view a drop in pressure translates to applying a net-force upstream to the neck of the stenosis. Potentially, such force carries the capability to tear off pieces of plaque from the diseased vessel, creating an embolus that blocks capillary bed further downstream. Measuring the transstenotic pressure drop is therefore a more direct measure of stenotic severity, as it unlike angiography evaluates the forces acting on the vulnerable plaque and not only its anatomical shape (Baim and Grossman 2000; Tonino, Bruyne, et al. 2009). In principal, this allows for classifying even low-grade stenosis as vulnerable in cases where large pressure forces are acting upon the upstream neck of the stenosis, which also has been confirmed by Pijls, and Tonino *et al.* (N. H. J. Pijls et al. 1996; Tonino, Fearon, et al. 2010).

1.1.2 Downside to measuring pressure in today's clinic

As mentioned, transstenotic pressure is assessed by means of invasive devices, either in the form of a wire or the more frequently used catheter. Typically, such devices require vascular access through the brachial or femoral artery before being threaded to the region of interest (Seldinger 1953). An example of the latter procedure is presented in Fig. 1.2. Here, the lesional pressure drop ΔP, is obtained by measuring the difference between distal pressure (P_A), and proximal pressure (P_B). Despite the advantages offered by pressure catheters in terms of less inter-operator dependency, and a more functional

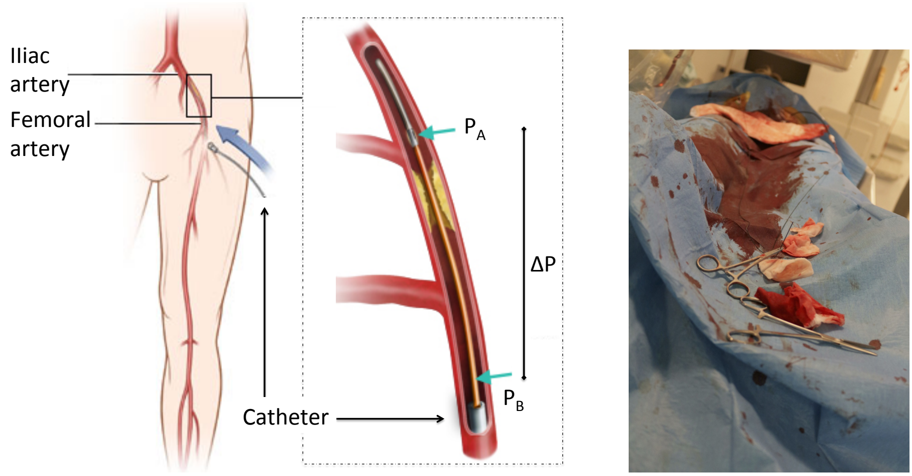

Figure 1.2: (A) Catheter in the femoral artery measuring the drop in pressure that exists across the diseased region (the figure is modified from (St Jude Medical 2014)). (B) shows a patient's bed after successfully completing a vascular intervention using catheters.

severity analysis, these procedures suffer some severe limitations as they are all highly invasive and require the use of ionizing radiation for guidance of the device. Furthermore, routinely employed catheters have shown imprecision of up to 24 %, due to their bulk dimensions in reference to the small size of the vessels they are examining (Vecchi et al. 2014). In addition, all invasive devices are sought avoided from anywhere above the heart, as contact with the neck's arterial walls, could make vulnerable plaque rupture, causing arterial blockage further downstream in the cerebral system (Al-Ameri et al. 2009). The invasive nature of catheterization, furthermore, precludes the possibility of running routine examinations for screening purposes, limiting the application of pressure sensing devices even further.

1.2 Non-invasive alternatives for assessing stenotic severity

To overcome the limitations of invasive procedures, non-invasive imaging modalities such as medical ultrasound and MRI have suggested various solutions for obtaining more functional severity assessments of a stenosis. Among the techniques are elastography imaging, hemodynamic analysis based on the Doppler shift, analysis of the effective orifice area, and others (Bonow et al. 1998; Celermajer et al. 1992; Felix et al. 1976; Garcia, Pibarot, Dumesnil, et al. 2000; Giddens, Zarins, and Glagov 1993; Kips, Segers, and Bortel 2008; Ophir et al. 1991), but none of these have yet managed to supersede clinical catherization. The following section presents an overview of the techniques that have been developed as non-invasive alternatives for measuring the intravascular pressure. Common for all the techniques is their approach of analyzing hemodynamic behaviors, and from there derive a measure for the pressure using either, an orifice equation, the Bernoulli equation, or the more general approach introduced by the Navier-Stokes equations.

1.2.1 Medical ultrasound

The motivation to assess intravascular pressure variations of less-invasive approaches first received attention in the 1970s. In 1977, Fairbank and Scully (Fairbank and Scully 1977) proposed a method for estimating local pressure changes using microbubbles. The suggested method relied on injecting gas-filled bubbles into the circulatory system and measure the frequency shift that occurred in the scattered spectrum as ultrasonic waves were applied. The idea of using microbubbles for obtaining estimates of pressure led the way for a range of methods devised from this technique (Adam, Sapunar, and Burla 2005; Andersen and Jensen 2009; Bouakaz et al. 1999; Forsberg, Dave, et al. 2008; Forsberg, Liu, et al. 2005; Shi et al. 1999). Despite being less invasive techniques, they still require the injection of microbubbles. Furthermore, microbubble techniques only provide a short time window of approximately 10–20 s (Cosgrove and Lassau 2010) for imaging, as the bubbles are taken up by the liver or rupture in the acoustic pressure field produced by the ultrasound transducer.

In 1976, Holen *et al.* (Holen, Aaslid, and Landmark 1976) introduced the first fully non-invasive alternative for estimating intravascular pressure based on Doppler ultrasound. Analysing audio signals of the frequency shifts received from the mitral jet revealed the peak systolic velocity. From this, the local pressure gradients were calculated using an orifice equation. The usability of the method was demonstrated in studies on 25 patients with mitral stenosis and 10 without. An example of the results they obtained from the first non-invasive pressure estimation technique is shown in Fig. 1.3. The method was attractive due to its avoidance of catheterization, but was faced with difficulties associated with the ultrasound scanner technology of that time, e.g. poor signal-to-noise ratios and inferior temporal and spatial resolutions. However, the dominant drawback of the method was its reliance on a single velocity estimate, which made the method highly sensitive to hemodynamic factors unrelated to the constricted vessel's effect on the peak velocity, e.g. abnormal cardiac output. The method presented by Holen *et al.* was further studied in 1989 by Evans *et al.* (Evans et al. 1989), and later tested against clinical pressure catheters by Strauss- and Baumgartner *et al.* (Baumgartner, Schima, et al. 1993; Baumgartner, Stefenelli, et al. 1999; Strauss, F. J. Roth, and Rieger 1993). The latter studies agreed that non-invasive pressure estimation was achievable through the simplified Bernoulli equation, however, the obtained pressure estimates were greatly dependent on the size of the examined vessel and the examiners' ability to correct for the Doppler angle. Further advancement in non-invasive techniques for improving pressure estimates have been proposed over the past decades (Bermejo et al. 2002; Beulen et al. 2011; Garcia,

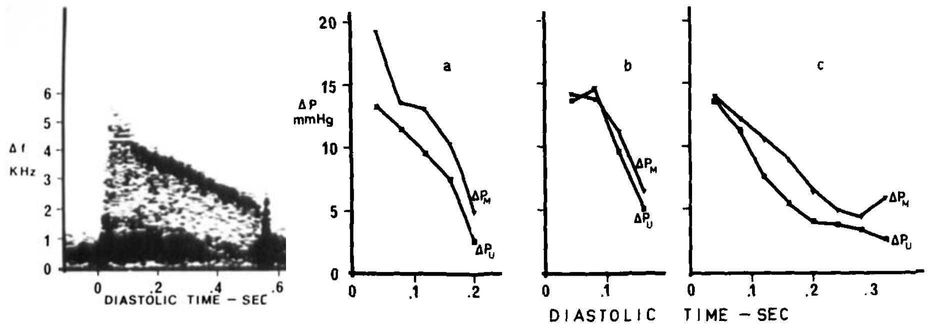

Figure 1.3: In 1976, Holen *et al.* presented the first attempt to measure intravascular pressure non-invasively using medical ultrasound. The Doppler shift frequency spectrum seen to the left is acquired from the mitral valve, and the three graphs to the right show pressures estimated from the peak velocity using an orifice equation, (ΔP_U). Here, the obtained results are compared to pressure measurements performed with a cardiac catheter, (ΔP_M).

Dumesnil, et al. 2003; Garcia, Pibarot, and Durand 2005; Greenberg et al. 2001; Meinders and Hoeks 2004; Ohtsuki and Tanaka 2003; Reddy et al. 2003; Thomas and Popovic 2005; Yotti et al. 2004), but none of these have as yet successfully managed to supercede pressure catheters.

1.2.2 Magnetic resonance imaging

Deriving intravascular pressure changes from blood flow has also been explored in the field of MRI. Here, the ability to detect all three spatial velocity components (Kilner et al. 1993) offers the advantage of deriving fields of pressure gradients without uncertainties related to the neglection of the out-of-plane movement (Bock et al. 2011). Most MRI studies on deriving pressure from flow data are based on the Navier-Stokes equations using either vector velocity data (Bock et al. 2011; Ebbers et al. 2001; Herment et al. 2008; Moftakhar et al. 2007; Thompson and McVeigh 2003) or directly from acceleration data (Tasu et al. 2000). The spatial resolution in MRI provides a solid basis for calculating the convective acceleration used in the Navier-Stokes equations. However, flow estimation techniques in MRI rely on data acquisitions from several cardiac cycles through electrocardiogram gating to image a full cycle. This prevents real-time imaging of pressure variations and is further at the expense of the temporal resolution. The degradation of the temporal resolution impairs the estimation of the local acceleration. This affects the accuracy of the pressure estimator when using equations such as the Navier-Stokes. The lack of a proper temporal resolution poses a significant downside to MRI, when measuring on highly dynamic flow systems such as larger arteries. Furthermore, MRI requires each velocity component to be measured separately. This precludes simultaneous data acquisition of the vector velocity fields used for deriving the intravascular pressure.

1.2.3 Particle image velocimetry

In optics, velocity fields are also used in deriving pressure. Particle image velocimetry (PIV) illuminates tracer particles seeded into a fluid of interest, thereby visualizing the movement and trajectory of the flow that carries the particles around (Adrian and Yao 1985). Modern PIV systems are capable of detecting 3-D fluid movement; this has paved the way for a wide range of non-invasive techniques for determining pressure flow fields (Charonko et al. 2010; Kajitani and Dabiri 2005; Oudheusden 2013). Although, less-clinical relevant, this field of optics has published some of the most advanced studies on deriving pressure from vector velocity fields, and many of their findings and conclusions can be used when deriving in-vivo pressure using for example medical ultrasound or MRI techniques.

1.3 Objective

The thesis seeks to explore and develop a method for determining pressure changes from vector velocity ultrasound data. Prior to this, new estimators for minimizing the transfer of noise from the velocity estimate onto the derived pressure is warranted. Hereafter, the developed technique is evaluated on fabricated flow phantoms, and the results are compared with simulation models to demonstrate the feasibility of the technique. Finally, the developed method is tested in-vivo over the carotid bifurcation on healthy volunteers.

1.4 Scientific contributions

The thesis compiles the research presented in two manuscripts that have been submitted for publication in ISI journals, and two patent applications that were taken up by Analogic. Additionally, four conference proceedings and an abstract are included in the project. Besides the included papers, the author has contributed to publications on flow rate estimation both experimentally and during clinical settings. A full publication list is given below.

1.4.1 Journal papers

I **J. B. Olesen**, M. S. Traberg, M. J. Pihl, and J. A. Jensen. Noninvasive estimation of 2-D pressure gradients in steady flow using ultrasound. In *IEEE Trans. Ultrasons., Ferroelec., Freq. Contr.*, Vol. 61, No. 8, 2014, p. 1409-1418.

II **J. B. Olesen**, C. A. Villagómez-Hoyos, M. S. Traberg, A. J. Y. Chee, B. Y. S. Yiu, C. K. Ho, K. L. Hansen, A. C. H. Yu, M. B. Nielsen, and J. A. Jensen. Non-invasive estimation of intravascular pressure changes using vector velocity Ultrasound. In *IEEE Trans. Ultrasons., Ferroelec., Freq. Contr.*, Submitted on November 3, 2015.

1.4.2 Conference papers

III **J. B. Olesen**, M. S. Traberg, M. J. Pihl, and J. A. Jensen. Non-invasive measurement of pressure gradients using ultrasound. In *Proc. SPIE Ultrasound Imaging. Symp.*, Vol. 8675, p. 11, 2013.

IV **J. B. Olesen**, M. S. Traberg, M. J. Pihl, P. M. Hansen, M. B. Nielsen, and J. A. Jensen. Non-invasive Measurement of Pressure Gradients in Pulsatile Flow using Ultrasound. In *Proc. IEEE Ultrasons. Symp.*, p. 2022-2025, 2013.

V **J. B. Olesen**, C. A. Villagomez-Hoyos, M. S. Traberg, and J. A. Jensen. Non-invasive estimation of pressure gradients in pulsatile flow using ultrasound. In *Proc. IEEE Ultrasons. Symp.*, p. 2257-2260, 2014.

VI **J. B. Olesen**, C. A. Villagomez-Hoyos, M. S. Traberg, and J. A. Jensen. Non-invasive Estimation of Intravascular Pressure Changs using Ultrasound. In *Proc. IEEE Ultrasons. Symp.*, p. TBC, 2015.

1.4.3 Abstracts

I **J. B. Olesen**, C. A. Villagomez-Hoyos, M. S. Traberg, A. J. Y. Chee, B. Y. S. Yiu, C. K. Ho, A. C. H. Yu, and J. A. Jensen. Preliminary investigation of an ultrasound method for estimating pressure changes in deep-positioned vessels. In *SPIE Medical Imaging 2016*, Accepted for oral presentation.

1.4.4 Patent application

I **J. B. Olesen**, C. A. Villagomez-Hoyos, and J. A. Jensen. Non-invasive Estimation of Intravascular Pressure Changes using Vector Velocity Ultrasound (US), International Patent Application, filed on March 3, 2015, number: ANA1268-WO (BKM-10-7778-PCT).

II **J. B. Olesen**, C. A. Villagomez-Hoyos, and J. A. Jensen. Flow Acceleration Estimation Directly From Beamformed Ultrasound Data, International Patent Application, filed on September 23, 2015, number: ANA1282-WO-US (BKM-10-7837-US-PCT).

1.4.5 Second-author journal paper

SA-I P. M. Hansen, **J. B. Olesen**, M. J. Pihl, T. Lange, S. Heerwagen, M. M. Pedersen, M. Rix, L. Lönn, J. A. Jensen, and M. B. Nielsen. Volume Flow in Arteriovenous Fistulas using Vector Velocity Ultrasound. *Ultrasound Med. Biol.*, Vol. 40, No. 11, p. 2707-2714, 2014.

SA-II J. Jensen, **J. B. Olesen**, M. B. Stuart, P. M. Hansen, M. B. Nielsen, and J. A. Jensen. Vector Velocity Volume Flow Estimation: Sources of Error and Corrections. *Ultrasonics*, Submitted on October 16, 2015.

1.4.6 Additional papers and patents

Additional publications are listed here in chronological order.

2013

- J. A. Jensen, M. J. Pihl, **J. B. Olesen**, P. M. Hansen, K. L. Hansen, M. B. Nielsen. New Developments in Vector Velocity Imaging using the Transverse Oscillation Approach. *Proc. SPIE Ultrasound Imaging. Symp.*, p. 86750F-1–86750F-19, 2013.

- P. M. Hansen, S. Heerwagen, M. M. Pedersen, M. Rix, L. Lönn, M. B. Nielsen, **J. B. Olesen**, M. J. Pihl, and J. A. Jensen. Vector volume flow in arteriovenous fistulas. *Proc. IEEE Ultrasons. Symp.*, p. 2026-2029, 2013.

2014

- J. Jensen, **J. B. Olesen**, P. M. Hansen, M. B. Nielsen, and J. A. Jensen. Accuracy and Sources of Error for an Angle Independent Volume Flow Estimator. *Proc. IEEE Ultrasons. Symp.*, p. 1714-1717, 2014.

2015

- A. H. Brandt, **J. B. Olesen**, K. L. Hansen, M. Rix, J. A. Jensen, and M. B. Nielsen. Surveillance of hemodialysis vascular access with ultrasound vector flow imaging. *Proc. SPIE Ultrasound Imaging. Symp.*, p. 94190U-1–94190U-7, 2015.

- K. L. Hansen, H. Møller-Sørensen, J. Kjaergaard, M. B. Jensen, J. T. Lund, M. M. Pedersen, **J. B. Olesen**, J. A. Jensen, and M. B. Nielsen. Vector flow imaging compared with conventional Doppler ultrasound and thermodilution for estimation of blood flow in the ascending aorta. *Ultrasonic Imaging*, Accepted for publication on November 10, 2015.

2016

- C. A. Villagomez-Hoyos, M. B. Stuart, **J. B. Olesen**, and J. A. Jensen. Novel Tissue Filtering Approach For Perfusion and Slow-Flow Imaging, International Patent Application, filling date on January 19, 2016, number: ANA1293-WO.

1.5 Outline of the thesis

The structure of the thesis is two-fold. The first two chapters introduce the technical background related to the conducted research. The subsequent chapters concern the scientific contributions and are structured to demonstrate the progress of project. The thesis is presented as a whole, and the chapters are intended to be read in succession. To improve the flow of the text, not all details from the described studies have been included, and the reader is therefore occasionally referred to the appended papers.

Chapter 2 introduces the theory and the previous published literature on deriving pressure changes from velocity data. The chapter, further, describes a filtering approach for finding derivatives from estimated flow data, using a method developed by Savitzky and Golay in 1964.

Chapter 3 concerns a theoretical description of the two vector velocity estimators that are employed in the project. First presented is the Transverse Oscillation approach, which is capable of measuring the two in-plane velocity components by manipulating the sensitivity of the ultrasound probe. Further, examples of vector flow imaging acquired by a commercial ultrasound system using Transverse Oscillation are shown. The chapter continues by explaining the second flow estimator, which is based on synthetic aperture imaging. Here, vector velocities are found by cross-correlating a series of directional lines beamformed in the direction of the flow.

Chapter 4 presents an overview of the results obtained in the first peer-reviewed paper appended in the project. The study investigates the feasibility of deriving pressure gradients from vector velocity data acquired using a commercial ultrasound scanner. The chapter concludes with a discussion of the concerns related to calculating pressure gradients from velocity data.

Chapter 5 introduces a technique for deriving temporal accelerations from noisy velocity data. The technique performs a decomposition of the measured flow profile into a series of sinusoids. The sinusoids are then weighted and phase-modulated before reassembled to form a filtered velocity profile and its first-order derivative with only minimum noise contamination. The proposed technique was taken up by Analogic, who in collaboration with the author wrote the first patent proposal included in the project.

Chapter 6 presents an overview of the second peer-reviewed paper that is appended. The study investigates a method for deriving intravascular pressure changes along streamlines. The method is tested experimentally on fabricated flow phantoms and evaluated by comparison to numerical simulation models. Additionally, the chapter presents the first results from testing the method in-vivo on two healthy volunteers before it concludes with a discussion on limitations.

Chapter 7 deviates from the previous chapters as it presents a new flow estimator that not only relates to the detection of pressure changes, but also can be found valuable in other clinical aspects. The chapter describes an estimator that calculates the temporal/spatial acceleration of flow directly from beamformed ultrasound data, by introducing a double cross-correlation scheme. The developed technique was taken up by Analogic and a second patent proposal was written.

Chapter 8 concludes the thesis by summarizing some of the major learnings that were achieved in the process of deriving pressure changes from vector velocity ultrasound data. The chapter further provides suggestions for future research, before putting the project into perspective.

CHAPTER 2

Pressure Estimation Based on Vector Velocity Data

A wide avenue of different approaches has been established in the pursue of deriving transstenotic pressures from measured velocity data. Holen *et. al* (Holen, Aaslid, and Landmark 1976) started in 1976 using an orifice equation similar to the one introduced by Gorlin and Gorlin (R. Gorlin and S. G. Gorlin 1951). The equation related the rate of flow through an orifice to its approximated shape and the peak velocity through it. The approach was later shown to be greatly dependent on measuring the orifice shape correctly, which in clinical use gave rise to highly erroneous pressure estimates (Skjaerpe, Hegrenaes, and Hatle 1985). Instead, research groups began to use the Bernoulli equation, usually implemented in its simplified form, where viscous and temporal effects are neglected (Teirstein, Yock, and Popp 1985). The main advantage of the simplified Bernoulli equation ($\Delta P = 4V_{distal}^2$) is that the relative pressure drop is obtainable through only a single velocity estimate found distally to the lesion. This is, however, also the major disadvantage of the technique, as it becomes greatly dependent on the operator's ability to detect the true peak velocity. Further, for the method to be valid it requires the distal peak flow to be much greater than the peak flow seen proximate to the constriction, thus, limiting the method to only severe cases of arterial narrowing (Yoganathan et al. 1988).

Recent developments in ultrasound flow estimators provide the opportunity of studying blood flow in two, and three dimensions, independently of the insonifying angle (Bohs et al. 2000; Bonnefous 1988; Dunmire et al. 2000; Holbek et al. 2014; Jensen 2003; Jensen and Munk 1998; Jensen and Nikolov 2002; Løvstakken et al. 2006; Pihl and Jensen 2014; Pihl, Stuart, et al. 2014; Tortoli, Bambi, and Ricci 2006; Udesen et al. 2008). This allows for a better understanding of in-vivo flow patterns, making it possible to derive features such as vascular pressure, through a more general approach, such as the Navier-Stokes equations.

2.1 Navier-Stokes equations

The following section describes how intravascular pressure gradients can be calculated from the Navier-Stokes equations:

$$\rho\left[\frac{\partial\vec{v}}{\partial t}+\vec{v}\cdot\nabla\vec{v}\right]=-\nabla p\,+\,\rho\vec{g}\,+\,\mu\nabla^2\vec{v}, \tag{2.1}$$

presuming the conservation of mass and linear momentum. Eq. (2.1) describes the development of a fluid's velocity field $\vec{v}(\vec{r},t)=(v_x(t),v_y(t),v_z(t))$ by relating the forces acting on an incompressible volume to its acceleration and density throughout time, t, and space, $\vec{r}$. The left-hand side sums the local $\frac{\partial\vec{v}}{\partial t}$ and convective fluid acceleration $\vec{v}\cdot\nabla\vec{v}$, where ρ is the density of the fluid and ∇ is the spatial differential operator $(\frac{\partial}{\partial x},\frac{\partial}{\partial y},\frac{\partial}{\partial z})$. The right-hand side shows the surface and volume forces that are responsible for the acceleration of the fluid. The forces constitute a pressure drop $-\nabla p$, a gravitational force $\vec{g}$, and a viscous drag caused by the viscosity of the fluid $\mu\nabla^2\vec{v}$, where $\nabla^2\vec{v}$ is the Laplacian of the velocity field. The gravitational term is usually neglected, as a patient undergoing an ultrasound scan is placed in a supine position, hence, the buoyancy force cancels out the gravitational force.

For most clinical applications, the effect of the viscous term in (2.1) can be omitted, as this has no significant influence on the net-force in comparison with the inertial forces. This is especially the case in larger vessels for which the area of the boundary layer is small compared with the flow region beyond this layer, where flow is said to behave as an inviscid fluid (Prandtl 1952; Wood 1999). A way of determining the ratio of inertial forces to viscous forces is by studying the Reynolds number, Re. The Reynolds number emerges from rewriting the Navier-Stokes equations into a dimensionless form (Truskey, Yuan, and Katz 2004) and is expressed as,

$$Re=\frac{inertial\,forces}{viscous\,forces}=\frac{\rho\langle L\rangle\langle v\rangle}{\mu}. \tag{2.2}$$

Here $\langle L\rangle$ and $\langle v\rangle$ are characteristic measures of the flow system, e.g. the diameter of the vessel and the average flow velocity, respectively. Flow conditions, for which the Reynolds number is larger than unity, are governed by inertial forces, while a smaller Reynolds number indicates that flow is dominated by viscous forces.

Keeping the viscous term in (2.1) but neglecting the gravitational forces gives the following expression when solving for the pressure gradient term;

$$\nabla p\;=-\rho\left[\frac{\partial\vec{v}}{\partial t}+\vec{v}\cdot\nabla\vec{v}\right]\,+\,\mu\nabla^2\vec{v}. \tag{2.3}$$

Eq. (2.3) states that all three spatial vector components of $\vec{v}(\vec{r},t)$ must be known to estimate the pressure gradient ∇p. However, this study employs flow estimators that measure the 2-D in-plane velocity vector $\vec{v}(\vec{r},t)=(v_x(t),v_z(t))$, thus, the proposed methods are developed assuming that the out-of-plane velocity $v_y(t)$ is zero. The methods can however, easily be extended if full 3-D velocity information is available. Such data become accessible using for instance a matrix probe, and the velocity estimator proposed by Pihl and Jensen (Pihl and Jensen 2011; Pihl and Jensen 2012). The reduced form of (2.3) is expressed here in rectangular coordinates,

$$\begin{bmatrix} \dfrac{\partial p}{\partial x} \\ \\ \dfrac{\partial p}{\partial z} \end{bmatrix} = -\rho \begin{bmatrix} \dfrac{\partial v_x}{\partial t} + v_x \dfrac{\partial v_x}{\partial x} + v_z \dfrac{\partial v_x}{\partial z} \\ \\ \dfrac{\partial v_z}{\partial t} + v_x \dfrac{\partial v_z}{\partial x} + v_z \dfrac{\partial v_z}{\partial z} \end{bmatrix} + \mu \begin{bmatrix} \dfrac{\partial^2 v_x}{\partial x^2} + \dfrac{\partial^2 v_x}{\partial z^2} \\ \\ \dfrac{\partial^2 v_z}{\partial x^2} + \dfrac{\partial^2 v_z}{\partial z^2} \end{bmatrix}. \tag{2.4}$$

From (2.4) it becomes apparent that the two in-plane pressure gradients $\frac{\partial p}{\partial x}$, and $\frac{\partial p}{\partial z}$ depend entirely on the method's ability to derive the temporal and spatial acceleration. Methods that depend on finding derivatives from discrete velocity estimates are, however, highly sensitive to noisy data. Numerical noise from the velocity estimator, or electronic noise from the sampling system, poses a significant threat, as the difference quotient basically works as a high-pass filter, thereby, enhancing whatever high-frequent noise that is present in the original estimates. To avoid drowning the acceleration estimates in noise, an approach based on polynomial filtering is initially proposed for obtaining the different derivatives.

2.2 Calculating derivatives based on Savitzky-Golay filtering

The derivatives in (2.4) can be calculated from vector velocity data using a polynomial smoothing filter. Such method fits a low-degree polynomial to a subset of adjacent data points by the linear least-squared method. If data points are equally spaced, an analytical solution to the least-squared method can be reached by expressing it as a generic set of convolution coefficients. Applying the convolution coefficients onto the subset of data points produces an estimate of the smoothed signal together with its derivatives at the central point of the subset. Smoothing a data set using convolution coefficients was first introduced by Savitzky and Golay in 1964 (Savitzky and Golay 1964). The values of the convolution coefficients depend solely on the size of the subset and the order of the polynomial that is fitted to the subset. For instance, fitting a second-order polynomial to a subset of five data points gives the following equations for approximating the zero, first, and second-order derivatives (Orfanidis 1996):

$$y_n = \frac{1}{35}(-3x_{n-2} + 12x_{n-1} + 17x_n + 12x_{n+1} - 3x_{n+2}), \tag{2.5}$$

$$\dot{y}_n = \frac{1}{35}(-7x_{n-2} - 3.5x_{n-1} + 3.5x_{n+1} + 7x_{n+2}), \tag{2.6}$$

$$\ddot{y}_n = \frac{1}{35}(10x_{n-2} - 5x_{n-1} - 10x_n - 5x_{n+1} + 10x_{n+2}). \tag{2.7}$$

Eqs. (2.6)–(2.7) find the first, and second-order derivatives of y_n at x_n, where n is the central data point of the subset. Each window of five data points is weighted by the

Savitzky-Golay convolution coefficients, $\vec{B}_k$, which for the two derivatives are, $\vec{B}_1 = \frac{1}{35}\left[-7, -3.5, 0, 3.5, 7\right]$ and $\vec{B}_2 = \frac{1}{35}\left[10, -5, -10, -5, 10\right]$, respectively.

CHAPTER 3

Vector Velocity Estimation

Abnormal blood flow is considered a diagnostic marker in determining the physiological state of a diseased vessel. Measuring flow velocities is therefore of great importance in medical ultrasound, as it provides a non-invasive tool for monitoring blood flow. Commonly used ultrasound techniques for measuring blood velocities are spectral Doppler and color flow mapping (CFM). Here, ultrasound pulses are emitted into the tissue at a certain pulse repetition frequency. Each pulse returns an echo that is recorded by the transducer. If the backscattering tissue moves in-between successive emissions, there will be a slight time-shift between the received echoes. From this shift, the velocity of the moving scatterer can be found. However, both spectral Doppler and CFM suffer from the limitation that they are only capable of detecting movement parallel to the ultrasound beam. Therefore, in situations where blood moves at an angle relative to the ultrasound beam, the measured flow needs to be compensated for by that angle, and this is performed manually by the operator. The compensation is done by dividing the measured velocity with cosine to the angle, α, between the emitted beam and the position of the vessel wall, $\frac{1}{\cos(\alpha)}$. Hence, finding the actual blood velocity is greatly dependent on the operator's ability to correct for the exact angle - a dependency that increases with the angle, as illustrated in Fig. 3.1. The angle-dependency hinders the possibility of measuring blood

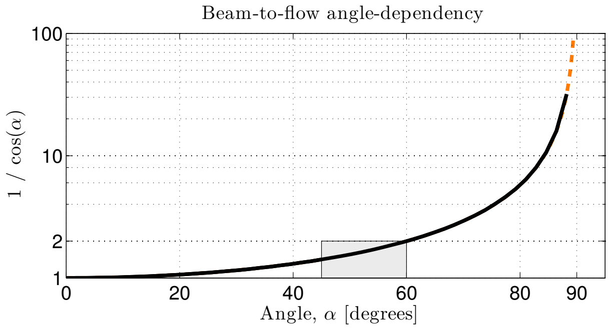

Figure 3.1: Blood velocity estimation in a vessel that is oriented at an angle, α, to the emitted ultrasound beam needs to be compensated by a factor of $\frac{1}{\cos(\alpha)}$. The compensation factor increases exponentially with an increasing angle, thus, more weight is put on the operator's ability to detect, and compensate for the beam to flow angle.

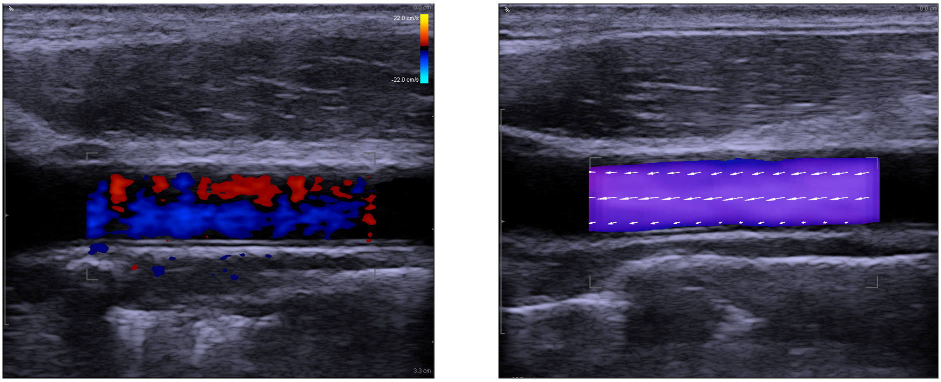

(a) (b)

Figure 3.2: (a) and (b) show blood flow through a vessel that lies perpendicular to the insonifying beam, using conventional color flow mapping, and Transverse Oscillation, respectively. (a) reveals that the conventional method is incapable of detecting the actual flow, as the movement of the blood causes no shift between successive echoes received by the transducer. The same situation is displayed in (b), but now using the TO approach. Here, the resulting image shows an unambiguous map of the flow with vector velocities indicating both directions and magnitudes of the backscattering blood cells. The figure is from (BK Medical 2015).

flow in vessels oriented at an angle close to 90°, which is unfortunate as most superficial vessels lie perpendicular to the skin, and therefore also to the insonation angle. Literature suggests that the angle of insonation should be kept between 45° and 60° to obtain the must reliable flow estimate (Kruskal et al. 2004).

As mentioned in Chapter 2, several techniques have been proposed to remedy the angle-dependency problem. Among the techniques are Transverse Oscillation (TO) as suggested by Jensen and colleagues (Jensen 1996a, 2000; Jensen and Munk 1998; Udesen and Jensen 2006), and 2-D directional beamforming for flow imaging as introduced by Nikolov and Jensen (Jensen and S. I. Nikolov 2002). Both techniques play a vital role in this project as they are both employed for acquiring the velocity data used in the proposed pressure estimator. Therefore, for the remainder of this chapter only these two techniques are explained, thereby limiting the technical background to the velocity estimators implemented. Further, to date, the TO approach is the only vector velocity estimator implemented on a commercial available platform (Hansen et al. 2011). An example of the implementation is seen in Fig. 3.2, where blood flow through a vessel lying perpendicular to the insonation angle is measured by conventional color flow mapping, and the TO approach.

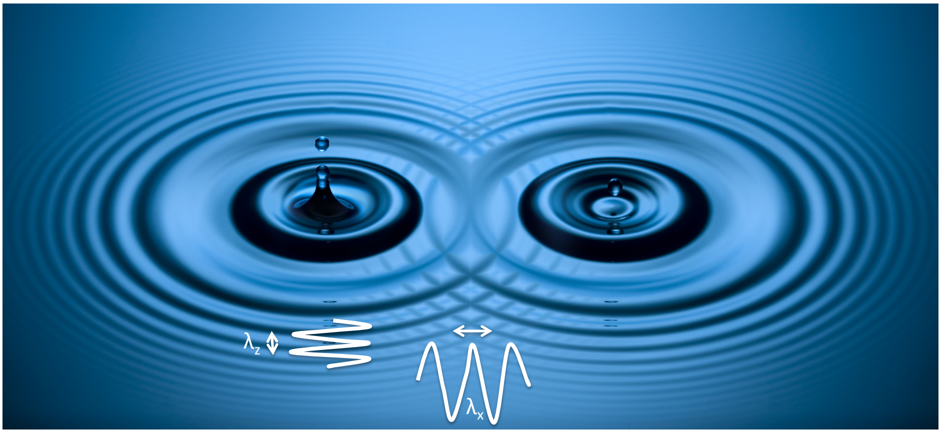

Figure 3.3: Two rain drops hitting a still water surface generate oscillations that travel out from their origins. In regions where the two oscillation patterns interfere, a double-oscillating field is created. The figure is from (Bredeson 2015)

3.1 Transverse Oscillation

The basic idea of Transverse Oscillation follows the same mechanism as in conventional velocity estimation, namely the build-up of an oscillating pressure field. In conventional Doppler techniques, the oscillating field is generated along the direction of the propagating pulse, from which the axial velocity component can be determined. Whereas, for TO a transverse oscillation is introduced perpendicular to the propagation of the pulse, and this enables detection of the lateral velocity component. The generation of the transverse oscillation is best described by considering the interference pattern occurring in the far-field when two point sources are emitting pulsed signals simultaneously. The interference pattern forms a double-oscillating field that varies spatially in respect to axial oscillations, seen along the direction of the propagating wave, and lateral oscillation seen in the regions where the two waves meet. This is sought illustrated by the two droplets in Fig. 3.3. The axial wavelength, λ_z, is determined by the center frequency of the emitted pulse and the speed of which it is travelling. The lateral oscillation wavelength is a bit more complex, and changes as a function of both the axial wavelength, depth, and the distance between the two point sources. Given that the Fraunhofer approximation is valid, the spatial wavelength of the transverse oscillation can be approximated as (Udesen and Jensen 2006),

$$\lambda_x(z) = 2\lambda_z \frac{z}{d} \ . \tag{3.1}$$

Here d is the distance between the point sources, z is the depth, and λ_z is the spatial period of the emitted pulse. The ratio between the depth and the distance between the sources is also known as the F-number, $F_{\#} = \frac{z}{d}$.

EMULATING TWO DROPLETS IN AN ULTRASOUND SYSTEM

The analogy of creating a double-oscillating field using two droplets can be translated to an ultrasound system, by regarding the transducer's elements as sources that generates propagating waves. Then, an aperture transmitting pulses simultaneously from two distinct areas of the probe will generate an oscillating pressure field, equivalent to that of the two rain drops. An example of such is seen in Fig. 3.4(b). Here, a double-oscillating field is created using the apodization function introduced by (Jensen and Munk 1998). The function describes two windows of active elements, as illustrated on top of the transducer in Fig. 3.4(a). Whether this double-windowed apodization function is implemented in the transmit stage, or in the receive stage of the emission sequence, is indifferent for the resulting pressure map observed by the probe. Thus, any apodization function comprising two distinct peaks, as in Fig. 3.4(a), will create a double-oscillating sensitivity pattern from where detection of the axial and lateral velocity component is possible.

DIRECTIONAL INFORMATION OF THE FLOW

In axial velocity estimation, a Hilbert transformed is performed to yield the in-phase signal and the quadrature signal. The two signals are characterized by being 90° phase shifted to each other, which allows for calculating the instantaneous phase of the received signal. Calculating the phase is essential as this will show changes across multiple emissions, if the targeted tissue moves between successive pulses. The sign of the phase change, further, reveals the direction of the movement. Therefore, studying the in-phase, and the quadrature signals across several emissions, enables detection of the flow direction. For the conventional flow estimator, these two signals are obtained by sampling the received signal at a frequency that is four times greater than the center frequency of the emitted pulse, thereby, automatically having a 90° phase shift between successive samples. Sampling at four times the center frequency is equivalent to sampling the received signal at instances that are spatially separated by $\lambda_z/4$ in the axial direction. To achieve the same type of spatial sampling in the lateral direction, two lines separated by $\lambda_x/4$ are needed to be beamformed. An example of this is shown in Fig. 3.4(a), where two lines are beamformed in receive. The expanding distance between the lines is the result of the lateral wavelength increasing as a function of depth, see (3.1).

DISPLAYING THE 2-D VECTOR VELOCITY FIELD

The spatial quadrature signals found in both the axial and the lateral direction enables determination of the phase change occuring in these directions. The size of the calculated phase change is then proportional to the velocity of the moving scatterer. How velocities

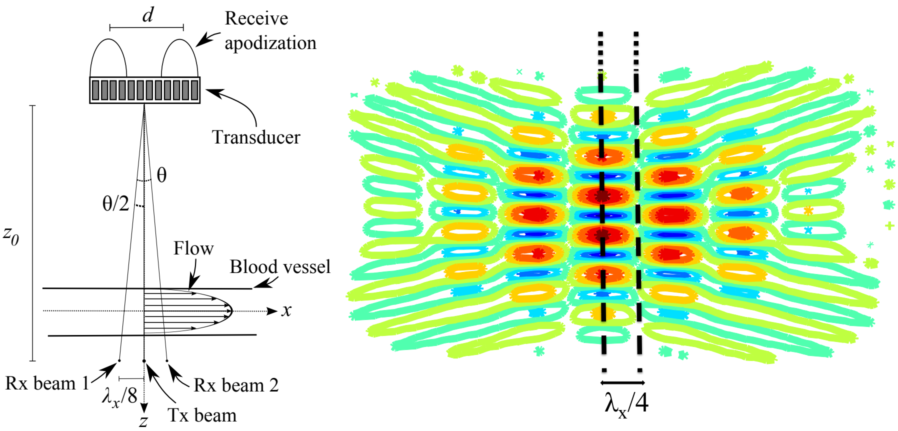

(a) (b)

Figure 3.4: The top part of (a) illustrates the two apodization windows needed to generate a double-oscillating field in either transmit of receive. The two angled lines that originate from the surface of the transducer indicate where to beamform in receive to obtain the in-phase, and the quadrature signal in the lateral direction. The field in (b) shows the double-oscillating field that is generated by the TO apodization function. The figures are from (Jensen and Munk 1998).

are derived, based on change in phases, is described in detail by Jensen (Jensen 1996b, 2001). From the above, it follows that by transmitting a conventional ultrasound pulse and receiving using either conventional apodization, or a double-windowed function, it is possible to measure the two in-plane velocity components. The components are then superimposed onto a B-mode image, thereby, visualizing the 2-D vector velocity field. An example of such is illustrated in Fig. 3.2, where a screen dump visualizing the result of having TO implemented on a commercial platform, is displayed.

3.2 Synthetic aperture flow imaging

Currently, the implementation of TO on modern commercial scanners generates vector flow images by sequentially probing in the different directions of the image. Therefore, dependent on the size of the image and the desired penetration depth, the scanners are confined to frame rates of 15 Hz – 30 Hz. Generally, such frame rates are too low for capturing all of the flow features occurring during a cardiac cycle, especially when complex flow is present. Further, the sequential probing prevents generation of high-quality 3-D flow images (S. I. Nikolov and Jensen 2003).

As an alternative the use of broader beams was proposed. A broader beam illuminates a larger region than conventional line-by-line scanning. This means that more image lines can be beamformed simultaneously, thus, reducing the time spend on constructing the image (Shattuck et al. 1984). However, doing so led to the generation of wider side-lobes and therefore degradation of the image quality. To retrieve the quality of the image, approaches such as synthetic aperture imaging (SAI) were developed for ultrasound systems. SAI is capable of producing images at high temporal resolution, while maintaining a spatial resolution equivalent to conventional ultrasound imaging techniques. This is, however, at the expense of higher computational load compared with conventional techniques. The general concept of SAI, and how this can be used for estimating vector flow images, is described in the following.

3.2.1 Synthetic aperture imaging

In synthetic aperture imaging, diverging waves are emitted from the aperture by placing virtual sources behind the transducer (Bae and Jeong 2000; Frazier and O'Brien 1998; Karaman, Li, and O'Donnell 1995; S. I. Nikolov and Jensen 2002; O'Donnell and Thomas 1992). The backscattered signals are then received by all the individual transducer elements, before focusing the data in every direction of the scan plane, producing a full image from only a single firing. Due to the unfocused transmission, the image is said to have a low resolution where only focusing in receive is possible. So, to recover the missing effect of not having a transmit focus, multiple low resolution images are combined. This essentially creates a high resolution image that is focused synthetically in transmit, and thereby creates an image that is fully focused in every image point. An illustration of the technique is shown in Fig. 3.5. The number of images or emissions combined to form the high resolution image determines the contrast of the image. Generally, to achieve the same image contrast as in conventional line-by-line imaging, the same number of emissions as lines in the image, is required. The major advantage of SAI, however, becomes apparent when updating the acquired image. Whereas conventional imaging requires a whole new set of focused emissions to build up the image line by line, SAI can update the full image by emitting once (Jensen, S. Nikolov, et al. 2006). This essentially breaks with conventional way of generating an ultrasound image, and enables a temporal resolution proportional to the pulse repetition frequency while remaining fully focused everywhere in the image.

Another major advantage of SAI is the width of the transmitted beam. As expanding waves are emitted, illuminating the whole region of interest, it is possible to beamform lines in any direction, and not only in the narrow beam profile available by conventional focused emissions. This can be used for directional tracking of fluid particles (Jensen 2003; Jensen and Lacasa 1999).

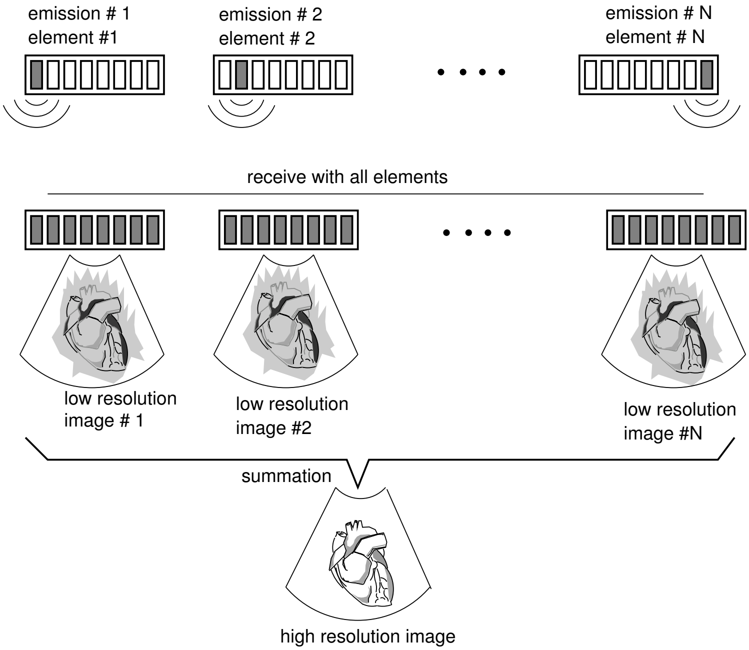

Figure 3.5: Basic principle of synthetic aperture imaging. The figure is from (S. I. Nikolov 2001)

3.2.2 Velocity estimation using SAI and directional beamforming

Insonifying a broad region of interest, allows focusing in any direction, from where velocity estimation is possible. Consider for instance Fig. 3.6, where only two distinct emissions are used for simplicity. The figure displays four signals from a single moving point target measured at two different aperture configurations. The first and third transmission are made with one type of aperture, while transmission two and four are acquired with another type of aperture configuration. They pairwise form two identical point spread functions that are spatially shifted as the targeted scatterer moves between emissions. The velocity and the direction of the moving target can be determined through directional beamforming using a two-fold process. First, a set of velocities is calculated for each emission pair, then, the velocity sets from the two emission pairs are compared. The comparison will show a crossing between the estimated velocities, and this crossing reveals the correct velocity and the direction of the moving scatterer.

Each set of velocities is found by cross-correlating directional lines that are beamformed in numerous directions within every low resolution image pair. For each directional line, a velocity is estimated. Repeating this for a variety of directional lines will essentially

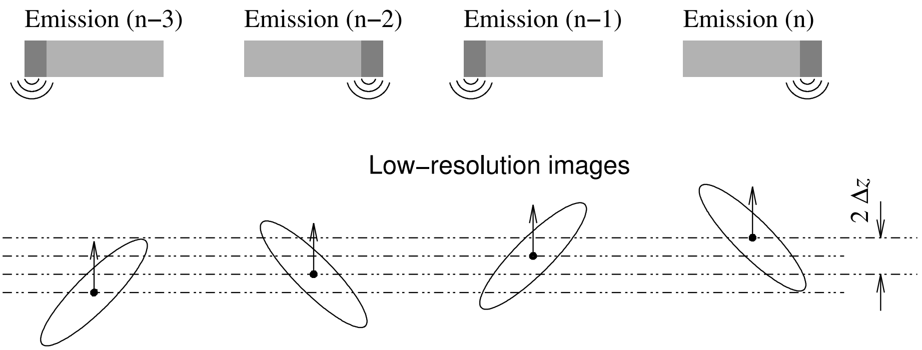

Figure 3.6: The figure shows four signals of a moving point target. The four signals are measured at two different aperture settings, where transmission one and three form one emission pair and transmission two and three form another. The figure is modified from (S. I. Nikolov 2001)

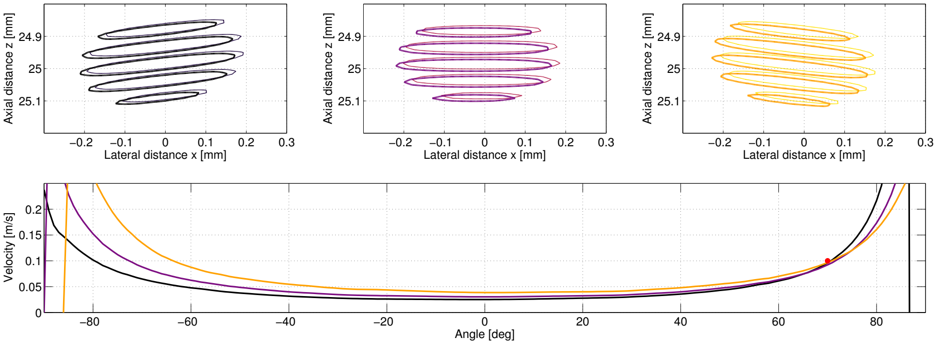

Figure 3.7: Signals measured of a point target moving with $0.1\,\mathrm{m\,s^{-1}}$ at an angle of 70°. Top row shows three emission pairs measured with three different aperture configurations. Bottom row displays three velocity-to-angle profiles found from the three emissions pairs, respectively. The actual velocity of the moving target is found at the intersection of the three lines, which here is marked by the red dot. The figure is from (Villagomez-Hoyos et al. 2015)

produce a velocity-to-angle profile, such as the curves shown in the bottom of Fig. 3.7. The profiles reveal a point of intersection, and this point represents the true velocity and it's appurtenant flow angle.

The advantage of estimating flow movement using SAI directional beamforming is that the velocity can be accurately found in any direction, and independently of the beam-to-flow angle. Further, it enables generation of a vector flow image using only few emissions, whereas a commercial scanner would need hundreds of emissions to fill out a single vector flow map (VFM). Also, as data are continuously available it allows for better clutter filtering as the length of the filter can approach any optimal size, and further, opens up for the possibility of using adaptive filters.

CHAPTER 4

Study I
Non-invasive Estimation of 2-D Pressure Gradients in Steady Flow Using Ultrasound

Summary *This chapter presents an overview of the findings made in the first peer-reviewed paper that is included in the project. The paper concerns a study that derives pressure gradients from vector velocity data acquired using a commercial ultrasound scanner. First part of the chapter provides a brief description of the paper's overall purpose, and the experimental set-up used for achieving this. For a further in-depth explanation of the technical details, the reader is referred to Paper I in appendix. The second part presents the obtained results, before concluding the chapter with a discussion of the concerns that should be considered when deriving pressure gradients from vector velocity data.*

4.1 Purpose

The paper introduces a technique for measuring 2-D pressure gradients in a steady flow environment based on TO velocity data. Measurements are performed using a commercially available ultrasound scanner equipped with a research interface that allows for extraction of beamformed data. Vector velocity imaging scans are made on a flow phantom that mimics a carotid bifurcation. Pressure gradients are then derived from the acquired flow data using a model based on the Navier-Stokes equations. Results are evaluated through comparison with a 3-D numerical simulation model. The study tests the hypothesis that pressure gradients can be measured non-invasively from vector velocity data acquired using an already clinical available ultrasound system.

4.2 Calculation of spatial derivatives

Given the steady nature of the investigated flow system, the suggested method is reduced to calculating pressure gradients from spatial velocity derivatives only,

$$\begin{bmatrix} \dfrac{\partial p}{\partial x} \\ \\ \dfrac{\partial p}{\partial z} \end{bmatrix} = -\rho \begin{bmatrix} v_x \dfrac{\partial v_x}{\partial x} + v_z \dfrac{\partial v_x}{\partial z} \\ \\ v_x \dfrac{\partial v_z}{\partial x} + v_z \dfrac{\partial v_z}{\partial z} \end{bmatrix} + \mu \begin{bmatrix} \dfrac{\partial^2 v_x}{\partial x^2} + \dfrac{\partial^2 v_x}{\partial z^2} \\ \\ \dfrac{\partial^2 v_z}{\partial x^2} + \dfrac{\partial^2 v_z}{\partial z^2} \end{bmatrix}. \tag{4.1}$$

Every derivative in (4.1) is calculated for a window of five adjacent data points by pairwise multiplying the window elements and the convolution coefficients. For instance, the axial velocity component and the derivatives that change with respect to this direction, are here calculated discretely for each position in the scan plane:

$$\frac{\mathrm{d}^k \tilde{v}_s(i,j)}{\mathrm{d}z^k} \approx \frac{1}{\Delta z^k} \sum_{p=i-h_w}^{i+h_w} v_s(p,j)\, B_k(p-(i-h_w)+1), \tag{4.2}$$

where k goes from 0 to 2, and s indicates either the axial direction, z, or the lateral direction, x. The position within each field is given by (i,j), and Δz is the sampling interval of the velocity field in the axial direction. The index number p, is found from half the window size of the selected subset, which is calculated by: $h_w = \frac{N_{set}+1}{2} - 1$, where N_{set} is the number of samples in the subset. Each window is weighted by the Savitzky-Golay convolution coefficients $\vec{B}_k$ as given in 2.2. For the lateral velocity component and its derivatives that change in this direction, the equation used is,

$$\frac{\mathrm{d}^k \tilde{v}_s(i,j)}{\mathrm{d}x^k} \approx \frac{1}{\Delta x^k} \sum_{p=j-h_w}^{j+h_w} v_s^T(p,i)\, B_k(p-(j-h_w)+1), \tag{4.3}$$

where v_s^T is the transposed of v_s, and Δx the sampling interval in the lateral direction.

4.3 Experimental set-up

A BK Ultrasound Pro Focus system (2202 Pro Focus UltraView, BK Ultrasound, Herlev, Denmark) is used for acquiring vector velocity data. Measurements are made during steady flow conditions on a C70-SSEA flow phantom (Shelley Medical Imaging Technologies, Toronto, Canada) using a linear array probe (BK8670, BK Ultrasound, Herlev, Denmark). The phantom models a carotid bifurcation having a constriction at the beginning of the internal branch reducing the cross-sectional area of the lumen by 70 %. The common part of the artery measures 8 mm in diameter, while the external and post-constriction internal branch measure 4.65 mm and 5.55 mm, respectively. A full representation of the

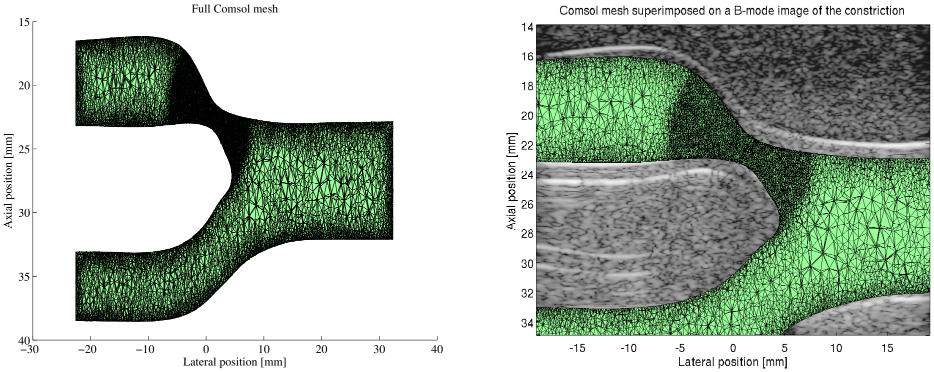

(a) (b)

Figure 4.1: (a) Full representation of a carotid flow phantom's fluid domain. The phantom is designed to have a $70\,\%$ constriction on the internal carotid artery. (b) B-mode image of the area insonified by the ultrasound probe plotted along with the mesh skeleton of the simulation model. The figures are from Paper III and Paper IV in the appendix.

phantom is seen in Fig. 4.1(a), and the section insonified by the ultrasound probe is shown in Fig. 4.1(b). The modeled vessel is embedded in agar to mimic the characteristics of human tissue, and it is encased in a rigid, airtight acrylic box with an acoustic window that makes it compatible with ultrasound imaging as well as MRI. The phantom is connected to a CompuFlow 1000 Flow system (Shelley Medical Imaging Technologies, Toronto, Canada) that is set to circulate a blood-mimicking fluid at a constant flow rate of $1.0\,\mathrm{mL\,s^{-1}}$.

4.3.1 Data acquisition using the commercial platform

Flow data are extracted from the ultrasound system using an in-house build research interface, designed by BK Ultrasound. The scanner is set to emit weakly-focused emissions at a pulse repetition frequency of $1.3\,\mathrm{kHz}$ for creating a duplex sequence of both B-mode and vector flow images. Each line of the vector flow map is found using an autocorrelation approach based on 16 sequential firings. Both axial and lateral velocities are calculated from the principles explain in Section 3.1. Here, a conventional pulse is focused a few centimeters below the center of the flow box, to ensure a wider pressure field at the vessel, where the build-up of a transverse oscillating field can be synthesized.

The connected research interface allows for extraction of already beamformed data, from which the axial and lateral velocity components are found. The axial velocity estimator takes in data that are beamformed conventionally, having a single apodization

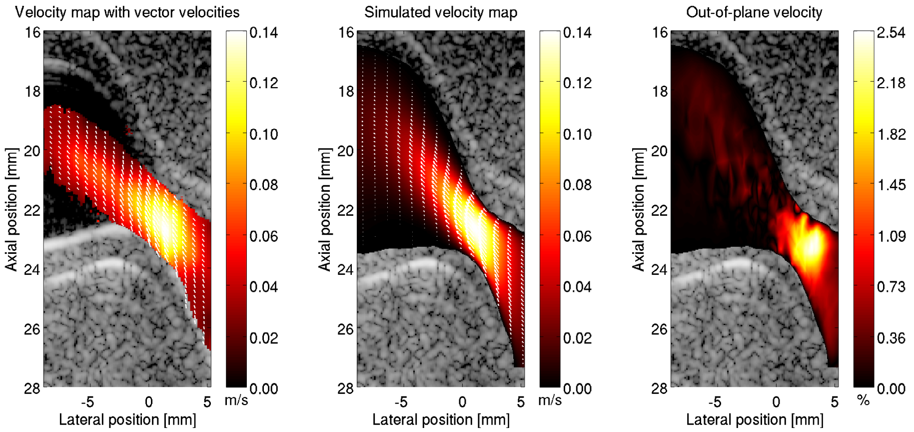

(a) (b) (c)

Figure 4.2: Vector velocity fields. (a) shows the mean estimated velocity field from the ultrasound data, while (b) shows the simulated velocity field. (c) shows the size of the out-of-plane simulated velocity component in reference to the simulated peak velocity. Note that the largest out-of-plane velocity is less than $3\,\%$ of the total velocity.

profile in receive, whereas, the lateral flow estimator relies on data that are acquired from having a double-windowed apodization profile, as shown in the top of Fig. 3.4(a). The spatial sampling required for determining the direction of the lateral flow direction is obtained by beamforming two parallel lines. The lines are separated by a fixed distance set to match the theoretical lateral wavelength calculated from (3.1) at a depth equal to the center of the color flow box. For the presented set-up, the scanner is capable of providing velocity data that are recorded at a frame rate of 18 frames per second.

4.4 Measured and simulated velocity fields

A display of the measured and simulated velocity fields from where the spatial derivatives are calculated is seen in Fig. 4.2. The first two sub-plots display 2-D vector velocity fields of a fluid that flows through the constricted phantom from right to left. Fig. 4.2(a) shows the measured ultrasound velocity field, while Fig. 4.2(b) displays the simulated velocities plotted for the same position. The figures show flow that accelerates towards the center of the constriction, reaching peak velocities of roughly $0.14\,\mathrm{m\,s^{-1}}$, before decelerating as the cross-sectional area of the vessel expanse again. Fig. 4.2(c) presents the magnitude of the out-of-plane velocity component, v_y, which is determined from the 3-D simulation

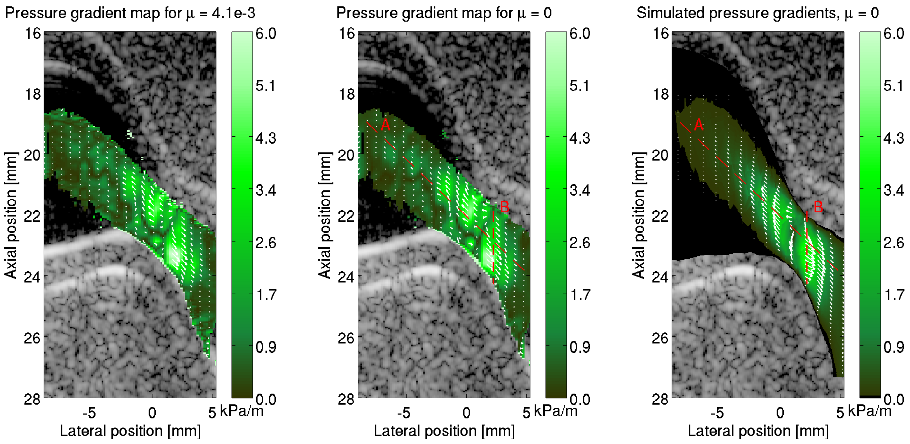

(a) (b) (c)

Figure 4.3: Pressure gradient fields. (a) shows the estimated pressure gradient field derived from (2.4), while (b) shows the same field but without including the effect of viscous forces. (c) displays the output of the simulation model.

model. It reveals that the out-of-plane component accounts for less than 2.5 % of the true velocity, $|\vec{v}| = \sqrt{v_x^2 + v_y^2 + v_z^2}$, and that the largest out-of-plane motions are seen at the center of the constriction.

4.5 Pressure gradients derived from the steady flow fields

The following presents the results and a discussion of the derived pressure gradients calculated from the steady flow fields in. The results are displayed in Fig. 4.3 as 2-D maps, where the plotted arrows and their background colors indicate the direction and the magnitude of the gradients, respectively. Figs. 4.3(a)–(b) show fields of pressure gradients calculated with and without including the influence of viscosity. It appears that no major changes are introduced when including the viscous term - an observation that is also supported by the Reynolds number, which at the center of the constriction is calculated to 68. The missing effect of including the viscous force indicates that the flow primarily is governed by inertial forces, suggesting that it is reasonable to neglect the viscous term for this particular set-up. Excluding the viscosity results in a reduced level of noise, as the noise from the second-order numerical differential is avoided (Ahnert and Abel 2007). Fig. 4.3(c) displays the simulated pressure gradient field.

4.5.1 Performance measures of the estimator

The performance of the proposed estimator is evaluated along the red lines in Fig. 4.3(b), and compared with the results of the simulation model. Standard deviations (Std) and biases are calculated as:

$$Std = \frac{1}{pg_{max}} \sqrt{\frac{1}{N} \sum_{m=1}^{N} \sigma^2(m)} \qquad \text{and} \tag{4.4}$$

$$Bias = \frac{1}{pg_{max} N} \sum_{m=1}^{N} \mu_{est}(m) - \mu_{sim}(m)\,, \tag{4.5}$$

where N is the number of data points along the spatial path that is investigated. The mean of the variance σ^2, is calculated over time for every position along the red lines, before taking the square-root to yield the standard deviation of the estimator. The bias is found from the average distance between the mean estimated value over time $\mu_{est}(m)$, and the results from the simulation model, $\mu_{sim}(m)$. Both standard deviation and bias are found as means across the entire investigated line, before normalized to the peak absolute value of the measured data, pg_{max}.

4.5.2 Verification of the estimated pressure gradients

A comparison between the estimated and simulated pressure gradients is shown in Fig. 4.4. The figure displays mean magnitudes of the axial and lateral pressure gradients along the longitudinal and cross-sectional direction of the constriction. The magnitudes are plotted together with ± one standard deviation, and the output from the reference model. The results show pressure gradients varying from -8 kPa m^{-1} to 9 kPa m^{-1} along the investigated lines. Normalized biases of -7 % to 3 %, and -8 % to 4 % are found for the axial and lateral vector component, respectively. The standard deviations in the four cases vary between 5 % to 32 %, and 30 % to 57 % for the axial and lateral vector component.

4.6 Discussion

The study derived pressure gradients from 2-D vector velocity data that were within the range of the reference model. This indicates that pressure gradients can be measured non-invasively, using data from a commercially available ultrasound system.

No previous studies on the subject have estimates pressure gradients from 2-D vector velocity ultrasound data. The presented method, further, allows for inclusion of full 3-D data, though this would not have contributed much as the out-of-plane motion, was insignificant in the presented set-up, (see Fig. 4.2(c)). However, in other scenarios where more complex flow features exist, this becomes increasingly more important and should, therefore, be considered.

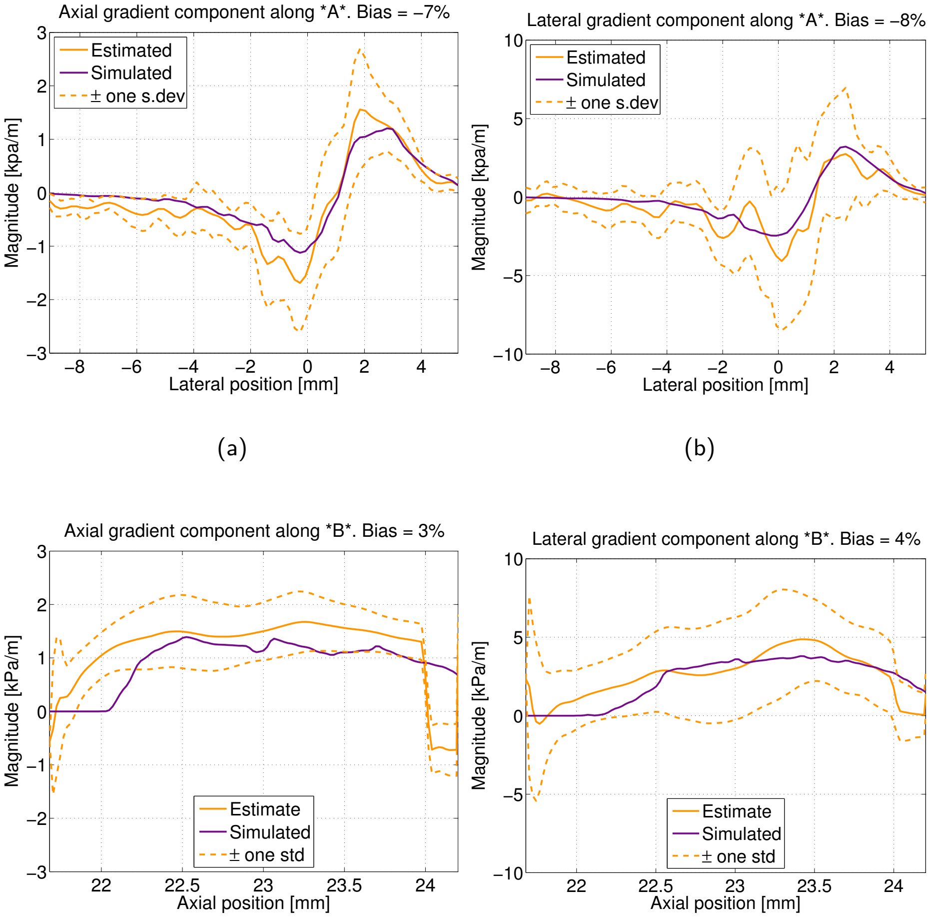

(a) (b)

(c) (d)

Figure 4.4: Estimated and simulated pressure gradients along the longitudinal and transversal direction of the carotid phantom at the site of the constrictions. Graphs (a)–(c) and (b)–(d) show the axial and lateral component of the pressure gradient, respectively.

As the study relies on vector velocity data acquired using a linear array transducer, it is limited in the field of view (FOV) to a maximum depth of approximately 4 cm – 5 cm. The FOV can, however, be greatly expanded if other transducers, with larger penetration depth and with the same capability of generating vector flow images are used. For instance, in 2012 it was demonstrated that vector velocities can be measured down to a depth of 15 cm with a phased-array transducer (Marcher, Pihl, and Jensen 2012; Pihl, Marcher, and Jensen 2012; Pihl, Stuart, et al. 2014), and in 2013 the vector velocity technique was shown feasible in conjunction with a convex-array transducer (Jensen 2013).

4.6.1 Limitations and future considerations

Generally, this initial study on deriving pressure gradients from ultrasound flow data showed promising results. However, challenges were realized, especially on the precision of the obtained pressure gradients, which need to be addressed before the method is suitable for clinical use.

Unacceptable standard deviations

The study showed pressure gradients varying between 5 % and 57 % of the peak estimated gradient. Such standard deviations are far to high for clinical diagnosis and need to be reduced. First step in doing so, is to understand their cause. As mentioned in Chapter 2, the differential operator basically performs as a high-pass filter on the measured flow data, thereby enhancing higher frequency content, which usually is associated with noise. Further, for every increase in differential order, this effect becomes progressively higher, and that ruins the precision of the derived pressure gradients, unless noise-free velocity estimates are obtained from the start.

A way of decreasing the standard deviation is by reducing the noise floor in the velocity estimates before calculating the derivatives. A method for achieving this is by averaging across velocity frames, thereby eliminating some of the random fluctuations that constitute noise. Averaging is, however, at the expense of temporal resolution, which drops exponentially with the number of frames averaged over. Most commercially available ultrasound systems display flow images at a frame rate of 15 Hz – 30 Hz. This is just at the acceptable limit for cardiac flow imaging, where capturing the peak systolic phase is of utmost importance. The low frame rate leaves no room for averaging across frames without severely hampering the temporal resolution and thereby the capturing of the full cardiac cycle. Yet, in the presented study, despite having an initial temporal resolution of only 18 Hz, three frames of velocity were averaged before calculating the pressure gradients. This was permitted as steady flow was considered. However, had the flow been time-dependent then averaging would not have been allowed, and instead the standard deviations would be between 59 % to 110 % as shown in Fig. 4.5.

So, to obtain robust velocity estimates through averaging without compromising the systolic phase of the cardiac cycle, alternative flow estimators are required. For instance, synthetic aperture flow imaging (SAFI) offers the possibility of generating vector velocity fields at a frame rate proportional to the pulse repetition frequency, e.g., 0.5 kHz – 15 kHz. Such a frame rate permits averaging across image frames without compromising the peak systolic flow and is therefore a potential solution for obtaining more reliable estimates.

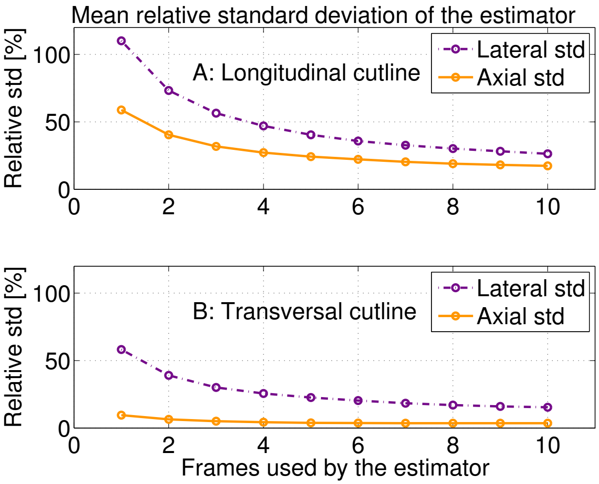

Figure 4.5: Relationship between estimator precision and the number of frames used in calculating the pressure gradients. The standard deviations are given in reference to the peak estimated pressure gradient. The graphs were made during steady flow conditions. Each graph shows the results from both the axial and lateral component of the pressure gradient. The time interval between consecutive frames is 1/18 seconds.

VISUALIZATION OF PRESSURE CHANGES

Another aspect to consider when studying pressure gradients is the visualization. The images in Fig. 4.3 present the full 2-D information on how the pressure changes in every position relatively to its neighboring points. This however, has shown to be a less intuitive way of displaying the information, as clinicians are more concerned with the overall pressure drop across the diseased region. To accommodate the clinical preferences, the derived pressures should be displayed over an area of interest. An example of such is shown in Fig. 4.6. Here, the overall transstenotic pressure drop is calculated by summing all the individual gradients along the direction of the constriction. The result of this is seen in red for three cardiac cycles on the left hand side of the figure. The display serves as an example on how the estimated pressure drop can be visualized. Here, data are obtained by a SAFI emission sequence used during pulsating flow conditions.

4.7 Study conclusion

A method for estimating 2-D fields of pressure gradients from vector velocity data has been presented. The initial results showed that data from an already commercially available ultrasound scanner can be used for determining pressure gradients non-invasively.

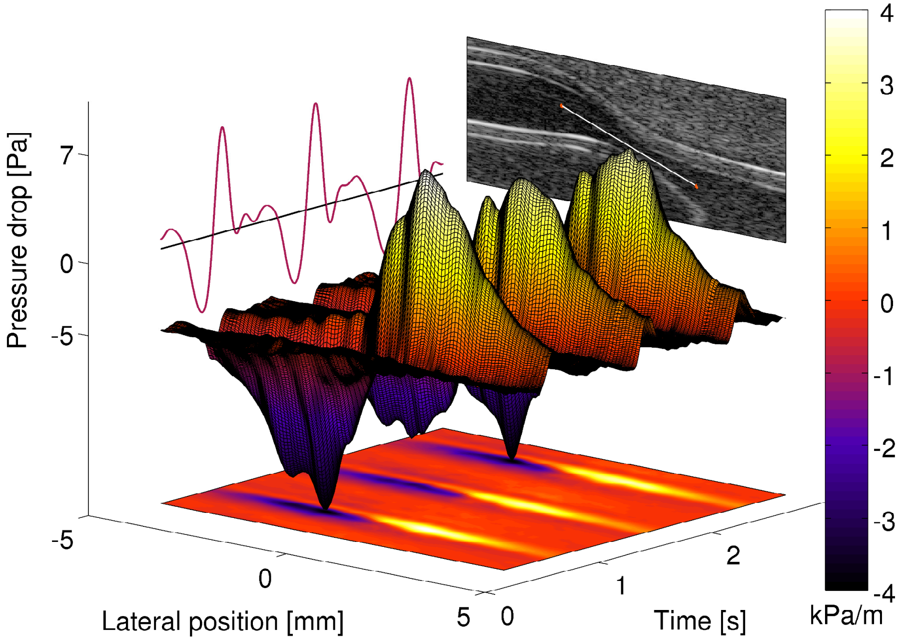

Figure 4.6: An example on how to visualize the pressure changes measured non-invasively using an ultrasound system. The figure displays the pressure drop that exists across of the constriction seen on the B-mode image in the back. The center of the plot shows the individual pressure gradients along the white line as a function of time. Summing the individual gradients along the line gives the total transstenotic pressure drop. This drop in pressure is presented by the red curve on the left. The figure is from Paper VI in appendix.

However, significant challenges were identified which need to be addressed for obtaining more reliable estimates of pressure. Among the challenges is the level of noise present in the original velocity estimates, which deteriorates as it passes through even advanced differential operators. To overcome the destructive nature of the inherent noise, more advanced flow estimators are required.

Where a steady flow set-up may be a great environment for testing the feasibility of the proposed method, the really interesting application of the suggested method lies in pulsating flow environments and in in-vivo settings. Therefore, the following chapters describe improvements of the proposed technique, making it more suitable for clinical testing. First, however, the conclusion drawn in this study is that pressure estimation from vector velocity data is achievable, but changes to the employed flow estimator and the noise removal procedure is unquestionably required.

CHAPTER 5

Patent I
Deriving Temporal Acceleration from Velocity Ultrasound Data

Summary *This chapter presents a technique for deriving temporal acceleration from a measured velocity profile without passing vast amounts of noise through the differential operator. The developed technique was taken up by Analogic, who in collaboration with the author wrote the first proposal seen in Appendix (Patent I). Essentially, the method performs a Fourier decomposition of the measured flow profile into a series of sinusoids. A collection of sinusoids are then selected by a specified criteria, before a derivative operation is employed on the trigonometric series. This provides the optimal building blocks for reconstructing the measured flow profile and its derivative with only a minimum level of error and noise contamination. The chapter commences by introducing the purpose and the technical content of the proposed method, before concluding with a discussion of the advantages and limitations of using such processing scheme.*

5.1 Purpose

A main concern when deriving pressure gradients from measured velocity data, is the level of noise that passes through the differential operator. Even the slightest amount of noise present in the recorded flow data can affect the precision of the derived pressures dramatically. So, to remedy the pressure estimator's high sensitivity to noisy velocity data, this chapter seeks to introduce a method capable of calculating accurate and robust derivatives despite having a noisy starting point.

5.2 Description of the processing scheme

The proposed method is two-fold. Initially, the measured velocity data are filtered by selecting a distinct set of frequencies in the Fourier domain. The selected frequencies are written into a trigonometric series that when derived produces a smoothed reconstruction of the acceleration profile. An explanation of the two processing steps is elaborated in the following.

5.2.1 Step 1: Filtering the recorded velocity data

First step in deriving the acceleration profile is to discriminate frequency content of the measured velocity data that does not contain significant information on the shape of the flow profile. This is achieved in the Fourier domain, for instance by choosing a criteria that only the N frequency bins of highest spectral energy are kept and the rest ignored. As noise from the sampling system presumably is white, it will be spread out all over the spectrum, and thus removed, when only including the N bins containing the majority of the signal's energy. Then, summing N sinusoids where each signal oscillates at one of the selected frequencies, yields a reconstruction of the original waveform, without including a pronounced portion of the contaminating noise. The trigonometric series can be written as:

$$\tilde{v}(n,t) \approx \sum_{p=0}^{N-1} |V_p(n)| \cos(2\pi f_p t + \varphi_p(n)), \tag{5.1}$$

where N is the number of selected frequencies used for reconstructing the flow profile. V_p and φ_p are the amplitude and the phase of the frequency component f_p. $\tilde{v}(n,t)$ is the reconstructed flow profile for a given position, n, within the velocity field.

An example of the noise removal technique is shown in Figs. 5.1–5.2. Fig. 5.1 presents a fictive velocity profile from a common carotid artery sampled at 2,500 Hz with -20 dB of added Gaussian noise. Moving the contaminated signal into the Fourier domain, and selecting the eight frequencies of highest energy levels to reconstruct the original signal, yields the graph in Fig. 5.2. The figure shows that a waveform, having a noise floor

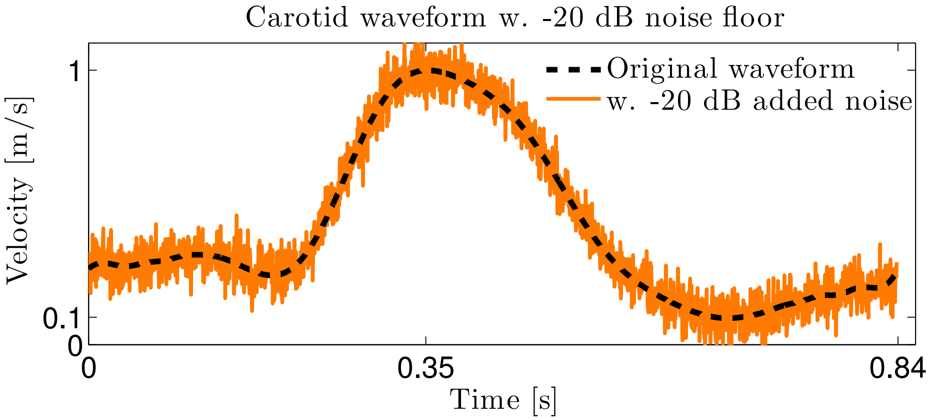

Figure 5.1: The dotted curve represents a fictive waveform of a typical flow profile seen in the carotid artery. Beneath this is the same waveform but with an added -20 dB noise floor.

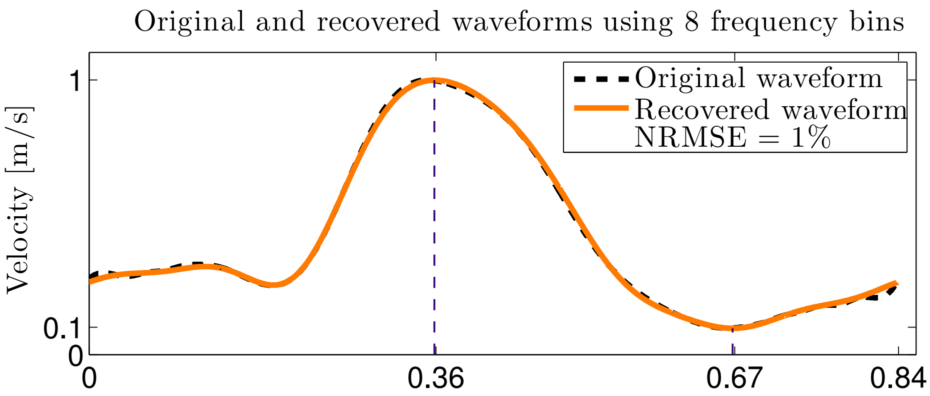

Figure 5.2: Original and recovered waveform from the contaminated signal in Fig. 5.1. The recovered waveform is the summation of eight sinusoids, each oscillating with one of the eight selected frequencies.

of -20 dB, can be 99 % recovered using only eight frequency bins. The normalized root mean square error (NRMSE) between the recovered acceleration profile and the reference profile is calculated by,

$$\text{NRMSE} = \frac{1}{x_{o,max} - x_{o,min}} \sqrt{\frac{1}{N} \sum_{m=1}^{N} (x_o(m) - x_n(m))^2}, \tag{5.2}$$

where x_o is original signal, and x_n the noise contaminated signal. Reconstructing the flow profile from a sum of sinusoids is possible as the flow is somewhat periodic over the cardiac cycle (Evans et al. 1989; Womersley 1955).

The number of sinusoids needed to make a realistic reconstruction of the original flow waveform depends on the frequency content of the profile and the amount of noise present in the signal. Fig. 5.3 shows a parametric study on the number of sinusoids needed to reconstruct the profile from Fig. 5.1, with a minimal error, as a function of an increasing noise floor. In this project, the N frequency bins that contain the majority of the spectral energy are selected for reconstructing the measured flow profile. However, other criteria could also be used for selecting the frequency content, e.g. frequency bins covering information on a reflection wave, or other flow features that may be of interest.

5.2.2 Step 2: Deriving the temporal acceleration

The acceleration profile is derived by phase shifting the trigonometric series 90°. Such a phase shift is essentially equivalent to performing a differential operation on the filtered

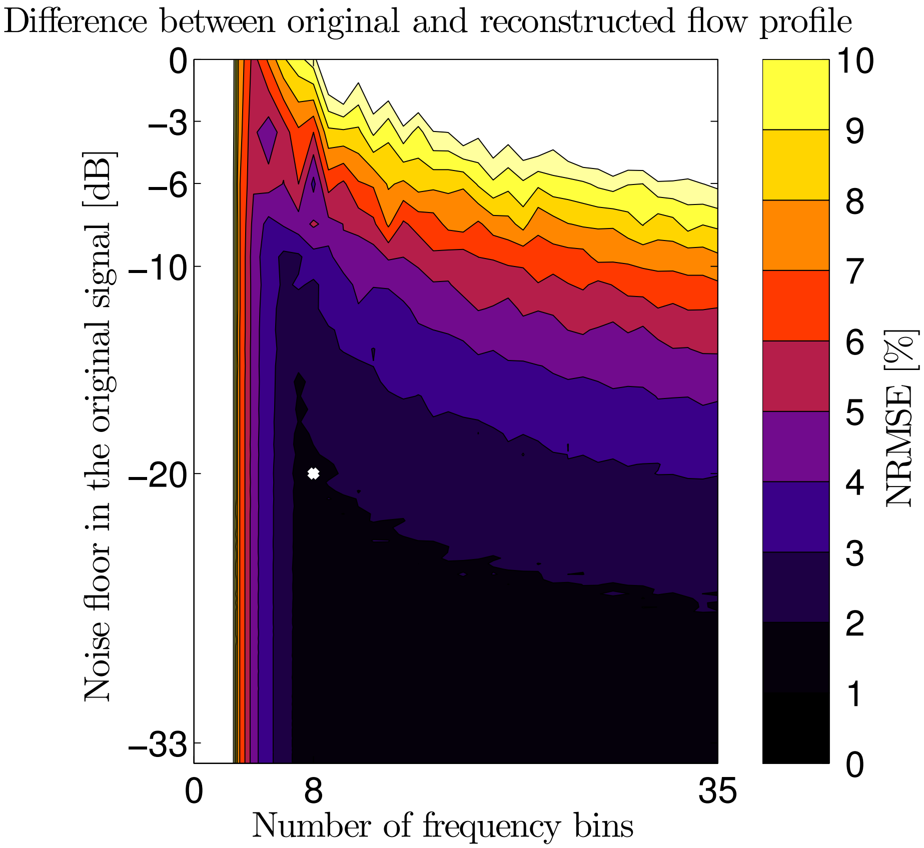

Figure 5.3: Number of sinusoids required for reconstructing the original inlet waveform, Fig. 5.1, when the level of noise increases in the measured signal. A 99% recovery can be made from a sum of eight sinusoids, despite having a noise floor of -20 dB.

time signal. However, the advantage here is that the operation is performed on a analytical expression and this can potentially minimize discretization errors. Phase shifting the trigonometric series by 90° is equivalent to summing a series of sinuses instead of cosines, which otherwise was the case in (5.1). The analytical expression of the acceleration curve can be expressed as:

$$\frac{\mathrm{d}\tilde{v}(n,t)}{\mathrm{d}t} \approx -\sum_{p=0}^{N-1} |V_p(n)|\; 2\pi f_p\; \sin(2\pi f_p t + \varphi_p(n)). \tag{5.3}$$

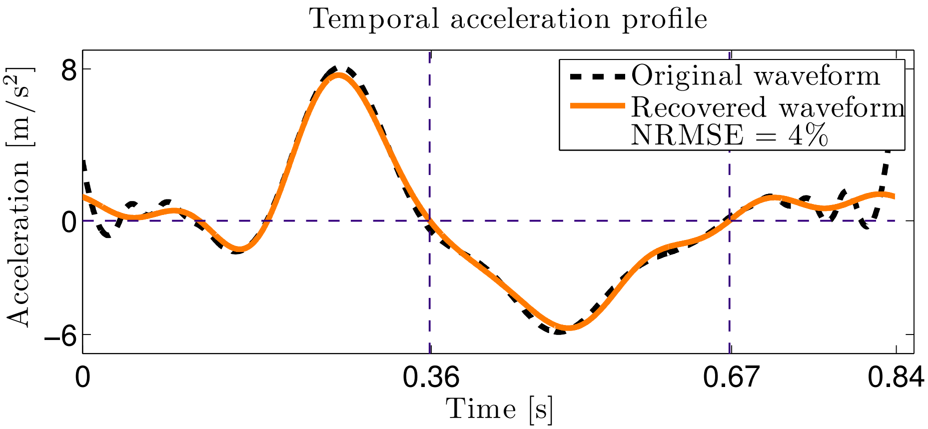

Figure 5.4: Acceleration profile constructed from the summation of eight sine-functions. Each sinusoid oscillates at one of the eight frequencies that showed the highest levels of spectral energy after having performed a Fourier decomposition of the noisy velocity profile in Fig. 5.1. The dotted curve represents the first-order derivative of the noise free velocity waveform also shown in Fig. 5.1.

The result of doing this for the contaminated signal in Fig. 5.1 is shown in Fig. 5.4. Here, the derived acceleration profile is plotted next to the derivative of the original waveform found by the in-built Matlab algorithm, `diff.m`. The result shows that a 96 % recovery can be achieved from summing eight sinuses oscillating in frequencies most representative for the noisy signal.

5.3 Discussion and perspectives

The presented technique provides a neat method for calculating the temporal acceleration waveform despite having noisy velocity estimates as a starting point. The key feature of the patent proposal is the analytical expression of the acceleration curve, which is based on a user-dependent selection of distinct frequencies. Another example of a selection-criterion could be only to consider the frequencies that are associated with the fundamental period and its harmonics. Such a criterion is beneficial when having velocity data that are highly contaminated with noise. Most conventional low-pass filters would in this scenario not be able to differentiate between the frequency bins related to the actual flow data and the bins that arise from low-frequent noise. However, as the presented technique uses a priori knowledge of the flow profile, it can select the frequencies related to the harmonics of the flow profile, and thereby, constructing the acceleration curve more precisely, and with fewer frequency bins.

A disadvantage of the proposed technique is its recursive nature. The method is based a priori information from a full cardiac cycle and this poses as a concern for real-time implementation. The method is, therefore, at this stage more suitable for post-processing use.

CHAPTER 6

Study II
Noninvasive Estimation of Intravascular Pressure Changes using Vector Velocity Ultrasound

Summary *The chapter summarizes the results from the second peer-reviewed paper included in the project. The paper introduces a method for deriving pressure changes along streamlines, which then are verified experimentally on fabricated flow phantoms before tested in-vivo. First part of the chapter introduces the purpose of the study, and the alterations made to the initial proposed method, thereby, transferring it into a streamline representation. Second part evaluates the results obtained on the two fabricated phantoms during steady and pulsating flow conditions. Lastly, the chapter describes the results from testing the method in-vivo on two healthy volunteers before concluding with a discussion on limitations and on considerations for future investigations. For a further in-depth description of the study the reader is referred to Paper II in the appendix.*

6.1 Purpose

The presented study demonstrates the feasibility of determining pressure changes from velocity data acquired at a frame rate on the order of kilohertz. The high frame rate allows for averaging across velocity frames without losing temporal information and is therefore a suitable match for obtaining reliable estimates of pressure. Flow data are measured using a synthetic aperture flow imaging (SAFI) sequence implemented for a linear array transducer connected to the experimental scanner, SARUS. Experimental results from fabricated phantoms are evaluated by comparison with two 3-D simulation models with similar flow geometries. The study tests the hypothesis that pressure changes along streamlines can be measured from high frame rate velocity data with an accuracy and precision of more than 90 % of the peak pressure drop.

6.2 Pressure changes along streamlines

To accommodate the clinical preferences of having a tool that is capable of displaying overall pressure changes across a desired region, the initially proposed method is re-written into a streamline representation. A streamline representation enables easy calculation of the pressure drop over larger regions, by integrating the individual pressure gradients found along the investigated streamline. Re-writing the initial method (2.4), into a scalar equation that follows a streamline, and omitting the influence of gravity and viscosity yields the following,

$$\frac{\partial p}{\partial s} = -\rho \left[\frac{\partial v_s}{\partial t} + v_s \frac{\partial v_s}{\partial s} \right]. \tag{6.1}$$

Here, v_s is the scalar product of $\vec{v}(\vec{r},t)$ and the vector that lies tangent to the streamline $d\vec{s} = (\hat{s}_x, \hat{s}_y, \hat{s}_z)$, where $d\vec{s}$ is an element of distance along the streamline, which runs in the direction, s. Omitting the effect of viscosity is thought reasonable as the Reynolds number in the presented set-up is found to more than 1,000. Then, integrating the individual pressure gradients from (6.1) along the flow direction of the streamline gives the total drop in pressure that occurs over the course of the flow line,

$$\Delta P(t) = \int_0^L \frac{\partial p}{\partial s}\, ds. \tag{6.2}$$

Again, eqs. (6.1)–(6.2) state the need for having all three spatial vector components of $\vec{v}_s$ available for estimating the pressure gradient $\frac{\partial p}{\partial s}$. This study, however, employs a velocity estimator capable of measuring the two in-plane vector velocity component $\vec{v}_s = (v_x, v_z)$, thus, the proposed method is developed assuming that the out-of-plane velocity v_y is zero.

The temporal derivative in (6.1) is reconstructed from decomposing the measured flow profile at every position along the streamline into a series of sinusoids, as introduced in Chapter 5. Reconstructing the acceleration profile from a sum of sinusoids is possible as the flow is somewhat periodic over the cardiac cycle. The spatial derivative on the other hand, is not necessarily periodic across the examined region. Thus, it is not convenient to approximate it by a sum of sinusoids. Instead, the spatial derivative is found equivalent to the method introduced in Chapter 4 where polynomial filtering is used. A second-order polynomial is fitted to a subset of adjacent data points along the path of the streamline by convolving the data to a window of convolution coefficients.

6.3 Experimental set-up

The proposed method is validated on straight-tube phantoms during steady and pulsating flow conditions before tested in-vivo on two healthy volunteers. Two straight tube phantoms with an inner diameter of 8 mm are designed, each with a concentric constriction of 36 % and 70 %, respectively, and a length of 260 mm. Sections of the models are shown

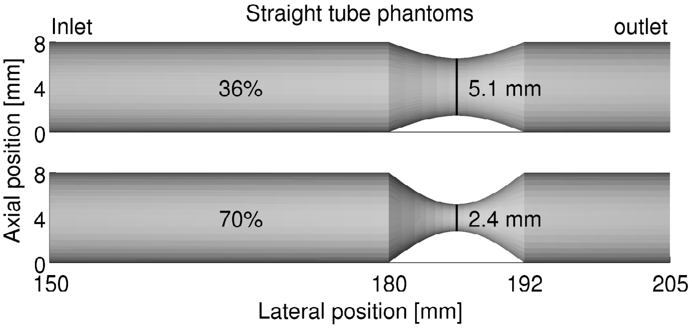

Figure 6.1: Two straight tube phantoms with an inner diameter of 8 mm are used for validating the proposed method. Each model has a length of 260 mm and a concentric constriction of either 36 % and 70 % of the inlet diameter.

in Fig. 6.1. The geometry of the vessels is drafted in SolidWorks (Education edition, Dassault Systèmes SolidWorks Corp., Vélizy, France) and exported as an STL file to stereolithography, which constitutes the core of the phantom's fluid flow domain (Lai et al. 2013). The 3-D printed cores are fixed in individual containers before cast in polyvinyl alcohol (PVA) cryogel to make the surrounding medium mimic the properties of human tissue. The PVA cryogel is made using an in-house formula, containing 15 % PVA, 1 % silicon dioxide, 0.3 % potassium sorbate, and 83.7 % distilled water. The nature of cryogel allows for controlling its elastic properties by varying the number of freeze-thaw cycles it undergoes. Two freeze-thaw cycles are used, each half-cycle of 24 h duration, with freeze settings of $-20\,°\mathrm{C} \pm 0.5\,°\mathrm{C}$ and thaw of $4\,°\mathrm{C} \pm 0.5\,°\mathrm{C}$. After completing two cycles, given a total duration of 96 h, the core was removed manually, thereby, leaving a core-less phantom with sound propagating properties of human tissue and a fluid domain identical to the 3-D printed structure.

The fabricated phantoms are connected to a flow system (CompuFlow 1000, Shelley Medical Imaging Technologies, Toronto, Canada) capable of generating customized flow waveforms. The first study is performed using a constant waveform and a flow rate of $5\,\mathrm{ml\,s^{-1}}$. The second study uses a time-varying waveform equivalent in shape to the dotted line in Fig. 5.1, and a peak flow rate of $5\,\mathrm{ml\,s^{-1}}$.

The two in-vivo measurements are carried out after approval by The Danish National Committee on Biomedical Research Ethics. A healthy female (age 52) and male (age 41) are scanned by an experienced radiologist. The volunteers are placed in a supine position for five minutes to obtain a steady heart rate. The examinations were performed over the left carotid bifurcation, producing a view of both the internal and external artery together with the carotid bulb. Intensity measurements were made prior to the examinations, showing energy levels and an MI within the limits set by the U.S. Food and Drug Administration.

Both, experimental and in-vivo scans are made using a BK8670 linear array transducer connected to the experimental research scanner SARUS (Jensen et al. 2013). A three-cycle pulse with a center frequency of 7 MHz is emitted at a pulse repetition frequency of 12.5 kHz to a depth of 4 cm. The acquired data are processed off-line in Matlab (The MathWorks Inc., Natick, MA, USA) following the processing scheme for SAFI with directional beamforming.

6.4 Vector velocity flow

Vector velocity flow images are measured from directional synthetic aperture flow imaging, as described in Section 3.2. A high-resolution image is created from the summation of five low-resolution images, producing an effective frame rate of 2,500 Hz. The performance of the suggested streamline method is evaluated for both steady and pulsatile flow condition at the constricted sites of the two fabricated models. Three seconds of flow data are recorded producing roughly 7,500 frames of vector velocity fields. Each field spanning an area of 10 mm×20 mm, and with an intermediate distance between the estimates of 0.2 mm in both the axial and lateral direction.

6.4.1 Steady and pulsating flow fields

Examples of vector flow imaging on the two fabricated phantoms are displayed in Fig. 6.2. The images show flow that accelerates towards the center of the constriction, producing a jet that then slowly decelerates as the lumen expands again. Black streamlines set to start from the center of the vessel are also displayed. Throughout this study, changes in pressure are derived along these dotted streamlines.

Peak velocities measured and simulated during steady flow are plotted as a function of time in Fig. 6.3. The figure reveals a standard deviation of 6 %, and 2 % relative to the reference model for the 36 %, and the 70 % constriction, respectively. Further, a bias of -17 % and -8 % is observed for the two measurements. The bias is a consequence of having misaligned the transducer to the exact center axis of the constriction, which becomes apparent when comparing the diameter of lumen seen on the B-mode images to the actual constriction sizes of the models from Fig. 6.1. Measuring the widths of the observed constrictions gives distances of approximately 4.40 mm and 2.30 mm for the 36 %, and the 70 % constricted phantom, respectively. Whereas, the true distances for the two models are 5.12 mm and 2.40 mm, thus, lower velocities are measured in the experimental set-up, as the peak flow velocities are outside the scan plane of the transducer. The calculated biases are, therefore, used for compensating the measured velocities. Bias compensation is performed to obtain as good resemblance between estimated and simulated velocities as possible, before inserting the measured velocities into the proposed estimator. This will ensure the best basis for comparing the derived

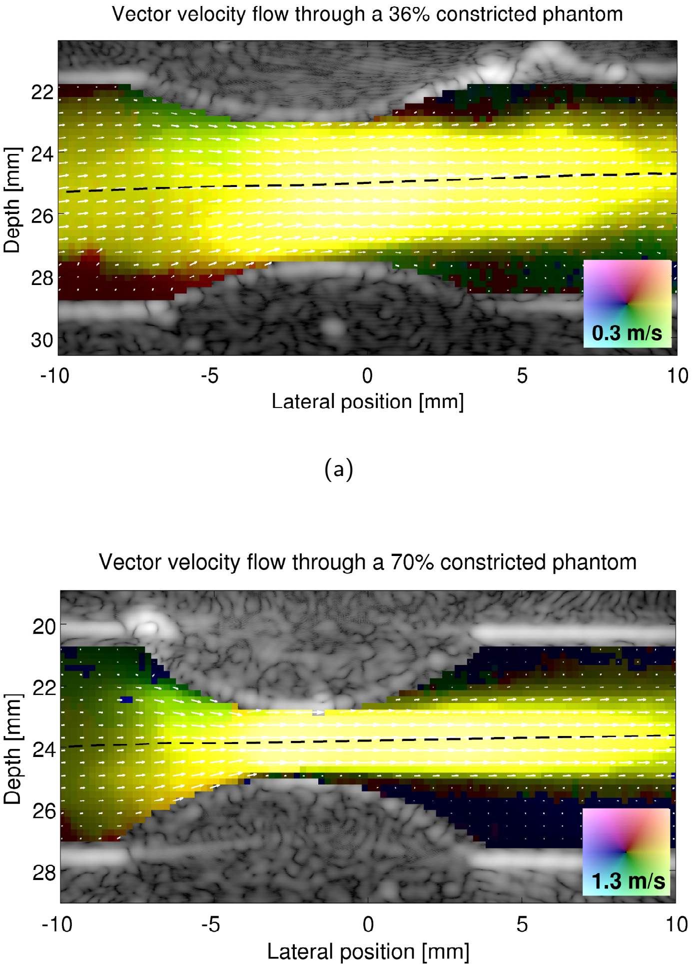

(a)

(b)

Figure 6.2: Vector velocity images at the constriction of two fabricated flow phantoms. Phantom (a) has a constriction of $36\,\%$, while (b)'s is $70\,\%$. The two images are captured during steady flow conditions. Black-dotted streamlines passing through the center of the constrictions are also displayed. The number in the colorbox indicates the maximum flow velocity that can be represented by a color in the color flow map

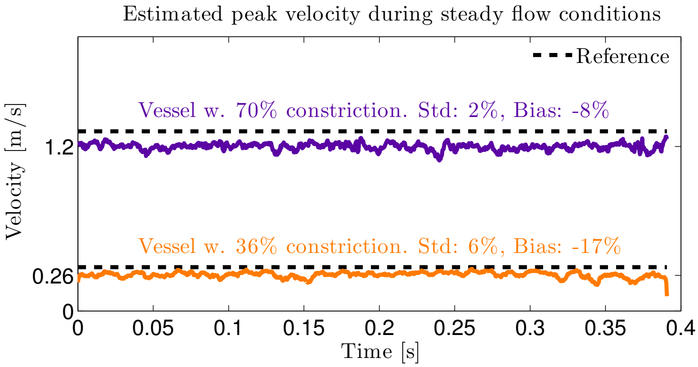

Figure 6.3: Estimated and simulated peak velocity from the center of the constriction during steady flow conditions.

pressures with the simulation model, as all discrepancies between the model and the reference, will be solely related to the actual performance of the suggested estimator. The result of compensating for the misalignment of the transducer is seen in Fig. 6.4, where pulsating flow has been measured.

The displayed flow profiles are reconstructed from the measured data using a sum of sinusoids, as explained in Chapter 5. A single pulse cycle can, as suggested by Fig. 5.3, be 99 % recovered from eight distinct frequency bins. Thus, to maintain the same level of accuracy when reconstructing three pulses that are not necessarily identical, 24 frequency bins are required. The inherent compliance of the flow system's afferent tubes increases the pulsatility of the time-varying flow, producing a flattening of the velocity profile compared with the profiles seen during constant flow.

6.4.2 In-vivo velocity fields

Two in-vivo measurements are carried out on the carotid artery of two healthy volunteers. The resulting vector flow images are shown in Figs. 6.5–6.6. The figures display longitudinal scans of the volunteers' left carotid bifurcations together with the measured flow fields. The images are captured at peak systole, yielding values in the carotid sinus of roughly $0.6\,\mathrm{m\,s^{-1}}$. The starting point of the superimposed streamlines are manually selected based on the criterion that the lines should include the peak velocity during the systolic phase.

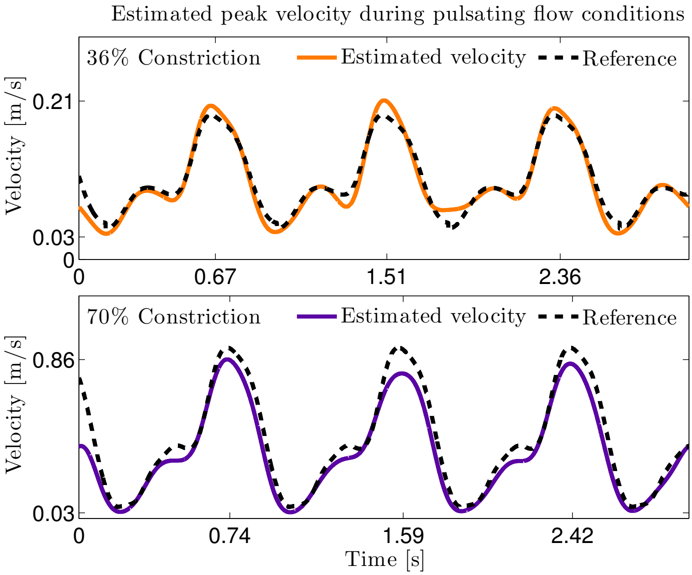

Figure 6.4: Estimated and simulated peak velocity from the center of the constriction during pulsating flow conditions.

6.5 Pressure changes derived along streamlines

The following presents the results from deriving pressure changes along streamlines using a high frame rate ultrasound technique. First presented are the results from the two flow phantoms measured during steady and pulsating flow conditions, before concluding by displaying the in-vivo results. All flow velocities that enter the proposed pressure estimator are filtered by a 3-D median filter. This is done to minimize the risk of transferring any inexpedient discontinuities from the estimated velocities, into the differential operator and further to the desired pressure estimate. The filter's in-plane window size is set to 10 data points, corresponding to an axial and lateral distance of 2 mm. A second median filter of 15 data points is applied temporally, equivalent to a window size of 6 ms.

6.5.1 Transstenotic pressure drop during steady flow

Streamline velocities from Fig. 6.2 are extracted and used for deriving the pressure drop that occur across the constriction. As only spatial velocity changes exist in the steady flow field, the temporal acceleration is neglected when employing (6.1). For every position along the streamline, an individual pressure gradient is calculated relative to its

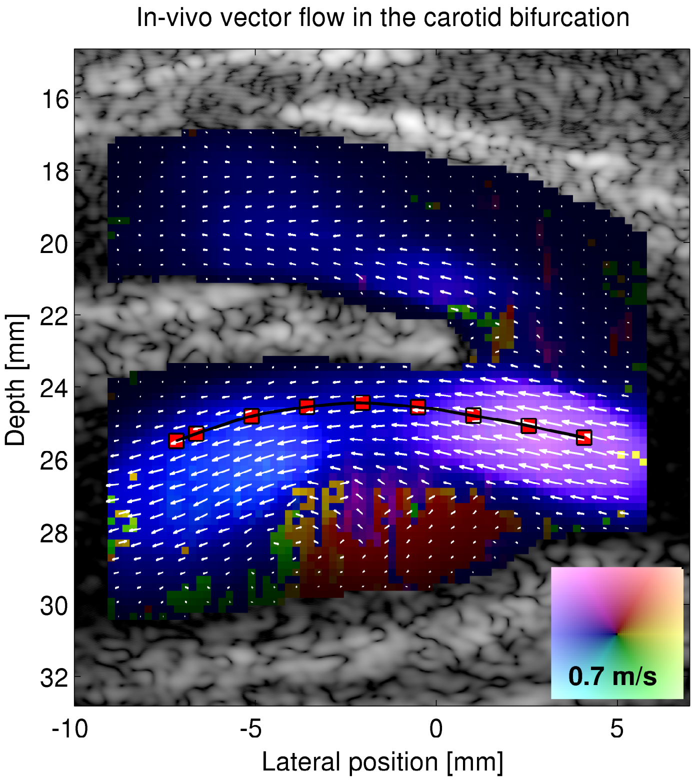

Figure 6.5: Volunteer 1: Longitudinal vector flow scan of the carotid bifurcation during peak systolic. Bottom branch shows the internal carotid artery in conjunction with the carotid bulb, in which a vortex is formed during rapid flow movement. A streamline following the vector velocity field is also displayed.

neighboring points. Then, calculating the cumulative sum of the local pressure changes along the direction of the flow, yields the drop in pressure that exists between the start of the streamline to any position along the line. The result of doing this for all velocity frames is shown in Fig. 6.7. The two graphs display the drop in pressure that occurs as the fluid moves through the constricted part of the studied phantoms. The shaded zone indicates a region of ± one standard deviation normalized to the number of frames recorded. The black-dotted lines in Fig. 6.7 are the outputs from the simulation models.

As in Chapter 4, the performance of the method is evaluated by its standard deviation and bias. However, instead of normalizing eqs. (4.4)–(4.5) by the peak estimated pressure

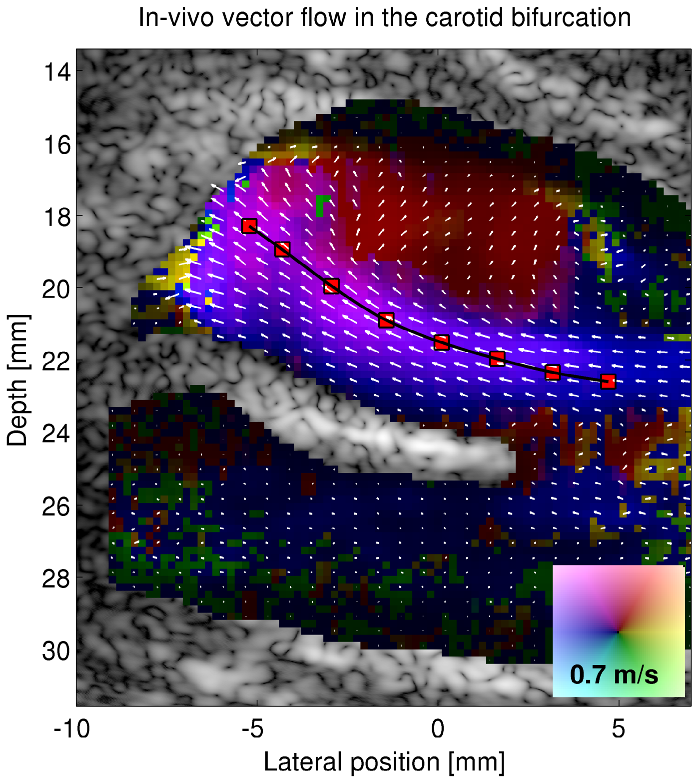

Figure 6.6: Volunteer 2: Longitudinal vector flow scan of the carotid bifurcation during peak systolic. Top artery shows the internal carotid artery in conjunction with the carotid bulb. Also here, a vortex is formed during the peak systolic phase of the cardiac cycle. A streamline following the vector velocity field is also displayed.

gradient, pg_{max}, they are normalized to the maximum pressure drop simulated. For steady flow, mean biases of $8\,\%$ and $7\,\%$ are calculated in the $36\,\%$, and $70\,\%$ constricted phantoms, respectively, with standard deviations of $9\,\%$, and $6\,\%$.

6.5.2 Transstenotic pressure drop during pulsating Flow

Calculating the pressure drop during pulsating flow condition follows the same data processing scheme as in the previous case. However, in this case the temporal acceleration is included. The results are shown in Fig. 6.8. Largest changes in pressure are observed in the systolic phase of the cycle, hence, emphasized in the two graphs. The systolic

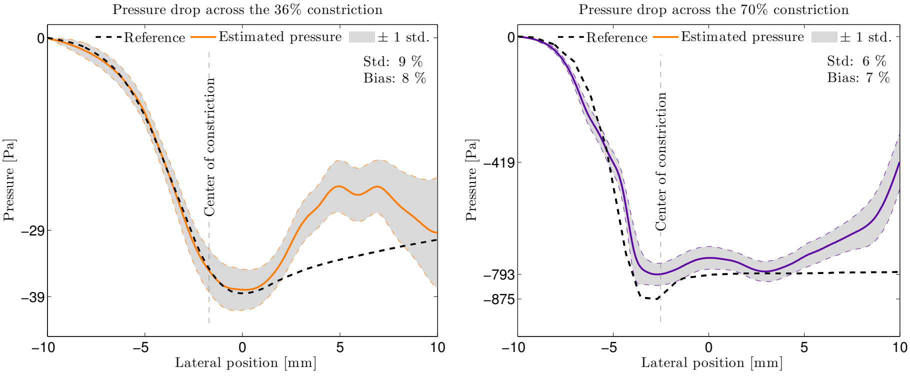

(a) (b)

Figure 6.7: Transstenotic pressure drop: Estimated and simulated pressure drop through the center of a 36 %, and 70 % constriction during steady flow. The mean estimate is plotted together with ± 1 standard deviation, along with the output from the FE models.

pressure drops from the three recorded cycles show a mean standard deviation of 1 % and 7 %, relatively to the peak simulated pressure drop for the 36 %, and 70 % constricted phantom, respectively. A mean bias over the entire course of the streamline is found to be 2 % for both cases in comparison with the FE models.

6.5.3 In-vivo examples of non-invasive pressure estimation

Vector velocities found along the streamlines of Figs. 6.5–6.6 are extracted for all time instances and inserted into the proposed algorithm. The resulting pressure drops are shown as 3-D plots in Figs. 6.9–6.10. The figures show pressure changes along the direction of the streamlines as a function of time. The plots' left wall defines the starting point of the streamline data. Changes in pressure are then found relatively to this point, by moving down-right, parallel to the lateral axis. Both cases show the largest pressure variations during the systolic phase of the cardiac cycle, with values between 0 Pa and -60 Pa.

6.6 Discussion

Non-invasive pressure changes have been calculated along streamlines using a high frame rate ultrasound technique. Pressure drops across two concentric constricted flow phantoms were examined, before measuring in-vivo pressures on two volunteers. The

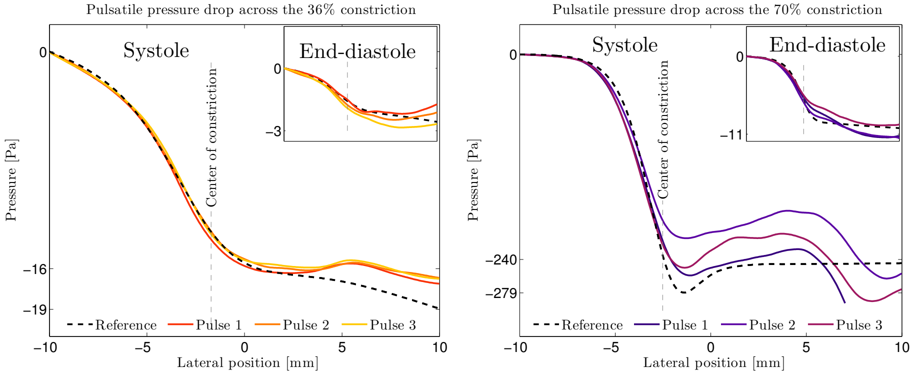

(a) (b)

Figure 6.8: Transstenotic pressure drop: Estimated and simulated pressure drop through the center of a 36 %, and 70 % constriction during pulsating flow. The pressure changes are plotted for the peak systolic phase of the cycle, as well as for the end-distolic phase. The black-dotted line represents the outputs from the FE models.

largest experimental pressure drop was seen in the 70 % constricted phantom, reaching a drop of −875 Pa. The largest mean standard deviation and bias that were found across the entire constriction were 9 %, and 8 %, respectively. Thereby, confirming the hypothesis that pressure changes can be attained with a precision that is within 90 % of the peak pressure drop using a SAFI sequence.

The SAFI sequence produced vector flow images down to a depth of 4 cm at an effective frame rate of 2,500 Hz. Today, no previously published literature has sought to measure intravascular pressure changes using a high frame rate ultrasonic technique. The obtained results clearly show the improvements in precision of doing so, at least in comparison with the results from Chapter 4. The high frame rate offered by SAFI allows averaging across estimates without compromising the peak of the profile. This is beneficial as it essentially performs a low-pass filtering of the velocity estimates before deriving the pressure changes, thus, avoiding the higher frequency content, which usually is associated with noise.

The in-vivo results show the feasibility of measuring pressure changes in the carotid artery. An area otherwise sought avoided by invasive catheter, as contact with the neck's arterial walls could make vulnerable plaque rupture causing arterial blockage of the vascular beds in the brain (Al-Ameri et al. 2009). The non-invasive nature of the proposed technique, furthermore opens the possibility of running routine examinations for screening purposes, thus, further expanding the application range of pressure sensing techniques.

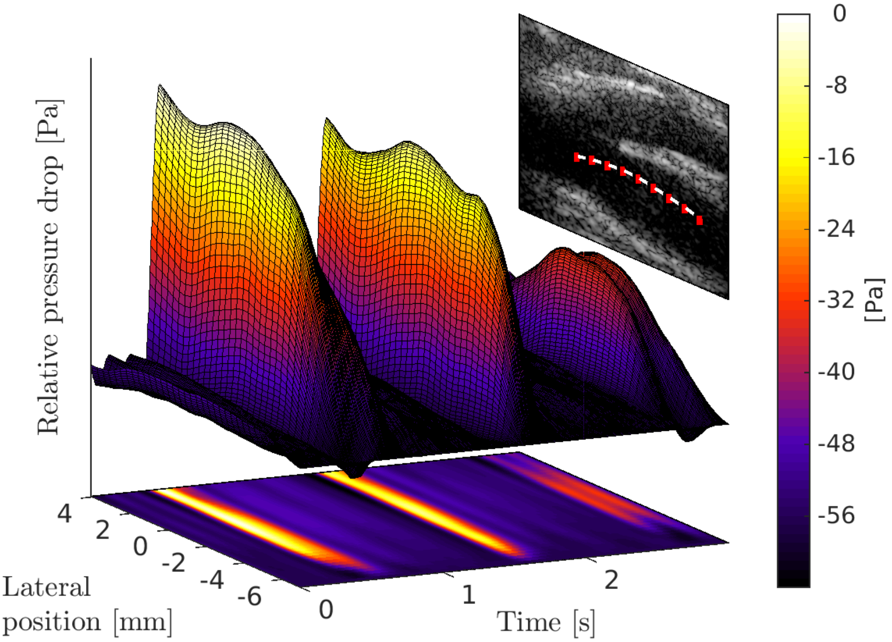

Figure 6.9: In-Vivo: Changes in intravascular pressure measured as a function of longitudinal position and time along the streamline from Fig. 6.5. The shown pressures are in reference to an arbitrary value, which for this study is set to zero at the beginning of the streamline.

6.6.1 Limitations and future considerations

In terms of estimator precision, the study clearly showed the benefit of using a high frame rate ultrasound technique when deriving pressure changes from flow data. However, the improved precision revealed the effect of other flow features, which in Chapter 4 may have been hidden by the large standard deviation of the employed estimator. Whereas, results from the experimental set-up looked great, the pressure changes derived in the in-vivo cases was a bit more distorted. The following describes considerations that will help to further improve the technique.

The influence of the out-of-plane velocity component

The presented technique essentially studies the flow pattern of a moving fluid, from which the pressure forcing the fluid to move is sought predicted. This makes the technique

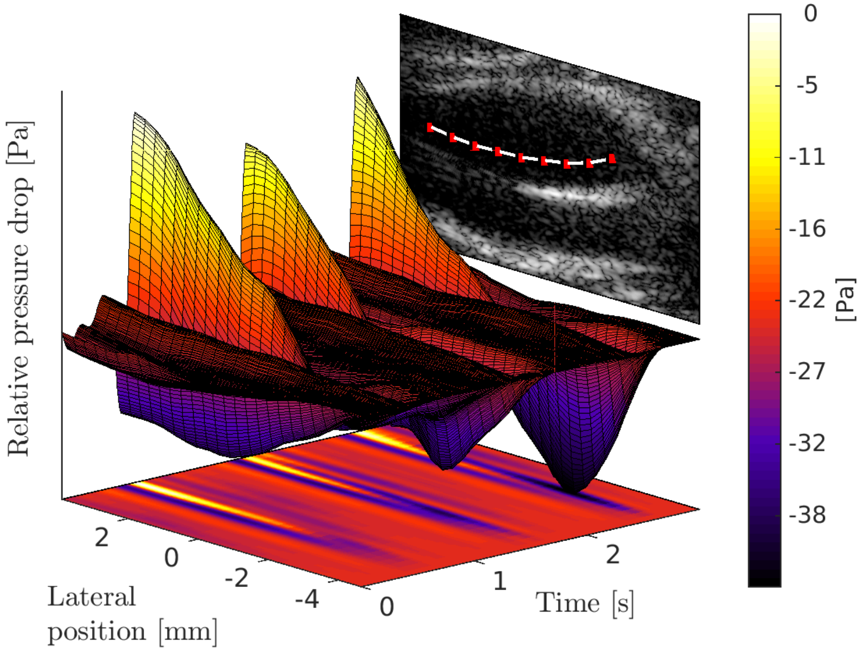

Figure 6.10: In-Vivo: Changes in intravascular pressure measured as a function of longitudinal position and time along the streamline from Fig. 6.6. The shown pressures are in reference to an arbitrary value, which for this study is set to zero at the beginning of the streamline.

vulnerable to the flow estimator's capability to detect the true movement of the particles. For instance, the proposed set-up uses a 2-D velocity estimator approach, meaning that the out-of-plane motion gets excluded from the pressure algorithm. Whether or not this is acceptable greatly depends on the complexity of the flow being examined. For example, studying the vector field in Fig. 6.6, it appears that the flow along the streamline accelerates through the carotid bulb, even though the lumen of the vessel expanse. Such flow behaviour is only possible if out-of-plane particles of higher velocities are pushed through the scanned plane, thus, leading to the false impression that in-plane velocities are accelerated from right to left in the image. Therefore, in case of Fig. 6.6, it would have been beneficial to have had access to the full 3-D velocity information before deriving the pressure drop. The missing information on the out-of-plane velocity component is likely the reason for why Fig. 6.10 appears more distorted than Fig. 6.9, where a more holistic view of the flow movement is captured within the scan plane.

PRESSURE CHANGES CAUSED BY VISCOUS DRAG

The influence of viscosity has been neglected in this study, as flow in larger vessels was studied, and a Reynolds number of more than a 1,000 was found during the peak systolic phase. However, moving into smaller vessels with a lower Reynolds number makes this assumption invalid thus, pressure estimation based on the Navier-Stokes equation should for those vessels take the viscous forces into account.

Moreover, diseased vessels with clinically significant stenoses rarely show curvatures as neat as the phantoms used in this study. Usually, highly irregular shapes are seen in stenotic arteriae leading to more complex flow patterns, and thereby also a larger prevalence of turbulent flow features. Features such as eddies, localized turbulence, and jets that all contribute to the dissipation of energy, will accelerate an increasing drop in pressure as the fluid passes through the stenotic region (Gould 1985; Young, Cholvin, and Roth 1975). Therefore, more studies measuring in more irregular geometries with increasing constriction-rates are recommended to determine the limits of the method's application range. Moreover, to clinically strengthen the validation of the proposed method, future work should include comparison with fluid-filled pressure catheters, as these are the current clinical practice for how intravascular pressure changes are measured.

6.7 Study conclusion

Based on experimental results this study concludes that pressure changes along streamlines are obtainable to a precision of more than 90 % of the maximum pressure drop through synthetic aperture flow imaging. However, transferring into in-vivo cases where blood vessels usually follow complex flow geometries, the influence of the out-of-plane component becomes increasingly important. Therefore, for scans using a 1-D transducer it is crucial that the part of the flow field, which contributes the most to intravascular pressure changes, is captured within the FOV of the probe. This will minimize the error of not having the third velocity component available when deriving pressure changes. Further, moving towards smaller vessels will increase the need for adding the viscous effect to the model. For the proposed method, this means that calculation of second order derivatives are required, thus making the method increasingly more sensitive to noise. Therefore, to strengthen the model in small vessel geometries, a new flow estimator is introduced in the next chapter, which completely avoids noise generated by the differential operator. Overall, the presented study displayed the advantages in precision of using a high frame rate flow estimator, when deriving intravascular pressure changes.

CHAPTER 7

Patent II
Flow Acceleration Estimation Directly From Beamformed Ultrasound data

Summary *The chapter proposes a method capable of determining the temporal and the spatial acceleration of flow directly from beamformed ultrasound data. Such a method essentially breaks with the conventional way of deriving accelerations, as the need for a differential operator is omitted. The presented work was made in the final stage of the project and has therefore not yet been introduced to the proposed pressure estimator. However, the developed technique was taken up by Analogic, who in collaboration with the author wrote the second patent proposal seen in Appendix (Patent II). The method calculates acceleration directly from beamformed ultrasound data by introducing a double cross-correlation scheme. Derivation of the estimator is detailed in the first part of the chapter. The second part concerns the results from testing the technique on simulated flow data generated using Field II. The last section discusses the initially obtained results and gives perspective on the method.*

7.1 Purpose

The purpose of this chapter is to introduce a temporal/spatial acceleration estimator based directly on beamformed ultrasound data. The motivation for doing this comes from the ever present concern of deriving accelerations from estimated velocities, namely, the transferring of noise through the differential operator. As previous mentioned, the operator works as a high-pass filter on the measured velocity data, thereby enhancing frequency content that primarily is related to noise. Data are, therefore, required to be filtered before entering the differential quotient to minimize the noise floor. Filtering is at the expense of temporal and spatial resolution, which degrades the degree of details that can be expressed in the flow field. Therefore, to circumvent the need for a differential operator, the chapter introduces a new method capable of measuring the acceleration of flow directly from the beamformed ultrasound data.

7.2 Derivation of the acceleration estimator

The basic principle of the proposed estimator is to study the trend of cross-correlation functions found from a series of consecutive RF signals. Cross-correlating signals that are displaced in time will bring forth a correlation function that peaks at a lag proportional to the time-shift between the signals. For instance, emitting two consecutive pulses in the direction of a moving scatterer will show a time shift between the backscattering signals that is (Jensen 1996a),

$$t_s = \frac{2\big|v(t)\big|}{c} T_{prf}, \tag{7.1}$$

where $\big|v(t)\big|$ is the velocity of the moving scatterer, c the speed of sound, and T_{prf} the time between emissions. Cross-correlating the two signals will reveal the time shift, t_s, that can be identified at the position of the function's maximum value. Cross-correlation two time signals is expressed mathematically as,

$$R(\tau) = \frac{1}{2T} \int_T r_{s1}(t)\, r_{s2}(t-\tau)\, dt. \tag{7.2}$$

where, T is the duration of the signals, r_{s1} and r_{s2}, while τ is the running lag. The correlation function $R(\tau)$ peaks when τ equals the time shift, t_s, multiplied by the system's sampling frequency, f_s. This is sought represented in Fig. 7.1, where signals from the same aperture configuration are cross-correlated to yield a series of $R(\tau)$.

The position of the peak will change over time if pulsating flow is measured and the rate of this change is proportional to the flow acceleration. The acceleration can, thus be

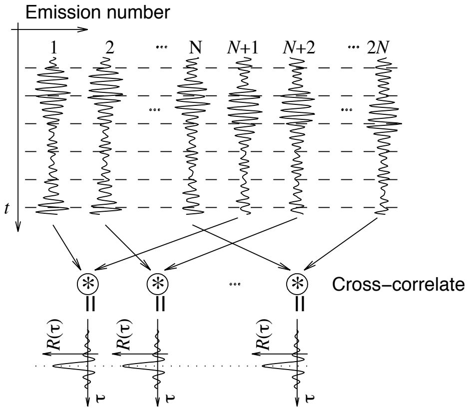

Figure 7.1: Estimating the cross-correlation function from received RF signals measured with the same aperture configuration. The lag at the function's maximum value is proportional to the velocity of the targeted scatterer. The figure is modified from (Nikolov and Jensen 2003)

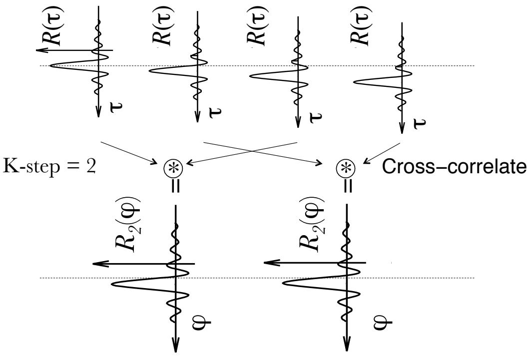

Figure 7.2: Finding the cross-correlation of already calculated correlation functions. The lag at $R_2(\varphi)$ maximum value is proportional to the acceleration of the insonified scatterer.

found from correlation of the correlation functions. The process of this is illustrated in Fig. 7.2, where the correlation, $R_2(\varphi)$, between correlation functions, $R(\tau)$, is shown. A skipping step, K, is used in the presented set-up, which ensures a larger separation between the correlation functions. Separating the functions reduces the effect of jitter, however, it can potentially lead to the detection of false peak, as the signals decorrelate more. Choosing a proper step size is therefore always a balance between jitter effects and the system's tolerance limit for determining incorrect peaks; both leads to erroneous estimates. The second cross-correlation function is calculated as,

$$R_2(\varphi) = \frac{1}{2L} \sum_{\tau=-L}^{L} R^{(1)}(\tau)\, R^{(1+K)}(\tau - \varphi)\,, \tag{7.3}$$

where $R^{(1)}$ and $R^{(1+K)}$ are the previous calculated correlations functions, and L is the number of data points in the two functions. Eq. (7.3) will show a function that peaks at lag,

$$\varphi_{peak} = \Delta t_s\, f_s = \frac{2\Delta\big|v(t)\big|\, f_s}{c} T_{prf}. \tag{7.4}$$

The change in velocity, $\Delta\big|v(t)\big|$ is the acceleration, $a(t)$, of the scatterer multiplied by the observation window. For the case of determining the temporal acceleration, the observation window is KT_{prf}, while for the spatial acceleration, the window is $K\Delta r$, where Δr is the spatial distance between the correlation functions. From (7.4) is becomes apparent that the temporal and spatial acceleration can be determined as,

$$|a_t| = \frac{\varphi_{peak}\, c}{2Kf_sT_{prf}^2}\ , \ and \tag{7.5}$$

$$|a_s| = \frac{\varphi_{peak}\, c}{2Kf_s\Delta rT_{prf}}, \tag{7.6}$$

respectively, where φ_{peak} is the position of the second cross-correlation function's maximum value.

7.3 Proof-of-concept

The following presents the initial results from testing the proposed estimator on simulated flow data. Data are generated using Field II (Jensen 1996b), and simulate a parabolic time-varying flow profile through a rigid tube of a 12 mm diameter, with a beam-to-flow angle of 75°. The profile is set to oscillate as a sine-function with a frequency of 1 Hz, and a peak velocity of $0.1\,\mathrm{m\,s^{-1}}$. An emission sequence equivalent to that of Chapter 6 is designed, and the resulting velocity estimates are displayed in Fig. 7.3. The figure

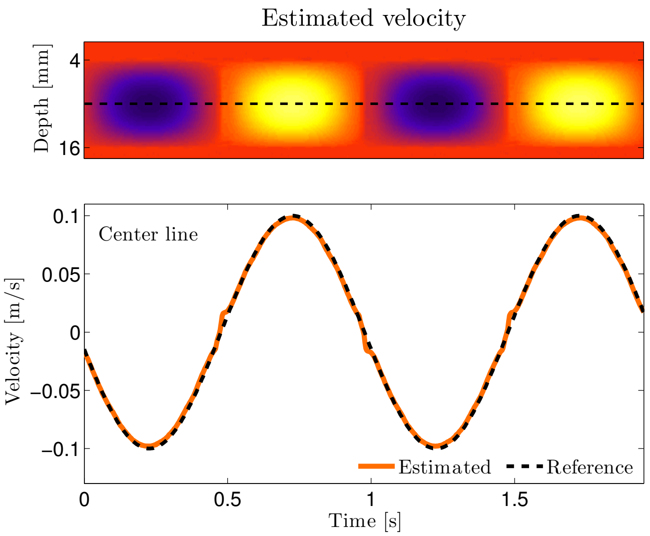

Figure 7.3: Estimated flow velocities from simulated data. The velocities are estimated using a cross-correlation approach based on directional beamformed lines, equivalent to the technique used in Study 2 (Chapter 6).

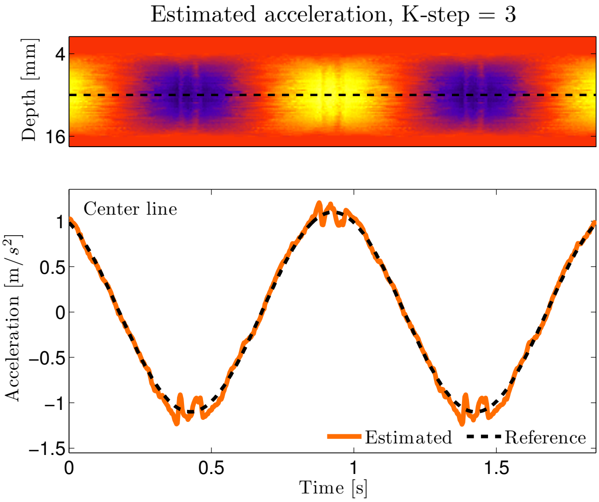

Figure 7.4: Estimated temporal acceleration from simulated flow data. The acceleration is calculated using the proposed double cross-correlation approach, and compared to a cosine-function, which is the first-derivative of the original simulated sine-function.

shows velocities that are calculated by cross-correlating directional lines from successive emission with identical aperture configurations. However, instead of finding the velocities from a single cross-correlation, a second correlation is performed enabling detection of the flow acceleration. The resulting estimated temporal acceleration is shown in Fig. 7.3. Here, a skipping step of three has been tested to lower the influence of jitter. The estimated acceleration is compared with a cosine-function, which is the derivative of the input to the simulation model.

7.4 Discussion and perspectives

The preliminary results show a good correspondence between estimated and simulated data indicating the feasibility of the proposed technique. The presented double cross-correlation approach omits the need for having to estimate flow velocities before deriving the temporal/spatial acceleration. This means that the configuration of the acceleration estimator, in terms of skipping step, and length of the correlation function become independent from what is used by the velocity estimator. Having an independent estimator allows for more flexibility, and this potentially leads to more reliable acceleration data. For instance, noise in the velocity estimates introduced by jitter or decorrelation effects, will in conventional methods transfer directly to the desired acceleration estimates. This is, however, no longer an issue with the proposed technique, making the acceleration data more robust. More reliable acceleration data will eventually lead to better estimates of pressure when using approaches such as the Bernoulli or the Navier-Stokes equations.

Moreover, besides improving pressure estimators that rely on flow data, the technique could also benefit other clinical areas. For instance, ultrasound studies on the aorta have shown links between ventricular performance and the acceleration of blood flow (Bennett et al. 1984; Noble, Trenchard, and Guz 1966; Sabbah et al. 1986). Such studies could essentially also draw advantages from the proposed technique, as the need for manually analysing the shape of the recorded spectrogram is removed.

CHAPTER 8

Project Conclusion and Perspectives

This thesis has presented the results of the PhD project titled Imaging of In-vivo Pressure using Ultrasound. The main objective of the project has been to develop a method that without the need of invasive devices is capable of determining intravascular pressure changes. To achieve this, a modified version of the Navier-Stokes equation was investigated in conjunction with 2-D vector velocity fields acquired from state-of-the-art ultrasound techniques. Pressure changes derived by the proposed method were compared with results from numerical simulation models, having the same flow geometries as the models being investigated.

In Chapter 4, a first attempt to derive pressure gradients from flow data was presented. The study was carried out in flow phantoms, where vector velocity data acquired using a commercial available ultrasound system were used. The study demonstrated the feasibility of deriving pressure gradients from 2-D ultrasound flow data. But perhaps more importantly, the study revealed some significant challenges that needed further attention to make the method applicable for clinical use. Most crucial, was the noise contamination seen in the recorded velocity data. Despite implementation of advanced filters, the noise influenced the estimated pressures, and this hampered the precision of the estimator. To solve the problem of noisy velocity estimates, two initiatives were taken. First, a new filtering approach was introduced in Chapter 5, subsequently in Chapter 6 the use of synthetic aperture flow imaging (SAFI) is proposed. The two initiatives were tested on data acquired using the experimental ultrasound scanner, SARUS. SAFI offered an imaging system that was fully focused in every image cell, and further, was capable of generating flow images at a frame rate on the order of kilohertz. This allowed for averaging across velocity frames without losing temporal information, leading to highly precise and quantitative flow data. The high precision flow data provided ideal conditions for deriving the desired pressure changes. This was confirmed by the improvement in precision of the results in Chapter 6. Here, the study showed a standard deviation and bias across two fabricated phantoms of 9 % and 8 %, respectively. The study, further, presented the first in-vivo examples of deriving pressure changes from 2-D vector velocity ultrasound data.

Unlike other methods that use ultrasound flow data to derive the intravascular pressure, this method is based on 2-D angle-independent velocity fields captured in the entire image plane. This provides a wider information background for determining the pressure changes, and as the method is independent of the insonifying angle it facilitates a scan procedure that is less operator-dependent. The above described improvements may assist, and even exceed the need for invasive pressure catheters that otherwise remain a frequently used tool.

The project has shown that non-invasive determination of pressure changes from 2-D flow data is indeed feasible. Moreover, the project demonstrated that a SAFI sequence offered the high precision flow data needed to obtain reliable pressure estimates. Based on these findings, it is proposed that SAFI should be the imaging method of choice when introducing the technique to the clinic. However, when transferring the method into the clinic, where blood vessels follow more complex flow geometries, the influence of the out-of-plane component becomes increasingly more important. Therefore, for scans using a 1-D transducer it is crucial that the out-of-plane flow component is negligible.

Next step is to compare the developed technique with catheters. Such a comparison is, however, not without concerns. Numerous studies have presented results showing discrepancies between Doppler derived pressures and the pressure measured by catheters (Baumgartner, Schima, et al. 1993; Baumgartner, Stefenelli, et al. 1999; Garcia et al. 2003; Levine et al. 1989; Smith et al. 1985). It is believed by the author that the discrepancies arise for two reasons. First, pressure catheters are usually difficult to position. Flow instabilities seen downstream of an arterial narrowing makes it cumbersome to maintain a steady position of the catheter, especially, in the region of vena contracta. Therefore, a catheter would usually be placed a few centimeters downstream from the narrowing. This means that the catheters might end up in an area where pressure recovery has occurred. Hence, the detected pressure drop will be less than the actual transstenotic pressure drop. Furthermore, a study by Vecchi *et al.* demonstrated that the catheter itself disturbs the pressure field it is measuring. The effect of this showed inaccuracies of upto 24 % of the true pressure drop (Vecchi et al. 2014). This might also add to the explanation for why discrepancies are seen between Doppler derived pressure and the pressure measured by catheters.

Another explanation for the discrepancies is found in the accuracy of the employed Doppler system that is used for acquiring the input data to the model. Most of the ultrasound techniques presented in the literature are based on Doppler velocities provided by the spectrogram. This is unfortunate as this measure of velocity is highly sensitive to the flow being examined. Difficulties related to detecting the correct beam-to-flow angle will often lead to imprecision of the derived pressure. Detection of the correct velocity becomes even more difficult and also more important, when moving into diseased vessels, where vessel geometries often follow highly irregularly paths. Further, from studying the vector flow fields in Figs. 6.5–6.6, it becomes obvious that more than just single beam-to-flow angle exists. Every point in the fields has its own flow angle, and that angle varies over time depending on when in the cardiac cycles it is measured. This is also seen in the clinical examples presented by Hansen *et al.*(Hansen et al. 2009). Therefore, only compensating the measured Doppler flow by a single fixed angle is a crude oversimplification and it will lead to greater discrepancies between Doppler derived pressure and the pressure measured by catheters.

With the introduction of a non-invasive alternative for measuring intravascular pressure, the clinician becomes independent of catheterization, and the need for using ionizing radiation. This leads to the possibility of making routine scans, enabling screening procedures and follow-up studies over the progression of the disease, without the discomfort related to surgical intervention. The non-invasive nature of the technique, furthermore, allows measurement of the pressure field in the carotid arteries – an area that otherwise is off-limits for catheters, due to the risks of provoking a rupture of vulnerable plaque. Uncovering the carotid pressure field, and especially, the field around the baroreceptors, is of great interest, as the vascular pressure here governs the systemic blood pressure of the whole body. It would therefore be interesting to investigate, if an abnormal pressure distribution at the baroreceptors has a negative effect on the overall blood pressure.

The proposed project does not solve all problems related to non-invasive pressure estimation, but it is believed to be a step in the right direction. Hopefully, one day a method such as the one presented will mitigate, or even supersede the need for invasive catheters, providing a safer procedure for the patients and a more problem-free work environment for the clinicians.

Bibliography

References from Chapter 1

Adam, D., M. Sapunar, and E. Burla (2005). “On the relationship between encapsulated ultrasound contrast agent and pressure”. In: *Ultrasound Med. Biol.* 31, pp. 673–686 (cit. on p. 4).

Adrian, R. J. and C.-S. Yao (1985). “Pulsed laser technique application to liquid and gaseous flows and the scattering power of seed materials”. In: *Appl. Opt.* 24.1, pp. 44–52 (cit. on p. 6).

Ambrose, J. A., M. A. Tannenbaum, D. Alexopoulos, C. E. Hjemdahl-Monsen, J. Leavy, M. Weiss, S. Borrico, R. Gorlin, and V. Fuster (1988). “Angiographic progression of coronary artery disease and the development of myocardial infarction”. In: *J. Am. Coll. Cardiol.* 12.1, pp. 56–62 (cit. on p. 2).

Al-Ameri, H., M. L. Thomas, A. Yoon, G. S. Mayeda, S. Burstein, R. A. Kloner, and D. M. Shavelle (2009). “Complication rate of diagnostic carotid angiography performed by interventional cardiologists”. In: *Catheter Cardiovasc Interv.* 73, pp. 661–665 (cit. on p. 3).

Andersen, K. S. and J. A. Jensen (2009). “Ambient pressure sensitivity of microbubbles investigated through a parameter study”. In: *J. Acoust. Soc. Am.* 126, pp. 3350–3358 (cit. on p. 4).

Baim, D. S. and W. Grossman (2000). *Grossman’s cardiac catheterization, angiography, and intervention*. Lippincott Williams & Wilkins (cit. on p. 2).

Baumgartner, H., H. Schima, G. Tulzer, and P. Kühn (1993). “Effect of Stenosis Geometry on the Doppler-Catheter Gradient Relation In Vitro: A Manifestation of Pressure Recovery”. In: *J. Am. Coll. Cardiol.* 21.4, pp. 1018–1025 (cit. on p. 4).

Baumgartner, H., T. Stefenelli, J. Niederberger, H. Schima, and G. Maurer (1999). “Overestimation of catheter gradients by Doppler ultrasound in patients with aortic stenosis: A predictable manifestation of pressure recovery”. In: *J. Am. Coll. Cardiol.* 33.6, pp. 1655–1661 (cit. on p. 4).

Bermejo, J., J. C. Antoranz, I. G. Burwash, J. L. Alvarez, M. Moreno, M. A. Garcia-Fernandez, and C. M. Otto (2002). “In-vivo analysis of the instantaneous transvalvular pressure difference-flow relationship in aortic valve stenosis: implications of unsteady fluid-dynamics for the clinical assessment of disease severity”. In: *J. Heart Valve Dis.* 11.4, pp. 557–566 (cit. on p. 4).

Beulen, B. W. A. M. M., N. Bijnens, G. G. Koutsouridis, P. J. Brands, M. C. M. Rutten, and F. N. van de Vosse (2011). "Toward noninvasive blood pressure assessment in arteries by using ultrasound". In: *Ultrasound Med. Biol.* 37.5, pp. 788–797 (cit. on p. 4).

Blausen (2014). *Blausen gallery 2014* (cit. on p. 1).

Bock, J., A. Frydrychowicz, R. Lorenz, D. Hirtler, A. J. Barker, K. M. Johnson, R. Arnold, H. Burkhardt, J. Hennig, and M. Markl (2011). "In vivo noninvasive 4D pressure difference mapping in the human aorta: phantom comparison and application in healthy volunteers and patients". In: *Magn. Reson. Med.* 66.4, pp. 1079–1088 (cit. on p. 5).

Bonow, R. O., B. Carabello, A. C. de leon, L. H. Edmunds, B. J. Fedderly, M. D. Freed, W. H. Gaasch, C. R. McKay, R. A. Nishimura, P. T. O'Gara, R. J. Gibbons, R. O. Russell, T. J. Ryan, and S. C. Smith (1998). "ACC/AHA Guidelines for the Management of Patients With Valvular Heart Disease". In: *J. Am. Coll. Cardiol.* 32.5, pp. 1486–1582 (cit. on p. 3).

Bouakaz, A., P. J. Frinking, N. de Jong, and N. Bom (1999). "Noninvasive measurement of the hydrostatic pressure in a fluid-filled cavity based on the disappearance time of micrometer-sized free gas bubbles". In: *Ultrasound Med. Biol.* 25, pp. 1407–1415 (cit. on p. 4).

Bruyne, B. D., T. Baudhuin, J. A. Melin, N. H. Pijls, S. U. Sys, A. Bol, W. J. Paulus, G. R. Heyndrickx, and W. Wijns (1994). "Coronary Flow Reserve Calculated From Pressure Measurements in Humans". In: *Circulation* 89, pp. 1013–1022 (cit. on p. 2).

Celermajer, D. S., K. E. Sorensen, V. M. Gooch, Miller, I. D. Sullivan, J. K. Lloyd, J. E. Deanfield, and D. J. Spiegelhalter (1992). "Non-invasive detection of endothelial dysfunction in children and adults at risk of atherosclerosis". In: *Lancet* 340.8828, pp. 1111–1115 (cit. on p. 3).

Charonko, J. J., C. V. King, B. L. Smith, and P. P. Vlachos (2010). "Assessment of pressure field calculations from particle image velocimetry measurements". In: *Meas. Sci. Technol.* 21.10, p. 105401 (cit. on p. 6).

Cosgrove, D. and N. Lassau (2010). "Imaging of perfusion using ultrasound". In: *Eur. J. Nucl. Med. Mol. Imaging*, s65–s85 (cit. on p. 4).

Donohue, T. J., M. J. Kern, F. V. Aguirre, R. G. Bach, T. Wolford, C. A. Bell, and J. Segal (1993). "Assessing the hemodynamic significance of coronary artery stenosis: Analysis of translesional pressure-flow velocity relations in patients". In: *J. Am. Coll. Cardiol.* 22.2, pp. 449–458 (cit. on p. 2).

Ebbers, T., L. Wigström, A. F. Bolger, J. Engvall, and M. Karlsson (2001). "Estimation of relative cardiovascular pressures using time-resolved three dimensional phase contrast MRI". In: *Magn. Reson. Med.* Pp. 872–879 (cit. on p. 5).

Evans, D. H., W. N. McDicken, R. Skidmore, and J. P. Woodcock (1989). *Doppler Ultrasound, Physics, Instrumentation, and Clinical Applications*. New York: John Wiley & Sons (cit. on p. 4).

Fairbank, W. M. and M. O. Scully (1977). “A new noninvasive technique for cardiac pressure measurements: resonant scattering of ultrasound from bubbles”. In: *IEEE Trans. Biomed. Eng.* 24, pp. 107–110 (cit. on p. 4).

Felix, W. R., B. Sige, R. J. Gibson, J. Williams, G. L. Popky, A. L. Edelstein, and J. R. Justin (1976). “Pulsed Doppler ultrasound detection of flow disturbances in arteriosclerosis”. In: *J. Clin. Ultrasound* 4.4, pp. 275–282 (cit. on p. 3).

Forsberg, F., J. Dave, V. G. Halldorsdottir, L. M. Leodore, F. Lin, A. L. Hall, and K. Thomenius (2008). “Applying real-time noninvasive pressure estimation obtained from subharmonic contrast microbubble signals”. In: *Proc. IEEE Ultrason. Symp.* Pp. 1694–1697 (cit. on p. 4).

Forsberg, F., J.-B. Liu, W. T. Shi, J. Furuse, M. Shimizu, and B. B. Goldberg (2005). “In Vivo Pressure Estimation Using Subharmonic Contrast Microbubble Signals: Proof of Concept”. In: *IEEE Trans. Ultrason., Ferroelec., Freq. Contr.* 52.4, pp. 581–583 (cit. on p. 4).

Garcia, D., J. G. Dumesnil, L.-G. Durand, L. Kadem, and P. Pibarot (2003). “Discrepancies between catheter and Doppler estimates of valve effective orifice area can be predicted from the pressure recovery phenomenon”. In: *J. Am. Coll. Cardiol.* 41.3, pp. 435–442 (cit. on p. 4).

Garcia, D., P. Pibarot, J. G. Dumesnil, F. Sakr, and L.-G. Durand (2000). “Assessment of Aortic Valve Stenosis Severity: A New Index Based on the Energy Loss Concept”. In: *Circulation* 101, pp. 765–771 (cit. on p. 3).

Garcia, D., P. Pibarot, and L.-G. Durand (2005). “Analytical modeling of the instantaneous pressure gradient across the aortic valve”. In: *J. Biomech.* 38, pp. 1303–1311 (cit. on p. 5).

Giddens, D. P., C. K. Zarins, and S. Glagov (1993). “The Role of Fluid Mechanics in the Localization and Detection of Atherosclerosis”. In: *J. Biomech. Eng.* 115, pp. 588–594 (cit. on p. 3).

Gould, K. L. (1985). “Quantification of Coronary Artery Stenosis in Vivo”. In: *Circ Res.* 57.3, pp. 341–353 (cit. on p. 2).

Greenberg, N. L., P. M. Vandervoort, M. S. Firstenberg, M. J. Garcia, and J. D. Thomas (2001). “Estimation of diastolic intraventricular pressure gradients by Doppler M-mode echocardiography”. In: *Am. J. Physiol. Heart Circ. Physiol.* 280.6, pp. 2507–2515 (cit. on p. 5).

Herment, A., G. Besson, C. Pellot-Barakat, and F. Frouin (2008). “Estimation of pressure gradient images from velocity encoded MR acquisitions”. In: *Computers in Cardiology* 35, pp. 933–936 (cit. on p. 5).

Holen, J., R. Aaslid, and K. Landmark (1976). “Determination of pressure gradient in Mitral stenosis with a non-invasive ultrasound Doppler technique”. In: *Acta med. scand.* 32, pp. 455–460 (cit. on p. 4).

Kajitani, L. and D. Dabiri (2005). “A full three-dimensional characterization of defocusing digital particle image velocimetry”. In: *Meas. Sci. Technol.* 16, pp. 790–804 (cit. on p. 6).

Kavey, R.-E. W., S. R. Daniels, R. M. Lauer, D. L. Atkins, L. L. Hayman, and K. Taubert (2003). “American heart association guidelines for primary prevention of atherosclerotic cardiovascular disease beginning in childhood”. In: *J. Pediatr.* 142.4, pp. 368–372 (cit. on p. 1).

Kilner, P. J., G. Z. Yang, R. H. Mohiaddin, D. N. Firmin, and D. B. Longmore (1993). “Helical and retrograde secondary flow patterns in the aortic arch studied by three-directional magnetic resonance velocity mapping”. In: *Circulation* 88.5, pp. 2235–2247 (cit. on p. 5).

Kips, J. G., P. Segers, and L. M. V. Bortel (2008). “Identifying the vulnerable plaque: A review of invasive and non-invasive imaging modalities”. In: *Artery Research* 2.1, pp. 21–34 (cit. on p. 3).

Little, W. C., M. Constantinescu, R. J. Applegate, M. A. Kutcher, M. T. Burrows, F. R. Kahl, and W. P. Santamore (1988). “Can Coronary Angiography Predict the Site of a Subsequent Myocardial Infarction in Patients With Mild-to-Moderate Coronary Artery Disease?” In: *Circulation* 78.5, pp. 1157–1166 (cit. on p. 2).

Lovett, J. K., P. J. Gallagher, L. J. Hands, J. Walton, and P. M. Rothwell (2004). “Histological Correlates of Carotid Plaque Surface Morphology on Lumen Contrast Imaging”. In: *Circulation* 110, pp. 2190–2197 (cit. on p. 2).

Meinders, J. M. and A. P. G. Hoeks (2004). “Simultaneous assessment of diameter and pressure waveforms in the carotid artery”. In: *Ultrasound Med. Biol.* 30.2, pp. 147–154 (cit. on p. 5).

Moftakhar, R., B. Aagaard-Kienitz, K. Johnson, P. A. Turski, A. S. Turk, D. B. Niemann, D. Consigny, J. Grinde, O. Wieben, and C. A. Mistretta (2007). “Noninvasive measurement of intra-aneurysmal pressure and flow pattern using phase contrast with vastly undersampled isotropic projection imaging”. In: *Am. J. Neuroradiol.* 28, pp. 1710–1714 (cit. on p. 5).

Naghavi, M., P. Libby, E. Falk, S. W. Casscells, S. Litovsky, J. Rumberger, J. J. Badimon, C. Stefanadis, P. Moreno, G. Pasterkamp, Z. Fayad, P. H. Stone, D. P. Zipes, P. K. Shah, and J. T. Willerson (2003). “From Vulnerable Plaque to Vulnerable Patient A Call for New Definitions and Risk Assessment Strategies: Part 1”. In: *Circulation* 108, pp. 1664–1672 (cit. on p. 1).

Ohtsuki, S. and M. Tanaka (2003). “Doppler pressure field deduced from the Doppler velocity field in an observation plane in a fluid”. In: *Ultrasound Med. Biol.* 29.10, pp. 1431–1438 (cit. on p. 5).

Ophir, J., I. Céspedes, H. Ponnekanti, Y. Yazdi, and X. Li (1991). “Elastography: A Quantitative Method for Imaging the Elasticity of Biological Tissues”. In: *Ultrason. Imaging* 13.2, pp. 111–134 (cit. on p. 3).

Osarumwense, D., R. Pararajasingam, P. Wilson, J. Abraham, and S. R. Walker (2005). “Carotid Artery Imaging in the United Kingdom: A Postal Questionnaire of Current Practice”. In: *Vascular* 13.3, pp. 173–177 (cit. on p. 1).

Oudheusden, B. W. van (2013). “PIV-based pressure measurement”. In: *Meas. Sci. Technol.* 24.3, p. 032001 (cit. on p. 6).

Pijls, N. H. J., B. D. Bruyne, K. Peels, P. H. van der Voort, H. J. Bonnier, J. Bartunek, and J. J. Koolen (1996). “Measurement of Fractional Flow Reserve to Assess the Functional Severity of Coronary-Artery Stenoses”. In: *N. Engl. J. Med* 334, pp. 1703–1708 (cit. on p. 2).

Pijls, N. H., B. D. Bruyne, G. J. W. Bech, F. Liistro, G. R. Heyndrickx, H. J. Bonnier, and J. J. Koolen (2000). “Coronary Pressure Measurement to Assess the Hemodynamic Significance of Serial Stenoses Within One Coronary Artery”. In: *Circulation* 102, pp. 2371–2377 (cit. on p. 2).

Reddy, A. K., G. E. Taffet, S. Madala, L. H. Michael, M. L. Entman, and C. J. Hartley (2003). “Noninvasive blood pressure measurement in mice using Doppler ultrasound”. In: *Ultrasound Med. Biol.* 29.3, pp. 379–385 (cit. on p. 5).

Saba, L., M. Anzidei, R. Sanfilippo, R. Montisci, P. Lucatelli, C. Catalano, R. Passariello, and G. Mallarini (2012). “Imaging of the carotid artery”. In: *Atherosclerosis* 220, pp. 294–309 (cit. on p. 2).

Seldinger, S. I. (1953). “Catheter replacement of the needle in percutaneous arteriography: A new technique”. In: *Acta Radiologica* 39, pp. 368–376 (cit. on p. 2).

Shi, W. T., F. Forsberg, J. S. Raichlen, and L. Needleman (1999). “Pressure dependence of subharmonic signals from contrast microbubbles”. In: *Ultrasound Med. Biol.* 25, pp. 275–283 (cit. on p. 4).

St Jude Medical, S. (2014). *FFR Measurement System with Agile Tip Technology*. URL: `Available%20at:%20http://professional.sjm.com/products/vas/intravascular-diagnostics-imaging,%20[Accessed%2015%20March%2023]` (cit. on p. 3).

Strauss, A. L., F. J. Roth, and H. Rieger (1993). “Noninvasive assessment of pressure gradients across iliac artery stenoses: duplex and catheter correlative study”. In: *J. Ultrasound Med.* 12.1, pp. 17–22 (cit. on pp. 2, 4).

Stroud, J. S., S. A. Berger, and D. Saloner (2002). “Numerical Analysis of Flow Through a Severely Stenotic Carotid Artery Bifurcation”. In: *J. Biomech. Eng.* 124.1, pp. 9–20 (cit. on p. 2).

Tasu, J. P., E. Mousseaux, A. Delouche, C. Oddou, O. Jolivet, and J. Bittoun (2000). “Estimation of pressure gradients in pulsatile flow from magnetic resonance acceleration measurements”. In: *Magn. Reson. Med.* 44.1, pp. 66–72 (cit. on p. 5).

Taylor, C. A., T. A. Fonte, and J. K. Min (2013). “Computational Fluid Dynamics Applied to Cardiac Computed Tomography for Noninvasive Quantification of Fractional Flow Reserve”. In: *J. Am. Coll. Cardiol.* 61.22, pp. 2233–2241 (cit. on p. 2).

Thomas, J. D. and Z. B. Popovic (2005). “Intraventricular pressure differences a new window into cardiac function”. In: *Circulation* 112, pp. 1684–1686 (cit. on p. 5).

Thompson, R. B. and E. R. McVeigh (2003). “Fast measurement of intracardiac pressure differences with 2D breath-hold phase-contrast MRI”. In: *Magnetic Resonance in Medicine* 49.6, pp. 1056–1066 (cit. on p. 5).

Tonino, P. A. L., B. D. Bruyne, N. H. J. Pijls, U. Siebert, F. Ikeno, M. vant Veer, V. Klauss, G. Manoharan, T. Engstrøm, K. G. Oldroyd, P. N. V. Lee, P. A. MacCarthy, and W. F. Fearon (2009). “Fractional Flow Reserve versus Angiography for Guiding Percutaneous Coronary Intervention”. In: *N. Engl. J. Med* 360.3, pp. 213–224 (cit. on p. 2).

Tonino, P. A. L., W. F. Fearon, B. D. Bruyne, K. G. Oldroyd, M. A. Leesar, P. N. V. Lee, P. A. MacCarthy, M. vant Veer, and N. H. J. Pijls (2010). “Angiographic Versus Functional Severity of Coronary Artery Stenoses in the FAME Study”. In: *J. Am. Coll. Cardiol.* 55.25, pp. 2816–2821 (cit. on p. 2).

Vecchi, A. de, R. E. Clough, N. R. Gaddum, M. C. M. Rutten, P. Lamata, T. Schaeffter, D. A. Nordsletten, and N. P. Smith (2014). “Catheter-induced errors in pressure measurements in vessels: An in-vitro and numerical study”. In: *IEEE Trans. Biomed. Eng.* 61.6, pp. 1844–1850 (cit. on p. 3).

Wardlaw, J. M., F. M. Chappell, J. J. K. Best, K. Wartolowska, and E. Berry (2006). “Non-invasive imaging compared with intra-arterial angiography in the diagnosis of symptomatic carotid stenosis: a meta-analysis”. In: *Lancet* 367.9521, pp. 1503–1512 (cit. on p. 1).

Wasserman, B. A., R. J. Wityk, H. H. Trout, and R. Virmani (2005). “Looking beyond the lumen with MRI”. In: *Stroke* 36, pp. 2504–2013 (cit. on p. 2).

World Health Organization, W. (2014). *The top 10 causes of death*. URL: `Available%20at:%20http://www.who.int/mediacentre/factsheets/fs310/en/.%20[Accessed%2015%20March%2015]` (cit. on p. 1).

Yotti, R., J. Bermejo, J. C. Antoranz, J. L. Rojo-Alvarez, C. Allue, J. Silva, M. M. Desco, M. Moreno, and M. A. Garcia-Fernandez (2004). “Noninvasive assessment of ejection intraventricular pressure gradients”. In: *J. Am. Coll. Cardiol.* 43.9, pp. 1654–1662 (cit. on p. 5).

Young, D. F., N. R. Cholvin, and A. C. Roth (1975). “Pressure Drop across Artificially Induced Stenoses in the Femoral Arteries of Dogs”. In: *Circ Res.* 36, pp. 735–743 (cit. on p. 2).

References from Chapter 2

Bohs, L. N., B. J. Geiman, M. E. Anderson, S. C. Gebhart, and G. E. Trahey (2000). “Speckle tracking for multi-dimensional flow estimation”. In: *Ultrasonics* 38, pp. 369–375 (cit. on p. 11).

Bonnefous, O. (1988). “Measurement of the complete (3D) velocity vector of blood flows”. In: *Proc. IEEE Ultrason. Symp.* Pp. 795–799 (cit. on p. 11).

Dunmire, B., K. W. Beach, K.-H. Labs., M. Plett, and D. E. Strandness (2000). “Cross-beam vector Doppler ultrasound for angle independent velocity measurements”. In: *Ultrasound Med. Biol.* 26, pp. 1213–1235 (cit. on p. 11).

Gorlin, R. and S. G. Gorlin (1951). “Hydraulic formula for calculation of the area of the stenotic mitral valve, other cardiac valves, and central circulatory shunts”. In: *Am. Heart J.* 41.1, pp. 1–29 (cit. on p. 11).

Holbek, S., M. Pihl, C. Ewertsen, M. Nielsen, and J. A. Jensen (2014). "3-D Velocity Estimation for Two Planes in vivo". In: *Proc. IEEE Ultrason. Symp.* Pp. 1706–1709 (cit. on p. 11).

Holen, J., R. Aaslid, and K. Landmark (1976). "Determination of pressure gradient in Mitral stenosis with a non-invasive ultrasound Doppler technique". In: *Acta med. scand.* 32, pp. 455–460 (cit. on p. 11).

Jensen, J. A. (2003). "Directional velocity estimation using focusing along the flow direction: I: Theory and simulation". In: *IEEE Trans. Ultrason., Ferroelec., Freq. Contr.* 50, pp. 857–872 (cit. on p. 11).

Jensen, J. A. and P. Munk (1998). "A New Method for Estimation of Velocity Vectors". In: *IEEE Trans. Ultrason., Ferroelec., Freq. Contr.* 45, pp. 837–851 (cit. on p. 11).

Jensen, J. A. and S. I. Nikolov (2002). "Transverse flow imaging using synthetic aperture directional beamforming". In: *Proc. IEEE Ultrason. Symp.* Pp. 1488–1492 (cit. on p. 11).

Løvstakken, L., S. Bjærum, D. Martens, and H. Torp (Feb. 2006). "Blood Flow Imaging - A New Real-Time, 2-D Flow Imaging Technique". In: *IEEE Trans. Ultrason., Ferroelec., Freq. Contr.* 53.2, pp. 289–299 (cit. on p. 11).

Orfanidis, S. J. (1996). *Introduction to signal processing*. Pearson Education, Inc. (cit. on p. 13).

Pihl, M. J. and J. A. Jensen (2011). "3D Velocity Estimation using a 2D Phased Array". In: *Proc. IEEE Ultrason. Symp.* Pp. 430–433 (cit. on p. 13).

Pihl, M. J. and J. A. Jensen (2012). "Measuring 3D Velocity Vectors using the Transverse Oscillation Method". In: *Proc. IEEE Ultrason. Symp.* Pp. 1881–1885 (cit. on p. 13).

Pihl, M. J. and J. A. Jensen (2014). "A Transverse Oscillation Approach for Estimation of Three-Dimensional Velocity Vectors. Part I: Concept and Simulation Study". In: *IEEE Trans. Ultrason., Ferroelec., Freq. Contr.* 61, pp. 1599–1607 (cit. on p. 11).

Pihl, M. J., M. B. Stuart, B. G. Tomov, M. F. Rasmussen, and J. A. Jensen (2014). "A Transverse Oscillation Approach for Estimation of Three-Dimensional Velocity Vectors. Part II: Experimental Validation". In: *IEEE Trans. Ultrason., Ferroelec., Freq. Contr.* 51.10, pp. 1608–1618 (cit. on p. 11).

Prandtl, L. (1952). *Essentials of Fluid Dynamics*. London: Blackie & Son (cit. on p. 12).

Savitzky, A. and M. J. E. Golay (1964). "Smoothing and differentiation of data by simplified least squares procedures". In: *Anal. Chem.* 36.8, pp. 1627–1639 (cit. on p. 13).

Skjaerpe, T., L. Hegrenaes, and L. Hatle (1985). "Noninvasive estimation of valve area in patients with aortic stenosis by Doppler ultrasound and two-dimensional echocardiography". In: *Circulation* 72, pp. 810–818 (cit. on p. 11).

Teirstein, P. S., P. G. Yock, and R. L. Popp (1985). "The accuracy of Doppler ultrasound measurement of pressure gradients across irregular, dual, and tunnellike obstructions to blood flow". In: *Circulation* 72, pp. 577–584 (cit. on p. 11).

Tortoli, P., G. Bambi, and S. Ricci (Aug. 2006). “Accurate Doppler angle estimation for vector flow measurements”. In: *IEEE Trans. Ultrason., Ferroelec., Freq. Contr.* 53.8, pp. 1425–1431 (cit. on p. 11).

Truskey, G. A., F. Yuan, and D. F. Katz (2004). *Transport Phenomena in Biological Systems*. Pearson Education, Inc., Pearson Prentice Hall (cit. on p. 12).

Udesen, J., F. Gran, K. L. Hansen, J. A. Jensen, C. Thomsen, and M. B. Nielsen (2008). “High Frame-Rate Blood Vector Velocity Imaging Using Plane Waves: Simulations and Preliminary Experiments”. In: *IEEE Trans. Ultrason., Ferroelec., Freq. Contr.* 55.8, pp. 1729–1743 (cit. on p. 11).

Wood, N. B. (1999). “Aspects of fluid dynamics applied to the large arteries”. In: *J. Theor. Biol.* 199.953, pp. 137–161 (cit. on p. 12).

Yoganathan, A. P., E. G. Cape, H.-W. Sung, F. P. Williams, and A. Jimoh (1988). “Review of hydrodynamic principles for the cardiologist: Applications to the study of blood flow and jets by imaging techniques”. In: *J. Am. Coll. Cardiol.* 12.5, pp. 1344–1353 (cit. on p. 11).

References from Chapter 3

Bae, M. H. and M. K. Jeong (2000). “A study of synthetic-aperture imaging with virtual source elements in B-mode ultrasound imaging systems”. In: *IEEE Trans. Ultrason., Ferroelec., Freq. Contr.* Vol. 47, pp. 1510–1519 (cit. on p. 20).

BK Medical (Mar. 2015). *http://bkultrasound.com/bk-medical/VectorFlow* (cit. on p. 16).

Bredeson, D. (2015). *Water Drops Ripples*. http://www.dreamstime.com (cit. on p. 17).

Frazier, C. H. and W. D. O’Brien (1998). “Synthetic aperture techniques with a virtual source element”. In: *IEEE Trans. Ultrason., Ferroelec., Freq. Contr.* 45, pp. 196–207 (cit. on p. 20).

Hansen, P. M., M. M. Pedersen, K. L. Hansen, M. B. Nielsen, and J. A. Jensen (2011). “Demonstration of a vector velocity technique”. In: *Ultraschall in Med.* 32, pp. 213–215 (cit. on p. 16).

Jensen, J. A. (1996a). *Apparatus and method for determining movements and velocities of moving objects*. International patent PCT/DK97/00287 (cit. on p. 16).

— (1996b). *Estimation of Blood Velocities Using Ultrasound: A Signal Processing Approach*. New York: Cambridge University Press (cit. on p. 19).

— (Oct. 2000). *Estimation of vector velocity*. International patent PCT/DK00/00243 (cit. on p. 16).

— (2001). “A New Estimator for Vector Velocity Estimation”. In: *IEEE Trans. Ultrason., Ferroelec., Freq. Contr.* 48.4, pp. 886–894 (cit. on p. 19).

— (2003). “Directional velocity estimation using focusing along the flow direction: I: Theory and simulation”. In: *IEEE Trans. Ultrason., Ferroelec., Freq. Contr.* 50, pp. 857–872 (cit. on p. 20).

Jensen, J. A. and I. R. Lacasa (1999). “Estimation of blood velocity vectors using transverse ultrasound beam focusing and cross-correlation”. In: *Proc. IEEE Ultrason. Symp.* Pp. 1493–1497 (cit. on p. 20).

Jensen, J. A. and P. Munk (1998). “A New Method for Estimation of Velocity Vectors”. In: *IEEE Trans. Ultrason., Ferroelec., Freq. Contr.* 45, pp. 837–851 (cit. on pp. 16, 18, 19).

Jensen, J. A. and S. I. Nikolov (2002). “Transverse flow imaging using synthetic aperture directional beamforming”. In: *Proc. IEEE Ultrason. Symp.* Pp. 1488–1492 (cit. on p. 16).

Jensen, J. A., S. Nikolov, K. L. Gammelmark, and M. H. Pedersen (2006). “Synthetic Aperture Ultrasound Imaging”. In: *Ultrasonics* 44, e5–e15 (cit. on p. 20).

Karaman, M., P. C. Li, and M. O’Donnell (1995). “Synthetic aperture imaging for small scale systems”. In: *IEEE Trans. Ultrason., Ferroelec., Freq. Contr.* 42, pp. 429–442 (cit. on p. 20).

Kruskal, J. B., P. A. Newman, L. G. Sammons, and R. A. Kane (2004). “Optimizing Doppler and Color Flow US: Application to Hepatic Sonography”. In: *Radiographics* 24.3, pp. 657–675 (cit. on p. 16).

Nikolov, S. I. (2001). “Synthetic Aperture Tissue and Flow Ultrasound Imaging”. PhD thesis. 2800, Lyngby, Denmark: Ørsted•DTU, Technical University of Denmark (cit. on pp. 21, 22).

Nikolov, S. I. and J. A. Jensen (2002). “Virtual ultrasound sources in high-resolution ultrasound imaging”. In: *Proc. SPIE - Progress in biomedical optics and imaging.* Vol. 3, pp. 395–405 (cit. on p. 20).

— (2003). “In-vivo Synthetic Aperture Flow Imaging in Medical Ultrasound”. In: *IEEE Trans. Ultrason., Ferroelec., Freq. Contr.* 50.7, pp. 848–856 (cit. on p. 20).

O’Donnell, M. and L. J. Thomas (1992). “Efficient synthetic aperture imaging from a circular aperture with possible application to catheter-based imaging”. In: *IEEE Trans. Ultrason., Ferroelec., Freq. Contr.* 39, pp. 366–380 (cit. on p. 20).

Shattuck, D. P., M. D. Weinshenker, S. W. Smith, and O. T. von Ramm (1984). “Explososcan: A parallel processing technique for high speed ultrasound imaging with linear phased arrays”. In: *J. Acoust. Soc. Am.* 75, pp. 1273–1282 (cit. on p. 20).

Udesen, J. and J. A. Jensen (2006). “Investigation of Transverse Oscillation Method”. In: *IEEE Trans. Ultrason., Ferroelec., Freq. Contr.* 53, pp. 959–971 (cit. on pp. 16, 17).

Villagomez-Hoyos, C. A., M. B. Stuart, K. L. Hansen, M. B. Nielsen, and J. A. Jensen (2015). “Accurate Angle Estimator for High Frame Rate 2-D Vector Flow Imaging”. In: *IEEE Trans. Ultrason., Ferroelec., Freq. Contr.* Submitted (cit. on p. 22).

References from Chapter 4

Ahnert, K. and M. Abel (2007). “Numerical differentiation of experimental data: local versus global methods”. In: *Comput. Phys. Commun.* Pp. 764–774 (cit. on p. 29).

Jensen, J. A. (July 2013). “Optimization of transverse oscillating fields for vector velocity estimation with convex arrays”. In: *Proc. IEEE Ultrason. Symp.* Pp. 1753–1756 (cit. on p. 32).

Marcher, J., M. J. Pihl, and J. A. Jensen (2012). “The Transverse Oscillation Method using a Phased Array Transducer”. In: *Proc. IEEE Ultrason. Symp.* Pp. 1890–1893 (cit. on p. 32).

Pihl, M. J., J. Marcher, and J. A. Jensen (2012). “Phased-Array Vector Velocity Estimation Using Transverse Oscillations”. In: *IEEE Trans. Ultrason., Ferroelec., Freq. Contr.* 59.12, pp. 2662–2675 (cit. on p. 32).

Pihl, M. J., M. B. Stuart, B. G. Tomov, M. F. Rasmussen, and J. A. Jensen (2014). “A Transverse Oscillation Approach for Estimation of Three-Dimensional Velocity Vectors. Part II: Experimental Validation”. In: *IEEE Trans. Ultrason., Ferroelec., Freq. Contr.* 51.10, pp. 1608–1618 (cit. on p. 32).

References from Chapter 5

Evans, D. H., W. N. McDicken, R. Skidmore, and J. P. Woodcock (1989). *Doppler Ultrasound, Physics, Instrumentation, and Clinical Applications*. New York: John Wiley & Sons (cit. on p. 37).

Womersley, J. R. (1955). “Oscillatory motion of a viscous liquid in a thin-walled elastic tube. I: The linear approximation for long waves”. In: *Phil. Mag.* 46, pp. 199–221 (cit. on p. 37).

References from Chapter 6

Al-Ameri, H., M. L. Thomas, A. Yoon, G. S. Mayeda, S. Burstein, R. A. Kloner, and D. M. Shavelle (2009). “Complication rate of diagnostic carotid angiography performed by interventional cardiologists”. In: *Catheter Cardiovasc Interv.* 73, pp. 661–665 (cit. on p. 51).

Gould, K. L. (1985). “Quantification of Coronary Artery Stenosis in Vivo”. In: *Circ Res.* 57.3, pp. 341–353 (cit. on p. 54).

Jensen, J. A., H. Holten-Lund, R. T. Nilsson, M. Hansen, U. D. Larsen, R. P. Domsten, B. G. Tomov, M. B. Stuart, S. I. Nikolov, M. J. Pihl, Y. Du, J. H. Rasmussen, and M. F. Rasmussen (2013). “SARUS: A Synthetic Aperture Real-time Ultrasound System”. In: *IEEE Trans. Ultrason., Ferroelec., Freq. Contr.* 60.9, pp. 1838–1852 (cit. on p. 44).

Lai, S. S. M., B. Y. S. Yiu, A. K. K. Poon, and A. C. H. Yu (2013). “Design of Anthropomorphic Flow Phantoms Based on Rapid Prototyping of Compliant Vessel Geometries”. In: *Ultrasound Med. Biol.* 39.9, pp. 1654–1664 (cit. on p. 43).

Young, D. F., N. R. Cholvin, and A. C. Roth (1975). “Pressure Drop across Artificially Induced Stenoses in the Femoral Arteries of Dogs”. In: *Circ Res.* 36, pp. 735–743 (cit. on p. 54).

References from Chapter 7

Bennett, E. D., S. A. Barclay, A. L. Davis, D. Mannering, and N. Metha (1984). "Ascending aortic blood velocity and acceleration using Doppler ultrasound in the assessment of left ventricular function". In: *Cardiovascular Research*, pp. 632–638 (cit. on p. 60).

Jensen, J. A. (1996a). *Estimation of Blood Velocities Using Ultrasound: A Signal Processing Approach*. New York: Cambridge University Press (cit. on p. 56).

— (1996b). "Field: A Program for Simulating Ultrasound Systems". In: *Med. Biol. Eng. Comp.* 10th Nordic-Baltic Conference on Biomedical Imaging, Vol. 4, Supplement 1, Part 1, pp. 351–353 (cit. on p. 58).

Nikolov, S. I. and J. A. Jensen (2003). "In-vivo Synthetic Aperture Flow Imaging in Medical Ultrasound". In: *IEEE Trans. Ultrason., Ferroelec., Freq. Contr.* 50.7, pp. 848–856 (cit. on p. 56).

Noble, M. I. M., D. Trenchard, and A. Guz (1966). "Left Ventricular Ejection in Conscious Dogs: I. Measurement and Significance of the Maximum Acceleration of Blood from the Left Ventricle". In: *Circulation*, pp. 139–147 (cit. on p. 60).

Sabbah, H. N., F. Khaja, J. F. Brymer, T. M. McFarland, D. E. Albert, J. E. Snyder, S. Goldstein, and P. D. Stein (1986). "Noninvasive evaluation of left ventricular performance based on peak aortic blood acceleration measured with a continuous-wave Doppler velocity meter". In: *Circulation* 74.2, pp. 323–329 (cit. on p. 60).

References from Chapter 8

Baumgartner, H., H. Schima, G. Tulzer, and P. Kühn (1993). "Effect of Stenosis Geometry on the Doppler-Catheter Gradient Relation In Vitro: A Manifestation of Pressure Recovery". In: *J. Am. Coll. Cardiol.* 21.4, pp. 1018–1025 (cit. on p. 62).

Baumgartner, H., T. Stefenelli, J. Niederberger, H. Schima, and G. Maurer (1999). "Overestimation of catheter gradients by Doppler ultrasound in patients with aortic stenosis: A predictable manifestation of pressure recovery". In: *J. Am. Coll. Cardiol.* 33.6, pp. 1655–1661 (cit. on p. 62).

Garcia, D., J. G. Dumesnil, L.-G. Durand, L. Kadem, and P. Pibarot (2003). "Discrepancies between catheter and Doppler estimates of valve effective orifice area can be predicted from the pressure recovery phenomenon". In: *J. Am. Coll. Cardiol.* 41.3, pp. 435–442 (cit. on p. 62).

Hansen, K. L., J. Udesen, F. Gran, J. A. Jensen, and M. B. Nielsen (2009). "In-vivo examples of complex flow patterns with a fast vector velocity method". In: *Ultraschall in Med.* 30, pp. 471–476 (cit. on p. 62).

Levine, R. A., A. Jimoh, E. G. Cape, S. McMillan, A. P. Yoganathan, and A. E. Weyman (1989). "Pressure recovery distal to a stenosis: Potential cause of gradient verestimation by Doppler echocardiography". In: *J. Am. Coll. Cardiol.* 13.3, pp. 706–715 (cit. on p. 62).

Smith, M. D., P. L. Dawson, J. L. Elion, D. C. Booth, R. Handshoe, O. L. Kwan, G. F. Earle, and A. N. DeMaria (1985). “Correlation of continuous wave doppler velocities with cardiac catheterization gradients: An experimental model of aortic stenosis”. In: *J. Am. Coll. Cardiol.* 6.6, pp. 1306–1314 (cit. on p. 62).

Vecchi, A. de, R. E. Clough, N. R. Gaddum, M. C. M. Rutten, P. Lamata, T. Schaeffter, D. A. Nordsletten, and N. P. Smith (2014). “Catheter-induced errors in pressure measurements in vessels: An in-vitro and numerical study”. In: *IEEE Trans. Biomed. Eng.* 61.6, pp. 1844–1850 (cit. on p. 62).

Paper I

Noninvasive Estimation of 2-D Pressure Gradients in Steady Flow Using Ultrasound

Jacob Bjerring Olesen, Marie Sand Traberg, Michael Johannes Pihl, and Jørgen Arendt Jensen

IEEE Trans. Ultrasons., Ferroelec., Freq. Contr., vol. 61, no. 8, p. 1409 – 1418, August 2014.

Noninvasive Estimation of 2-D Pressure Gradients in Steady Flow Using Ultrasound

Jacob Bjerring Olesen, Marie Sand Traberg, Michael Johannes Pihl, and Jørgen Arendt Jensen

***Abstract*—A noninvasive method for estimating 2-D pressure gradients from ultrasound vector velocity data is presented. It relies on vector velocity fields acquired using the transverse oscillation method during steady flow conditions. The pressure gradients are calculated from the velocity fields using the Navier–Stokes equations. Scans of a carotid bifurcation phantom with a 70% constriction are performed using a linear transducer connected to a scanner. The performance of the estimator is evaluated by comparing its results to those of a computational fluid dynamics model of the carotid bifurcation phantom. The geometry of the model is determined from magnetic resonance imaging. The presented study is conducted assuming steady flow using velocity data acquired at 18 frames per second. The proposed method shows pressure gradients at the constricted region from −8 kPa/m to 9 kPa/m, with a maximum bias of −7% for the axial component and −8% for the lateral component. The relative standard deviation of the estimator is 5% (axial component) and 30% (lateral component) when studying the pressure gradient across the constriction using 3 velocity frames per pressure estimate. The study shows that 2-D pressure gradients can be achieved noninvasively using ultrasound data in a constant flow environment.**

I. INTRODUCTION

LOCAL pressure gradients in hemodynamics can provide important information for diagnosing various cardiovascular diseases such as atherosclerosis [1]. The gradients are used as an indication of how changes in the flow caused by plaque formation affect the risk of embolism. This is, for instance, applicable in determining the severity of stenotic vessels or in studying the pressure drop over heart valves. Today, pressure gradients are measured by means of catheters inserted into the blood vessel and threaded to the region of interest. Although this procedure is reported to be reliable and of low risk [2], it remains an invasive procedure exposing the patients to ionizing radiation during angiography guidance [3]. Furthermore, the catheter causes inconvenient disturbances to the surrounding fluid flow, thereby affecting the pressure field it is measuring. A less invasive method for measuring the local pressure gradients is proposed by Fairbank and Scully [4]. The method relies on injecting contrast agent microbubbles into the circulatory system and measuring the frequency shift in the scattered spectrum as ultrasonic waves are applied. A variety of other methods for estimating pressure changes has also been devised based on the injection of microbubbles [5]–[10]. Despite being a less invasive procedure, it still requires the injection of microbubbles. Furthermore, it only provides a short time window of approximately 10 to 20 s [11] for imaging before the bubbles are taken up by the liver or are burst by the applied acoustic pressure field produced by the ultrasound transducer.

In 1976, Holen *et al.* [12] suggested a noninvasive method for estimating local pressure gradients using the peak systolic blood velocity measured from ultrasound data. The orifice equation introduced by Gorlin and Gorlin [13] was employed to calculate the pressure gradient from the velocity data. This noninvasive estimate of the pressure gradients, however, suffers from major flaws because it is solely dependent on a single velocity estimate and does not take complex flow patterns into account. Deducing a pressure gradient based on a single velocity estimate makes it sensitive to a series of unwanted hemodynamic factors that are uncorrelated to the actual constrictions effect on the peak velocity, e.g., abnormal cardiac output caused by cardiomyopathy. Hence, a more refined method for estimating the pressure gradients was suggested in 2003 by Ohtsuki and Tanake [14]. This method also relies on ultrasound data, but the estimated pressure gradients are instead based on a simplified version of the Navier–Stokes equations. The Navier–Stokes equations describe the motion of fluids and provide access to information regarding the temporal and spatial pressure variations in the system, making this method suitable for time-varying flow phenomena having complex features. Ohtsuki and Tanake assume the viscosity and the external forces on the system to be negligible. Furthermore, they assume the velocity normal to the scan plane is zero. The suggested method uses the axial velocity component found from spectral Doppler to deduce a measurement of the transverse velocity component. The Navier–Stokes equations are then used to find the pressure gradients from the two velocity components. Applying the two in-plane velocity components to the Navier–Stokes equations offers the advantage of including spatial pressure variations into the estimator, unlike the method suggested by Holen *et al.* [12]. A shortcoming of the method suggested by Ohtsuki and Tanake [14] is that the estimated pressure is solely based on the detected axial velocity. This makes the estimator inadequate for measuring the velocity component parallel to the ultrasound transducer and thus, insufficient for calculating pressure gradients in complex flow phenomena, such as vortices that are common in hemodynamics [15], [16].

Magnetic resonance imaging (MRI) is able to produce velocity measurements in all three spatial directions [15],

---

Manuscript received February 18, 2014; accepted May 9, 2014. This work was supported by grant 024-2008-3 from the Danish Advanced Technology Foundation and BK Medical ApS, Denmark.

The authors are with the Department of Electrical Engineering, Center for Fast Ultrasound Imaging, Technical University of Denmark, Kgs. Lyngby, Denmark (e-mail: jbjol@elektro.dtu.dk).

DOI http://dx.doi.org/10.1109/TUFFC.2014.3050

which enables derivation of pressure gradients without uncertainties related to the assumptions of out-of-plane motion [3]. Most examples in the literature on deducing pressure gradients using MRI are derived from the Navier–Stokes equations on either vector velocity data [3], [17], [18] or directly from accelerations data [19]. The high spatial resolution in MRI is a good basis for calculating the convective acceleration used in the estimator presented here. However, MRI techniques often require data from several cardiac cycles through ECG gating to image a full cycle, thus, preventing real-time imaging of pressure variations. This poses a significant downside to MRI when performing measurements on dynamic flow systems such as the cardiovascular system. Furthermore, MRI requires each velocity component to be measured separately, thus preventing a simultaneous data acquisition of vector velocity fields. This study presents pressure gradients estimated from ultrasound vector velocity data by exploiting the transverse oscillation (TO) method developed by Jensen and Munk [20]; Anderson [21] suggested a similar approach. Unlike the method proposed by Ohtsuki and Tanake [14], the TO method is able to estimate the two spatial velocity components within the ultrasound scan plane independently of each other. This allows for determination of flow patterns such as vortices or other complex features that are likely to occur when fluid passes through a constricted vessel. Estimating pressure gradients from vector velocities using the Navier–Stokes equations was initially suggested by Henze [22]. Henze used velocity fields derived from directional beamforming, but never published a validation of this technique. The purpose of this paper is to compare pressure gradients derived from TO data to pressure gradients obtained using a computational fluid dynamics model. The hypothesis to be tested is that pressure gradients can be measured noninvasively using ultrasound vector velocity data acquired from the TO approach. The presented results are all obtained from data recorded on a flow model, which mimics a constricted carotid artery. This ensures that the estimated velocity field and its derived pressure field will vary as a function of space, which is preferred when examining local pressure changes. The experimental work is conducted on a steady-flow system to verify the feasibility of the suggested method. The gradients are estimated using the Navier–Stokes equations, and the results are compared with a finite element simulation of the flow model. The geometry of the flow simulation model is reproduced using MRI data, thereby providing identical flow domains in measurement and simulation.

II. Estimation of Pressure Gradients

The following section presents the method for calculating pressure gradients using ultrasound vector velocity data. The method is based on the Navier–Stokes equations for an isotropic incompressible Newtonian fluid as expressed here in vector form:

$$\rho\left[\frac{\partial\vec{v}}{\partial t}+\vec{v}\cdot\nabla\vec{v}\right]=-\nabla p+\rho\vec{g}+\mu\nabla^2\vec{v}. \tag{1}$$

The equation describes the development of fluid vector velocity $\vec{v}(v_x, v_y, v_z)$ by relating the body forces acting on the isotropic fluid volume to its acceleration and density, where ρ is the density of the fluid and μ its viscosity. The left-hand side sums the local $\partial\vec{v}/\partial t$ and convective fluid acceleration $\vec{v}\cdot\nabla\vec{v}$, where ∇ is the spatial differential operator $(\partial/\partial x, \partial/\partial y, \partial/\partial z)$; the right-hand side sums the surface and volume forces. The terms on the right-hand side include the pressure gradients $-\nabla p$, as well as a gravitational force $\mathbf{g}$ and a term describing the viscous drag caused by the viscosity of the fluid $\mu\nabla^2\vec{v}$, where $\nabla^2\vec{v}$ is the Laplacian of the velocity. For most clinical applications, the effect of the viscous term in (1) can be omitted, as this has no significant influence on the net-force in comparison to the inertial forces. This is especially the case in larger vessels, for which the area of the boundary layer is small compared with the flow region beyond this layer, where flow is said to behave as an inviscid fluid [23], [24]. One way of determining the ratio of inertial forces to viscous forces is to study the Reynolds number, Re. The Reynolds number emerges from rewriting the Navier–Stokes equations into dimensionless form [25], and is expressed as

$$\mathrm{Re}=\frac{\text{inertial forces}}{\text{viscous forces}}=\frac{\rho\langle L\rangle\langle v\rangle}{\mu}. \tag{2}$$

Here, $\langle L\rangle$ and $\langle v\rangle$ are characteristic measures of the flow system, e.g., the diameter of the vessel and the average flow velocity, respectively. Flow conditions for which the Reynolds number is larger than unity are governed by inertial forces, whereas a smaller Reynolds number indicates that flow is dominated by viscous forces. The gravitational force contribution in (1) can usually be neglected, because a patient undergoing an ultrasound scan is placed in a supine position. Furthermore, the temporal acceleration $(\partial v/\partial t)$ is neglected in this study; no changes in velocity will occur with respect to time because steady flow is considered. The pressure gradient is therefore directly linked to the spatial derivatives in the velocity field, $\vec{v}$:

$$\nabla p=-\rho\vec{v}\cdot\nabla\vec{v}+\mu\nabla^2\vec{v}. \tag{3}$$

Eq. (3) states that all three vector components of $\vec{v}(v_x, v_y, v_z)$ must be known to estimate the pressure gradient ∇p. Using the TO approach, the scanner is able to measure the 2-D in-plane velocity vector $\vec{v}=(v_x, v_y)$ [26], [27]. The proposed method is therefore developed assuming that the out-of-plane velocity v_y is zero. The method can be extended to use full 3-D data, which can be acquired from ultrasound data using the experimental method presented by Pihl and Jensen [28], [29]. Assuming that v_y is zero makes 2-D pressure gradients obtainable in the presented setup. The consequence of this assumption is investigated in Section VI. The reduced form of the Navier–Stokes equations is expressed here in rectangular coordinates:

$$\begin{bmatrix} \dfrac{\partial p}{\partial x} \\ \dfrac{\partial p}{\partial z} \end{bmatrix} = -\rho \begin{bmatrix} v_x \dfrac{\partial v_x}{\partial x} + v_z \dfrac{\partial v_x}{\partial z} \\ v_x \dfrac{\partial v_z}{\partial x} + v_z \dfrac{\partial v_z}{\partial z} \end{bmatrix} + \mu \begin{bmatrix} \dfrac{\partial^2 v_x}{\partial x^2} + \dfrac{\partial^2 v_x}{\partial z^2} \\ \dfrac{\partial^2 v_z}{\partial x^2} + \dfrac{\partial^2 v_z}{\partial z^2} \end{bmatrix}. \quad (4)$$

The spatial derivatives in (4) are calculated from vector velocity data using a polynomial smoothing filter. This method fits a low-degree polynomial to a subset of adjacent data points by the linear least-squared method. If data points are equally spaced, an analytical solution to the least-squared method can be reached by expressing it as a generic set of convolution coefficients. Applying the convolution coefficients onto the subset of data points produces an estimate of the smoothed signal together with its derivatives at the central point of the subset. Smoothing a data set using convolution coefficients was first introduced by Savitzky and Golay in 1964 [30]. The values of the convolution coefficients depend solely on the size of the examined subset and the order of the polynomial that is fitted to the subset.

A flow profile of a fluid moving at steady state through a constricted vessel usually displays a somewhat parabolic shape, thus, a second-order polynomial is sufficient in fitting the subset of measured data points. Each subset consists of five data points, which, given the largest sampling interval, corresponds to a physical length of less than 1 mm in the presented setup. This subset size ensures a proper estimate of the second-order derivatives, while minimizing the pollution from vessel boundaries to be smeared into the region of interest. The following equations are obtained from fitting a second-order polynomial to a subset of five data points using the analytical solution to the least-squared method [31]:

$$y_n = \frac{1}{35}(-3x_{n-2} + 12x_{n-1} + 17x_n + 12x_{n+1} - 3x_{n+2}), \quad (5)$$

$$\dot{y}_n = \frac{1}{35}(-7x_{n-2} - 3.5x_{n-1} + 3.5x_{n+1} + 7x_{n+2}), \quad (6)$$

$$\ddot{y}_n = \frac{1}{35}(10x_{n-2} - 5x_{n-1} - 10x_n - 5x_{n+1} + 10x_{n+2}). \quad (7)$$

The first equation calculates the smoothed value y_n that replaces the measured data point, x_n, where n is the central data point of the subset. The weighted coefficients in front of the data samples are the Savitzky–Golay convolution coefficients. Eqs. (6) and (7) calculate the first- and second-order derivatives of x_n, respectively. These filter functions are used for smoothing and calculating the different spatial derivatives of (4). Here, the smoothed axial velocity component and the derivatives that change with respect to this direction are calculated discretely for each position in the scan plane:

$$\frac{\mathrm{d}^k \vec{\tilde{v}}_s(i,j)}{\mathrm{d}s^k} \approx \frac{1}{\Delta s^k} \sum_{p=i-h_w}^{i+h_w} \vec{v}_s(p,j) \vec{B}_k(p - (i - h_w) + 1), \quad (8)$$

where k goes from 0 to 2, and s indicates either the axial direction, z, or the lateral direction, x. The smoothed values are expressed as $\vec{\tilde{v}}_s$; the measured data are $\vec{v}_s$. The position within each field is given by (i, j). The Δs is the sampling interval of the velocity field in either the axial or lateral direction. The index number p is found from half the window size of the selected subset, which is calculated by $h_\mathrm{w} = (N_\mathrm{set} + 1)/2 - 1$, where N_set is the number of samples in the subset. The Savitzky-Golay convolution coefficients are expressed in $\vec{B}_k$ as

$$\vec{B}_0 = \frac{1}{35}\begin{bmatrix} -3 \\ 12 \\ 17 \\ 12 \\ -3 \end{bmatrix}, \quad \vec{B}_1 = \frac{1}{35}\begin{bmatrix} -7 \\ -3.5 \\ 0 \\ 3.5 \\ 7 \end{bmatrix}, \quad \vec{B}_2 = \frac{1}{35}\begin{bmatrix} 10 \\ -5 \\ -10 \\ -5 \\ 10 \end{bmatrix}. \quad (9)$$

In the case of calculating the smoothed lateral velocity component and its derivatives that change in this direction, the equation used is

$$\frac{\mathrm{d}^k \vec{\tilde{v}}_s(i,j)}{\mathrm{d}s^k} \approx \frac{1}{\Delta s^k} \sum_{p=j-h_\mathrm{w}}^{j+h_\mathrm{w}} \vec{v}_s^{\mathrm{T}}(p,i) \vec{B}_k(p - (j - h_\mathrm{w}) + 1), \quad (10)$$

where $\vec{v}_s^{\mathrm{T}}$ is the transpose of $\vec{v}_s$.

III. Experimental Model

The following section describes the acquisition of ultrasound data used in estimating the pressure gradients. A BK Medical 2202 Pro Focus UltraView scanner (BK Medical, Herlev, Denmark) equipped with a UA2227 research interface [32] is used for obtaining ultrasound radio-frequency data. A C70-SSEA flow phantom (Shelley Medical Imaging Technologies, Toronto, Canada) is scanned using a BK8670 linear array transducer at 18 frames per second. The flow phantom models the bifurcation at the carotid artery as having a constriction at the beginning of the internal branch reducing the cross-sectional area of the lumen by 70%. The common part of the artery measures 8 mm in diameter, whereas the external and post-constriction internal branches measure 4.65 and 5.55 mm, respectively. The flow phantom is embedded in agar to mimic the characteristics of human tissue, and it is encased in a rigid, airtight acrylic box with an acoustic window, making it compatible with ultrasound imaging as well as MRI. A constant flow profile is generated using a CompuFlow 1000 Flow system (Shelley Medical Imaging Technologies). The flow rate is set to 1.0 mL/s, and the ultrasonic pulse repetition frequency of 1.3 kHz is used, ensuring a good representation of both the peak velocity and the smaller velocities that exist near the boundaries of the vessel. Having a dynamic range that captures both the smallest and largest velocities gives the best basis for comparing the estimated measurements to the results from the simulation model. A blood-mimicking fluid (BMF-US,

TABLE I. Measurement Settings When Acquiring Data.

Parameter name	Notation	Value	Unit
BK scanner			
Transducer	BK8670	—	Linear array
Mode	Carotid TVI	—	Transverse vector imaging
B-mode transmit frequency	$B_{\text{Xmit},f}$	10	MHz
Flow-mode transmit frequency	$F_{\text{Xmit},f}$	5	MHz
Pulse repetition frequency	f_{prf}	1.3	kHz
Frame rate	FPS	18	Hz
Number of acquired frames	N_{frames}	51	—
Lateral velocity sampling interval	Δx	$5.8 \cdot 10^{-1}$	mm
Axial velocity sampling interval	Δz	$6.5 \cdot 10^{-2}$	mm
Flow setup			
Constriction	—	70%	—
Depth to constriction	—	2.3	cm
Fluid density	ρ	1,037	kg/m^3
Fluid viscosity	μ	$4.1 \cdot 10^{-3}$	Pa·s
Volumetric flow rate	—	1.0	mL/s

Shelley Medical Imaging Technologies) with a density of 1037 kg/m^3 and a viscosity of 4.1 mPa·s is used. The experimental acquisition settings are listed in Table I.

IV. Simulation Model

The reliability of the pressure gradients produced under steady flow conditions is evaluated through comparison to a finite-element model. The geometry of this model is constructed from MRI data of the flow phantom obtained using a 3-T scanner (Magnetom Trio, Siemens AG, Munich, Germany) at the Department of Diagnostic Radiology at Rigshospitalet, Denmark. The MRI data are loaded into a commercial segmentation software, ScanIP v5.1 (Simpleware Ltd., Exeter, UK), which is used to construct the 3-D geometry of the phantom's fluid domain. The geometry is exported as a 3-D point cloud to SolidWorks 2013 (Education edition, Dassault Systèmes Corp., Waltham, MA), where the outlet boundaries of the model are extruded. Extruding the model minimizes the influence of the selected boundary conditions in the region of the constriction, thus, producing a more realistic image of the flow through this region. The extruded model is transferred to Comsol Multiphysics (v4.4, Comsol AB, Stockholm, Sweden), which uses finite-element algorithms to simulate flow. The algorithms are based on the conservation laws for fluid transport, such as mass and linear momentum balances. The imported model has been smoothed by a Gaussian filter to avoid any inexpedient sharp edges that otherwise could lead to computational divergence. Such sharp edges occur if the spatial resolution in the scan images is smaller than the resolution required by Comsol. The dimension of the filter varies over its different directions because the spatial resolution of the acquired MRI data is anisotropic. This is a consequence of the scan sequence used during the acquisition of data. A summary of the settings used for creating the geometry of the simulation model is listed in Table II.

TABLE II. Settings for Constructing the Geometry of the Simulation Model.

Parameter name	Value	Unit
Magnetom Trio Siemens scanner		
Strength	3.0	T
Scan sequence	Time-of-flight 3-D	
Voxel size	0.7 × 0.7 × 1.0	mm
ScanIP		
Up-sampling	$(x, y, z) = (0.9, 0.15, 0.15)$	mm
Filter size	$(x, y, z) = (3.0, 0.5, 0.5)$	mm
SolidWorks		
Extruding outlet boundaries	75	mm

V. Data Processing

The following section describes how maps of pressure gradients are estimated. The processing of the ultrasound data is performed off-line using Matlab (The MathWorks Inc., Natick, MA), whereas the finite-element analysis is performed in Comsol. Vector velocity maps of the flow through the constricted region of the phantom are estimated from ultrasound data by employing the TO method as described by Jensen and Munk [20] and the TO velocity estimator [33]. Maps of pressure gradients are then calculated from the derived velocity fields using (3). The spatial derivatives in (3) are found using a second-order Savitzky–Golay filter with a window size of five data points. Before employing the filter, the velocity estimates were interpolated to improve visual quality, thus increasing the number of data points by a factor of three in each dimension of the scan plane. The mean of the acquired velocity frames is calculated before deriving the pressure gradients to reduce the noise from the TO approach. Calculating the mean of numerous velocity frames is, of course, not applicable in clinical conditions because of the time-varying nature of a cardiac cycle. The effect of using several velocity frames for calculating a single frame of pressure gradients is therefore investigated in Section VI.

The simulated flow parameters mimic the actual flow conditions in the experimental setup. These conditions are

TABLE III. SIMULATION SETTINGS IN COMSOL.

Parameter name	Notation	Value	Unit
Simulation study			
Physics	Flow	Laminar	—
Geometry	LiveLink for SolidWorks	3-D	—
Stationary solver	Parallel Direct Sparse Solver	Direct	—
Mesh	Physics-controlled mesh	Extra coarse	—
Fluid properties			
Compressibility	—	Incompressible	—
Density	ρ	1037	kg/m^3
Viscosity	μ	$4.1 \cdot 10^{-3}$	Pa·s
Initial conditions			
Velocity field	—	$(x, y, z) = (0, 0, 0)$	m/s
Pressure	—	0	Pa
Inlet conditions			
Inflow	Laminar	—	—
Volumetric flow rate	—	1	mL/s
Entrance length	—	1	m
Outlet conditions			
Outflow	Pressure, no viscous stress	—	—
Pressure	—	0	Pa
Wall			
Condition	—	No-slip	—

listed in Table III. Stationary laminar flow of an incompressible fluid is selected. The initial velocity and pressure are zero with a forced laminar flow condition at the inlet of the model. The flow rate is 1 mL/s, which is equivalent to the flow rate in the experimental setup.

The result of the proposed estimator is studied by considering its average standard deviation $\hat{\sigma}$ and bias $\hat{\beta}$ in reference to the simulated data. The two are calculated as

$$\hat{\sigma} = \frac{1}{|P_\mathrm{g}|_\mathrm{max}} \sqrt{\frac{1}{N}\sum_{m=1}^{N} \sigma^2(m)} \quad \text{and}$$

$$\hat{\beta} = \frac{1}{|P_\mathrm{g}|_\mathrm{max} N} \sum_{m=1}^{N} \nu_\mathrm{est}(m) - \nu_\mathrm{sim}(m),$$

where N is the number of data points along the spatial path that is investigated and ν_est is the estimated pressure gradients at each point. The mean variance of the estimated gradients σ^2 is calculated along the investigated path to derive the mean standard deviation $\hat{\sigma}$. The simulated data along the inspected path is denoted ν_sim. Both standard deviation and bias are normalized by the peak estimated pressure gradient, $|P_\mathrm{g}|_\mathrm{max} = \max(|\nu_\mathrm{est}|)$.

The estimated pressure gradients are calculated in the 2-D scan plane of the ultrasound beam, but they are compared with simulation results obtained from a 3-D model. This is managed by solving the simulation model as a 3-D problem and then extracting the pressure gradients found in the same 2-D plane as scanned by the transducer.

VI. RESULTS

The following section presents the results of the proposed estimator. All results are based on vector velocity data acquired at 18 frames per second. Data are captured from the carotid phantom at the site of the constriction.

A. Vector Velocity Fields

The proposed estimator for calculating pressure gradients relies solely on spatial variations of the measured velocity fields. An example of such a velocity field is displayed in Fig. 1. The plots show the velocity of the blood-mimicking fluid that flows through the constricted phantom from right to left. Fig. 1(a) displays the mean of all the estimated velocity frames derived from the ultrasound data, whereas Fig. 1(b) shows the 2-D simulated velocity field at the same position. It is seen that the flow accelerates toward the center of the constriction, reaching a peak velocity of roughly 0.14 m/s, then it decelerates as the cross-sectional area expands again. A visual comparison between the estimated and simulated velocity fields demonstrates their similarity. The agreement between the two velocity fields provides a proper base for comparing the later-derived pressure fields with the simulated ones. Fig. 1(c) shows the magnitude of the out-of-plane velocity component, v_y, extracted from the 3-D simulation model. It reveals that the out-of-plane component accounts for less than 2.5% of the true velocity, $|\vec{v}| = \sqrt{v_x^2 + v_y^2 + v_z^2}$.

B. Pressure Gradient Fields

Maps of pressure gradients are estimated using the velocity data presented in Fig. 1, and the result is shown in Fig. 2. Fig. 2(a) displays pressure gradients calculated by employing the proposed estimator from (4). The arrows and their background colors indicate the direction and magnitude of the gradients, respectively. The plot presents arrows that tend to point away from the center of the constriction, indicating that a low pressure is present here, as a gradient always points in the direction of increasing values. Fig. 2(b) shows estimated pressure gradients, but compared with Fig. 2(a), the viscous forces are neglected, i.e., $\mu = 0$. Fig. 2(c) is the simulated in-plane pressure gradients from the simulation model.

The first two plots in Fig. 2 reveal the actual effect of including the viscosity term, when estimating gradients in the presented setup. It appears that no major changes are introduced, when including the viscosity term. This observation is also supported by studying the Reynolds number, which at the center of the constriction is calculated to be 68. This indicates flow primarily governed by inertial forces. Both the Reynolds number and the visual similarity when including the viscous term in Fig. 2 suggest that it is reasonable to neglect the viscous forces throughout the rest of this paper. Excluding the viscosity term results in a reduced level of noise, because the noise from the second-order numerical differential is avoided [34]. Such noise arises from the differential operator because it subtracts successive data points, thus removing the low-frequency content of the measured data, where most of the desired signal's energy is present. The simulated pressure gradients in Fig. 2(c) are calculated using the Navier–Stokes equations with the viscosity, μ, set to zero. The red dotted lines in Figs. 2(b) and 2(c) indicate the positions used for the quantitative plots shown in the next section.

C. Quantitative Results of the Proposed Estimator

A quantitative study of the estimator is made during steady flow conditions by investigating its standard deviation and bias. Because the proposed estimator is based on estimated velocity fields, its standard deviation is influenced by the precision of the velocity estimator. The standard deviation of the suggested estimator is therefore tested using the average of one to ten velocity frames, thereby increasing the precision of velocity estimate. The performance study is made along the red dotted lines in Figs. 2(b) and 2(c). The results for the axial and lateral components of the estimated pressure gradients are shown in Fig. 3.

The graphs are normalized in reference to the peak estimated gradient. The standard deviation decreases when increasing the number of velocity frames in estimating the pressure gradients. However, the improved standard deviation is at the expense of temporal resolution, for which maps of pressure gradients can be presented. Using three vector velocity frames for calculating one frame of pressure gradient makes the true frame rate drop to 6 Hz.

Figs. 4 and 5 show the results of the estimator taken along the four dotted lines in Fig. 2. The presented results are calculated at a frame rate of 6 Hz. Figs. 4 and 5 show the mean magnitude of the axial and lateral pressure gradients along the longitudinal and cross-sectional direction of the constriction. The magnitudes are plotted together with plus/minus one average standard deviation, $\hat{\sigma}$. The blue line shows the simulated pressure gradients along the same path.

The estimator produces pressure gradients of magnitudes varying from −8 kPa/m to 9 kPa/m along the selected paths. The average normalized bias, $\hat{\beta}$, along this path is −7% to 3% and −8% to 4% for the axial and lateral vector components, respectively. The biases are normalized by the size of the peak estimated gradient in each respective direction. The average standard deviations, when using three velocity frames for each estimate, were 32% and 57% for the axial and lateral components in the longitudinal direction of the constriction. The study conducted along the cross-sectional line showed standard deviations between 5% and 30% for the two vector components.

VII. Discussion

The proposed method shows pressure gradients during steady flow conditions with a maximum bias of −7% and −8% in the axial and lateral direction, respectively. The standard deviation of the estimator varied according to the amount of averaging employed, e.g., using three velocity frames per pressure gradient frame resulted in a standard deviation of 5% to 23% in the axial direction and from 30% to 57% in the lateral direction. One way to increase this frame rate, while maintaining the presented precision, is to shrink the width of the colorbox used during the acquisition of velocity data, because fewer pulses are required for covering a narrower region. Other possibilities are to use fast plane wave vector flow imaging as presented by Udesen *et al.* [35] or to use directional synthetic aperture flow imaging [36]. Both techniques are capable of estimating vector flow velocities at a good spatial resolution with frame rates equivalent to the pulse repetition frequency, e.g., 0.5 to 15 kHz. The standard deviation of the suggested method is affected by the precision of the velocity data that is fed to the estimator. Directional synthetic aperture flow imaging is capable of producing velocity estimates with a standard deviation of 1% [36], thus, providing the ideal base for calculating the pressure gradients. The reason for using the transverse oscillation approach as the velocity estimator in the presented setup is that this method is already implemented on clinical scanners.

Deriving pressure gradients using ultrasound data has its advantages, because the velocity fields used by the pressure estimator can be obtained over a single cardiac cycle, thus enabling the possibility of producing maps of real-time pressure gradients. The computational load involved in calculating the pressure gradients can be addressed in terms of floating point operations needed. The velocity estimates entering the Navier–Stokes equation, takes approximately 350 point operations per estimate, and thereafter the pressure gradient calculation uses 30. An image sequence of 208 × 27 estimates shown at a frame rate of 18 Hz, therefore, requires roughly 38 Mflops per second. This is within the capabilities of standard CPUs, which currently perform more than 1 Gflops per second. Thus, a real-time implementation of the estimator is feasible.

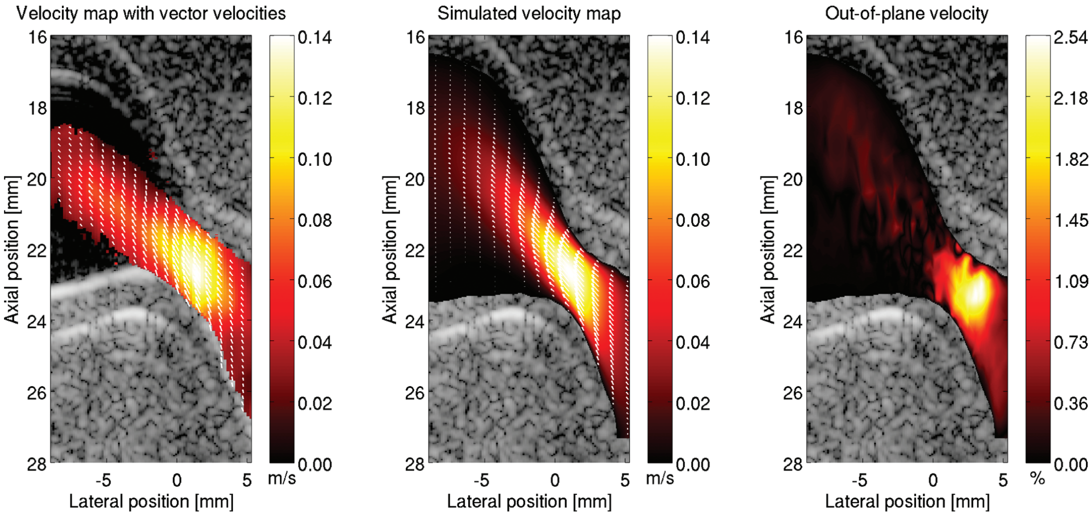

(a) (b) (c)

Fig. 1. Vector velocity fields: (a) the mean estimated velocity field from the ultrasound data, and (b) the simulated velocity field. (c) The size of the out-of-plane simulated velocity component in reference to the absolute simulated velocity. Note that the largest out-of-plane velocity is less than 3% of the total velocity.

Fig. 2 shows pressure gradients that tend to point away from the area of high velocities. This observation is in accordance with expectations because there is a physical relationship between a fluid's pressure and its velocities. A way of clarifying this relationship is to consider the energy of a constricted flow system in which no energy is exchanged between the fluid and the vessel walls, meaning that the energy level is constant throughout the system (no heat transfer). The total energy of the system is then composed of the sum of potential energy and kinetic en-

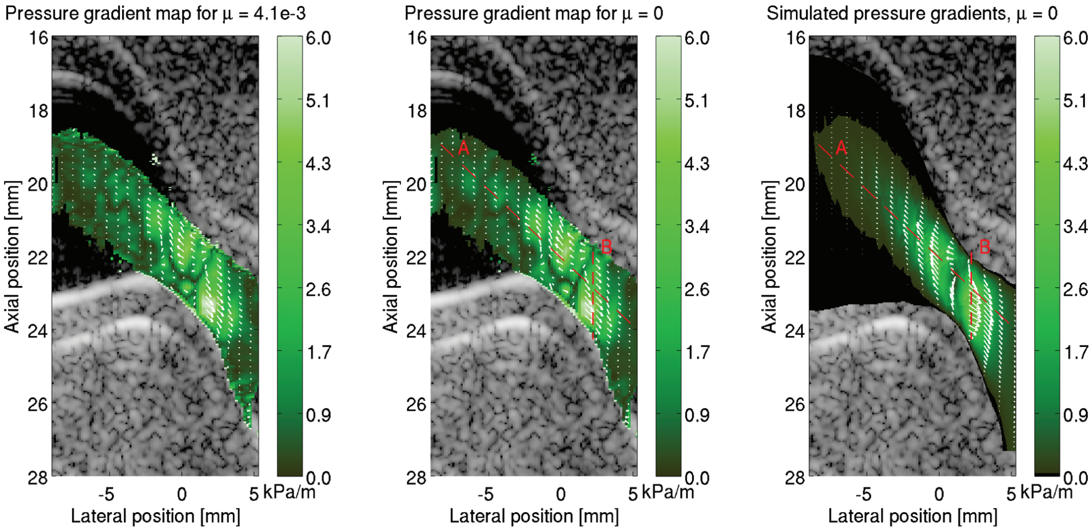

(a) (b) (c)

Fig. 2. Pressure gradient fields: (a) the estimated field of pressure gradient, (b) estimated pressure gradient without the contribution from the viscous forces, and (c) the simulated pressure gradients.

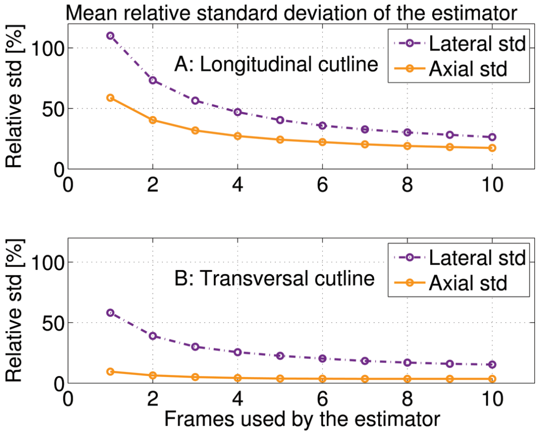

Fig. 3. Standard deviation of the estimator given in reference to the peak estimated pressure gradient. The graphs were made during steady flow conditions. Each graph shows the results from both the axial and lateral component of the pressure gradient. The time interval between consecutive frames is 1/18 s.

ergy. If the gravitational force can be neglected, the only force giving rise to the potential energy is pressure. As the fluid flows into the constriction, it starts to accelerate to keep up a constant flow rate and the kinetic energy increases. Because no energy is put into the flow system from its surroundings, the increase in kinetic energy must come from the potential energy, thereby decreasing the pressure in areas of high velocities. As the fluid flows past the constriction, it decelerates, turning kinetic energy back into potential energy. This explains why pressure gradients tend to point away from sites of higher velocities because pressure is lowest there. The assumption of a constant energy level is of course not entirely true in the experimental setup; energy dissipation will occur because the fluid is not inviscid. However, the amount of energy dissipation is very limited in comparison to the total change in energy that exists along the constriction.

No previous study on the subject has managed to estimate 2-D pressure gradients from vector velocity data obtained using the TO approach. Unlike the method suggested by Holen *et al.* [12], this method is able to take the convective acceleration into consideration. Every term in the estimator is calculated relative to neighboring velocity estimates, yielding gradients that are independent of systemic flow factors, such as abnormalities in the cardiac output. Furthermore, the method can be extended to use full 3-D data, although this would not have contributed too much in the presented setup, because the out-of-plane motion is low in this example, [see Fig. 1(c)].

A shortcoming of the available data is the missing information of the out-of-plane velocity component v_y. This makes the estimator vulnerable in complex flow environments that have vector velocity components in all three spatial directions. However, Pihl and Jensen [28], [29] have recently presented a technique for measuring the out-of-plane velocity using a 2-D array transducer connected to an ultrasound research system. Exploiting this technique would yield 3-D vector velocity fields that could be included in the suggested pressure gradient estimator, removing the assumption that v_y is zero. The method presented in this paper relies on vector velocity data that are acquired from the TO approach using a linear array transducer; thus, the field of view is limited to a maximum depth of approximately 4 to 5 cm. However, because the proposed method solely relies on vector velocities, it can be imple-

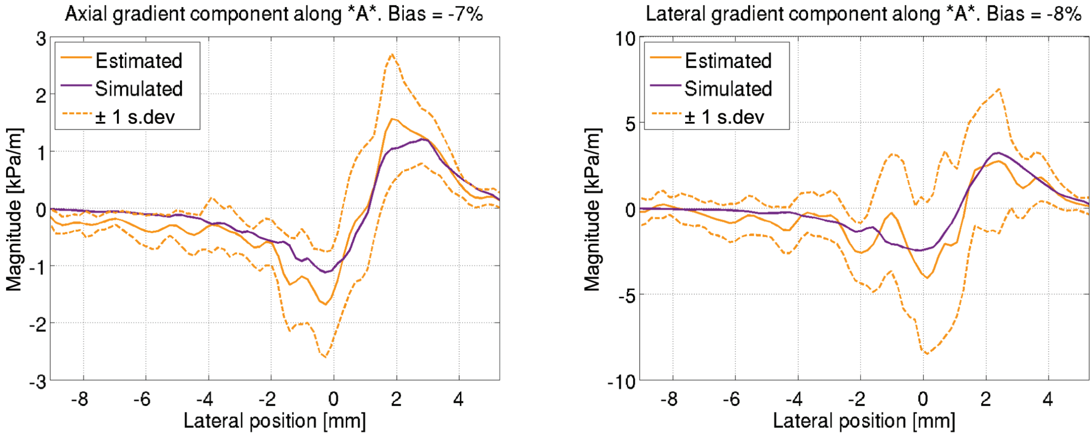

(a) (b)

Fig. 4. Estimated and simulated pressure gradients along the longitudinal direction of the carotid phantom at the site of the constrictions. The two graphs show the axial and lateral component of the pressure gradient, respectively.

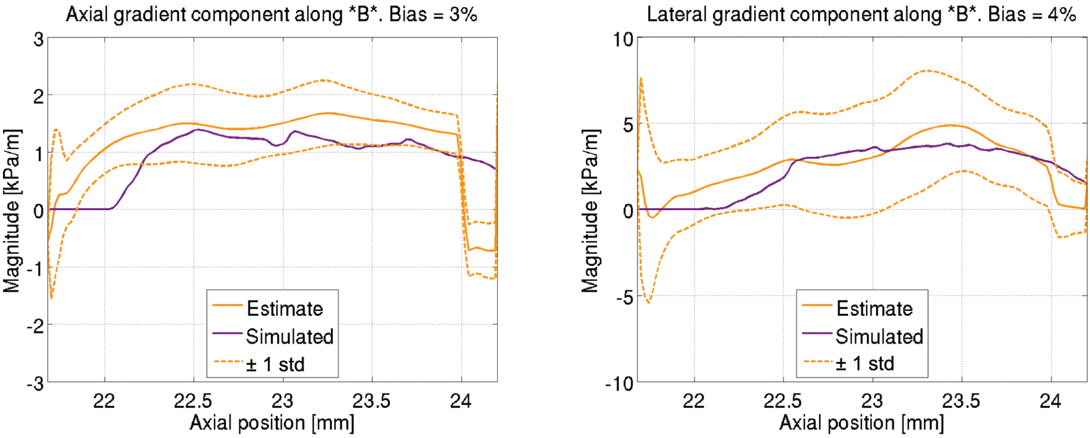

(a) (b)

Fig. 5. Estimated and simulated pressure gradients along the transverse direction of the carotid phantom at the site of the constrictions. The two graphs show the axial and lateral component of the pressure gradient, respectively.

mented on any type of transducer that is able to detect such vectors. In 2012, it was demonstrated that vector velocities can be measured by the TO method down to a depth of 15 cm with a phased-array transducer [37], [38]. Furthermore, Jensen [39] showed that the TO method is suitable for use in conjunction with a convex-array transducer.

Future studies include investigation of the presented estimator's ability to detect pressure gradients in a pulsatile flow environment.

VIII. CONCLUSION

A noninvasive method for deriving pressure gradients using vector velocity ultrasound data was presented. The pressure gradients were derived using the Navier–Stokes equations for incompressible fluids. The vector velocities inserted into the equations were estimated using the TO method, yielding the two in-plane velocity components. The pressure gradients were estimated during steady flow conditions and evaluated by comparison to a simulation model with the same 3-D geometry as the flow phantom used in the experimental setup. The 3-D geometry was obtained from MRI data. The employed method estimated pressure gradients within the flow phantom of magnitudes varying from −8 kPa/m to 9 kPa/m. Proof of concept studies conducted along the longitudinal and cross-sectional direction of a constricted part of the phantom showed a maximum normalized bias of −7% for the axial component and −8% for the lateral component with a standard deviation given in reference to the peak gradient of 4% to 59% (axial direction) and 15% to 110% (lateral direction), depending on the number of velocity frames used by the estimator.

REFERENCES

[1] D. S. Baim and W. Grossman, *Grossman's Cardiac Catheterization, Angiography, and Intervention*. Philadelphia, PA: Lippincott Williams & Wilkins, 2000.

[2] J. S. Skinner and P. C. Adams, "Outpatient cardiac catheterisation," *Int. J. Cardiol.*, vol. 53, no. 3, pp. 209–219, Mar. 1996.

[3] J. Bock, A. Frydrychowicz, R. Lorenz, D. Hirtler, A. J. Barker, K. M. Johnson, R. Arnold, H. Burkhardt, J. Hennig, and M. Markl, "In vivo noninvasive 4D pressure difference mapping in the human aorta: Phantom comparison and application in healthy volunteers and patients," *Magn. Reson. Med.*, vol. 66, no. 4, pp. 1079–1088, 2011.

[4] W. M. Fairbank and M. O. Scully, "A new noninvasive technique for cardiac pressure measurements: Resonant scattering of ultrasound from bubbles," *IEEE Trans. Biomed. Eng.*, vol. 24, no. 2, pp. 107–110, 1977.

[5] A. Bouakaz, P. J. Frinking, N. de Jong, and N. Bom, "Noninvasive measurement of the hydrostatic pressure in a fluid-filled cavity based on the disappearance time of micrometer-sized free gas bubbles," *Ultrasound Med. Biol.*, vol. 25, no. 9, pp. 1407–1415, 1999.

[6] W. T. Shi, F. Forsberg, J. S. Raichlen, and L. Needleman, "Pressure dependence of subharmonic signals from contrast microbubbles," *Ultrasound Med. Biol.*, vol. 25, no. 2, pp. 275–283, 1999.

[7] D. Adam, M. Sapunar, and E. Burla, "On the relationship between encapsulated ultrasound contrast agent and pressure," *Ultrasound Med. Biol.*, vol. 31, no. 5, pp. 673–686, 2005.

[8] F. Forsberg, J.-B. Liu, W. T. Shi, J. Furuse, M. Shimizu, and B. B. Goldberg, "In vivo pressure estimation using subharmonic contrast microbubble signals: Proof of concept," *IEEE Trans. Ultrason. Ferroelectr. Freq. Control*, vol. 52, no. 4, pp. 581–583, 2005.

[9] K. S. Andersen and J. A. Jensen, "Ambient pressure sensitivity of microbubbles investigated through a parameter study," *J. Acoust. Soc. Am.*, vol. 126, no. 6, pp. 3350–3358, 2009.

[10] F. Forsberg, J. Dave, V. G. Halldorsdottir, L. M. Leodore, F. Lin, A. L. Hall, and K. Thomenius, "Applying real-time noninvasive pressure estimation obtained from subharmonic contrast microbubble signals," in *Proc. IEEE Ultrasonics Symp.*, 2008, pp. 1694–1697.

[11] D. Cosgrove and N. Lassau, "Imaging of perfusion using ultrasound," *Eur. J. Nucl. Med. Mol. Imaging*, vol. 37, suppl. 1, pp. s65–s85, 2010.

[12] J. Holen, R. Aaslid, and K. Landmark, "Determination of pressure gradient in mitral stenosis with a noninvasive ultrasound Doppler technique," *Acta Med. Scand.*, vol. 199, no. 6, pp. 455–460, 1976.

[13] R. Gorlin and S. G. Gorlin, "Hydraulic formula for calculation of the area of the stenotic mitral valve, other cardiac valves, and central circulatory shunts," *Am. Heart J.*, vol. 41, no. 1, pp. 1–29, 1951.

[14] S. Ohtsuki and M. Tanaka, "Doppler pressure field deduced from the Doppler velocity field in an observation plane in a fluid," *Ultrasound Med. Biol.*, vol. 29, no. 10, pp. 1431–1438, 2003.

[15] P. J. Kilner, G. Z. Yang, R. H. Mohiaddin, D. N. Firmin, and D. B. Longmore, "Helical and retrograde secondary flow patterns in the aortic arch studied by three-directional magnetic resonance velocity mapping," *Circulation*, vol. 88, no. 5, pt. 1, pp. 2235–2247, 1993.

[16] K. L. Hansen, J. Udesen, F. Gran, J. A. Jensen, and M. B. Nielsen, "In-vivo examples of complex flow patterns with a fast vector velocity method," *Ultraschall Med.*, vol. 30, no. 5, pp. 471–477, 2009.

[17] R. B. Thompson and E. R. McVeigh, "Fast measurement of intracardiac pressure differences with 2D breath-hold phase-contrast MRI," *Magn. Reson. Med.*, vol. 49, no. 6, pp. 1056–1066, 2003.

[18] A. Herment, G. Besson, C. Pellot-Barakat, and F. Frouin, "Estimation of pressure gradient images from velocity encoded MR acquisitions," *Comput. Cardiol.*, vol. 35, pp. 933–936, 2008.

[19] J. P. Tasu, E. Mousseaux, A. Delouche, C. Oddou, O. Jolivet, and J. Bittoun, "Estimation of pressure gradients in pulsatile flow from magnetic resonance acceleration measurements," *Magn. Reson. Med.*, vol. 44, no. 1, pp. 66–72, 2000.

[20] J. A. Jensen and P. Munk, "A new method for estimation of velocity vectors," *IEEE Trans. Ultrason. Ferroelectr. Freq. Control*, vol. 45, no. 3, pp. 837–851, 1998.

[21] M. E. Anderson, "Multi-dimensional velocity estimation with ultrasound using spatial quadrature," *IEEE Trans. Ultrason. Ferroelectr. Freq. Control*, vol. 45, no. 3, pp. 852–861, 1998.

[22] L. Henze, "Ultrasound flow estimation," Master's thesis, Dept. Electr. Eng., Technical University of Denmark, Lyngby, Denmark, 2008.

[23] L. Prandtl, *Essentials of Fluid Dynamics.* London, UK: Blackie & Son, 1952.

[24] N. B. Wood, "Aspects of fluid dynamics applied to the large arteries," *J. Theor. Biol.*, vol. 199, no. 2, pp. 137–161, 1999.

[25] G. A. Truskey, F. Yuan, and D. F. Katz. *Transport Phenomena in Biological Systems.* Upper Saddle River, NJ: Pearson Education, 2004.

[26] D. H. Evans, J. A. Jensen, and M. B. Nielsen, "Ultrasonic colour Doppler imaging," *Interface Focus*, vol. 1, no. 4, pp. 490–502, 2011.

[27] P. M. Hansen, M. M. Pedersen, K. L. Hansen, M. B. Nielsen, and J. A. Jensen, "Demonstration of a vector velocity technique," *Ultraschall Med.*, vol. 32, no. 2, pp. 213–215, 2011.

[28] M. J. Pihl and J. A. Jensen, "3D velocity estimation using a 2D phased array," in *Proc. IEEE Ultrasonics Symp.*, 2011, pp. 430–433.

[29] M. J. Pihl and J. A. Jensen, "Measuring 3D velocity vectors using the transverse oscillation method," in *Proc. IEEE Ultrasonics Symp.*, 2012, pp. 1881–1885.

[30] A. Savitzky and M. J. E. Golay, "Smoothing and differentiation of data by simplified least squares procedures," *Anal. Chem.*, vol. 36, no. 8, pp. 1627–1639, 1964.

[31] S. J. Orfanidis, *Introduction to Signal Processing.* Upper Saddle River, NJ: Pearson Education, 1996.

[32] M. C. Hemmsen, S. I. Nikolov, M. M. Pedersen, M. J. Pihl, M. S. Enevoldsen, J. M. Hansen, and J. A. Jensen, "Implementation of a versatile research data acquisition system using a commercially available medical ultrasound scanner," *IEEE Trans. Ultrason. Ferroelectr. Freq. Control*, vol. 59, no. 7, pp. 1487–1499, 2012.

[33] J. A. Jensen, "A new estimator for vector velocity estimation," *IEEE Trans. Ultrason. Ferroelectr. Freq. Control*, vol. 48, no. 4, pp. 886–894, 2001.

[34] K. Ahnert and M. Abel, "Numerical differentiation of experimental data: Local versus global methods," *Comput. Phys. Commun.*, vol. 117, no. 10, pp. 764–774, 2007.

[35] J. Udesen, F. Gran, K. L. Hansen, J. A. Jensen, C. Thomsen, and M. B. Nielsen, "High frame-rate blood vector velocity imaging using plane waves: Simulations and preliminary experiments," *IEEE Trans. Ultrason. Ferroelectr. Freq. Control*, vol. 55, no. 8, pp. 1729–1743, 2008.

[36] J. A. Jensen and S. I. Nikolov, "Directional synthetic aperture flow imaging," *IEEE Trans. Ultrason. Ferroelectr. Freq. Control*, vol. 51, no. 9, pp. 1107–1118, 2004.

[37] J. Marcher, M. J. Pihl, and J. A. Jensen, "The transverse oscillation method using a phased array transducer," in *Proc. IEEE Ultrason. Symp.*, 2012, pp. 1890–1893.

[38] M. J. Pihl, J. Marcher, and J. A. Jensen, "Phased-array vector velocity estimation using transverse oscillations," *IEEE Trans. Ultrason. Ferroelectr. Freq. Control*, vol. 59, no. 12, pp. 2662–2675, 2012.

[39] J. A. Jensen, "Optimization of transverse oscillating fields for vector velocity estimation with convex arrays," in *Proc. IEEE Ultrasonics Symp.*, 2013, pp. 1753–1756.

Jacob Bjerring Olesen was born in 1987. In August 2012, he received his M.Sc. degree in biomedical engineering from the Technical University of Denmark and the University of Copenhagen, Denmark. He is currently pursuing his Ph.D. degree in biomedical engineering at the Center for Fast Ultrasound Imaging at the Technical University of Denmark. The topic of his Ph.D. research is imaging of *in vivo* pressure using ultrasound.

Marie Sand Traberg was born in Denmark, on July 5, 1982. She received her M.Sc. degree in biomedical engineering from the Technical University of Denmark and University of Copenhagen, Denmark, in July 2008. In January 2012, she received her Ph.D. degree from the Technical University of Denmark. The Ph.D. thesis work was focused on predicting the biomechanics of abdominal aortic aneurysms using ultrasound blood flow data, magnetic resonance imaging, and advanced material models.

She is currently an assistant professor in the biomedical engineering section of the Department of Electrical Engineering at the Technical University of Denmark. In addition to her research in arterial biomechanics, she teaches courses on physiological fluid mechanics and tissue biomechanics at both undergraduate and graduate levels.

Michael J. Pihl was born in 1983. He received his M.Sc. degree in biomedical engineering in 2009 from the Technical University of Denmark (DTU) and the University of Copenhagen, Denmark. In 2007, he spent seven months in the Biomedical Engineering Department at Duke University, Durham, NC, researching ultrasonic clutter. In 2012, he earned his Ph.D. degree in biomedical engineering at the Center for Fast Ultrasound Imaging at DTU, where he is currently a postdoctoral associate. His main research area is ultrasonic velocity estimation, in particular, the estimation of all three spatial velocity components. His other interests include medical imaging and digital signal processing.

Jørgen Arendt Jensen earned his Master of Science degree in electrical engineering in 1985 and the Ph.D. degree in 1989, both from the Technical University of Denmark. He received the Dr.Techn. degree from the university in 1996, and is an IEEE Fellow. He has published more than 250 journal and conference papers on signal processing and medical ultrasound and the book *Estimation of Blood Velocities Using Ultrasound*, published by Cambridge University Press in 1996. His main contributions are in ultrasound imaging and simulation. The Field II simulation program he developed is considered a gold standard, and is used by all major ultrasound manufacturers and numerous research groups. He is the inventor of the transverse oscillation vector flow approach that was FDA approved and commercially introduced in a BK Medical ultrasound scanner in 2012. He has also been a pioneer in synthetic aperture imaging, and especially fast vector flow imaging. Dr. Jensen has developed several systems for SA imaging and proven that these techniques can work in the clinic.

Paper II

Non-invasive estimation of intravascular pressure changes using vector velocity Ultrasound.

Jacob Bjerring Olesen, Carlos Armando Villagómez-Hoyos, Marie Sand Traberg, Adrian J. Y. Chee, Billy Y. S. Yiu, Chung Kit Ho, Kristoffer Lindskov Hansen, Alfred C. H. Yu, Michael Bachmann Nielsen, and Jørgen Arendt Jensen

IEEE Trans. Ultrasons., Ferroelec., Freq. Contr.,

Submitted on November 3, 2015.

Non-invasive Estimation of Intravascular Pressure Changes using Vector Velocity Ultrasound

Jacob Bjerring Olesen*, Carlos Armando Villagómez-Hoyos*, Marie Sand Traberg*,
Adrian J. Y. Chee†, Billy Y. S. Yiu†, Chung Kit Ho†, Kristoffer Lindskov Hansen‡,
Alfred C. H. Yu§, Michael Bachmann Nielsen‡ and Jørgen Arendt Jensen*
*Center for Fast Ultrasound Imaging, Dept. of Elec. Eng., Bldg. 349,
Technical University of Denmark, DK-2800 Kgs. Lyngby, Denmark.
†Medical Engineering Program, University of Hong Kong, Pokfulam, Hong Kong.
‡Department of Radiology, Rigshospitalet, DK-2100 Copenhagen, Denmark.
§Department of Electrical and Computer Engineering, University of Waterloo,
Waterloo, Ontario, Canada.

***Abstract*—A non-invasive method for estimating intravascular pressure changes using ultrasound is presented. The suggested method estimates pressure gradients from 2-D vector velocity fields. Changes in pressure are derived using a model based on the Navier-Stokes equation. Experimental scans are performed on two fabricated flow phantoms having constrictions of 36 % and 70 %, before scanning the carotid bifurcation of two healthy volunteers. All scans are carried out using a linear array transducer connected to the experimental scanner, SARUS. 2-D fields of angle-independent vector velocities are acquired to a depth of 4 cm using directional synthetic aperture vector flow imaging. The performance of the suggested estimator is evaluated by comparing the results from the two flow phantoms to 3-D numerical simulation models with equivalent geometries. The study showed pressure drops across the constricted phantoms varying from −875 Pa to 0 Pa with a mean standard deviation across the profile of 9 %. The proposed method had a mean bias of 8 % in reference to the simulation models. In-vivo data acquisitions on two human volunteers revealed the feasibility of measuring pressure changes through the proposed vector flow technique. Pressure drops ranging from −60 Pa to 0 Pa were measured over the carotid bulb for the two healthy volunteers.**

I. INTRODUCTION

Abnormal changes in intravascular blood pressure are usually an indication of a diseased vessel. Measuring pressure variations is therefore used clinically as a diagnostic marker in assessing the physiological state of a cardiovascular region [1]. Intravascular pressure is currently assessed by inserting pressure sensing wires or catheters in the femoral artery and threading them to the region of interest. These procedures, however, suffer some severe limitation as they are highly invasive and require the use of ionizing radiation for guidance of the pressure sensory devices. A recent report from De Vecchi *et al.* [2] demonstrated that the accuracy of catheters is greatly dependent on the physical size and shape of the catheter. A 24 % overestimation of the peak systolic pressure was found from using a routinely employed catheter compared to the gold standard using a wire [2], [3].

The motivation to assess intravascular pressure variations of less-invasive approaches first received attention in the 1970s. Fairbank and Scully [4] proposed in 1977 a method for estimating local pressure changes using microbubbles. The suggested method relied on injecting gas-filled bubbles into the circulatory system and measure the frequency shift that occurred in the scattered spectrum as ultrasonic waves were applied. The idea of using microbubbles for obtaining estimates of pressure led the way for a range of methods devised from this technique [5]–[10]. Despite the less invasive procedures, they still require the injection of microbubbles. Furthermore, microbubble techniques only provide a short time window of approximately 10–20 s [11] for imaging, as the bubbles are taken up by the liver or rupture in the acoustic pressure field produced by the ultrasound transducer.

In 1976, Holen *et al.* [12] introduced the first fully non-invasive alternative for estimating intravascular pressure based on Doppler ultrasound. Analysing audio signals of the frequency shifts received from the mitral jet revealed the peak systolic velocity. From this, the local pressure gradients were calculated using an orifice equation. The utility of the method was demonstrated on 25 patients with mitral stenosis and 10 without. The method was attractive due to its avoidance of catheterization, but was faced with difficulties associated with ultrasound scanner technology of that time, e.g. poor signal-to-noise ratios, and inferior temporal and spatial resolutions. However, the dominant drawback of the method was its reliance on a single velocity estimate, which made the method highly sensitive to hemodynamic factors unrelated to the constricted vessel's effect on the peak velocity, e.g. abnormal cardiac output. The method presented by Holen *et al.* was further studied in 1989 by Evans *et al.* [13], and later tested against clinical pressure catheters by Strauss- and Baumgartner *et al.* [14]–[16]. The latter studies agreed that non-invasive pressure estimation through a simplified version of the Bernoulli equation was achievable, however, the obtained pressure estimates were greatly dependent on the size of the examined vessel and the examiners ability to correct for the Doppler angle. Further advancement in non-invasive techniques for improving pressure estimates have been proposed over the past decades [17]–[25], but none of these have as yet successfully managed to supercede pressure catheters in the clinic.

Deriving intravascular pressure changes from blood flow has also been explored in the field of magnetic resonance imaging

(MRI). Here, the ability to detect all three spatial velocity components [26] offers the advantage of deriving fields of pressure gradients without uncertainties related to the neglection of the out-of-plane movement [27]. Most MRI studies on deriving pressure from flow data are based on the Navier-Stokes equations using either vector velocity data [27]–[31] or directly from acceleration data [32]. The spatial resolution in MRI provides a solid basis for calculating the convective acceleration used in the Navier-Stokes equations. However, flow estimation techniques in MRI rely on data acquisitions from several cardiac cycles through electrocardiogram gating to image a full cycle. This prevents real-time imaging of pressure variations and is further at the expense of temporal resolution, thus, impairing estimation of the local acceleration, which also goes into the Navier-Stokes equations. The lack of a proper temporal resolution poses a significant downside to MRI, when measuring on dynamic flow systems such as in the larger arteries. Furthermore, MRI requires each velocity component to be measured separately. This precludes simultaneous data acquisition of the vector velocity fields used for deriving the intravascular pressure.

In optics, velocity fields are also used in deriving pressure. Particle image velocimetry (PIV) illuminates tracer particles seeded into a fluid of interest, thereby visualizing the movement and trajectory of the flow that carries the particles around [33]. Modern PIV systems are capable of detecting 3-D fluid movement, which has paved the way for a wide range of non-intrusive techniques for determining pressure flow fields [34]–[36]. However, less-clinical relevant, this field of optics has published some of the most advanced studies on deriving pressure from vector velocity fields, and many of their findings and conclusions can be used when deriving pressure in-vivo using for example medical ultrasound or MRI techniques.

The paper develops a method for estimating pressure changes from vector velocity ultrasound data, and compares the results to 3-D finite-element (FE) simulation models. The study concludes by testing the method in-vivo on two healthy volunteers. For the validation process, two flow phantoms with concentric constrictions of 36 % and 70 % are fabricated, and scanned during steady and pulsatile flow condition. The constricted models ensure the built-up of a velocity field that varies as a function of both time and space, which is preferred when evaluating pressure gradient techniques. The presented paper is an extension of previous papers published by the authors [37], [38], and further includes a new estimator based on an ultrafast flow imaging technique, along with a display of the first in-vivo examples.

II. PRESSURE GRADIENT CALCULATIONS USING VECTOR VELOCITIES

The following section describes the employed method for calculating intravascular pressure gradients. It is based on the Navier-Stokes equations:

$$\rho\left[\frac{\partial\vec{v}}{\partial t}+\vec{v}\cdot\nabla\vec{v}\right]=-\nabla p+\rho\vec{g}+\mu\nabla^2\vec{v}, \tag{1}$$

presuming the conservation of mass and linear momentum. Eq. (1) describes the development of a fluid's velocity field $\vec{v}(\vec{r},t)=(v_x(t),v_y(t),v_z(t))$ by relating the forces acting on an incompressible volume to its acceleration and density throughout time, t, and space, $\vec{r}$. The left-hand side sums the local $\frac{\partial\vec{v}}{\partial t}$ and convective fluid acceleration $\vec{v}\cdot\nabla\vec{v}$, where ρ is the density of the fluid and ∇ is the spatial differential operator $(\frac{\partial}{\partial x},\frac{\partial}{\partial y},\frac{\partial}{\partial z})$. The right-hand side shows the surface and volume forces that are responsible for the acceleration of the fluid. The forces constitute a pressure drop $-\nabla p$, a gravitational force $\vec{g}$, and a viscous drag caused by the viscosity of the fluid $\mu\nabla^2\vec{v}$, where $\nabla^2\vec{v}$ is the Laplacian of the velocity field. The gravitational term is usually neglected, as a patient undergoing an ultrasound scan is placed in a supine position, hence, the buoyancy force cancels out the gravitational force. Further, Prantdl and Wood [39], [40] suggested that the effect of the viscous term is neglectable when studying blood flow in larger arteries, as it only has a small influence on the overall movement of flow.

A full view of the relative intravascular pressure distribution can be mapped through solving a least-square approximation of the derived pressure gradient field, $-\nabla p$, using the Pressure-Poisson equation [35], [41]. However, this has shown to be greatly dependent on an accurate segmentation of the vessels and its boundaries to set the necessary boundary conditions needed for solving the pressure equation [42], [43]. Instead, a different approach of deriving pressure is considered. The high precision and temporal frame-rate offered by synthetic aperture flow imaging [44], [45] allows for tracking of particles or blood scatterers, which intuitively can be visualized by either a streamline or a pathline representation. Rewriting (1) into a scalar equation following a streamline, and where the influences of gravity and viscosity are omitted, yields the following;

$$\frac{\partial p}{\partial s}=-\rho\left[\frac{\partial v_s}{\partial t}+v_s\frac{\partial v_s}{\partial s}\right]. \tag{2}$$

Here, v_s is the scalar product of $\vec{v}(\vec{r},t)$ and the vector that lies tangent to the streamline $d\vec{s}=(\hat{s}_x,\hat{s}_y,\hat{s}_z)$, where $d\vec{s}$ is an element of distance along the streamline, which runs in the direction, s. Integrating the individual pressure gradients from (2) along the flow direction of the streamline gives the total pressure drop across the line,

$$\Delta P(t)=\int_0^L\frac{\partial p}{\partial s}ds. \tag{3}$$

Eqs. (1)–(3) state that the three spatial vector components of $\vec{v}$ must be known to estimate the pressure gradient ∇p. This study employs a velocity estimator, which yields the two-dimensional (2-D) in-plane vector velocity field $\vec{v}=(v_x,v_z)$. The proposed method is, thus, developed assuming that the out-of-plane velocity v_y is zero.

As the method relies on finding temporal and spatial changes in discrete velocity estimates, it becomes highly sensitive to noisy data. Erroneous velocity estimates from electronic noise in the sampling process is a potential error source when calculating derivatives, since the difference quotient basically works as a high-pass filter, thereby, enhancing noise present in the original estimates. To avoid drowning the acceleration estimates in noise, two approaches are proposed to minimize

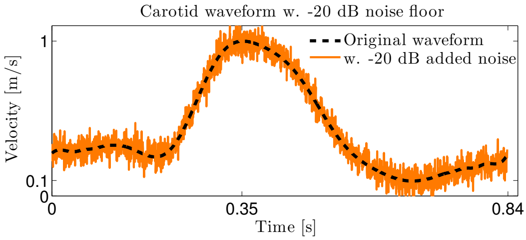

Fig. 1. Waveform mimicking the typical flow in a carotid artery.

numerical noise. The temporal acceleration is based on a Fourier analysis of the measured flow profile, and the calculation of the spatial derivative employs polynomial filtering.

A. Calculating the Temporal Acceleration

The temporal derivative in (2) is approximated analytically by decomposing the measured flow profile into a series of sinusoids through a Fourier transform. The profile and its derivative can then be reconstructed by summing sine- or cosine-functions oscillating at frequencies most representative for the measured signal [13], [46]. Reconstructing the flow profile from a sum of sinusoids is possible as the flow is somewhat periodic over the cardiac cycle. Further, performing a 90° phase shift of the selected frequencies before summing, gives an approximated expression for the flow profile's acceleration curve as the derivative of a cosine is a sine function. The acceleration curve can, therefore, be expressed as:

$$\frac{\mathrm{d}v_s(n,t)}{\mathrm{d}t} \approx -\sum_{p=1}^{N} |V_p(n)|\, 2\pi f_p\, \sin(2\pi f_p t + \varphi_p(n)), \qquad (4)$$

where N is the number of sinusoids used in reconstructing the flow profile. V_p and φ_p are the amplitude and the phase of the frequency component f_p. The index number, n, denotes the position along the examined streamline in the vector velocity field. The selected frequencies, f_p, are chosen based on their level of energy in the frequency domain. For this study, the N frequency bins that contain the majority of the spectral energy are selected for reconstructing the measured flow profile, and its derivative. As an example, blood flow in larger vessels is mainly govern by the pulsating motion of the heart, hence, the frequencies of highest energy levels are generally associated to the fundamental period of the heart's cycle, and its harmonics. These would then be the bins chosen for the reconstruction.

The noise removal technique is exemplified in Figs. 1–2. Fig. 1 presents a fictive velocity profile from a common carotid artery sampled at 2,500 Hz with -20 dB of added Gaussian noise. Moving the contaminated signal into the Fourier domain, and selecting the eight frequencies of highest energy levels to reconstruct the original signal, yields the top graph in Fig. 2. The figure shows that a waveform, having a signal-to-noise ratio of -20 dB, can be 99 % recovered using only eight frequency bins. Performing a 90° phase shift of the eight bins, before summing them, gives the acceleration curve of the contaminated signal. The result of this is shown in the bottom of Fig. 2.

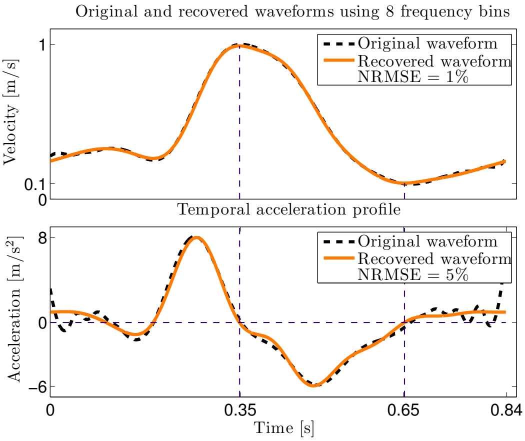

Fig. 2. Recovered waveform and its acceleration profile based on summing eight sinusoidal functions of different frequency, amplitude and phase.

The normalized root mean square error (NRMSE) between the recovered acceleration profile and the reference profile is calculated by,

$$\mathrm{NRMSE} = \frac{1}{x_{o,max} - x_{o,min}} \sqrt{\frac{1}{N}\sum_{m=1}^{N} (x_o(m) - x_n(m))^2}, \qquad (5)$$

where x_o is original signal, and x_n the noise contaminated signal. The acceleration profile is 95% recovered from summing eight sinusoids with phases that are shifted 90°. The number of sinusoids needed to make a realistic reconstruction of the original flow waveform depends on the frequency content of the profile and the amount of noise present in the signal. Fig. 3 shows the ideal number of sinusoids needed to reconstruct the profile from Fig. 1 as a function of an increasing noise floor.

B. Calculating the Spatial Acceleration

The spatial derivative in (2) is, unlike the previous case, not necessarily periodic across the examined region. Thus, it is not convenient to approximate the spatial acceleration by a sum of sinusoids. Instead, the derivative is found using polynomial filtering of the measured velocities along the investigated streamline. A second-order polynomial is fitted to a subset of adjacent data points by the linear least-squared method as suggested by Savitzky and Golay in 1964 [47]. Convolution coefficients from the model are then used for finding the first-order derivative [37]. The values of the convolution coefficients depend solely on the size of the examined subset and the order of the polynomial that is fitted to the subset. For instance, a window of five data points yields the following equation for calculating the derivative:

$$\dot{y}_n = \frac{1}{35}(-7x_{n-2} - 3.5x_{n-1} + 3.5x_{n+1} + 7x_{n+2}). \qquad (6)$$

Eq. (6) finds the derivative in x_n, where n is the central data point of the subset. Each window of five data points

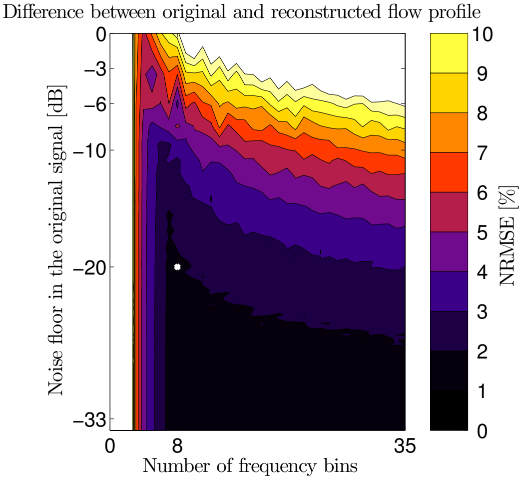

Fig. 3. Number of sinusoids required for reconstructing the original inlet waveform, Fig. 1, when the level of noise increases in the measured signal. A 99% recovery can be made from a sum of eight sinusoids, despite having a signal to noise ratio of -20 dB.

is weighted by the Savitzky-Golay convolution coefficients, $\vec{B}$, which for the chosen window size and polynomial order are: $\vec{B} = \frac{1}{35}[-7, -3.5, 0, 3.5, 7]$. The spatial acceleration is calculated by pair-wise multiplication of the elements in the velocity window and the convolution coefficients before summing and scaling the five multiplication terms,

$$\frac{\mathrm{d}v_s(n,t)}{\mathrm{d}s} \approx \frac{1}{\Delta s} \sum_{p=n-h_w}^{n+h_w} v_s(p,t) B(p-(n-h_w)+1). \quad (7)$$

Here, Δs is the sampling interval along the direction of the streamline. The index number p, is found from half the window size of the selected subset, calculated as: $h_w = \frac{N_{set}+1}{2} - 1$, where N_{set} is the number of samples in the subset. Fitting a second-order polynomial to overlapping subsets of the data, eventually, produces a high order curve that follows the course of the estimated velocity data. This is valid within the assumption that a parabolic function is representable for the trend of the subset's data points, thus, a window size of only five points, equivalent to 1 mm, is selected. Having higher order fluctuations in the flow profile over a region of 1 mm is considered unphysical.

III. EXPERIMENTAL SET-UP AND EQUIPMENT

The performance of the method is validated on straight-tube phantoms during steady and pulsating flow conditions, before testing the method in-vivo on two healthy volunteers. Two straight tube phantoms with an inner diameter of 8 mm are designed, each with a concentric constriction of 36 % and 70 %, respectively, and a length of 260 mm. Sections of the models are shown in Fig. 4. The geometry of the vessels is drafted in SolidWorks (Education edition, Dassault Systèmes SolidWorks Corp., Vélizy, France) and exported as an STL file to stereolithography, which constitutes the core of the phantom's fluid flow domain [48]. The 3-D printed cores are fixed in individual containers before cast in polyvinyl alcohol (PVA) cryogel to make the surrounding medium mimic the properties of human tissue. The PVA cryogel is made using an in-house formula, containing 15 % PVA, 1 % silicon dioxide, 0.3 % potassium sorbate, and 83.7 % distilled water. The nature of cryogel allows for controlling its elastic properties by varying the number of freeze-thaw cycles it undergoes. Two freeze-thaw cycles are used, each half-cycle of 24-hours duration, with freeze settings of −20 °C ± 0.5 °C and thaw of 4 °C ± 0.5 °C. After completing two cycles, given a total duration of 96 hours, the core was removed manually, thereby, leaving a core-less phantom with sound propagating properties of human tissue and a fluid domain identical to the 3-D printed structure.

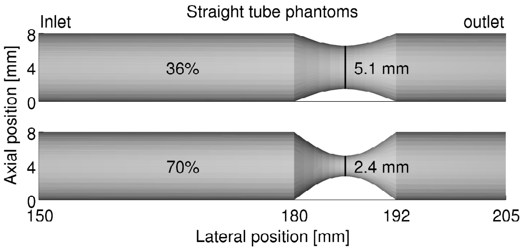

Fig. 4. Two straight tube phantoms with an inner diameter of 8 mm are used for validating the proposed method. Each model has a length of 260 mm and a concentric constriction of either 36 % and 70 % of the inlet diameter.

The fabricated phantoms are connected to a flow system (CompuFlow 1000, Shelley Medical Imaging Technologies, Toronto, Canada) capable of generating customized flow waveforms. The first study is performed using a constant waveform and a flow rate of 5 ml/s. The second study uses a time-varying waveform equivalent in shape to the dotted line in Fig. 1, and a peak flow rate of 5 ml/s.

Two in-vivo acquisitions are carried out after approval by The Danish National Committee on Biomedical Research Ethics. A healthy female (age 52) and male (age 41) are scanned by an experienced radiologist. The volunteers are placed in a supine position for five minutes to obtain a steady heart rate. The examinations were performed over the left carotid bifurcation, producing a view of both the internal and external artery together with the carotid bulb. Intensity measurements were made prior to the examinations, showing energy levels and an MI within the limits set by the U.S. Food and Drug Administration.

Both, experimental and in-vivo scans are made using a BK8670 linear array transducer connected to the experimental research scanner SARUS [49]. A three-cycle pulse with a center frequency of 7 MHz is emitted at a pulse repetition frequency of 12.5 kHz to a depth of 4 cm. Five low-resolution images are summed for each high resolution image producing an effective frame-rate of 2,500 Hz. The ultrasound data are processed off-line using Matlab (The MathWorks Inc., Natick, MA, USA).

Table I
SIMULATION SETTINGS IN COMSOL

Parameter name	Setting/Notation	Value
Simulation study		
Physics	Flow	Laminar
Geometry	Import from SolidWorks	STL-format
Solver	Direct	MUMPS
Mesh	Physics-controlled mesh	Extra coarse
Fluid properties		
Compressibility	-	Incompressible
Density	ρ	1,030 kg/m^3
Viscosity	μ	4.1×10^{-3} Pa s
Reynolds number	During peak systolic phase (70% constricted phantom)	1,200
Initial conditions		
Pressure	-	0 Pa
Inlet conditions		
Inflow	Laminar	-
Peak flow rate	During constant flow	5 ml/s
Average flow rate	During pulsating flow	1.283 ml/s
Entrance length	-	1 m
Outlet conditions		
Outflow	Pressure	0 Pa
Wall		
Condition	-	No-slip

IV. SIMULATION MODEL

The accuracy of the derived pressure is evaluated through comparison to FE models made in Comsol (Comsol Multiphysics v5.1, Comsol AB, Stockholm, Sweden). The geometry of each model is based on the same STL file as used in the stereolithography (Fig. 4), thereby, ensuring identical flow domains between simulations and experimental models. Flow parameters in the simulation models are set to mimic the actual flow conditions in the experimental set-up. Equivalent to the experimental set-up, an average input flow rate of 5 ml/s, and 1.283 ml/s is chosen for the constant and pulsatile flow simulation, respectively. Further, the simulated fluid's viscosity (4.1×10^{-3} Pa s) and density (1,030 kg/m^3) are set to match the properties of the blood-mimicking fluid (BMF-US, Shelley Medical Imaging Technologies, Toronto, Canada) that circulates the actual flow system. A summary of the settings used in the simulation model is listed in Table I. The peak systolic phase in the simulation models showed a maximum Reynolds number of roughly 1,200, which is below the transient zone to turbulent flow (2,300 <), thus, a laminar flow model is considered.

V. EVALUATION MEASURES

The performance of the proposed estimator is evaluated by its standard deviation (Std), and bias in reference to the simulation model. The two quantities are calculated as:

$$Std = \frac{1}{sim_{max}} \sqrt{\frac{1}{N} \sum_{m=1}^{N} \sigma^2(m)} \qquad \text{and} \tag{8}$$

$$Bias = \frac{1}{sim_{max} N} \sum_{m=1}^{N} \mu_{est}(m) - \mu_{sim}(m), \tag{9}$$

where N is the number of data points along the spatial path that is investigated. The mean of the variance σ^2, is calculated over time for every position along the streamline, before taking the square-root to yield the standard deviation of the estimator. The bias is found from the average distance between the mean estimated value over time $\mu_{est}(m)$, and the results from the simulation model, $\mu_{sim}(m)$. Both, standard deviation and bias are found as means across the entire streamline, before normalised to the peak absolute value of the reference model, sim_{max}.

VI. VECTOR VELOCITY ESTIMATION

Velocities are estimated using directional synthetic aperture flow imaging, an approach explained by Villagómez-Hoyos *et al.* [44], [50]. Unfocused spherical waves are emitted from the aperture by placing virtual sources behind the transducer. A low-resolution image is created for each emission, and multi-directional lines are beamformed for every position within the insonified area. The flow angle and its velocity magnitude are found by cross-correlating beamformed lines to lines in successive low resolution images. An updated velocity frame is made for each newly generated low-resolution image, thus, the time-resolution of the velocity estimator can potentially be equal to the pulse repetition frequency. The method's performance is evaluated during steady and pulsatile flow condition at the constricted sites of the two fabricated models. Three seconds of flow data are recorded producing roughly 7,500 frames of velocity data. Each frame contains estimates separated by 0.2 mm in both the axial and lateral direction.

A. Vector Velocity Imaging during Steady and Pulsating Flow

Examples of vector flow images from the two fabricated phantoms are displayed in Fig. 5. The images show flow that accelerates toward the center of the constriction, producing a jet that then slowly decelerates as the lumen expands again. Black streamlines set to start from the center of the vessel are also displayed. Throughout the study, changes in pressure are derived along these dotted streamlines. The number in the colorbox indicate the maximum flow velocity that can be represented by a color in the color flow map.

Peak velocities from measured and simulated data are plotted as a function of time in Fig. 6. The figure reveals a standard deviation of 6 %, and 2 % relative to the reference model for the 36 %, and the 70 % constriction, respectively. Further, a bias of −17 % and −8 % is observed for the two constant measurements. The bias is a consequence of having misaligned the transducer to the exact center axis of the constriction, which becomes apparent when comparing the diameter of lumen seen on the B-mode images to the actual constriction sizes of the models from Fig. 4. Measuring the widths of the observed constrictions gives distances of approximately 4.4 mm and 2.3 mm for the 36 %, and the 70 % constricted phantom, respectively. Whereas, the actual distances for the two models are 5.12 mm and 2.40 mm, thus, lower velocities are measured in the experimental set-up as the peak flow velocities are outside the scan plane of the transducer. The calculated biases are, therefore, used for compensating the measured velocities. The result of doing this in the pulsatile flow case is seen in Fig. 7. Bias compensation is performed to

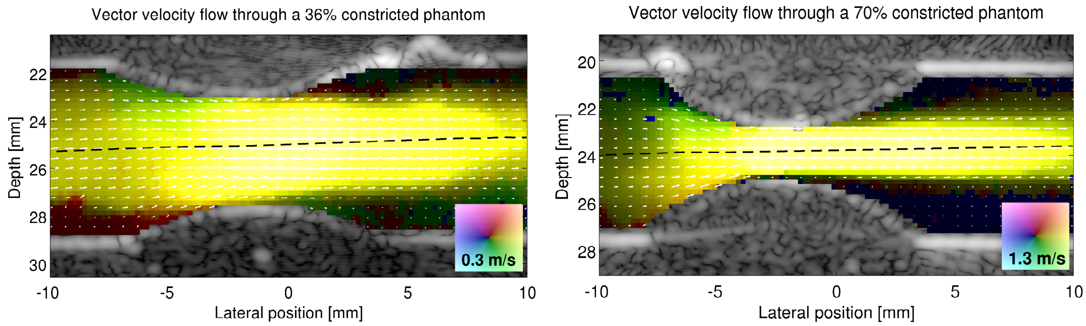

(a) (b)

Fig. 5. Vector velocity images at the constriction of two fabricated flow phantoms. Phantom (a) has a constriction of 36 %, while (b)'s is 70 %. The two images are captured during steady flow conditions. Black-dotted streamlines passing through the center of the constrictions are also displayed.

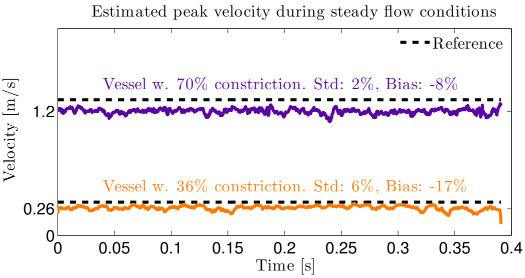

Fig. 6. Estimated and simulated peak velocity from the center of the constriction during constant flow rate.

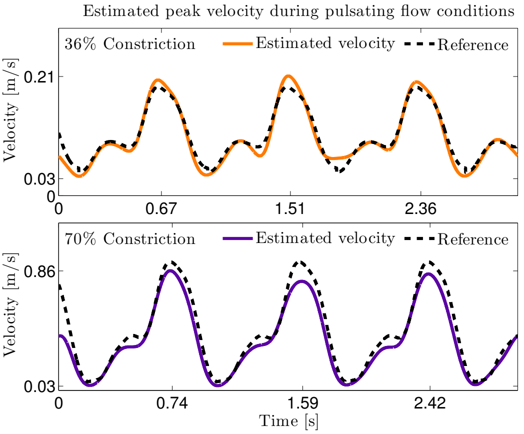

Fig. 7. Estimated and simulated peak velocity from the center of the constriction during pulsating flow conditions.

obtain as good resemblance between estimated and simulated velocities as possible, before inserting the measured velocities into the proposed estimator. This will ensure the best basis for comparing the derived pressures to the simulation model, as all discrepancies between the model and the reference, will be solely related to the actual performance of the suggested estimator. Bias correcting the estimated velocities is not an option during in-vivo scanning, as the true flow velocities are unknown.

The displayed flow profiles are reconstructed from the measured data using a sum of sinusoids, as explained in II-A. A single pulse cycle can, as suggested by Fig. 3, be 99 % recovered from eight distinct frequency bins. Thus, to maintain the same level of accuracy when reconstructing three pulses that are not necessarily identical, 24 frequency bins are required. The inherent compliance of the flow system's afferent tubes increases the pulsatility of the time-varying flow, producing a flattening of the velocity profile compared to the profiles seen during constant flow.

Two in-vivo measurements are carried out on the carotid artery of two healthy volunteers. The resulting vector flow images are shown in Figs. 8–9. The figures display longitudinal scans of the volunteers' left carotid bifurcations together with the measured flow field. The images are captured at peak systole, yielding values in the carotid sinus of roughly 0.6 m/s. The starting point of the superimposed streamlines are manually selected based on the criteria that the lines should include the peak spatial velocity during the systolic phase.

All velocities measured on the fabricated models and in the two in-vivo cases are filtered by a 3-D median filter, before entering the proposed pressure estimator. This is done to minimize the risk of transferring any inexpedient discontinuities from the estimated velocities, into the differential operator and further to the desired pressure estimate. The filter's in-plane window size is set to 10 data points, corresponding to a axial and lateral distance of 2 mm. A second median filter of 15 data points is applied temporally, equivalent to a window size of 6 ms.

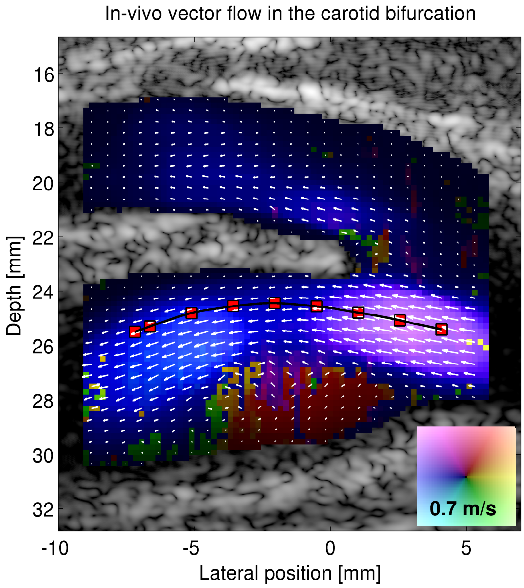

Fig. 8. Volunteer 1: Longitudinal vector flow scan of the carotid bifurcation during peak systolic. Bottom branch shows the internal carotid artery in conjunction with the carotid bulb, for which a vortex is formed during rapid flow movement. A streamline following the vector velocity field is also displayed.

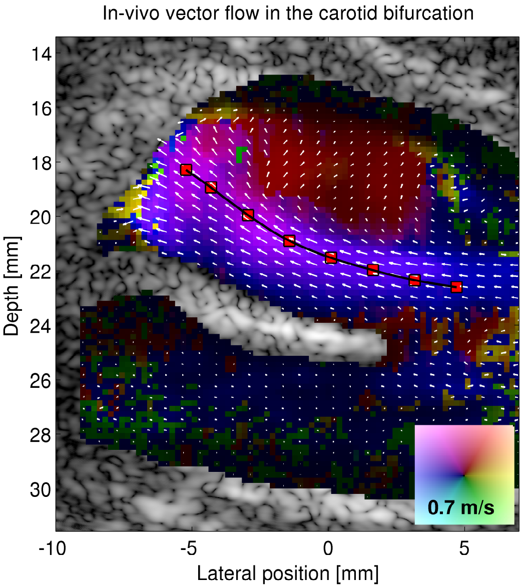

Fig. 9. Volunteer 2: Longitudinal vector flow scan of the carotid bifurcation during peak systolic. Top artery shows the internal carotid artery in conjunction with the carotid bulb, for which a vortex is formed during rapid flow movement. A streamline following the vector velocity field is also displayed.

VII. RESULTS

The following section presents the results from the proposed estimator. First presented are the results from the two flow phantoms measured during steady and pulsating flow conditions. The section concludes by displaying the first in-vivo examples of measuring pressure changes along flow streamlines using a 2-D ultrafast flow imaging technique.

A. *Estimated Pressure Drop during Constant Flow*

Streamline velocities from Fig. 5 are extracted and used for deriving the pressure drop that occur across the constriction. Since only spatial changes in the velocity field exist for steady flow the temporal acceleration in (2) is neglected. For every position along the streamline, an individual pressure gradient is calculated relative to its neighbouring estimates using (2). The individual gradients are found through polynomial filtering, using a moving window of five data points and a polynomial order of two. Then, calculating the cumulative sum of the local pressure changes along the direction of the flow, yields the drop in pressure that exist between the start of the streamline to any position along the line. The results of doing this for every frame of velocity estimated are shown in Fig. 10(a)–(b). The graphs display the pressure drop that occurs as the fluid moves through the constricted part of the phantoms. The shaded zone indicates a region of one standard deviation normalized to the number of frames recorded, which in the steady flow case were roughly 1,000 frames. The dotted dark curves in Figs. 10(a)–(b) are the results from the simulation models. Mean biases across the constricted area of 8 %, and 7 % are calculated using (9) in the 36 %, and 70 % constricted phantoms, respectively, with mean standard deviations of 9 %, and 6 %, for the steady flow case.

B. *Estimated Pressure Drop during Pulsatile Flow*

The calculation of the pressure drop during pulsating flow condition follows the same data processing scheme as in the previous case, however, this time the temporal acceleration is included. The results are shown in Fig. 11(a)–(b). Largest changes in pressure are observed in the systolic phase of the cycle, hence, emphasized in the two graphs. The systolic pressure drops from the three recorded cycles show a mean standard deviation of 1 % and 7 %, relatively to the peak simulated pressure drop for the 36 %, and 70 % constricted phantom, respectively. A mean bias over the entire course of the streamline is found to 2 %, in comparison to the FE models.

C. *In-vivo Examples*

Vector velocities found along the streamlines of Figs. 8–9 are extracted for all time instances and inserted into the proposed algorithm. The resulting pressure drops are shown as 3-D plots in Figs. 12–13. The figures show how pressure, changes along the direction of the streamlines as a function of time. The plots' left wall makes up the starting point of the streamline data.

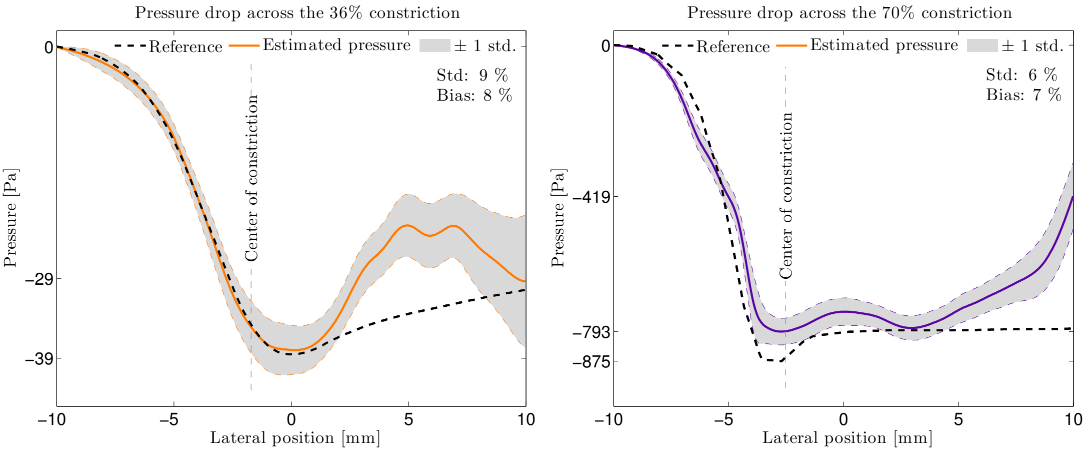

(a) (b)

Fig. 10. Constant flow: Estimated and simulated pressure drop through the center of a 36 %, and 70 % constriction. The mean estimate is plotted together with ± 1 standard deviation, along with the output from the FE models.

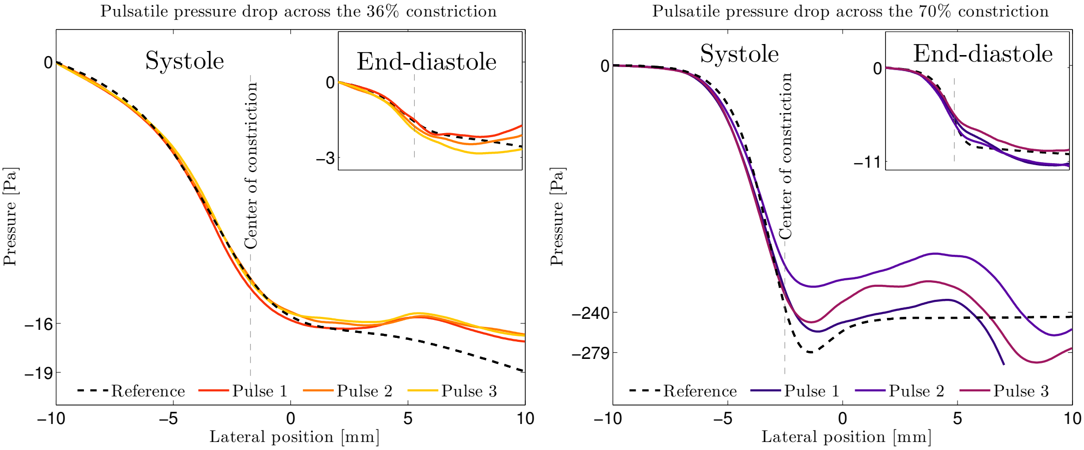

(a) (b)

Fig. 11. Pulsating flow: Estimated and simulated pressure drop through the center of a 36 %, and 70 % constriction. The pressure changes are plotted for the peak systolic phase of the cycle, as well as for the end-distolic phase. The thick dotted line represents the outputs from the FE models.

Changes in pressure are then found relatively to this point, by moving down-right, parallel to the lateral axis. Both cases show the largest pressure variations during the systolic phase of the cardiac cycle, with values between 0 Pa and -60 Pa.

VIII. Discussion

Non-invasive pressure changes have been calculated from vector velocity ultrasound data. Pressure drops across two concentric constricted flow phantoms were examine, before measuring in-vivo pressures on two volunteers. The largest experimental pressure drop was seen in the 70 % constricted phantom, reaching a drop of −875 Pa. The largest mean standard deviations and biases that were found across the entire constriction were 9 %, and 8 %, respectively.

For both steady and pulsating flow cases good correspondences were seen upstream, and at the center of the constriction between the measured and the reference data. However, greater misalignments were present downstream. Misaligning the transducer from the center axis of the concentric phantom, would make downstream pressure estimation more troublesome,

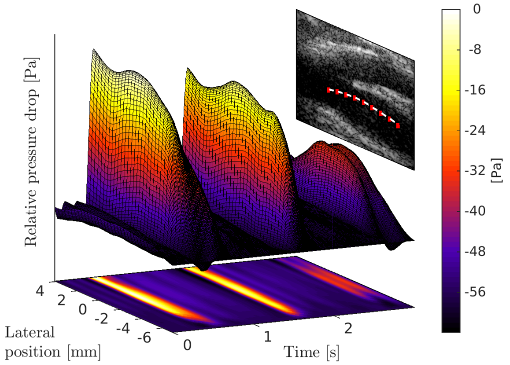

Fig. 12. In-Vivo: Changes in intravascular pressure measured as a function of time and longitudinal position along the streamline from Fig. 8. The shown pressures are in reference to an arbitrary value, which for this study is set to zero at the beginning of the streamline.

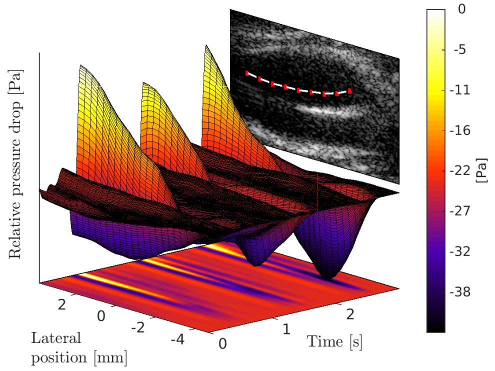

Fig. 13. In-Vivo: Changes in intravascular pressure measured as a function of time and longitudinal position along the streamline from Fig. 9. The shown pressures are in reference to an arbitrary value, which for this study is set to zero at the beginning of the streamline.

as the scan plane moves closer to the recirculation zone seen immediately after a post-stenotic region. A recirculation zone compose complex flow features that exhibit higher degrees of out-plane movements, thereby causing a more distorted vector field, when mapping flow velocities in the 2-D scan plane. Such misalignment could explain the disagreement seen between the estimated and the simulated results in Figs. 10(a)–(b), as the FE data are extracted from the exact center plane of the phantom's domain.

The proposed method employs vector velocity data, acquired to a depth of 4 cm using directional synthetic aperture flow imaging, producing 2,500 velocity frames a second. No previous studies on the topic have measured changes in pressure along streamlines using a high frame-rate ultrasonic technique. Such techniques allow for averaging across estimates without compromising the peak of the profile. Averaging is beneficial as it essentially performs a low-pass filtering of the estimates, thus, avoiding the higher frequency content, which usually is associated with noise. Noise cancellation is the key aspect to consider when deriving intravascular pressure changes from velocity data, as only a small amount of noise in the velocity signal can be devastating to the output pressure as the differential operator essentially performs a high-pass filtering the velocity estimates. This becomes increasingly more important when moving into higher order derivatives, as would have been the case if the effect of viscous forces had been included in the pressure estimator.

The influence of viscosity has been neglected in this study, as flow in larger vessels were studied, and a Reynolds number of more than a 1,000 was found during the peak systolic phase. However, moving into smaller vessels with lower Reynolds number, makes this assumption invalid, thus, pressure estimation based on the Navier-Stokes equation should for those vessels take the viscous forces into account.

The presented technique essentially studies the flow pattern of a moving fluid, from which the pressure forcing the fluid to move is sought predicted. This makes the technique vulnerable to the flow estimator's capability to detect the true movement of the particles. For instance, the proposed set-up uses a 2-D velocity estimator approach, meaning that the out-of-plane motion gets excluded from the pressure algorithm. Whether or not this is acceptable, is greatly dependent on the complexity of the flow being examined. For example, studying the vector field in Fig. 9, it appears that the flow along the streamline accelerates through the carotid bulb, though, the lumen of the vessel expanse. Such flow behaviour is only possible if out-of-plane particles of higher velocities are pushed through the scanned plane, thus, leading to the false impression that in-plane velocities are accelerated from right to left in the image. Therefore, in case of Fig. 9, it would have been beneficial to have had access to the full 3-D velocity information before deriving the pressure drop. An example of such velocity estimator could be for instance the one presented by Pihl and Jensen [51] using a 2-D phased array transducer. The missing information on the out-of-plane velocity component is likely the reason for why Fig. 13 appears more distorted than Fig. 12, where a more holistic view of the flow movement is captured within the scanned plane.

The study showed pressure changes from everywhere between zero to −875 Pa across the examined vessels. In terms of millimeters of mercury this translates to roughly 0–7 mmHg, which for a clinical found stenotic vessels, is on the low side. In 1993, Donohue *et al.* [52] presented an in-vivo pressure catheter study showing that stenotic vessels with 50 %–90 %% constrictions cause pressure drops from 2–80 mmHg. Eight out of their 101 patients had stenoses of 70.1±14.7 %, for which drops in pressure of 41.5±5.9 mmHg were detected. Comparing these values to the results from the 70% constricted phantom reveal a discrepancy of a factor of seven. The discrepancy is presumably a consequence of the following two factors: As shown by De Vecchi *et al.* [2], pressure catheters are, due to their bulk size, known for overestimating the intravascular pressure by 24 %. However, a more important factor when commenting on the discrepancy is the difference in physical shape between the vessels being compared. One side presents a phantom study made on a relatively short concentric stenosis, where for the other side clinical ill vessels are studied. The latter case rarely shows vessel curvatures as neat as the models designed in this study. Usually, highly irregular shapes are seen in actual arterial stenoses leading to more complex flow patterns, and thereby also a larger prevalence of turbulent flow features. Features such as eddies, localized turbulence, and jets that all contributes to the dissipation of energy, will accelerate an increasing drop in pressure as the fluid passes through the stenotic region [53], [54]. Future work therefore includes measuring on more irregular geometries with increasing constriction-rates to investigate the application range of the suggested method as flow approaches more turbulent conditions. Moreover, to clinically strengthen the validation of the proposed method, future work concerns a comparison to fluid-filled pressure catheters, as these are the current practice for how intravascular pressure changes are measured.

IX. CONCLUSION

A non-invasive method for deriving intravascular pressure differences using angle-independent vector velocity ultrasound data was presented. First, 2-D fields of velocity data were obtained with a temporal resolution of 400 μs using directional synthetic aperture flow imaging, before deriving pressure changes across the flow region using the Navier-Stokes equations. Pressure gradients along streamline were estimated, and summed to yield the drop in pressure that existed from one end of the vessel to the other. Two experimental flow phantoms were fabricated and scanned, before measuring in-vivo on the carotid bifurcation of two volunteers. The results from the experimental scans were compared to numerical simulation models. The estimator showed pressure values between -875 Pa and 0 Pa depending on when in the cycle they were measured, with a standard deviation of 9% and a bias of 8%. The results of the in-vivo scans demonstrated the feasibility of measuring pressure changes along streamlines using a 2-D vector velocity approach, but also the deficiency of only having the two in-plane vector velocity components available when deriving pressure changes, non-invasively.

REFERENCES

[1] D. S. Baim and W. Grossman, *Grossman's cardiac catheterization, angiography, and intervention.* Lippincott Williams & Wilkins, 2000.

[2] A. de Vecchi, R. E. Clough, N. R. Gaddum, M. C. M. Rutten, P. Lamata, T. Schaeffter, D. A. Nordsletten, and N. P. Smith, "Catheter-induced errors in pressure measurements in vessels: An in-vitro and numerical study," *IEEE Trans. Biomed. Eng.*, vol. 61, no. 6, pp. 1844–1850, 2014.

[3] J. J. Cavendish, L. I. Carter, and S. Tsimikas, "Recent advances in hemodynamics: Noncoronary applications of a pressure sensor angioplasty guidewire," *Catheter Cardiovasc Interv*, vol. 71, no. 6, pp. 748–758, 2008.

[4] W. M. Fairbank and M. O. Scully, "A new noninvasive technique for cardiac pressure measurements: resonant scattering of ultrasound from bubbles," *IEEE Trans. Biomed. Eng.*, vol. 24, pp. 107–110, 1977.

[5] A. Bouakaz, P. J. Frinking, N. de Jong, and N. Bom, "Noninvasive measurement of the hydrostatic pressure in a fluid-filled cavity based on the disappearance time of micrometer-sized free gas bubbles," *Ultrasound Med. Biol.*, vol. 25, pp. 1407–1415, 1999.

[6] W. T. Shi, F. Forsberg, J. S. Raichlen, and L. Needleman, "Pressure dependence of subharmonic signals from contrast microbubbles," *Ultrasound Med. Biol.*, vol. 25, pp. 275–283, 1999.

[7] D. Adam, M. Sapunar, and E. Burla, "On the relationship between encapsulated ultrasound contrast agent and pressure," *Ultrasound Med. Biol.*, vol. 31, pp. 673–686, 2005.

[8] F. Forsberg, J.-B. Liu, W. T. Shi, J. Furuse, M. Shimizu, and B. B. Goldberg, "In vivo pressure estimation using subharmonic contrast microbubble signals: Proof of concept," *IEEE Trans. Ultrason., Ferroelec., Freq. Contr.*, vol. 52, no. 4, pp. 581–583, 2005.

[9] K. S. Andersen and J. A. Jensen, "Ambient pressure sensitivity of microbubbles investigated through a parameter study," *J. Acoust. Soc. Am.*, vol. 126, pp. 3350–3358, 2009.

[10] F. Forsberg, J. Dave, V. G. Halldorsdottir, L. M. Leodore, F. Lin, A. L. Hall, and K. Thomenius, "Applying real-time noninvasive pressure estimation obtained from subharmonic contrast microbubble signals," *Proc. IEEE Ultrason. Symp.*, pp. 1694–1697, 2008.

[11] D. Cosgrove and N. Lassau, "Imaging of perfusion using ultrasound," *Eur. J. Nucl. Med. Mol. Imaging*, pp. s65–s85, 2010.

[12] J. Holen, R. Aaslid, and K. Landmark, "Determination of pressure gradient in mitral stenosis with a non-invasive ultrasound Doppler technique," *Acta med. scand.*, vol. 32, pp. 455–460, 1976.

[13] D. H. Evans, W. N. McDicken, R. Skidmore, and J. P. Woodcock, *Doppler Ultrasound, Physics, Instrumentation, and Clinical Applications.* New York: John Wiley & Sons, 1989.

[14] A. L. Strauss, F. J. Roth, and H. Rieger, "Noninvasive assessment of pressure gradients across iliac artery stenoses: duplex and catheter correlative study," *J. Ultrasound Med.*, vol. 12, no. 1, pp. 17–22, 1993.

[15] H. Baumgartner, H. Schima, G. Tulzer, and P. Kühn, "Effect of stenosis geometry on the Doppler-catheter gradient relation in vitro: A manifestation of pressure recovery," *J. Am. Coll. Cardiol.*, vol. 21, no. 4, pp. 1018–1025, 1993.

[16] H. Baumgartner, T. Stefenelli, J. Niederberger, H. Schima, and G. Maurer, "Overestimation of catheter gradients by Doppler ultrasound in patients with aortic stenosis: A predictable manifestation of pressure recovery," *J. Am. Coll. Cardiol.*, vol. 33, no. 6, pp. 1655–1661, 1999.

[17] N. L. Greenberg, P. M. Vandervoort, M. S. Firstenberg, M. J. Garcia, and J. D. Thomas, "Estimation of diastolic intraventricular pressure gradients by Doppler M-mode echocardiography," *Am. J. Physiol. Heart Circ. Physiol.*, vol. 280, no. 6, pp. 2507–2515, 2001.

[18] J. Bermejo, J. C. Antoranz, I. G. Burwash, J. L. Alvarez, M. Moreno, M. A. Garcia-Fernandez, and C. M. Otto, "In-vivo analysis of the instantaneous transvalvular pressure difference-flow relationship in aortic valve stenosis: implications of unsteady fluid-dynamics for the clinical assessment of disease severity," *J. Heart Valve Dis.*, vol. 11, no. 4, pp. 557–566, 2002.

[19] A. K. Reddy, G. E. Taffet, S. Madala, L. H. Michael, M. L. Entman, and C. J. Hartley, "Noninvasive blood pressure measurement in mice using Doppler ultrasound," *Ultrasound Med. Biol.*, vol. 29, no. 3, pp. 379–385, 2003.

[20] S. Ohtsuki and M. Tanaka, "Doppler pressure field deduced from the Doppler velocity field in an observation plane in a fluid," *Ultrasound Med. Biol.*, vol. 29, no. 10, pp. 1431–1438, 2003.

[21] J. M. Meinders and A. P. G. Hoeks, "Simultaneous assessment of diameter and pressure waveforms in the carotid artery," *Ultrasound Med. Biol.*, vol. 30, no. 2, pp. 147–154, 2004.

[22] R. Yotti, J. Bermejo, J. C. Antoranz, J. L. Rojo-Alvarez, C. Allue, J. Silva, M. M. Desco, M. Moreno, and M. A. Garcia-Fernandez, "Noninvasive assessment of ejection intraventricular pressure gradients," *J. Am. Coll. Cardiol.*, vol. 43, no. 9, pp. 1654–1662, 2004.

[23] J. D. Thomas and Z. B. Popovic, "Intraventricular pressure differences a new window into cardiac function," *Circulation*, vol. 112, pp. 1684–1686, 2005.

[24] D. Garcia, P. Pibarot, and L.-G. Durand, "Analytical modeling of the instantaneous pressure gradient across the aortic valve," *J. Biomech.*, vol. 38, pp. 1303–1311, 2005.

[25] B. W. A. M. M. Beulen, N. Bijnens, G. G. Koutsouridis, P. J. Brands, M. C. M. Rutten, and F. N. van de Vosse, "Toward noninvasive blood pressure assessment in arteries by using ultrasound," *Ultrasound Med. Biol.*, vol. 37, no. 5, pp. 788–797, 2011.

[26] P. J. Kilner, G. Z. Yang, R. H. Mohiaddin, D. N. Firmin, and D. B. Longmore, "Helical and retrograde secondary flow patterns in the aortic arch studied by three-directional magnetic resonance velocity mapping," *Circulation*, vol. 88, no. 5, pp. 2235–2247, 1993.

[27] J. Bock, A. Frydrychowicz, R. Lorenz, D. Hirtler, A. J. Barker, K. M. Johnson, R. Arnold, H. Burkhardt, J. Hennig, and M. Markl, "In vivo noninvasive 4D pressure difference mapping in the human aorta: phantom

comparison and application in healthy volunteers and patients," *Magn. Reson. Med.*, vol. 66, no. 4, pp. 1079–1088, 2011.

[28] T. Ebbers, L. Wigström, A. F. Bolger, J. Engvall, and M. Karlsson, "Estimation of relative cardiovascular pressures using time-resolved three dimensional phase contrast MRI," *Magn. Reson. Med.*, pp. 872–879, 2001.

[29] R. B. Thompson and E. R. McVeigh, "Fast measurement of intracardiac pressure differences with 2D breath-hold phase-contrast MRI," *Magnetic Resonance in Medicine*, vol. 49, no. 6, pp. 1056–1066, 2003.

[30] R. Moftakhar, B. Aagaard-Kienitz, K. Johnson, P. A. Turski, A. S. Turk, D. B. Niemann, D. Consigny, J. Grinde, O. Wieben, and C. A. Mistretta, "Noninvasive measurement of intra-aneurysmal pressure and flow pattern using phase contrast with vastly undersampled isotropic projection imaging," *Am. J. Neuroradiol.*, vol. 28, pp. 1710–1714, 2007.

[31] A. Herment, G. Besson, C. Pellot-Barakat, and F. Frouin, "Estimation of pressure gradient images from velocity encoded MR acquisitions," *Computers in Cardiology*, vol. 35, pp. 933–936, 2008.

[32] J. P. Tasu, E. Mousseaux, A. Delouche, C. Oddou, O. Jolivet, and J. Bittoun, "Estimation of pressure gradients in pulsatile flow from magnetic resonance acceleration measurements," *Magn. Reson. Med.*, vol. 44, no. 1, pp. 66–72, 2000.

[33] R. J. Adrian and C.-S. Yao, "Pulsed laser technique application to liquid and gaseous flows and the scattering power of seed materials," *Appl. Opt.*, vol. 24, no. 1, pp. 44–52, 1985.

[34] L. Kajitani and D. Dabiri, "A full three-dimensional characterization of defocusing digital particle image velocimetry," *Meas. Sci. Technol.*, vol. 16, pp. 790–804, 2005.

[35] J. J. Charonko, C. V. King, B. L. Smith, and P. P. Vlachos, "Assessment of pressure field calculations from particle image velocimetry measurements," *Meas. Sci. Technol.*, vol. 21, no. 10, p. 105401, 2010.

[36] B. W. van Oudheusden, "PIV-based pressure measurement," *Meas. Sci. Technol.*, vol. 24, no. 3, p. 032001, 2013.

[37] J. B. Olesen, M. S. Traberg, M. J. Pihl, and J. A. Jensen, "Noninvasive esimation of 2-D pressure gradients in steady flow using ultrasound," *IEEE Trans. Ultrason., Ferroelec., Freq. Contr.*, vol. 61, no. 8, pp. 1409–1418, 2014.

[38] J. B. Olesen, C. A. Villagomez-Hoyos, M. S. Traberg, and J. A. Jensen, "Non-invasive estimation of pressure gradients in pulsatile flow using ultrasound," in *Proc. IEEE Ultrason. Symp.* IEEE, 2014, pp. 2257–2260.

[39] L. Prandtl, *Essentials of Fluid Dynamics*. London: Blackie & Son, 1952.

[40] N. B. Wood, "Aspects of fluid dynamics applied to the large arteries," *J. Theor. Biol.*, vol. 199, no. 953, pp. 137–161, 1999.

[41] S. M. Song, R. M. Leahy, D. P. Boyd, B. H. Brundage, and S. Napel, "Determining cardiac velocity fields and intraventricular pressure distribution from a sequence of ultrafast CT cardiac images," *IEEE Trans. Med. Imag.*, vol. 13, no. 2, pp. 386–397, 1994.

[42] G.-Z. Yang, P. J. Kilner, N. B. Wood, S. R. Underwood, and D. N. Firmin, "Computation of flow pressure fields from magnetic resonance velocity mapping," *Magn. Reson. Med.*, vol. 36, no. 4, pp. 520–526, 1996.

[43] J. M. Tyszka, D. H. Laidlaw, J. W. Asa, and J. M. Silverman, "Three-dimensional, time-resolved (4D) relative pressure mapping using magnetic resonance imaging," *J. Magn. Reson. Imaging*, vol. 12, no. 2, pp. 321–329, 2000.

[44] J. A. Jensen and S. I. Nikolov, "Directional synthetic aperture flow imaging," *IEEE Trans. Ultrason., Ferroelec., Freq. Contr.*, vol. 51, pp. 1107–1118, 2004.

[45] J. A. Jensen and N. Oddershede, "Estimation of velocity vectors in synthetic aperture ultrasound imaging." *IEEE Trans. Ultrason., Ferroelec., Freq. Contr.*, vol. 25, pp. 1637–1644, 2006.

[46] J. R. Womersley, "Oscillatory motion of a viscous liquid in a thin-walled elastic tube. I: The linear approximation for long waves," *Phil. Mag.*, vol. 46, pp. 199–221, 1955.

[47] A. Savitzky and M. J. E. Golay, "Smoothing and differentiation of data by simplified least squares procedures," *Anal. Chem.*, vol. 36, no. 8, pp. 1627–1639, 1964.

[48] S. S. M. Lai, B. Y. S. Yiu, A. K. K. Poon, and A. C. H. Yu, "Design of anthropomorphic flow phantoms based on rapid prototyping of compliant vessel geometries," *Ultrasound Med. Biol.*, vol. 39, no. 9, pp. 1654–1664, 2013.

[49] J. A. Jensen, H. Holten-Lund, R. T. Nilsson, M. Hansen, U. D. Larsen, R. P. Domsten, B. G. Tomov, M. B. Stuart, S. I. Nikolov, M. J. Pihl, Y. Du, J. H. Rasmussen, and M. F. Rasmussen, "SARUS: A synthetic aperture real-time ultrasound system," *IEEE Trans. Ultrason., Ferroelec., Freq. Contr.*, vol. 60, no. 9, pp. 1838–1852, 2013.

[50] C. A. Villagomez-Hoyos, M. B. Stuart, and J. A. Jensen, "Adaptive multi-lag for synthetic aperture vector flow imaging," in *Proc. IEEE Ultrason. Symp.*, 2014, pp. 1722–1725.

[51] M. J. Pihl, M. B. Stuart, B. G. Tomov, M. F. Rasmussen, and J. A. Jensen, "A transverse oscillation approach for estimation of three-dimensional velocity vectors. Part II: Experimental validation," *IEEE Trans. Ultrason., Ferroelec., Freq. Contr.*, vol. 51, no. 10, pp. 1608–1618, 2014.

[52] T. J. Donohue, M. J. Kern, F. V. Aguirre, R. G. Bach, T. Wolford, C. A. Bell, and J. Segal, "Assessing the hemodynamic significance of coronary artery stenosis: Analysis of translesional pressure-flow velocity relations in patients," *J. Am. Coll. Cardiol.*, vol. 22, no. 2, pp. 449–458, 1993.

[53] D. F. Young, N. R. Cholvin, and A. C. Roth, "Pressure drop across artificially induced stenoses in the femoral arteries of dogs," *Circ Res.*, vol. 36, pp. 735–743, 1975.

[54] K. L. Gould, "Quantification of coronary artery stenosis in vivo," *Circ Res.*, vol. 57, no. 3, pp. 341–353, 1985.

Paper III

Non-invasive measurement of pressure gradients using ultrasound

Jacob Bjerring Olesen, Marie Sand Traberg, Michael Johannes Pihl, and Jørgen Arendt Jensen

Proceeding of SPIE Ultrasound Imaging. Symp., Vol. 8675, p. 11,

Accepted for oral presentation in Orlando, Florida, United States, 2013.

Non-invasive measurement of pressure gradients using ultrasound

Jacob Bjerring Olesen, Marie Sand Traberg, Michael Johannes Pihl and Jørgen Arendt Jensen

Center for Fast Ultrasound Imaging, Dept. of Elec. Eng., Bldg. 349,
Technical University of Denmark, DK-2800 Kgs. Lyngby, Denmark.

ABSTRACT

A non-invasive method for estimating 2-D pressure gradients from ultrasound vector velocity data is presented. The method relies on in-plane vector velocity fields acquired using the Transverse Oscillation method. The pressure gradients are estimated by applying the Navier-Stokes equations for isotropic fluids to the estimated velocity fields. The velocity fields were measured for a steady flow on a carotid bifurcation phantom (Shelley Medical, Canada) with a 70% constriction on the internal branch. Scanning was performed with a BK8670 linear transducer (BK Medical, Denmark) connected to a BK Medical 2202 UltraView Pro Focus scanner. The results are validated through finite element simulations of the carotid flow model where the geometry is determined from MR images. This proof of concept study was conducted at nine ultrasound frames per second. Estimated pressure gradients along the longitudinal direction of the constriction varied from 0 kPa/m to 10 kPa/m with a normalized bias of -9.1% for the axial component and -7.9% for the lateral component. The relative standard deviation of the estimator, given in reference to the peak gradient, was 28.4% in the axial direction and 64.5% in the lateral direction. A study made across the constriction was also conducted. This yielded magnitudes from 0 kPa/m to 7 kPa/m with a normalized bias of -5.7% and 13.9% for the axial and lateral component, respectively. The relative standard deviations of this study were 45.2% and 83.2% in the axial and lateral direction, respectively.

Keywords: Medical ultrasound, Pressure gradients, Flow, Stenosis, Navier-Stokes equation

1. INTRODUCTION

Local pressure gradients in hemodynamics provide important information for diagnosing various cardiovascular diseases such as atherosclerosis.[1] The gradients are used as an indication on how changes in the flow caused by plaque formation affects the risk of embolism. Today, pressure gradients are measured by means of catheters inserted into the femoral artery and threaded to the region of interest. Although this procedure is reported reliable and of low risk,[2] it remains an invasive procedure that exposes the patients to ionizing radiation during angiography guidance. Furthermore, the presence of the catheter causes inconvenient disturbances to the surrounding fluid flow, thereby affecting the pressure field it is measuring. A less invasive method for measuring the local pressure gradients was proposed by Fairbank and Scully.[3] The method relies on injecting contrast agent microbubbles into the circulatory system and measure the frequency shift in the scattered spectrum as ultrasonic waves are applied. A range of other methods for estimating pressure changes has also been devised based on the injection of microbubbles.[4–9] Despite the less invasive procedure, it still requires the injection of microbubbles. Furthermore, it only provides a short time window for imaging as the bubbles are taken up by the liver or ruptures due to the acoustic pressure field produced by the ultrasound transducer.

In 1976, Holen *et al.*[10] suggested a non-invasive method for estimating local pressure gradients by using the peak systolic blood velocity measured from ultrasound data. The velocity was used as input to a modified version of the orifice equation introduced by Golin[11] that related the peak velocity to the pressure gradient along the region of interest. This non-invasive assessment of the pressure gradients, however, suffers from major flaws as it is solely dependent on a single velocity estimate and does not take complex flow patterns into account. Deducing a pressure gradient based on a single velocity estimate makes it sensitive to a series of unwanted hemodynamic factors that are uncorrelated to the actual constrictions effect on the peak velocity, e.g. abnormal cardiac output caused by cardiomyopathy. Hence, a more refined method for estimating the pressure gradients was suggested in 2003 by Ohtsuki and Tanake.[12] This method also relied on ultrasound data, but the estimated pressure gradients were instead based on a simplified version of the Navier-Stokes equation. The Navier-Stokes equation describes

Medical Imaging 2013: Ultrasonic Imaging, Tomography, and Therapy, edited by Johan G. Bosch, Marvin M. Doyley,
Proc. of SPIE Vol. 8675, 86750G · © 2013 SPIE · CCC code: 1605-7422/13/$18 · doi: 10.1117/12.2006732

the motion of fluids and provides easy access to information regarding the temporal and spatial pressure variations in the system, making it suitable for time-varying flow phenomena having complex features. Ohtsuki and Tanake assumed the viscosity to be negligible along with the external forces on the system. In addition, they assumed that the velocity normal to the scan plane was zero. The suggested method uses the axial velocity component found from spectral Doppler to deduce a measurement of the transverse velocity component and then inputs both velocity components in the Navier-Stokes equation. Applying the two in-plane velocity components to the Navier-Stokes equation offers the advantage of including spatial pressure variations into the estimator, unlike the method suggested by Holen *et al.*[10] A shortcoming of the method suggested by Ohtsuki and Tanake[12] is that the estimated pressure is solely based on the detected axial velocity, making the estimator inadequate for flow parallel to the ultrasound transducer. The method cannot measure the flow perpendicular to the beam propagation direction independently of angle and the axial velocity, which makes it insufficient for estimating pressure gradients in complex flow phenomena, such as vortexes that are common in hemodynamics.

Magnetic resonance imaging (MRI) is able to produce simultaneous velocity measurements in all three spatial directions[13] , which enables derivation of pressure gradients without uncertainties related to the assumptions of out-of-plane motion.[14] Most examples in the literature on deducing pressure gradients from MRI data are derived using the Navier-Stokes equation.[14–17] The high spatial resolution in MRI forms a good foundation for calculating the convective acceleration used in the estimator. However, the temporal resolution is poor compared to ultrasound imaging. Often the temporal variation has to be acquired from several hundred cardiac cycles through ECG gating. This poses a significant downside to MRI, when performing pressure measurements on dynamic flow systems such as the cardiovascular system. Furthermore, MRI requires a long acquisition time when performing velocity measurements and is far more expensive than ultrasound imaging. A non-invasive alternative that addresses the mentioned issue is, thus, needed.

This paper presents pressure gradients estimated from ultrasound vector velocity data by exploiting the Transverse Oscillation (TO) method developed by Jensen and Munk[18] and Anderson[19] who suggested a similar approach. The TO method is unlike the method proposed by Ohtsuki and Tanake[12] able to estimate the two spatial velocity components within the ultrasound scan plane independently of each other. This allows for determination of for examples flow vortices or other complex features that are likely to be present in a constricted flow pattern. The method employed for estimating the gradients have initially been suggested by Henze.[20] The purpose of this paper is to compare pressure gradients derived from ultrasound data to pressure gradients obtained using fluid-simulation software. The idea is to show that pressure gradients can be measured non-invasively using ultrasound to replace or supplement catheterization. The presented results are all obtained from data recorded on a flow model that imitates a constricted carotid artery. The studies are conducted for a constant-flow system to verify the feasibility of the suggested method. Pressure gradients are estimated from ultrasound vector velocities using the Navier-Stokes equation and compared to a finite element simulation of the flow model. The geometry of the flow simulation model is reproduced using MRI data, thereby providing identical flow domains in measurement and simulation.

2. ESTIMATING PRESSURE GRADIENTS

The following section presents the method for calculating pressure gradients based on the Navier-Stokes equation using ultrasound vector velocity data.

The Navier-Stokes equation for an isotropic incompressible Newtonian fluid is given by

$$\rho\left[\frac{\partial \mathbf{v}}{\partial t} + \mathbf{v}\cdot\nabla\mathbf{v}\right] = -\nabla p + \rho\mathbf{g} + \mu\nabla^2\mathbf{v}. \tag{1}$$

The equation describes the development of fluid velocity $\mathbf{v}(v_x, v_y, v_z)$ by relating the body forces acting on the isotropic fluid volume to its acceleration and density, where ρ is the density of the fluid and μ its viscosity. The left-hand terms sum the local $\frac{\partial \mathbf{v}}{\partial t}$ and convective acceleration $\mathbf{v}\cdot\nabla\mathbf{v}$ of the velocity, where ∇ is the spatial differential operator $(\frac{\partial}{\partial x}, \frac{\partial}{\partial y}, \frac{\partial}{\partial z})$. The right-hand side sum-up the surface and volume forces, which include the desired pressure gradient $-\nabla p$, as well as a gravitational force $\mathbf{g}$ acting on the fluid volume and a viscous drag caused by the viscosity of the fluid $\mu\nabla^2\mathbf{v}$, where $\nabla^2\mathbf{v}$ is the Laplacian of the velocity. For clinical applications, the effect of the viscous term in (1) can be omitted as this has no significant influence on flow in larger vessels.[21,22] A patient undergoing an ultrasound scan is usually placed in a horizontal position, so the gravitational term can be neglected as well. The pressure gradient is, thus, directly linked to the acceleration field of the fluid

$$\nabla p = -\rho\left[\frac{\partial \mathbf{v}}{\partial t} + \mathbf{v}\cdot\nabla\mathbf{v}\right]. \tag{2}$$

As the conducted study considers flow that is in-variant with respect to time, no changes in the transient acceleration occur, thus

$$\nabla p = -\rho[\mathbf{v}\cdot\nabla\mathbf{v}]. \tag{3}$$

2.1 Implementation the estimator on ultrasound data

Equation (3) states that all three vector components of $\mathbf{v}(v_x, v_y, v_z)$ must be known to estimate the pressure gradient $-\nabla p$. Using the TO approach the scanner is able to measure the two-dimensional in-plane velocity vector[23,24] $\mathbf{v} = (v_x, 0, v_z)$. The method is therefore developed assuming that the out-of-plane velocity v_y is zero. Though, the method can easily be extended to use full three-dimensional data.

Assuming that v_y is zero makes two-dimensional pressure gradients obtainable in the presented set-up. The in-plane vector components of the pressure gradients are expressed here in rectangular coordinates:

$$\begin{bmatrix} \dfrac{\partial p}{\partial x} \\[2ex] \dfrac{\partial p}{\partial z} \end{bmatrix} = -\rho \begin{bmatrix} v_x\dfrac{\partial v_x}{\partial x} + v_z\dfrac{\partial v_x}{\partial z} \\[2ex] v_x\dfrac{\partial v_z}{\partial x} + v_z\dfrac{\partial v_z}{\partial z} \end{bmatrix}. \tag{4}$$

The derivatives in (4) are calculated from vector velocity ultrasound data using a finite central difference approximation.[25] The in-plane pressure gradient components are here calculated discretely for each position in the scan plane:

$$\frac{\Delta\mathbf{P}(i,j)}{\Delta x} \simeq -\rho \begin{bmatrix} \mathbf{V}_x(i,j)/2\Delta x \\ \mathbf{V}_z(i,j)/2\Delta z \end{bmatrix} \cdot \begin{bmatrix} \mathbf{V}_x(i-1,j) - \mathbf{V}_x(i+1,j) \\ \mathbf{V}_x(i,j-1) - \mathbf{V}_x(i,j+1) \end{bmatrix}$$

and

$$\frac{\Delta\mathbf{P}(i,j)}{\Delta z} \simeq -\rho \begin{bmatrix} \mathbf{V}_x(i,j)/2\Delta x \\ \mathbf{V}_z(i,j)/2\Delta z \end{bmatrix} \cdot \begin{bmatrix} \mathbf{V}_z(i-1,j) - \mathbf{V}_z(i+1,j) \\ \mathbf{V}_z(i,j-1) - \mathbf{V}_z(i,j+1) \end{bmatrix}, \tag{5}$$

respectively. Here $\mathbf{V}_x$, $\mathbf{V}_z$ and $\frac{\Delta\mathbf{P}}{\Delta x}$, $\frac{\Delta\mathbf{P}}{\Delta z}$ denote two-dimensional fields of discrete vector velocity components and pressure gradient components, respectively. The position in the field is given by (i, j), while Δx and Δz is the sampling interval of the velocity field in the axial and lateral direction, respectively. The calculated pressure gradients are low-pass filtered using a normalized Hann window $\mathcal{H}_{2D}$ to reduce noise from the numerical differentiation. The 2-D window is designed as:

$$\mathcal{H}_{2D} = 0.5\Big(1 - \cos\big(2\pi\frac{l'}{L-1}\big)\Big)0.5\Big(1 - \cos\big(2\pi\frac{l}{L-1}\big)\Big), \tag{6}$$

where l is a vector of integers from 0 to L-1 and L is the length of the window. The calculated gradient fields are filtered by convolving their individual vector components with the normalized Hann window as:

$$\frac{\Delta\mathbf{P}_F(i,j)}{\Delta x} = \frac{\mathcal{H}_{2D}}{\sum\limits_{r,s=1}^{N}\mathcal{H}_{2D}(r,s)} * \frac{\Delta\mathbf{P}(i,j)}{\Delta x} \quad \text{and} \quad \frac{\Delta\mathbf{P}_F(i,j)}{\Delta z} = \frac{\mathcal{H}_{2D}}{\sum\limits_{r,s=1}^{N}\mathcal{H}_{2D}(r,s)} * \frac{\Delta\mathbf{P}(i,j)}{\Delta z}. \tag{7}$$

Table 1: Measurement settings for acquiring data

	Parameter	Value
BK Scanner	Transducer	Linear array 8670
	Mode	Carotid TVI
	Pulse repetition frequency	1.3 kHz
	Frame rate	18 Hz
	Centre frequency	5 MHz
	No. frames	50
Flow setup	Volumetric flow rate	1.0 cm^3/s (constant)
	Inner radius	0.6 cm
	Constriction	70%
	Depth to constriction	2.3 cm
	Fluid density	1,037 kg/m^3
	Viscosity	$4.1 \cdot 10^{-3}$ Pa·s

3. DATA ACQUISITION

The following section describes the data acquisition for estimating and validating the pressure gradients during constant flow conditions.

A BK Medical 2202 UltraView Pro Focus scanner (BK Medical, Herlev, Denmark) equipped with an UA2227 research interface[26] is used for obtaining ultrasound RF data. A C70-SSEA flow phantom (Shelley Medical Imaging Technologies, Toronto, Canada) is scanned using a BK8670 linear array transducer at 18 frames per second. The flow phantom is a model of a carotid artery having a constriction at the beginning of the internal carotid artery that reduces the cross-sectional area of the lumen by 70%. The flow phantom is embedded in agar to mimic the characteristics of human tissue, and it is encased in an air tight acrylic box with an acoustic window making it compatible for ultrasound imaging as well as MRI. A constant flow profile driven by a CompuFlow 1000 Flow system (Shelley Medical Imaging Technologies, Toronto, Canada) is set for the phantom at a flow rate of 1.0 ml/s. Blood mimicking fluid is used with a density of 1,037 kg/m^3 and a viscosity of 4.1 mPa·s. A summary of the acquisition settings is listed in Table 1.

The reliability of the produced pressure gradients is evaluated through comparison to a finite element model. The geometry of this model is constructed from MRI data of the flow phantom performed at the Department of Diagnostic Radiology at Rigshospitalet, Denmark, using a 3 Tesla Magnetom Trio scanner (Siemens, Munich, Germany). The MRI data are loaded into the commercial segmentation-software, ScanIP (Simpleware Ltd. Exeter, UK), which is used to construct the skeleton of the phantom's fluid domain. The constructed skeleton is exported to Comsol (v4.2a, Stockholm, Sweden) as a mesh of tetrahedrons. The mesh is smoothed by a Gaussian filter (dimensions: $1.00 \times 0.01 \times 0.01$ mm) to avoid any inexpedient sharp edges that otherwise could lead to computational divergence. Such sharp edges occur, if the spatial resolution in the scan images is smaller than the resolution required by Comsol. The mesh consists of more than 600,000 tetrahedrons that are especially dense in the constricted area of the phantom to ensure a high spatial resolution in the this particular region (mesh size: 0.15 mm). A summary of the settings used for creating the geometry of the simulation model is listed in Table 2.

4. DERIVATION OF PRESSURE GRADIENTS

The following section describes how pressure gradient maps are estimated based on the vector velocity estimates.

A vector velocity map of the flow through the constricted region of the phantom is estimated using the ultrasound vector velocity data. They are calculated by employing the TO method as described by Jensen and Munk[18] and by using the TO estimation method,[27] yielding the two in-plane velocity components of the ultrasound beam. A low-pass filter is applied to the velocity estimates before calculating the convective acceleration to strengthen the robustness of the estimates. The filter is designed as in (6) for L= 5, corresponding to an axial length of 0.07 mm and a lateral width of 0.58 mm. Furthermore, the velocity estimates are interpolated to

Table 2: Measurement settings for acquiring validation data

	Parameter	Value
Magnetic resonance	Scanner	Siemens Magnetom Trio
	Strength	3.0 Tesla
	Scan sequence	TOF 3-D Multi-slab
	Voxel size	$0.7 \times 0.7 \times 1.0$ mm
ScanIP	Up-sampling	(x,y,z) = (0.9, 0.15, 0.15) mm
	Filter size	(x,y,z) = (1.0, 0.01, 0.01) mm
	Mesh size	0.15 mm

improve the visual quality of the image, yielding an increase in the number of data elements by a factor of three. As the study is conducted on a constant-flow system, every estimated velocity frame is roughly the same, thus the mean over 50 ultrasound frames is calculated and used for deriving the pressure gradients. The pressure gradients are then calculated using (5) and (7).

The imported Comsol-mesh forming the geometrical structure of the simulation model is assigned conditions that mimic the actual flow conditions in the experimental set-up. These conditions are listed in Table 3. Stationary laminar flow of an incompressible fluid is selected. The initial values of the fluids velocity field and its pressure is set to zero, while having a forced laminar flow condition at the inlet of the model. The peak velocity across the constriction is set to 0.15 m/s, equivalent to the velocity estimated from the ultrasound data.

The result of the suggested pressure gradient estimator is investigated by considering its average standard deviation $\hat{\sigma}$ and its bias $\hat{\mathbf{B}}$ in reference to the simulated data. They are calculated as:

$$\hat{\sigma} = \frac{1}{\hat{PG}_{max}} \sqrt{\frac{1}{N} \sum_{m=1}^{N} \boldsymbol{\sigma}_t^2(m)} \qquad \text{and} \qquad \hat{\mathbf{B}} = \frac{1}{\hat{PG}_{max} N} \sum_{m=1}^{N} \boldsymbol{\mu}_{est}(m) - \boldsymbol{\mu}_{sim}(m) \quad ,$$

where N is the number of data points along the spatial path that is investigated and $\boldsymbol{\mu}_{est}$ is the mean of these points. The standard deviation of the estimated gradient fields $\boldsymbol{\sigma}_t$ is averaged along the investigated path. The simulated data along the inspected path is denoted $\boldsymbol{\mu}_{sim}$. Both, standard deviation and bias are normalized to the peak mean estimated pressure gradient, $\hat{PG}_{max} = \max(\boldsymbol{\mu}_{est})$.

Table 3: Simulation settings in Comsol

	Parameter	Value
Study	Flow	Laminar
	Geometry	Three dimensional
	Stationary solver	Direct, MUMPS
Fluid properties	Compressibility	Incompressible
	Density	1,037 kg/m^3
	Viscosity	$4.1 \cdot 10^{-3}$ Pa·s
Initial conditions	Velocity field	(x,y,z) = (0,0,0) m/s
	Pressure	0 Pa
Inlet conditions	Inflow	Laminar
	Flow rate	2 cm^3/s
	Entrance length	1 m
Outlet conditions	Outflow	Pressure, no viscous stress
	Pressure	0 Pa
Wall	Condition	No-slip

5. RESULTS

The following section presents the results of the pressure gradient estimator. The results are based on vector velocity data acquired using a commercial ultrasound scanner at 18 frames per second. The presented results are all captured from the carotid flow phantom at the site of the constriction, shown in Fig. 1. It also shows the mesh of the simulation model superimposed onto the B-mode image. The estimated and simulated results will throughout the section be discussed as they are presented.

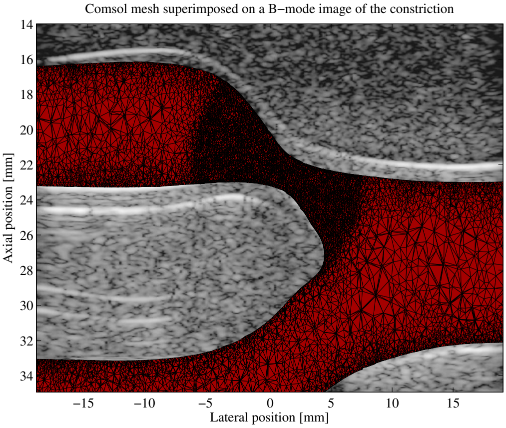

Figure 1: B-mode image of the carotid flow phantom at the site of the constriction plotted along with the mesh skeleton of the simulation model.

Presentation of the pressure gradients

A vector velocity map of the flow through the constricted area of the phantom is plotted in Fig. 2 along with the estimated and simulated pressure gradients. The fluid flows from right to left and reaches its peak velocity at the center of the constriction with 0.15 m/s. The center plot in Fig. 2 shows the estimated pressure gradients that are calculated using the velocities in the left plot. The plot to the right shows the simulated pressure gradients.

The background color indicates the magnitude of the arrows, while these show the direction and size of either the fluid velocity or of the pressure gradients. The two gradient plots display arrows that tend to point away from the center of the constriction, indicating that a low pressure is present here, as a gradient always point in direction of increasing values. The white-dotted lines on the center plot and on the right plot indicates the positions used for the quantitative plots shown in the next section.

Quantitative results of pressure gradient estimator

Quantitative results of the pressure gradient estimator are obtained by investigating its bias and standard deviation. These are calculated along the dotted lines in the two plots to the right of Fig. 2 for the axial and lateral component of the gradients.

Fig. 3 shows the mean magnitude of the axial and lateral pressure gradients along the longitudinal direction for 50 frames. It also shows the range of one standard deviation given at a frame rate of 9 Hz. The blue line shows the simulated pressure gradients along the same path.

The estimator produced pressure gradients of magnitudes varying from 0 kPa/m to 10 kPa/m. It has a normalized bias of -9.1% for the axial component and -7.9% for the lateral component with a standard deviation given in reference to the peak gradient of 28.4% and 64.5%, respectively. Increasing the number of velocity frames used in the estimator will improve the standard deviation of the estimates. Fig. 4 shows the effect of this by plotting the standard deviation as a function of averaging-time used by the estimator to produce a single two-dimensional

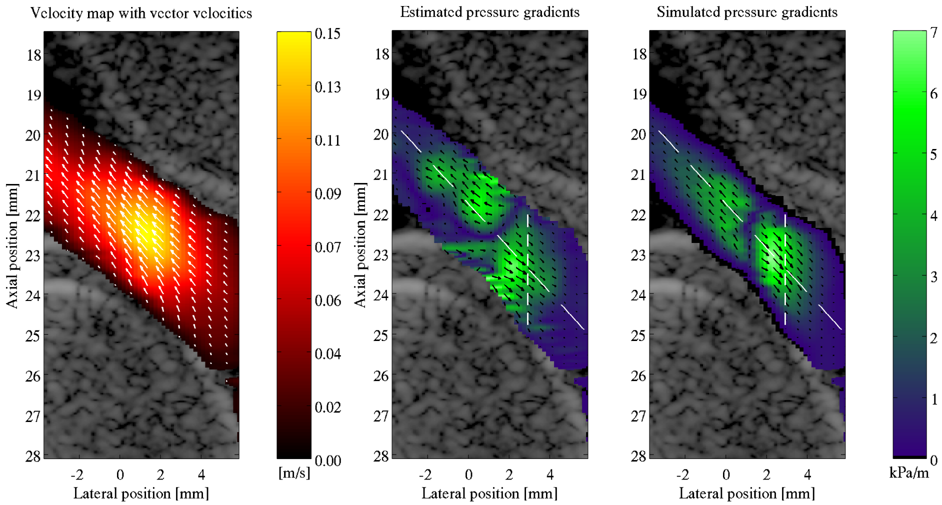

Figure 2: Vector velocity map along with the estimated and simulated pressure gradients. The plot to the left shows a vector velocity map of the blood mimicking fluid that flows through the constriction from right to left. The center plot show the pressure gradients estimated from vector velocity data, while the figure to the right show the simulated gradients.

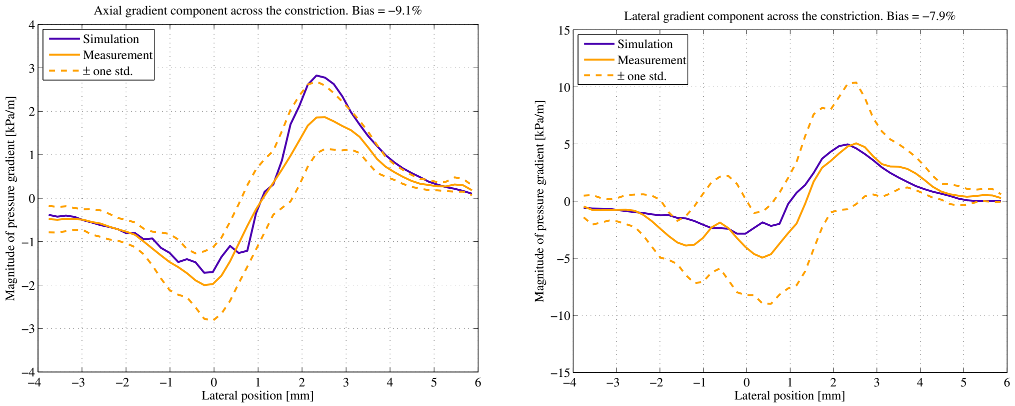

Figure 3: Estimated and simulated pressure gradients along the longitudinal direction of the constriction. The two graphs show the axial and lateral component of the pressure gradient, respectively.

pressure gradient field. More velocity frames are averaged as the time increases, making the estimates more robust in a noisy environment. However, the improved standard deviation is at the expense of temporal resolution as the estimators true frame rate drops proportional to the increase in averaging-time.

Quantitative results along the vertical white-line in Fig. 2 are presented in Fig. 5. The graphs in Fig. 5 present magnitudes of pressure gradient varying from 0 kPa/m to 7 kPa/m. A normalized bias was found for the axial component of -5.7% and for the lateral component it was 13.9% with a standard deviation of 45.2% and 83.2%. The spikes in the standard deviation seen to the right of the lateral position 24 mm, are artefacts caused by boundary effects. These artefacts can also be spotted at the vessel wall in the center plot of Fig.2.

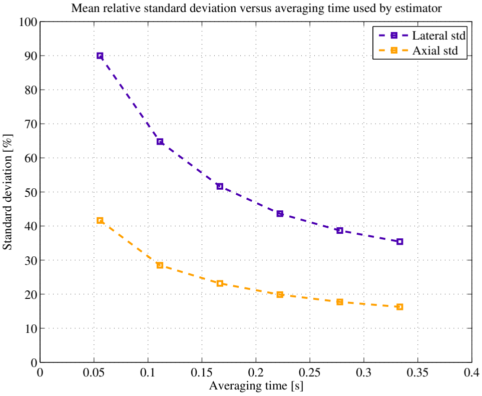

Figure 4: Mean standard deviation of the estimator given as a function of averaging-time used by the estimator to produce a single two-dimensional pressure gradients field.

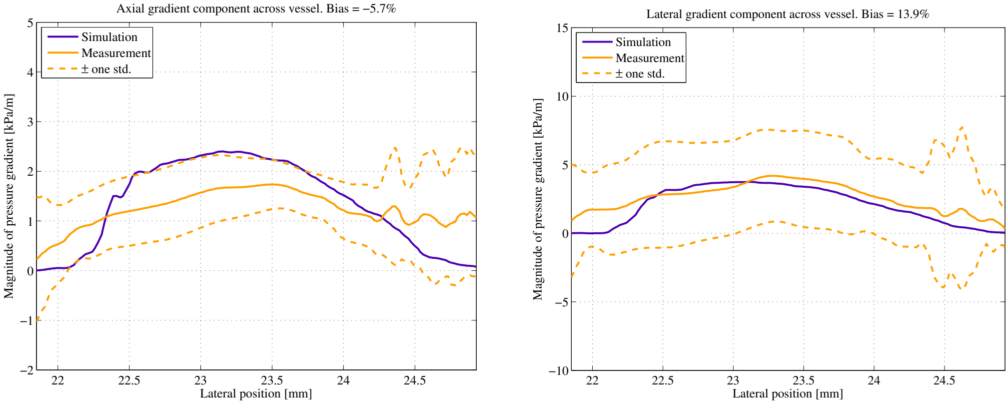

Figure 5: Estimated and simulated pressure gradients along the cross-sectional direction of the constriction. The two graphs show the axial and lateral component of the pressure gradient, respectively.

6. DISCUSSION

A non-invasive method for estimating pressure gradients using ultrasound vector velocity data has been presented. The method has managed to produce pressure gradients within fluid flow that has a maximum bias of -9.1% and 13.9% in the axial and lateral direction, respectively. The standard deviation of the estimator varied from 24.4–42.2% in the axial direction and from 64.5–83.2% in the lateral direction.

Fig. 2 shows pressure gradients that tend to point away from the area of high velocities. This observation is in accordance with expectations as there exist a clear physical relationship between fluids pressure and its velocities. A way of clarifying this relationship is to consider the energy of the flow system for which no energy is exchanged between the fluid and the vessel walls, meaning that the energy level is constant throughout the system. The total energy is composed by the sum of potential energy and kinetic energy. Since the gravitational force can be neglected, the only force giving rise to the potential energy is pressure. As the fluid flows into the constriction it starts to accelerate to keep up a constant flow rate and the kinetic energy increases. Since no energy is put into the flow system from its surroundings, the increase in kinetic energy must come from the potential energy, thereby decreasing the pressure in areas of high velocities. As the fluid flows past the constriction it decelerates, turning kinetic energy back into potential energy. This explains why the gradients tend to point away from the site of the highest velocities as pressure most be lowest there. The assumption of a constant energy level is of course not entirely true, since energy dissipation will occur as the fluid is not inviscid. However, the amount of energy dissipation is very limited in reference to the total change in energy that exist along the constriction.

No previous studies on the subject have managed to estimate and validate 2-D pressure gradients from vector velocity data obtained using the TO approach. Unlike the method suggested by Holen *et al.*,[10] this method is able to take convective fluid accelerations into consideration making it suitable for more complex flow phenomena. Every term in the estimator is calculated relative to neighboring velocity estimates, yielding gradients that are independent of systemic flow factors, such as abnormalities in the cardiac output. The proposed method also offers the advantage of including temporal pressure changes, however, this was not considered in this paper as constant flow was studied. Yet, being able to include temporal changes is essential for studies on the cardiovascular system. Such studies usually require a frame rate of approximately 20 Hz. Furthermore, the method can easily be extended to use full three-dimensional data. The estimator presented in this study produced images of pressure gradients at a frame rate of 9 Hz, since two velocity frames, sampled at 18 Hz, were used for calculating one frame of pressure gradients. A way of increasing this frame rate, while maintaining the presented precision, is to shrink the width of the colorbox used during the acquisition of velocity ultrasound data, as fewer pulses are required for covering a narrower region. A reason for the high standard deviation is found in the poor spatial resolution of ultrasound imaging, which gives rise to a significant noise contribution during the numerical differentiation of the velocity fields. However, the lack in spatial resolution can be considered counterbalanced by the temporal resolution, which is one of the most significant advantages in ultrasound imaging compared to MRI. The relative high temporal resolution is the result of a low data acquisition time enabling the possibilities of producing real-time pressure gradient images using ultrasound. This will give the physician a tool for viewing intra-vascular changes in pressure as they occur, for example during a cardiac cycle or changes observed over several cycles. More importantly, the physician would no longer have to insert catheters into the blood vessel to obtain a map of the pressure changes. A shortcoming of the proposed method is its lacking ability to estimate the out-of-plane velocity component v_y. This makes the estimator vulnerable in complex flow environments that has vector velocity components in all three spatial direction. However, Pihl and Jensen[28,29] recently presented a novel technique for measuring the out-of-plane velocity using an ultrasound system. Exploiting this technique, would yield three-dimensional vector velocity fields that could easily be included in the suggested pressure gradient estimator, leaving no-need for assuming that v_y is zero.

7. CONCLUSION

A non-invasive method for deriving pressure gradients using vector velocity ultrasound data has been presented. The pressure gradients were derived using the Navier-Stokes equation for incompressible fluids. The vector velocities inserted into the equation were estimated using the TO method yielding the two in-plane velocity components. The obtained pressure gradients were evaluated by comparison to a finite element simulation model, which geometry was obtained from MRI data. The employed method has successfully managed to produce pressure gradients within a constricted flow phantom of magnitudes varying from 0 kPa/m to 10 kPa/m. Proof of concept studies conducted along the longitudinal direction of a constricted flow phantom showed a normalized bias of -9.1% for the axial component and -7.9% for the lateral component with precision given in reference to the peak gradient of 28.4% and 64.5%, respectively. Studies made across the constriction were also conducted giving a normalized bias of -5.7% for the axial component and 13.9% for the lateral component at a precision of 45.2% and 83.2%.

ACKNOWLEDGMENTS

The authors would like the thank Jesper Rohde at BK Medical, Denmark, for putting their flow phantom at our disposal and Carsten Thomsen at Rigshospitalet, Denmark, for performing the MRI scans. The presented work has been financially supported by grant 024-2008-3 from the Danish Advanced Technology Foundation, BK Medical Aps, Denmark and Radiometer A/S, Denmark.

REFERENCES

[1] Baim, D. S. and Grossman, W., [*Grossman's cardiac catheterization, angiography, and intervention*], Lippincott Williams & Wilkins publishers (2000).

[2] Skinner, J. S. and Adams, P. C., "Outpatient cardiac catheterisation," *Int. J. Cardiol.* **53**, 209–219 (March 1996).

[3] Fairbank, W. M. and Scully, M. O., "A new noninvasive technique for cardiac pressure measurements: resonant scattering of ultrasound from bubbles," *IEEE Trans. Biomed. Eng.* **24**, 107–110 (1977).

[4] Bouakaz, A., Frinking, P. J., de Jong, N., and Bom, N., "Noninvasive measurement of the hydrostatic pressure in a fluid-filled cavity based on the disappearance time of micrometer-sized free gas bubbles," *Ultrasound Med. Biol.* **25**, 1407–1415 (1999).

[5] Shi, W. T., Forsberg, F., Raichlen, J. S., and Needleman, L., "Pressure dependence of subharmonic signals from contrast microbubbles," *Ultrasound Med. Biol.* **25**, 275–283 (1999).

[6] Adam, D., Sapunar, M., and Burla, E., "On the relationship between encapsulated ultrasound contrast agent and pressure," *Ultrasound Med. Biol.* **31**, 673–686 (2005).

[7] Forsberg, F., Liu, J.-B., Shi, W. T., Furuse, J., Shimizu, M., and Goldberg, B. B., "In vivo pressure estimation using subharmonic contrast microbubble signals: Proof of concept," *IEEE Trans. Ultrason., Ferroelec., Freq. Contr.* **52**(4), 581–583 (2005).

[8] Andersen, K. S. and Jensen, J. A., "In vitro measurement of ambient pressure changes using a realistic clinical setup," in [*Proc. IEEE Ultrason. Symp.*], 1096–1099 (2008).

[9] Forsberg, F., Dave, J., Halldorsdottir, V. G., Leodore, L. M., Lin, F., Hall, A. L., and Thomenius, K., "Applying real-time noninvasive pressure estimation obtained from subharmonic contrast microbubble signals," *Proc. IEEE Ultrason. Symp.* , 1694–1697 (2008).

[10] Holen, J., Aaslid, R., and Landmark, K., "Determination of pressure gradient in mitral stenosis with a non-invasive ultrasound Doppler technique," *Acta med. scand.* **32**, 455–460 (1976).

[11] Gorlin, R. and Gorlin, S. G., "Hydraulic formula for calculation of the area of the stenotic mitral valve, other cardiac valves, and central circulatory shunts," *Am. Heart J.* **41**, 1–29 (January 1951).

[12] Ohtsuki, S. and Tanaka, M., "Doppler pressure field deduced from the Doppler velocity field in an observation plane in a fluid," *Ultrasound Med. Biol.* **29**(10), 1431–1438 (2003).

[13] Kilner, P. J., Yang, G. Z., Mohiaddin, R. H., Firmin, D. N., and Longmore, D. B., "Helical and retrograde secondary flow patterns in the aortic arch studied by three-directional magnetic resonance velocity mapping," *Circulation* **88**(5), 2235–2247 (1993).

[14] Bock, J., Frydrychowicz, A., Lorenz, R., Hirtler, D., Barker, A. J., Johnson, K. M., Arnold, R., Burkhardt, H., Hennig, J., and Markl, M., "In vivo noninvasive 4D pressure difference mapping in the human aorta: phantom comparison and application in healthy volunteers and patients," *Magn. Reson. Med.* **66**(4), 1079–1088 (2011).

[15] Tasu, J. P., Mousseaux, E., Delouche, A., Oddou, C., Jolivet, O., and Bittoun, J., "Estimation of pressure gradients in pulsatile flow from magnetic resonance acceleration measurements," *Magn. Reson. Med.* **44**(1), 66–72 (2000).

[16] Thompson, R. B. and McVeigh, E. R., "Fast measurement of intracardiac pressure differences with 2D breath-hold phase-contrast MRI," *Magnetic Resonance in Medicine* **49**(6), 1056–1066 (2003).

[17] Herment, A., Besson, G., Pellot-Barakat, C., and Frouin, F., "Estimation of pressure gradient images from velocity encoded MR acquisitions," *Computers in Cardiology* **35**, 933–936 (2008).

[18] Jensen, J. A. and Munk, P., "A New Method for Estimation of Velocity Vectors," *IEEE Trans. Ultrason., Ferroelec., Freq. Contr.* **45**, 837–851 (1998).

[19] Anderson, M. E., "Multi-dimensional velocity estimation with ultrasound using spatial quadrature," *IEEE Trans. Ultrason., Ferroelec., Freq. Contr.* **45**, 852–861 (1998).

[20] Henze, L., *Ultrasound flow estimation*, Master's thesis, Dept. of Elec. Eng., Technical University of Denmark, Lyngby, Denmark (2008).

[21] Prandtl, L., [*Essentials of Fluid Dynamics*], London: Blackie & Son (1952).

[22] Wood, N. B., "Aspects of fluid dynamics applied to the large arteries," *J. Theor. Biol.* **199**, 137–161 (April 1999).

[23] Evans, D. H., Jensen, J. A., and Nielsen, M. B., "Ultrasonic colour Doppler imaging," *Interface Focus* **1**, 490–502 (August 2011).

[24] Hansen, P. M., Pedersen, M. M., Hansen, K. L., Nielsen, M. B., and Jensen, J. A., "Demonstration of a vector velocity technique," *Ultraschall in Med* **32**, 213–5 (2011).

[25] Smith, G. D., [*Numerical Solution of Partial Differential Equations: Finite Difference Methods*], Oxford University Press (1985).

[26] Hemmsen, M. C., Nikolov, S. I., Pedersen, M. M., Pihl, M. J., Enevoldsen, M. S., Hansen, J. M., and Jensen, J. A., "Implementation of a versatile research data acquisition system using a commercially available medical ultrasound scanner," *IEEE Trans. Ultrason., Ferroelec., Freq. Contr.* **59**(7), 1487–1499 (2011).

[27] Jensen, J. A., "A New Estimator for Vector Velocity Estimation," *IEEE Trans. Ultrason., Ferroelec., Freq. Contr.* **48**(4), 886–894 (2001).

[28] Pihl, M. J. and Jensen, J. A., "3D velocity estimation using a 2D phased array," in [*Proc. IEEE Ultrason. Symp.*], 430–433 (2011).

[29] Pihl, M. J. and Jensen, J. A., "Measuring 3D velocity vectors using the transverse oscillation method," in [*Proc. IEEE Ultrason. Symp.*], IEEE (2012).

Paper IV

Non-invasive Measurement of Pressure Gradients in Pulsatile Flow using Ultrasound

Jacob Bjerring Olesen, Marie Sand Traberg, Michael Johannes Pihl,
Peter Møller Hansen, Michael Bachmann Nielsen, and Jørgen Arendt Jensen

*Proceeding of IEEE Internation Ultrasonics Symposium, p. 2022-2025,
Accepted for poster presentation in Prague, Czech Republic, 2013.*

10.1109/ULTSYM.2013.0516

Non-invasive Measurement of Pressure Gradients in Pulsatile Flow using Ultrasound

Jacob Bjerring Olesen[*], Marie Sand Traberg[*], Michael Johannes Pihl[*], Peter Møller Hansen[†],
Michael Bachmann Nielsen[†] and and Jørgen Arendt Jensen[*]

[*]Center for Fast Ultrasound Imaging, Dept. of Elec. Eng., Bldg. 349,
Technical University of Denmark, DK-2800 Kgs. Lyngby, Denmark
[†]Department of Radiology, Rigshospitalet, DK-2100 Copenhagen, Denmark

Abstract—**This paper demonstrates how pressure gradients in a pulsatile flow environment can be measured non-invasively using ultrasound. The proposed method relies on vector velocity fields acquired from ultrasound data. 2-D flow data are acquired at 18-23 frames/sec using the Transverse Oscillation approach. Pressure gradients are calculated from the measured velocity fields using the Navier-Stokes equation. Velocity fields are measured during constant and pulsating flow on a carotid bifurcation phantom and on a common carotid artery *in-vivo*. Scanning is performed with a 5 MHz BK8670 linear transducer using a BK Medical 2202 UltraView Pro Focus scanner. The calculated pressure gradients are validated through a finite element simulation of the constant flow model. The geometry of the flow simulation model is reproduced using MRI data, thereby providing identical flow domains in measurement and simulation. The proposed method managed to estimate pressure gradients that varied from 0 kPa/m–7 kPa/m during constant flow and from 0 kPa/m–200 kPa/m in the pulsatile flow environments. The estimator showed, in comparison to the simulation model, a bias of -9% and -8% given in reference to the peak gradient for the axial and lateral gradient component, respectively.**

I. INTRODUCTION

Local pressure gradients in hemodynamics can provide important information for diagnosing various cardiovascular diseases such as atherosclerosis [1]. The gradients can be used as an indication on how changes in the flow, for instance caused by plaque formation, affect the risk of embolism. Current measures of pressure gradients are acquired using catheters inserted into a larger artery and threaded to the region of interest. Although this procedure is reported reliable and of low risk, it remains an invasive procedure. A less invasive method for measuring the local pressure gradients was proposed by Fairbank and Scully [2]. The method relies on injecting contrast agent microbubbles into the circulatory system and measuring the frequency shift in the scattered spectrum as ultrasonic waves are applied. Despite the less invasive procedure, it still requires the injection of microbubbles. Furthermore, it only provides a short time window for imaging as the bubbles are taken up by the liver or rupture due to the acoustic pressure field produced by the ultrasound transducer. This paper presents pressure gradients estimated from ultrasound vector velocity data by exploiting the Transverse Oscillation (TO) method developed by Jensen and Munk [3] and Anderson [4] who suggested a similar approach. The TO method is able to estimate the two spatial velocity components within the ultrasound scan plane independently of each other. This allows for determination of flow patterns such as vortices or other complex features that are likely to occur when fluid passes through a constricted vessel. The purpose of this paper is to show that pressure gradients can be measured non-invasively using ultrasound with the long-term aim of replacing or assisting catheterization. The paper compares pressure gradients estimated using the Navier-Stokes equation to gradients that is simulated in a finite element model.

II. METHODS

The following section presents the method used for calculating pressure gradients from vector velocity data using the Navier-Stokes equation. For an isotropic incompressible Newtonian fluid it is given by

$$\rho\left[\frac{\partial \mathbf{v}}{\partial t} + \mathbf{v}\cdot\nabla\mathbf{v}\right] = -\nabla p + \rho\mathbf{g} + \mu\nabla^2\mathbf{v}. \qquad (1)$$

The equation describes the development of fluid velocity $\mathbf{v} = (v_x, v_y, v_z)$ by relating the body forces acting on the isotropic fluid volume to its acceleration and density, where ρ is the density of the fluid and μ its viscosity. The left-hand terms sum the local $\frac{\partial \mathbf{v}}{\partial t}$ and convective acceleration $\mathbf{v}\cdot\nabla\mathbf{v}$ of the velocity, where ∇ is the spatial differential operator $(\frac{\partial}{\partial x}, \frac{\partial}{\partial y}, \frac{\partial}{\partial z})$. The right-hand side sum-up the surface and volume forces, which include the desired pressure gradient $-\nabla p$, as well as a gravitational force $\mathbf{g}$ acting on the fluid volume and a viscous drag caused by the viscosity of the fluid $\mu\nabla^2\mathbf{v}$, where $\nabla^2\mathbf{v}$ is the Laplacian of the velocity. For clinical applications, the effect of the viscous term in (1) can be omitted as this has no significant influence on flow in larger vessels [5], [6]. A patient undergoing an ultrasound scan is usually placed in a horizontal position, so the gravitational term can be neglected as well. The pressure gradient is, thus, directly linked to the acceleration field of the fluid, which is derived from the velocity field $\mathbf{v}$:

$$\nabla p = -\rho\left[\frac{\partial \mathbf{v}}{\partial t} + \mathbf{v}\cdot\nabla\mathbf{v}\right]. \qquad (2)$$

Eq. (2) states that all three vector components of $\mathbf{v}$ must be known to estimate the pressure gradient $-\nabla p$. Using the TO approach and a 1-D linear array the two-dimensional in-plane velocity vector can be measured. The proposed method for estimating the pressure gradients is therefore developed assuming that the out-of-plane velocity v_y is zero, (though, the

$$
\begin{aligned}
\frac{\Delta\mathbf{P}(i,j,k)}{\Delta x} &\simeq \frac{-\rho}{2\Delta t}\Big(\mathbf{V}_x(i,j,k+1)-\mathbf{V}_x(i,j,k-1)\Big)-\rho\begin{bmatrix}\mathbf{V}_x(i,j,k)/2\Delta x\\ \mathbf{V}_z(i,j,k)/2\Delta z\end{bmatrix}\cdot\begin{bmatrix}\mathbf{V}_x(i-1,j,k)-\mathbf{V}_x(i+1,j,k)\\ \mathbf{V}_x(i,j-1,k)-\mathbf{V}_x(i,j+1,k)\end{bmatrix}\\
\frac{\Delta\mathbf{P}(i,j,k)}{\Delta z} &\simeq \frac{-\rho}{2\Delta t}\Big(\mathbf{V}_z(i,j,k+1)-\mathbf{V}_z(i,j,k-1)\Big)-\rho\begin{bmatrix}\mathbf{V}_x(i,j,k)/2\Delta x\\ \mathbf{V}_z(i,j,k)/2\Delta z\end{bmatrix}\cdot\begin{bmatrix}\mathbf{V}_z(i-1,j,k)-\mathbf{V}_z(i+1,j,k)\\ \mathbf{V}_z(i,j-1,k)-\mathbf{V}_z(i,j+1,k)\end{bmatrix}
\end{aligned}
\tag{3}
$$

method can be extended to use full three-dimensional data). The two in-plane vector components of the pressure gradient are calculated using a finite central difference approximation [7]. The equations in (3) show how the vector components are calculated discretely for each position in the scan plane at every frame. $\mathbf{V}_x$, $\mathbf{V}_z$ and $\frac{\Delta\mathbf{P}}{\Delta x}$, $\frac{\Delta\mathbf{P}}{\Delta z}$ denote two-dimensional fields of discrete vector velocity components and pressure gradient components, respectively. The index position within each field is given by (i, j), while k represents the field or scan frame being calculated. Each consecutive field is separated in time by $\frac{1}{framerate} = \Delta t$. The Δx and Δz are the sampling interval of the velocity field in the axial and lateral direction, respectively. The calculated pressure gradients in each scan frame are low-pass filtered using a 2-D Hann window $\mathcal{H}_{2D}$ to reduce noise from the numerical differentiation.

III. EXPERIMENTAL SETUP

A BK Medical 2202 UltraView Pro Focus scanner (BK Medical, Herlev, Denmark) equipped with an UA2227 research interface is used for obtaining ultrasound RF data. A C70-SSEA flow phantom (Shelley Medical Imaging Technologies, Toronto, Canada) is scanned using a BK8670 linear array transducer at 18 and 21 frames per second, depending on the study. The flow phantom models a carotid artery having a constriction at the beginning of the internal branch, as seen in Fig. 1. The phantom is embedded in agar to mimic the characteristics of human tissue, and it is encased in an air tight acrylic box with an acoustic window making it compatible with ultrasound imaging as well as MRI. For the steady flow set-up, a constant flow rate of 1.0 mL/s is selected, while the pulsatile flow profile is set to mimic a simplified carotid profile with a period of 0.84 seconds and a flow rate of 5.0 mL/s. Blood-mimicking fluid is used with a density of 1,037 kg/m^3 and a viscosity of 4.1 mPa·s.

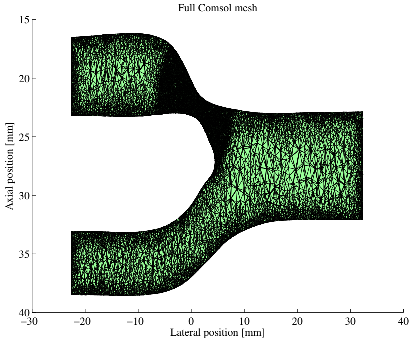

Figure 1. Outline of the flow phantoms fluid domain.

The accuracy of the pressure gradients estimated under steady flow conditions is evaluated through comparison to a finite element model. The geometry of this model is constructed from MRI data of the flow phantom performed at the Department of Diagnostic Radiology at Rigshospitalet, Denmark, using a 3 Tesla Magnetom Trio scanner (Siemens, Munich, Germany). The finite element model was composed of more than 600,000 tetrahedrons, which were especially dense in the constricted region of the phantom to ensure a high spatial resolution. The simulation study was carried out using Comsol (v4.2a, Stockholm, Sweden).

An *in-vivo* study of the common carotid artery on a healthy male volunteer was also made. The study was made using a pulse repetition frequency of 5.1 kHz for capturing 23 frames per second.

IV. RESULTS

The following section presents the results of the proposed estimator. The flow data used for validating the estimator were captured from the carotid flow phantom at the site of the constriction at 18 frames/sec. The result of the *in-vivo* study is shown at the end of the section.

A. Constant flow measurement

A vector velocity map of the flow through the constricted area of the phantom is plotted in Fig. 2 along with the estimated and simulated pressure gradients. The fluid flows from right to left and reaches a peak velocity of 0.15 m/s at the centre of the constriction. The centre panel in Fig. 2 shows the estimated pressure gradients calculated using the velocities in the left panel. The right-hand side of the figure shows the simulated pressure gradients. The background color and length of the arrows indicate the magnitude of the pressure gradients or velocity vectors, respectively. The arrows' direction indicates the angle of the vector. The two gradient plots display arrows that tend to point away from the centre of the constriction, indicating that a low pressure is present here, as a gradient always point in direction of increasing values.

Fig. 3 shows the result of the estimator taken along the red-dotted lines which run parallel to the fluid flow in Fig. 2. The results show a mean magnitude of the axial and lateral pressure gradients along with ± one standard deviation of the estimates. The blue line shows the simulated pressure gradients along the same path. The estimator produced pressure gradients of magnitudes varying from -3 kPa/m to 10 kPa/m with a bias normalized to the peak gradient of -9% and -8% for the axial and lateral vector component, respectively. The standard deviation when using the mean of two successive velocity frames for each estimate were 28% and 65% for the axial and lateral component.

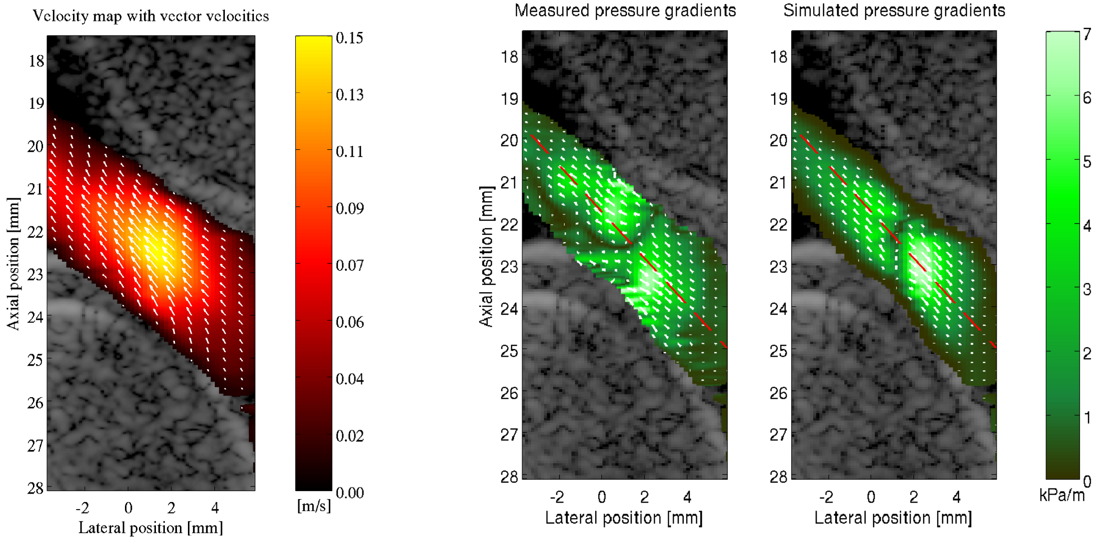

Figure 2. Vector velocity map along with the estimated and simulated pressure gradients. The left panel shows a vector velocity map of the blood mimicking fluid that flows through the constriction from right to left. The centre panel shows the pressure gradients estimated from vector velocity data, while the panel to the right shows the simulated gradients.

B. Pulsating flow measurement

Pressure gradients estimated from velocity data acquired at 21 frames/sec from the flow phantom during pulsatile flow are shown in Fig. 4. The graphs display both the mean velocity and the mean gradients over an area of $0.4\,\mathrm{mm}^2$, which is located just left of the centre of the constriction. The displayed gradients have been low-pass filtered by a normalized Hanning window across the velocity frames corresponding to 9 frames. The size of the gradients varies from 5 kPa/m in diastole to roughly 150 kPa/m in peak systole. The pressure gradients seen in the pulsatile flow measurement are more than twenty times greater at peak systole than the gradients measured during constant flow conditions, despite the flow rate being only five times larger. Thus, indicating that temporal changes in flow velocities play a dominant role in the magnitude of the pressure gradients.

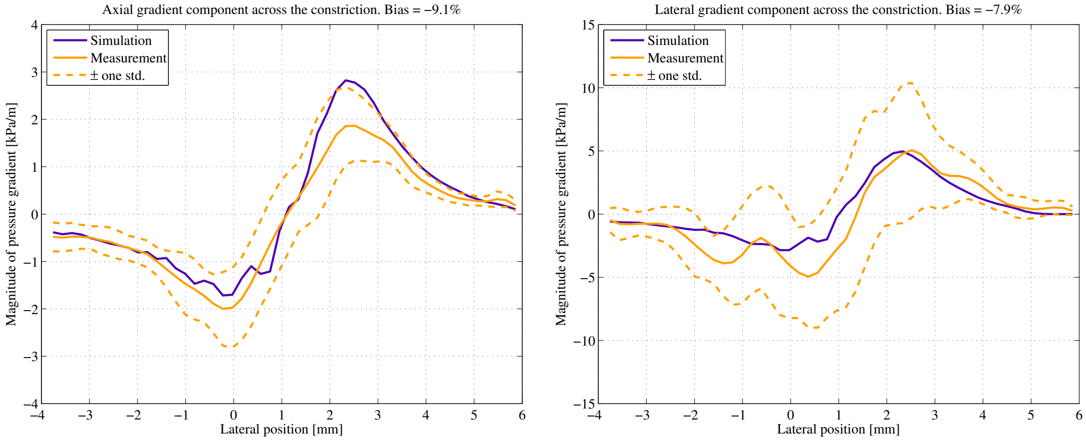

Figure 3. Estimated and simulated pressure gradients along the longitudinal direction of the constriction. The two graphs show the axial and lateral component of the pressure gradient, respectively.

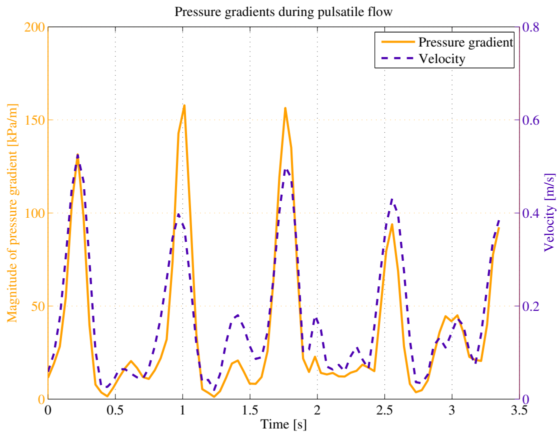

Figure 4. Estimated pressure gradients in pulsating flow together with the velocity of the fluid.

C. *In-vivo measurement*

An *in-vivo* study was performed by a medical doctor on a healthy volunteer. The study was made on the common carotid artery (CCA) using the linear array transducer at a pulse repetition frequency of 5.1 kHz, displaying 23 frames per second. Fig. 6 shows the estimated velocity fields and the pressure gradients during end-diastole and peak systole, respectively. The size of the estimated gradients are in some areas forty-times greater during peak systole than in end-diastole. This significant increase of the pressure gradients during peak systole is in agreement with the results obtained from the pulsating flow phantom. Thus, confirming that the size of a pressure gradient is highly governed by temporal velocity changes. This is especially the case in the CCA as the tortuous of the vessel is small, hence, the spatial velocity becomes unimportant. However, measuring pressure gradients in the carotid bulb or at its bifurcation would increase the role of the spatial acceleration as the flow patterns in these regions are more disrupted by the geometry of the vessel.

V. CONCLUSIONS

A non-invasive method for deriving pressure gradients using vector velocity ultrasound data has been presented. The pressure gradients were derived using the Navier-Stokes equation for incompressible fluids. The vector velocities inserted into the equation were estimated using the TO method yielding the two in-plane velocity components. The obtained pressure gradients were evaluated by comparison to a finite element simulation model, for which the geometry was obtained from MRI data. The employed method produced pressure gradients within a constricted flow phantom with magnitudes varying from -3 kPa/m to 10 kPa/m and from 5 kPa/m to 150 kPa/m for constant and pulsatile flow, respectively. An *in-vivo* study on the common carotid artery showed pressure gradients from roughly 20 kPa/m in end-diastole to more than 400 kPa/m in peak systole, indicating the dominant role of temporal velocity changes when estimating pressure gradients in the CCA. The advantage of using ultrasound for estimating pressure gradients is its capability of producing *in-vivo* images at a high frame-rate. This is crucial when measuring on a pulsatile flow environment.

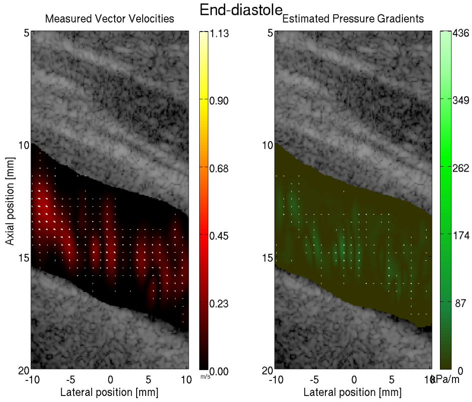

Figure 5. Vector velocity flow and pressure gradients measured on a common carotid artery in end-diastole.

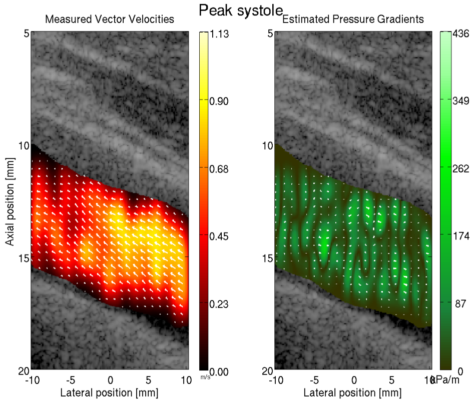

Figure 6. Vector velocity flow and pressure gradients measured on a common carotid artery in peak systole.

REFERENCES

[1] D. S. Baim and W. Grossman, *Grossman's cardiac catheterization, angiography, and intervention*. Lippincott Williams & Wilkins, 2000.

[2] W. M. Fairbank and M. O. Scully, "A new noninvasive technique for cardiac pressure measurements: resonant scattering of ultrasound from bubbles," *IEEE Trans. Biomed. Eng.*, vol. 24, pp. 107–110, 1977.

[3] J. A. Jensen and P. Munk, "A New Method for Estimation of Velocity Vectors," *IEEE Trans. Ultrason., Ferroelec., Freq. Contr.*, vol. 45, pp. 837–851, 1998.

[4] M. E. Anderson, "Multi-dimensional velocity estimation with ultrasound using spatial quadrature," *IEEE Trans. Ultrason., Ferroelec., Freq. Contr.*, vol. 45, pp. 852–861, 1998.

[5] L. Prandtl, *Essentials of Fluid Dynamics*. London: Blackie & Son, 1952.

[6] N. B. Wood, "Aspects of fluid dynamics applied to the large arteries," *J. Theor. Biol.*, vol. 199, no. 953, pp. 137–161, April 1999.

[7] G. D. Smith, *Numerical Solution of Partial Differential Equations: Finite Difference Methods*. Oxford University Press, 1985.

Paper V

Non-invasive estimation of pressure gradients in pulsatile flow using ultrasound

Jacob Bjerring Olesen, Carlos Armando Villagomez-Hoyos, Marie Sand Traberg, and Jørgen Arendt Jensen

Proceeding of IEEE International Ultrasonics Symposium, p. 2257-2260,
Accepted for poster presentation in Chicago, Illinois, United States, 2014.

10.1109/ULTSYM.2014.0562

Non-invasive Estimation of Pressure Gradients in Pulsatile Flow using Ultrasound

Jacob Bjerring Olesen, Carlos Armando Villagómez Hoyos, Marie Sand Traberg and Jørgen Arendt Jensen
Center for Fast Ultrasound Imaging, Dept. of Elec. Eng., Bldg. 349,
Technical University of Denmark, DK-2800 Kgs. Lyngby, Denmark

***Abstract*—This paper investigates how pressure gradients in a pulsatile flow environment can be measured non-invasively using ultrasound. The presented set-up is based on vector velocity fields measured on a blood mimicking fluid moving at a peak flow rate of 1 ml/s through a constricted vessel. Fields of pressure gradients are calculated using the Navier-Stokes equations. Flow data are acquired to a depth of 3 cm using directional synthetic aperture flow imaging on a linear array transducer producing 1500 image frames of velocity estimates per second. Scans of a carotid bifurcation phantom with a 70% constriction are performed using an experimental scanner. The performance of the presented estimator is evaluated by comparing its results to a numerical simulation model, which geometry is reconstructed from MRI data. The study showed pressure gradients varying from 0 kPa/m to 4.5 kPa/m with a maximum bias and standard deviation of 10% and 13%, respectively, relative to peak estimated gradient. The paper concludes that maps of pressure gradients can be measured non-invasively using ultrasound with a precision of more than 85%.**

I. INTRODUCTION

Measuring the intra-vascular blood pressure and its changes across constricted regions helps as a diagnostic marker for several cardiovascular diseases. In the clinic today, such measures are mostly obtained by pressure catheters introduced to the femoral artery and threaded to the region of interest. Despite this procedure being widely accepted, it suffers some severe limitation on both the accuracy of the measurement, and that it is a highly invasive procedure requiring ionizing radiation for X-ray guidance. Recently, Adelaide *et al.* [1] published a study on how the physical size and shape of a pressure catheter affects the accuracy of the intended measurement. The study showed that a routinely employed catheter induces a 24% overestimation of the peak systolic pressure compared to a wire estimate, which is considered the golden standard [2].

An interest of replacing invasive catheters by less invasive methods started to grow in the 1970's. In 1976, Holen *et al* [3] introduced the first fully noninvasive alternative for estimating intra-vascular pressure differences. They suggested a method that estimated local pressure gradients based on the peak systolic blood velocity measured using Doppler ultrasound. This noninvasive estimate may have moved itself from the errors related to catheterization, but were now facing the difficulties associated with ultrasound scanners of that time, e.g. poor signal-to-noise ratio and bad temporal and spatial resolution. Most damaging to the method was its solely dependence on a single velocity estimate, which made the method highly sensitive to hemodynamic factors that were unrelated to the constricted vessel's effect on the peak velocity, e.g., abnormal cardiac output. The last decades has led to advancements in noninvasive techniques for improving pressure estimates [4]–[6], but none of them have successfully managed to substitute pressure catheters in the clinic. This paper presents an estimator that relies on vector velocity data acquired at 1500 frames per second with a precision of 98% to the true value [7]. The authors believe that a method, which operates at a frame rate capable of capturing every flow feature that exist throughout the cardiac cycle, and has a high precision, is the key to one day substituting or assisting catherization.

II. DERIVING PRESSURE GRADIENTS

The following section presents a method for calculating pressure gradients using ultrasound vector velocity data. The method is based on Navier-Stokes equations for an isotropic incompressible Newtonian fluid:

$$\rho\left[\frac{\partial\vec{v}}{\partial t}+\vec{v}\cdot\nabla\vec{v}\right]=-\nabla p+\rho\vec{g}+\mu\nabla^2\vec{v}. \tag{1}$$

The equation describes the development of a fluid's velocity $\vec{v}(v_x,v_y,v_z)$ by relating the body forces acting on the isotropic volume to its acceleration and density, where ρ is the density of the fluid and μ its viscosity. The left-hand side sums the local $\frac{\partial\vec{v}}{\partial t}$ and convective fluid acceleration $\vec{v}\cdot\nabla\vec{v}$, where ∇ is the spatial differential operator $(\frac{\partial}{\partial x},\frac{\partial}{\partial y},\frac{\partial}{\partial z})$, while the right-hand side sums the surface and volume forces. The terms on the right-hand side include the pressure gradients $-\nabla p$, as well as a gravitational force $\mathbf{g}$ and viscous drag caused by the viscosity of the fluid $\mu\nabla^2\vec{v}$, where $\nabla^2\vec{v}$ is the Laplacian of the velocity. The gravitational term can usually be neglected, as a patient undergoing an ultrasound scan is placed in a supine position.

Eq. (1) states that all three vector components of $\vec{v}(v_x,v_y,v_z)$ must be known to estimate the pressure gradient ∇p. However, the method employed in this study image only the two-dimensional (2-D) in-plane velocity vector $\vec{v}=(v_x,v_z)$. The proposed method is therefore developed assuming that the out-of-plane velocity v_y is zero. The reduced form of the Navier-Stokes equations are expressed here in rectangular coordinates,

$$\begin{bmatrix}\dfrac{\partial p}{\partial x}\\[2ex]\dfrac{\partial p}{\partial z}\end{bmatrix}=-\rho\begin{bmatrix}\dfrac{\partial v_x}{\partial t}+v_x\dfrac{\partial v_x}{\partial x}+v_z\dfrac{\partial v_x}{\partial z}\\[2ex]\dfrac{\partial v_z}{\partial t}+v_x\dfrac{\partial v_z}{\partial x}+v_z\dfrac{\partial v_z}{\partial z}\end{bmatrix}$$

$$+\mu \begin{bmatrix} \dfrac{\partial^2 v_x}{\partial x^2} + \dfrac{\partial^2 v_x}{\partial z^2} \\ \\ \dfrac{\partial^2 v_z}{\partial x^2} + \dfrac{\partial^2 v_z}{\partial z^2} \end{bmatrix}. \qquad (2)$$

The derivatives in (2) are calculated from velocity data using polynomial filtering. A second-order polynomial is fitted to a subset of adjacent data points by the linear least-squared method, which results in a smoothed data set. From this data set the first and second-order derivatives are found using the convolution coefficients [8], [9].

III. DATA ACQUISITION AND EXPERIMENTAL SET-UP

Velocity data are acquired on a flow phantom mimicking the carotid bifurcation having a 70% constriction of the internal branch, (C70-SSEA Shelley Medical Imaging Technologies, Toronto, Canada). Ultrasound data are recorded over the constriction using a BK8670 linear array transducer connected to the experimental research scanner SARUS [10], capable of sampling individual RF data from 1024 channels. The flow estimator uses synthetic aperture imaging together with focusing in receive along the direction of the flow as suggested by Jensen and Nikolov [7]. The obtained signals are then cross-correlated to find the magnitude of the velocity. The carotid bifurcation phantom is connected to a flow system (CompuFlow 1000, Shelley Medical Imaging Technologies, Toronto, Canada) capable of generating time-varying waveforms. The pump is set to produce a waveform that mimics that of a carotid artery, see Fig. 1.

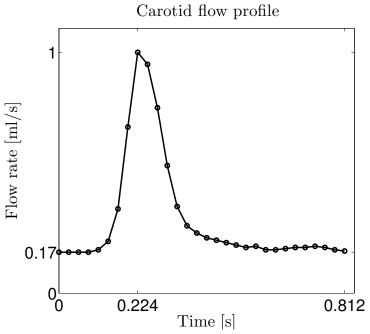

Fig. 1. Waveform produced by the pulsating flow pump

Data are recorded over three full cycles, producing roughly 3700 frames of velocity. Each velocity frame initially contains of 120×11 estimates, spanning an area of 11×10 mm. The velocity data is then up-sampled by a factor of five in the lateral direction. Up-sampling is made to reduce the effects of wall-signal being smeared into the lumen of the vessel when calculating the derivatives of the selected subset of data points. A sliding window covering 225 frames (≈ 0.15 s) is used for smooothing and calculating the temporal acceleration from the estimated velocities data, while the spatial derivatives were found using window sizes of 31 (≈ 3 mm) and 11 (≈ 2 mm) data points for the axial and lateral direction, respectively.

The accuracy of the estimated pressure gradients is evaluated through comparison to a finite-element model produced in Comsol (Comsol v4.4, Comsol AB, Stockholm, Sweden). The geometry of this model is constructed from MRI data of the flow phantom obtained using a 3-T scanner (Magnetom Trio, Siemens AG, Munich, Germany) at the Department of Diagnostic Radiology at Rigshospitalet, Denmark. The flow parameters in the simulation model are set to mimic the actual flow conditions in the experimental set-up. An inlet profile equivalent to the one in Fig. 1 is set for the simulation model and the viscosity and density is set to match the properties of the blood-mimicking fluid (BMF-US, Shelley Medical Imaging Technologies, Toronto, Canada) used in the experimental set-up.

IV. RESULTS

A map of vector velocities during peak systole is simulated and plotted for the center of the constricted vessel in Fig. 2A. The color indicates the magnitude of the velocity while the arrows point in the direction of flow movement. The flow accelerates toward the center of the constriction, reaching a peak velocity of 0.13 m/s, before decelerating as the cross-sectional area expands again. Figs. 2B and 2C show maps of pressure gradients derived from the velocity data plotted in Fig. 2A. Fig. 2B presents gradients that are the direct output from the simulation software Comsol, while Fig. 2C shows gradients derived from the simulated velocity data using the model suggested in (2). A comparison between the output from Comsol and the output from the model is made for the maximum pressure gradient found upstream to the constriction, indicated by the circle in the bright green region. The comparison is made for the axial and lateral gradient component and is plotted in Figs. 3-4. The root-mean-square deviation is calculated with respect to the observed range and is found to be 5.6 % for the axial component and 4.5 % for the lateral component. The resemblance between the Comsol output and the output from the suggested model indicates that the model is suitable for calculating pressure gradients.

The experimental results are plotted in Fig. 5. Fig. 5A shows vector velocities at peak systole estimated using the directional synthetic aperture flow imaging approach. As in the case with the simulated data, the flow accelerates toward the constriction reaching a peak velocity of approximately 0.15 m/s. The plotted velocities are used for deriving the pressure gradients. The result of this is seen in Fig. 5B. The overall appearance of the derived gradients shows the same tendencies as in the simulated set-up. Both cases display gradients that point away from the center of the constriction indicating that a low pressure is present here. The estimates at the vessel's boundaries are affected by the backscattering signal from the vessel wall, especially at the center of the constriction. This region is particular critical as high velocities are seen close to a region outside the flow domain, thus, producing large spatial decelerations, which creates false magnitudes in the derived pressure gradients. A

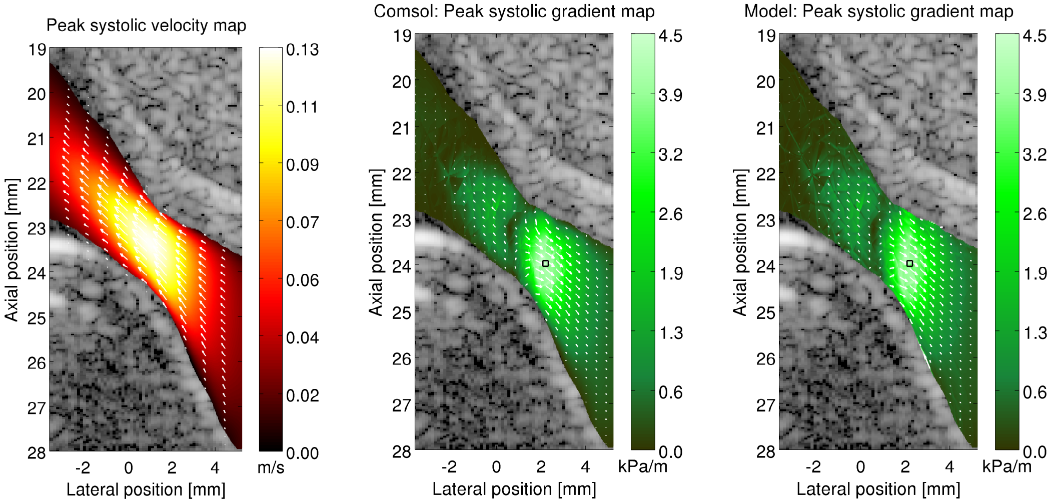

(a) (b) (c)

Fig. 2. Simulated data. (a) shows the simulated vector velocity field through the constricted region. (b) shows a map of the simulated pressure gradients. (c) display pressure gradients derived using (2) and the velocity data shown in (a).

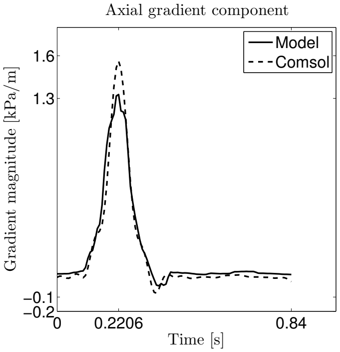

Fig. 3. Magnitude of axial pressure gradient component

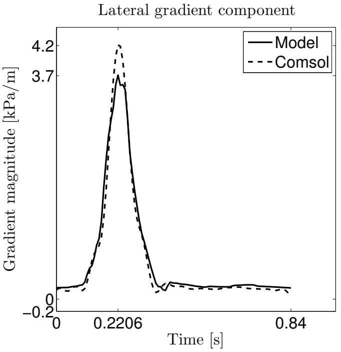

Fig. 4. Magnitude of lateral pressure gradient component

comparison between the estimated results and the simulation model is made for the peak gradient in the upstream region, see Figs. 6 and 7. The maximum bias was found for the axial component, which reached 10% of the peak estimated gradient. The standard deviation over the three cycles was calculated to 13% for both the axial and lateral component.

V. CONCLUSIONS

A non-invasive method for deriving pressure gradients in a pulsatile flow set-up using vector velocity ultrasound data was presented. The pressure gradients were derived using the Navier–Stokes equations for incompressible fluids. The vector velocities inserted into the equations were estimated using the directional synthetic aperture flow imaging at 1500 frames per second. Measurements were performed on a constricted carotid phantom and the results were compared to a numerical simulation model. The experiment showed at maximum bias of 10% and a relative standard deviation of 13%. The paper concludes that pressure gradients can be measured non-invasively using ultrasound to a precision of 85% when looking over three cardiac cycles.

REFERENCES

[1] A. de Vecchi, R. E. Clough, N. R. Gaddum, M. C. M. Rutten, P. Lamata, T. Schaeffter, D. A. Nordsletten, and N. P. Smith, “Catheter-induced

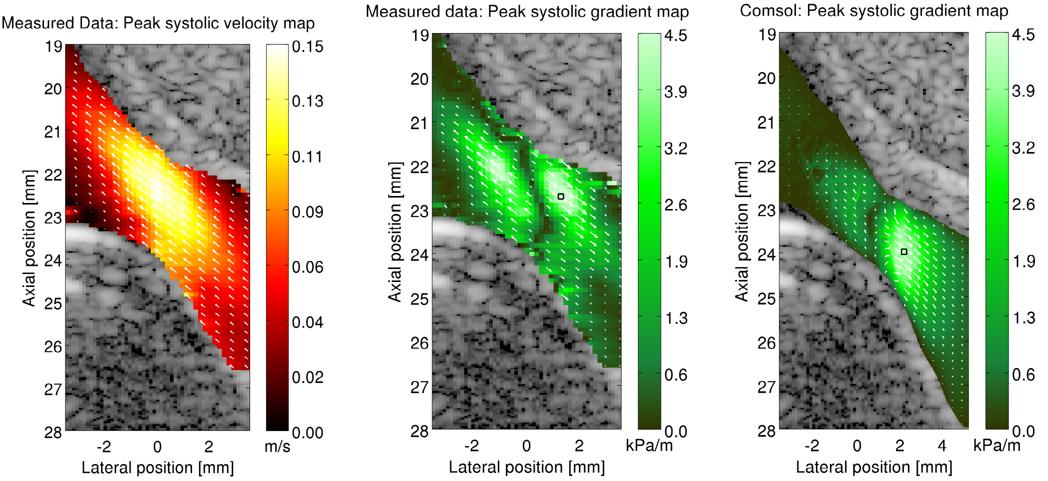

(a) (b) (c)

Fig. 5. Measured data. (a) shows the estimated vector velocity field through the constricted vessel. (b) displays a map of pressure gradients, estimated from the velocity data in (a) using (2). (c) shows the simulated pressure gradients, (same plot as Fig. 2b)

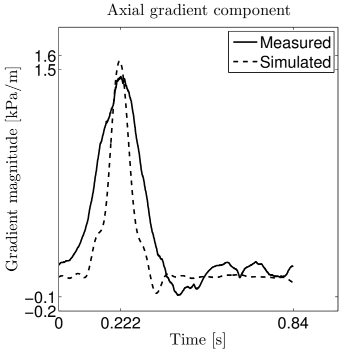

Fig. 6. Magnitude of axial pressure gradient component

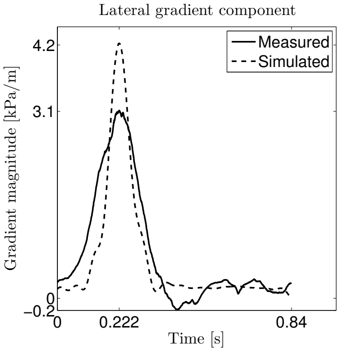

Fig. 7. Magnitude of lateral pressure gradient component

errors in pressure measurements in vessels: An in-vitro and numerical study,” *IEEE Trans. Biomed. Eng.*, vol. 61, no. 6, pp. 1844–1850, 2014.

[2] J. J. Cavendish, L. I. Carter, and S. Tsimikas, “Recent advances in hemodynamics: Noncoronary applications of a pressure sensor angioplasty guidewire,” *Catheter Cardiovasc Interv*, vol. 71, no. 6, pp. 748–758, 2008.

[3] J. Holen, R. Aaslid, and K. Landmark, “Determination of pressure gradient in mitral stenosis with a non-invasive ultrasound Doppler technique,” *Acta med. scand.*, vol. 32, pp. 455–460, 1976.

[4] S. Ohtsuki and M. Tanaka, “Doppler pressure field deduced from the Doppler velocity field in an observation plane in a fluid,” *Ultrasound Med. Biol.*, vol. 29, no. 10, pp. 1431–1438, 2003.

[5] A. Herment, G. Besson, C. Pellot-Barakat, and F. Frouin, “Estimation of pressure gradient images from velocity encoded MR acquisitions,” *Computers in Cardiology*, vol. 35, pp. 933–936, 2008.

[6] J. P. Tasu, E. Mousseaux, A. Delouche, C. Oddou, O. Jolivet, and J. Bittoun, “Estimation of pressure gradients in pulsatile flow from magnetic resonance acceleration measurements,” *Magn. Reson. Med.*, vol. 44, no. 1, pp. 66–72, 2000.

[7] J. A. Jensen and S. I. Nikolov, “Directional synthetic aperture flow imaging,” *IEEE Trans. Ultrason., Ferroelec., Freq. Contr.*, vol. 51, pp. 1107–1118, 2004.

[8] A. Savitzky and M. J. E. Golay, “Smoothing and differentiation of data by simplified least squares procedures,” *Anal. Chem.*, vol. 36, no. 8, pp. 1627–1639, 1964.

[9] J. B. Olesen, M. S. Traberg, M. J. Pihl, and J. A. Jensen, “Noninvasive esimation of 2-D pressure gradients in steady flow using ultrasound,” *IEEE Trans. Ultrason., Ferroelec., Freq. Contr.*, vol. 61, no. 8, pp. 1409–1418, 2014.

[10] J. A. Jensen, H. Holten-Lund, R. T. Nilsson, M. Hansen, U. D. Larsen, R. P. Domsten, B. G. Tomov, M. B. Stuart, S. I. Nikolov, M. J. Pihl, Y. Du, J. H. Rasmussen, and M. F. Rasmussen, “SARUS: A synthetic aperture real-time ultrasound system,” *IEEE Trans. Ultrason., Ferroelec., Freq. Contr.*, vol. 60, no. 9, pp. 1838–1852, 2013.

Paper VI

Non-invasive Estimation of Intravascular Pressure Changs using Ultrasound

Jacob Bjerring Olesen, Carlos Armando Villagomez-Hoyos, Marie Sand Traberg, and Jørgen Arendt Jensen

Proceeding of IEEE Internation Ultrasonics Symposium, p. TBC,
Accepted for oral presentation in Taipei, Taiwan, 2015.

10.1109/ULTSYM.2015.0067

Non-invasive Estimation of Pressure Changes along a Streamline using Vector Velocity Ultrasound

Jacob Bjerring Olesen, Carlos Armando Villagómez-Hoyos, Marie Sand Traberg, and Jørgen Arendt Jensen
Center for Fast Ultrasound Imaging, Dept. of Elec. Eng., Bldg. 349,
Technical University of Denmark, DK-2800 Kgs. Lyngby, Denmark

Abstract—**A non-invasive method for estimating pressure changes along a streamline using ultrasound is presented. The suggested method estimates pressure gradients from 2-D vector velocity fields. Changes in pressure are derived using a model based on the Navier-Stokes equations. Scans of a carotid bifurcation phantom with a 70% constriction are performed using a linear array transducer connected to the experimental scanner, SARUS. 2-D fields of angle-independent vector velocities are acquired to a depth of 3 cm using directional synthetic aperture vector flow imaging. The performance of the suggested estimator is evaluated by comparing its results to a 3-D numerical simulation model. The study showed pressure drops across the constricted phantom varying from -5 Pa to 7 Pa with a standard deviation of 4%. The proposed method had a normalised root-mean-square error of 10% in reference to the simulation model. Further, an in-vivo scan of the carotid bifurcation is made to show the feasibility of the technique in a less experimental environment.**

I. INTRODUCTION

Abnormal changes in intravascular blood pressure are usually an indication of a diseased vessel. Measuring pressure variations is therefore used clinically as a diagnostic marker in assessing the physiological state of a cardiovascular region [1]. Intravascular pressure is currently assessed by inserting pressure sensing wires or catheters to the femoral artery and threading them to the region of interest. These procedures, however, suffer some severe limitation as they are highly invasive and require the use of ionizing radiation for guidance of the pressure sensory device. A recent report from De Vecchi *et al.* [2] demonstrated that the accuracy of using catheters is greatly dependent on the physical size and shape of the catheter. It was found that a 24% overestimation of the peak systolic pressure can result from using a routinely employed catheter compared to the gold standard using a wire.

In 1976, Holen *et al.* [3] introduced the first fully non-invasive alternative for estimating intravascular pressure based on Doppler ultrasound. Analysing audio signals of the frequency shifts received from the mitral jet revealed the peak systolic velocity. From this the local pressure gradients were calculated using an orifice equation. The method was attractive due to its avoidance of catheterization, but suffered from the drawback that it was solely reliant on a single velocity estimate, which made the method highly sensitive to hemodynamic factors unrelated to the constricted vessel's effect on the peak velocity, e.g. abnormal cardiac output. The method presented by Holen *et al.* was further studied in 1989 by Evans *et al.* [4], and later tested against clinical pressure catheters by Strauss-and Baumgartner *et al.* [5]–[7]. The latter studies agreed that non-invasive pressure estimation through the simplified Bernoulli equation was achievable, however, the obtained pressure estimates were greatly dependent on the size of the examined vessel and the examiners ability to correct for the Doppler angle. Further advancement in non-invasive techniques for improving pressure estimates have been proposed over the past decades [8]–[17], but none of these have as yet successfully managed to supercede pressure catheters in the clinic.

The purpose of this paper is to present a technique for estimating pressure changes from vector velocity ultrasound data, and to compare these to results obtained using a 3-D finite-element (FE) simulation model. The presented data are obtained from a flow model, which mimics a constricted carotid artery. The study concludes by presenting an in-vivo example of the proposed technique.

II. PRESSURE ESTIMATION USING VECTOR VELOCITIES

The following section describes the employed method for calculating the pressure gradients. It is based on the Navier-Stokes equations:

$$\rho\left[\frac{\partial\vec{v}}{\partial t}+\vec{v}\cdot\nabla\vec{v}\right]=-\nabla p+\rho\vec{g}+\mu\nabla^2\vec{v}, \tag{1}$$

presuming the conservation of mass and linear momentum. Eq. (1) describes the development of a fluid's velocity field $\vec{v}(\vec{r},t)=(v_x(t),v_y(t),v_z(t))$ by relating the forces acting on an incompressible volume to its acceleration and density throughout time, t, and space, $\vec{r}$. The left-hand side sums the local $\frac{\partial\vec{v}}{\partial t}$ and convective fluid acceleration $\vec{v}\cdot\nabla\vec{v}$, where ρ is the density of the fluid and ∇ is the spatial differential operator $(\frac{\partial}{\partial x},\frac{\partial}{\partial y},\frac{\partial}{\partial z})$. The right-hand side shows the surface and volume forces that are responsible for the acceleration of the fluid. The forces constitute a pressure drop $-\nabla p$, a gravitational force $\vec{g}$, and a viscous drag caused by the viscosity of the fluid $\mu\nabla^2\vec{v}$, where $\nabla^2\vec{v}$ is the Laplacian of the velocity field. The gravitational term is usually neglected, as a patient undergoing an ultrasound scan is placed in a supine position, hence, the buoyancy force cancels out the gravitational force. Rewriting (1) into a scalar equation following a streamline, and where the influence of gravity is omitted, yields the following;

$$\frac{\partial p}{\partial s}=-\rho\left[\frac{\partial v_s}{\partial t}+v_s\frac{\partial v_s}{\partial s}\right]+\mu\frac{\partial^2 v_s}{\partial s^2}, \tag{2}$$

978-1-4799-8182-3/15/$31.00 ©2015 IEEE

where v_s is the scalar product of $\vec{v}(\vec{r},t)$ and the vector that lies tangent to the streamline $d\vec{s} = (\hat{s}_x, \hat{s}_y, \hat{s}_z)$. Here $d\vec{s}$ is an element of distance along the streamline, which runs in the direction, s. Integrating (2) along the flow direction of the streamline gives the drop in pressure across the line,

$$\Delta P(t) = \int_0^L \frac{\partial p}{\partial s}\, ds. \tag{3}$$

Eqs. (1)–(3) state that the three spatial vector components of $\vec{v}$ must be known to estimate the pressure gradient ∇p. This study employs a velocity estimator, which yields the two-dimensional (2-D) in-plane vector velocity field $\vec{v} = (v_x, v_z)$. The proposed method is, thus, developed assuming that the out-of-plane velocity v_y is zero.

A. Calculating the Temporal Acceleration

The temporal derivative in (2) is approximated analytically by decomposing the measured flow profile into a series of sinusoids through a Fourier transform. The profile and its derivative are then expressed by a sum of sinusoids, which oscillate at the frequencies containing the highest levels of energies. Reconstructing the flow profile from a sum of sinusoids is possible as the flow is periodic over the cardiac cycle [4], [18]. The first order derivative of a given flow profile is expressed as:

$$\frac{\mathrm{d}v_s(n,t)}{\mathrm{d}t} \approx -\sum_{p=1}^{N} |V_p(n)|\, 2\pi f_p\, \sin(2\pi f_p t + \varphi_p(n)), \tag{4}$$

where N is the number of sinusoids used in reconstructing the flow profile. V_p and φ_p are the amplitude and the phase of the frequency component f_p. n is the index number that runs along the streamline. The selected frequencies, f_p, are chosen based on they level of energy in the frequency domain. For instance, blood flow in larger vessels is mainly govern by the pulsating motion of the heart, hence, the frequencies of highest energy levels are generally associated to the fundamental period of the heart cycles, and its harmonics.

B. Calculating the Spatial Acceleration

The spatial derivatives in (2) are, unlike the previous case, not necessarily periodic across the examined region. Thus, it is not possible to express the spatial acceleration by a sum of sinusoids. The derivatives are therefore calculated using polynomial filtering of the measured velocity field. A second-order polynomial is fitted to a subset of adjacent data points by the linear least-squared method. Convolution coefficients are calculated from the least-squared model, which are used for finding the first-order derivatives [19]. The spatial accelerations, $\frac{\partial}{\partial s}$ and $\frac{\partial^2}{\partial s^2}$, in (2) are calculated by pair-wise multiplication of the elements in the velocity window and the convolution coefficients (B_k) before summing and scaling the five multiplication terms,

$$\frac{\mathrm{d}^k v_s(n,t)}{\mathrm{d}s^k} \approx \frac{1}{\Delta s^k} \sum_{p=n-h_w}^{n+h_w} v_s(p,t)\, B_k(p-(n-h_w)+1). \tag{5}$$

Here Δs is the sampling interval along the direction of the streamline. The index number p, is found from half the window size of the selected subset, calculated as: $h_w = \frac{N_{set}+1}{2} - 1$, where N_{set} is the number of samples in the subset. The convolution coefficients at k equal to 1 and 2, are $\vec{B}_1 = \frac{1}{35}[-7, -3.5, 0, 3.5, 7]$ and $\vec{B}_2 = \frac{1}{35}[10, -5, -10, -5, 10]$, respectively [19].

III. SIMULATION MODEL

The accuracy of the estimated pressure changes is evaluated through comparison to a FE model constructed in Comsol (Comsol v4.4, Comsol AB, Stockholm, Sweden). The geometry of the model is build from segmented MRI data of the flow phantom obtained using a 3-T scanner (Magnetom Trio, Siemens AG, Erlangen, Germany) at the Department of Diagnostic Radiology at Rigshospitalet, Denmark. The flow parameters of the simulation model are set to mimic the actual flow conditions in the experimental set-up.

IV. EXPERIMENTAL SET-UP AND EQUIPMENT

Vector velocity data are acquired from the upper branch of a flow phantom mimicking the carotid bifurcation, (C70-SSEA Shelley Medical Imaging Technologies, Toronto, Canada). Measurements are made using a BK8670 linear array transducer connected to the experimental research scanner SARUS [20]. A three-cycle pulse with a center frequency of 7 MHz is emitted at 12 kHz to a depth of 3 cm. Eight low-resolution images are summed for each high resolution image producing an effective frame-rate of 1,500 Hz.

V. RESULTS

Angle-independent velocities are estimated using directional synthetic aperture flow imaging, an approach explained by Villagomez-Hoyos *et al.* [21]. Flow data are recorded over three cardiac cycles, producing roughly 3,900 velocity frames.

The total pressure drop that exist across the scanned region is estimated as a function of time using (2). The spatial derivatives, $\frac{\partial v_s}{\partial s}$, which goes into the estimator, are calculated using polynomial filtering. A second-order polynomial is fitted to a subset of 71 adjacent velocity estimates covering a 1.4 mm line of the 10.7 mm long streamline. The window size and the order of the filter is selected to minimize the effect of estimator noise under the assumption that flow within a 1.4 mm region can be approximated by a second-order polynomial. Each individual gradient, $\frac{\partial p}{\partial s}$, gives an indication of how pressure at that particular position changes relative to neighbouring pressure values. Summing the discrete contributions from each estimate along the line, the relative drop in pressure that exist between the two ends of the streamline is obtained. The temporal evolution of the pressure drop for the three measured cardiac cycles is plotted in Fig. 1. The average standard deviation across the pulse is found to 4% in reference to the maximum pressure of 7 Pa. A plot of the three pulses shown on top of each other is seen in Fig. 2. The mean of the three measured pressure profiles is plotted together with the simulated pressure drop from the FE model in Fig. 3. A normalized root-mean-square error of 10% is found between the estimated data and the reference model.

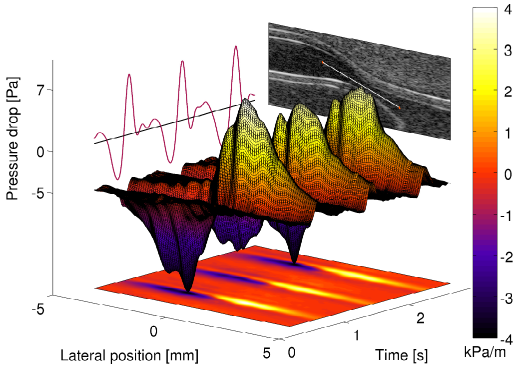

Fig. 1. Measured pressure drop across of the streamline seen on the B-mode image in the back. The center of the plot shows the individual pressure gradients along the line as a function of time. Summing the individual gradients along the streamline gives the total drop in pressure that exist across the stenotic region. This drop is presented by the red curve on the left.

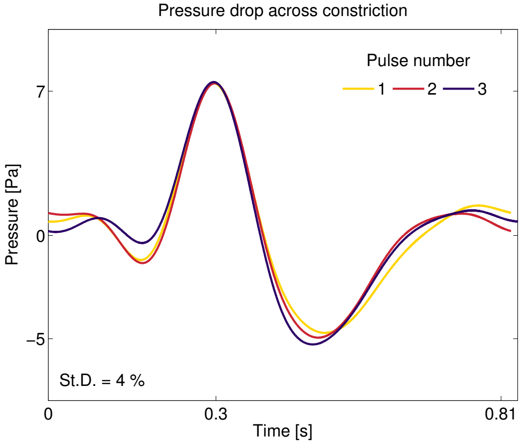

Fig. 2. Pressure drop between the two ends of the streamline for the three cardiac cycles.

A. *In-vivo Example*

An in-vivo measurement is carried out on the carotid artery of a healthy volunteer. The resulting vector flow image is shown in Fig. 4. The figure displays a longitudinal scan of the volunteer's left carotid bifurcations together with the measured flow field. The image is captured at peak systole, yielding values in the carotid sinus of roughly 0.6 m/s. Velocities along the streamline are extracted for all time instances and put into the proposed algorithm. The results are shown in Fig. 5. Relative pressure changes along the streamline are plotted as a function of time and lateral position. Here, the plot's left wall makes up the starting point of the streamline data. Changes in pressure are then found relatively to this point, by moving down-right, parallel to the lateral axis. The figure shows an example on how intravascular pressure changes can be mapped from 2-D velocity data obtained using a non-invasive ultrasound technique.

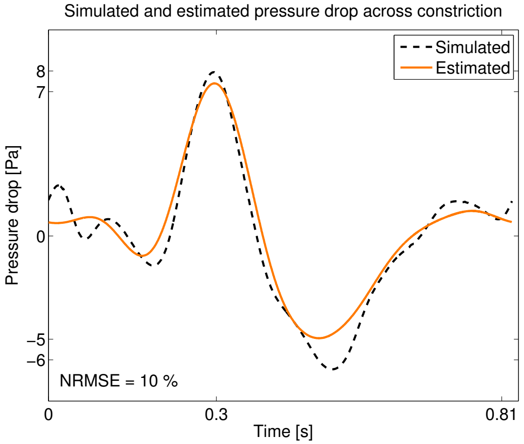

Fig. 3. Comparison of measured and simulated pressure drop. *Dotted-line*: Simulated pressure drop across the constricted flow phantom. *Solid-line*: Mean estimated pressure drop from the three cardiac cycles measured using ultrasound.

VI. DISCUSSION

Non-invasive measurement of pressure changes have been calculated from vector velocity data. The pressure drop along a streamline varied depending on when in the cardiac cycle it was measured. Phantom measurements showed a standard deviation of 4%, and a normalized error of 10%. No previous studies on the topic have measured changes in pressure along streamlines using high frame-rate ultrasonic techniques. Such techniques otherwise allow for averaging across estimates without compromising the peak of the profile. Averaging is beneficial as it essentially performs a low-pass filtering of the estimates, thus, avoiding the higher frequency content, which usually is associated with noise. Noise cancellation is crucial for deriving proper derivatives, and becomes increasingly more important when moving into higher order derivatives.

Having a method that can detect changes in pressure directly from ultrasound flow data, will provide the clinician with a non-invasive tool for assessing the severity of a stenosis, without the need for ionizing radiation. This allows for the opportunity of making follow-up studies over the course of a disease without the discomfort associated with invasive procedures.

VII. ACKNOWLEDGMENTS

The presented work has been financially supported by grant 024-2008-3 from the Danish Advanced Technology Foundation, BK Medical Aps, Denmark and Radiometer A/S, Denmark.

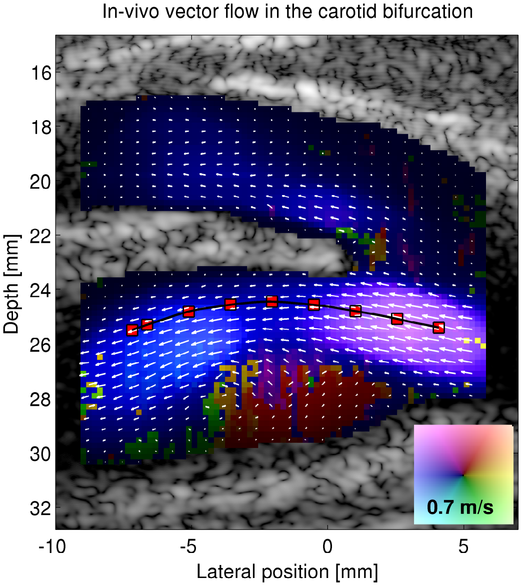

Fig. 4. Volunteer 1: Longitudinal vector flow scan of the carotid bifurcation during peak systolic. Bottom branch shows the internal carotid artery in conjunction with the carotid bulb, for which a vortex is formed during rapid flow movement. A streamline following the vector velocity field is also displayed.

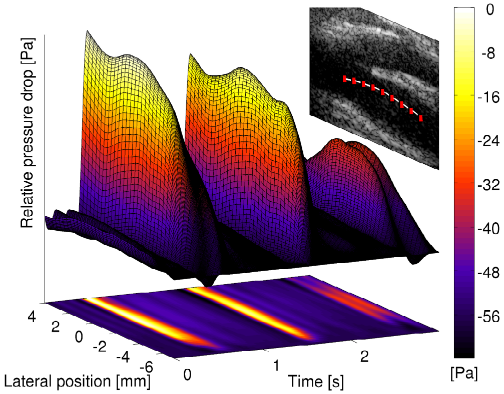

Fig. 5. In-Vivo: Changes in intravascular pressure measured as a function of time and lateral position along the streamline from Fig. 4. The shown pressures are in reference to an arbitrary value, which for this study is set to zero at the beginning of the streamline.

REFERENCES

[1] D. S. Baim and W. Grossman, *Grossman's cardiac catheterization, angiography, and intervention*. Lippincott Williams & Wilkins, 2000.

[2] A. de Vecchi, R. E. Clough, N. R. Gaddum, M. C. M. Rutten, P. Lamata, T. Schaeffter, D. A. Nordsletten, and N. P. Smith, "Catheter-induced errors in pressure measurements in vessels: An in-vitro and numerical study," *IEEE Trans. Biomed. Eng.*, vol. 61, no. 6, pp. 1844–1850, 2014.

[3] J. Holen, R. Aaslid, and K. Landmark, "Determination of pressure gradient in mitral stenosis with a non-invasive ultrasound Doppler technique," *Acta med. scand.*, vol. 32, pp. 455–460, 1976.

[4] D. H. Evans, W. N. McDicken, R. Skidmore, and J. P. Woodcock, *Doppler Ultrasound, Physics, Instrumentation, and Clinical Applications*. New York: John Wiley & Sons, 1989.

[5] A. L. Strauss, F. J. Roth, and H. Rieger, "Noninvasive assessment of pressure gradients across iliac artery stenoses: duplex and catheter correlative study," *J. Ultrasound Med.*, vol. 12, no. 1, pp. 17–22, 1993.

[6] H. Baumgartner, H. Schima, G. Tulzer, and P. Kühn, "Effect of stenosis geometry on the Doppler-catheter gradient relation in vitro: A manifestation of pressure recovery," *J. Am. Coll. Cardiol.*, vol. 21, no. 4, pp. 1018–1025, 1993.

[7] H. Baumgartner, T. Stefenelli, J. Niederberger, H. Schima, and G. Maurer, "Overestimation of catheter gradients by Doppler ultrasound in patients with aortic stenosis: A predictable manifestation of pressure recovery," *J. Am. Coll. Cardiol.*, vol. 33, no. 6, pp. 1655–1661, 1999.

[8] N. L. Greenberg, P. M. Vandervoort, M. S. Firstenberg, M. J. Garcia, and J. D. Thomas, "Estimation of diastolic intraventricular pressure gradients by Doppler M-mode echocardiography," *Am. J. Physiol. Heart Circ. Physiol.*, vol. 280, no. 6, pp. 2507–2515, 2001.

[9] J. Bermejo, J. C. Antoranz, I. G. Burwash, J. L. Alvarez, M. Moreno, M. A. Garcia-Fernandez, and C. M. Otto, "In-vivo analysis of the instantaneous transvalvular pressure difference-flow relationship in aortic valve stenosis: implications of unsteady fluid-dynamics for the clinical assessment of disease severity," *J. Heart Valve Dis.*, vol. 11, no. 4, pp. 557–566, 2002.

[10] A. K. Reddy, G. E. Taffet, S. Madala, L. H. Michael, M. L. Entman, and C. J. Hartley, "Noninvasive blood pressure measurement in mice using Doppler ultrasound," *Ultrasound Med. Biol.*, vol. 29, no. 3, pp. 379–385, 2003.

[11] S. Ohtsuki and M. Tanaka, "Doppler pressure field deduced from the Doppler velocity field in an observation plane in a fluid," *Ultrasound Med. Biol.*, vol. 29, no. 10, pp. 1431–1438, 2003.

[12] J. M. Meinders and A. P. G. Hoeks, "Simultaneous assessment of diameter and pressure waveforms in the carotid artery," *Ultrasound Med. Biol.*, vol. 30, no. 2, pp. 147–154, 2004.

[13] R. Yotti, J. Bermejo, J. C. Antoranz, J. L. Rojo-Alvarez, C. Allue, J. Silva, M. M. Desco, M. Moreno, and M. A. Garcia-Fernandez, "Noninvasive assessment of ejection intraventricular pressure gradients," *J. Am. Coll. Cardiol.*, vol. 43, no. 9, pp. 1654–1662, 2004.

[14] J. D. Thomas and Z. B. Popovic, "Intraventricular pressure differences a new window into cardiac function," *Circulation*, vol. 112, pp. 1684–1686, 2005.

[15] D. Garcia, P. Pibarot, and L.-G. Durand, "Analytical modeling of the instantaneous pressure gradient across the aortic valve," *J. Biomech.*, vol. 38, pp. 1303–1311, 2005.

[16] B. W. A. M. M. Beulen, N. Bijnens, G. G. Koutsouridis, P. J. Brands, M. C. M. Rutten, and F. N. van de Vosse, "Toward noninvasive blood pressure assessment in arteries by using ultrasound," *Ultrasound Med. Biol.*, vol. 37, no. 5, pp. 788–797, 2011.

[17] J. B. Olesen, M. S. Traberg, M. J. Pihl, and J. A. Jensen, "Noninvasive esimation of 2-D pressure gradients in steady flow using ultrasound," *IEEE Trans. Ultrason., Ferroelec., Freq. Contr.*, vol. 61, no. 8, pp. 1409–1418, 2014.

[18] J. R. Womersley, "Oscillatory motion of a viscous liquid in a thin-walled elastic tube. I: The linear approximation for long waves," *Phil. Mag.*, vol. 46, pp. 199–221, 1955.

[19] A. Savitzky and M. J. E. Golay, "Smoothing and differentiation of data by simplified least squares procedures," *Anal. Chem.*, vol. 36, no. 8, pp. 1627–1639, 1964.

[20] J. A. Jensen, H. Holten-Lund, R. T. Nilsson, M. Hansen, U. D. Larsen, R. P. Domsten, B. G. Tomov, M. B. Stuart, S. I. Nikolov, M. J. Pihl, Y. Du, J. H. Rasmussen, and M. F. Rasmussen, "SARUS: A synthetic aperture real-time ultrasound system," *IEEE Trans. Ultrason., Ferroelec., Freq. Contr.*, vol. 60, no. 9, pp. 1838–1852, 2013.

[21] C. A. Villagomez-Hoyos, M. B. Stuart, and J. A. Jensen, "Adaptive multi-lag for synthetic aperture vector flow imaging," in *Proc. IEEE Ultrason. Symp.*, 2014, pp. 1722–1725.

Abstract I

Preliminary investigation of an ultrasound method for estimating pressure changes in deep-positioned vessels

Jacob Bjerring Olesen, Carlos Armando Villagomez-Hoyos, Marie Sand Traberg, Adrian J. Y. Chee, Billy Y. S. Yiu, Chung Kit Ho, Alfred C. H. Yu, and Jørgen Arendt Jensen

Proceeding of SPIE Ultrasound Imaging. Symp., TBC,

Accepted for oral presentation in San Diego, California, United States, 2016.

Non-invasive ultrasound method for measuring large range pressure changes in deep-positioned vessels

Jacob Bjerring Olesen[a], Carlos Armando Villagmez-Hoyos[a], Marie Sand Traberg[a], Adrian J. Y. Chee[b], Billy Y. S. Yiu[b], Chung Kit Ho[b], Alfred C. H. YU[b], and Jørgen Arendt Jensen[a]

[a]Center for Fast Ultrasound Imaging, Dept. of Elec. Eng., Bldg. 349,
Technical University of Denmark, DK-2800 Kgs. Lyngby, Denmark
[b]Medical Engineering Program, University of Hong Kong, Pokfulam, Hong Kong

ABSTRACT

This abstract proposes a new non-invasive method for measuring pressure changes in deep-tissue vessels using vector velocity ultrasound data. The large penetration depth is ensured by acquiring data using a phased array transducer. Vascular pressure changes are then calculated from 2-D angle-independent vector velocity fields using a model based on the Navier-Stokes equations. Experimental scans are performed on a fabricated flow phantom having a constriction of 36% at a depth of 100 mm. Scans are carried out using a phased array transducer connected to the experimental scanner, SARUS. 2-D fields of angle-independent vector velocities are acquired using directional synthetic aperture vector flow imaging. The obtained results are evaluated by comparison to a 3-D numerical simulation model with equivalent geometry as the designed phantom. The study showed pressure drops across the constricted phantom varying from -40 Pa to 15 Pa with a standard deviation of 32%, and a bias of 25% found relative to the peak simulated pressure drop. This preliminary study shows that pressure can be estimated non-invasively to a depth that enables cardiac scans, and thereby, the possibility of detecting the pressure drops across the mitral valve.

Keywords: Medical ultrasound, pressure estimation, vector flow imaging, synthetic aperture

1. INTRODUCTION

Flow estimation using medical ultrasound has received an increasing amount of attention over the past decade. New methods have been introduced, which allow for flow estimation at a time-resolution near the pulse repetition frequency simultaneously at all positions in the image. The increased attention has lead to further advancements that goes beyond the scope of only predicting blood flow velocities. Methods such as flow rate estimation, perfusion imaging, and the estimation of pressure has emerged in the wake of the new developments made to the ultrasonic field. However, non-invasive pressure estimation using vector velocity data has until today been restricted to linear array transducers, thus, limiting the field of view to superficial vessels. But new developments in the velocity estimation scheme has made it possible to obtain angle-independent velocity data using phased array transducers, allowing for the opportunity to perform cardiac scans. This potentially leads to a method that can detect pressure changes across heart valves without using invasive catheters, or being dependent on the insonification angle of the ultrasonic beam.

This paper presents the first study of measuring pressure changes from vector velocity flow data acquired to depth of 100 mm using synthetic aperture with a phased array ultrasound probe.

Send correspondence to J. B. Olesen, E-mail: jbjol@elektro.dtu.dk

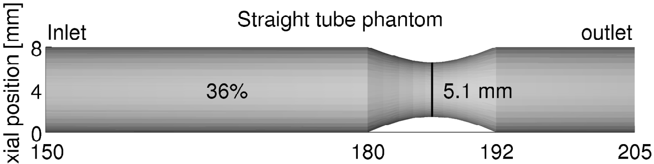

Figure 1. Fabricated flow model with a 36% constriction.

2. METHOD

The suggested method is based on the Navier-Stokes equations:

$$\rho\left[\frac{\partial\vec{v}}{\partial t}+\vec{v}\cdot\nabla\vec{v}\right]=-\nabla p\,+\,\rho\vec{g}\,+\,\mu\nabla^2\vec{v},\tag{1}$$

presuming the conservation of mass and linear momentum. Eq. 1 describes the development of a fluid's velocity field $\vec{v}(\vec{r},t)=(v_x(t),v_y(t),v_z(t))$ by relating the forces acting on an incompressible volume to its acceleration and density throughout time, t, and space, $\vec{r}$. The left-hand side sums the local time-dependent acceleration, $\frac{\partial\vec{v}}{\partial t}$, and convective fluid acceleration $\vec{v}\cdot\nabla\vec{v}$, where ρ is the density of the fluid and ∇ is the spatial differential operator $(\frac{\partial}{\partial x},\frac{\partial}{\partial y},\frac{\partial}{\partial z})$. The right-hand side shows the surface and volume forces that are responsible for the acceleration of the fluid. The forces constitute; a pressure drop $-\nabla p$, a gravitational force $\vec{g}$, and a viscous drag caused by the viscosity of the fluid $\mu\nabla^2\vec{v}$, where $\nabla^2\vec{v}$ is the Laplacian of the velocity field. The gravitational term is usually neglected, as a patient undergoing an ultrasound scan is placed in a supine position, hence, the buoyancy force cancels out the gravitational force.

The high precision and temporal frame-rate offered by synthetic aperture flow[1,2] allows for tracking of particles, which intuitively can be visualized by a streamline representation. Rewriting Eq. 1 into a one-dimensional equation following a streamline where the influence of gravity is omitted yields an extended version of the Euler equation;

$$\frac{\partial p}{\partial s}=-\rho\left[\frac{\partial v_s}{\partial t}+v_s\frac{\partial v_s}{\partial s}\right]\,+\,\mu\frac{\partial^2 v_s}{\partial s^2},\tag{2}$$

where v_s is the scalar product of $\vec{v}(\vec{r},t)$ and the unit vectors $(\hat{\mathbf{e}}_x,\hat{\mathbf{e}}_y,\hat{\mathbf{e}}_z)$. Integrating Eq. 2 along the flow direction of the streamline gives the drop in pressure that exist across the line,

$$\Delta P(t)=\int_0^L\frac{\partial p}{\partial s}\,ds\,+\,C.\tag{3}$$

As the integration constant, C, is unknown, it is the relative change in pressure that is detected.

3. EXPERIMENTAL SET-UP

The proposed method is evaluated on a straight-tube phantom with a 36% constriction during steady flow conditions. A part of the model is shown in Fig. 1. The phantom is connected to a flow system (CompuFlow 1000, Shelley Medical Imaging Technologies, Toronto, Canada) capable of generating customized flow waveforms. The study is performed using a constant waveform and a flow rate of 5 ml/s, and a 3 MHz phased array probe with 128 elements (Sound Technology, Analogic Ultrasound Group, State College, PA, USA). A two-cycle pulse is emitted at a pulse repetition frequency of 6.2 kHz to a depth of 120 mm, with an elevation focus at 80 mm. Five low-resolution images are summed for each high resolution flow image producing an effective frame-rate of 1.03 kHz. The ultrasound data are processed off-line using Matlab (The MathWorks Inc., Natick, MA, USA).

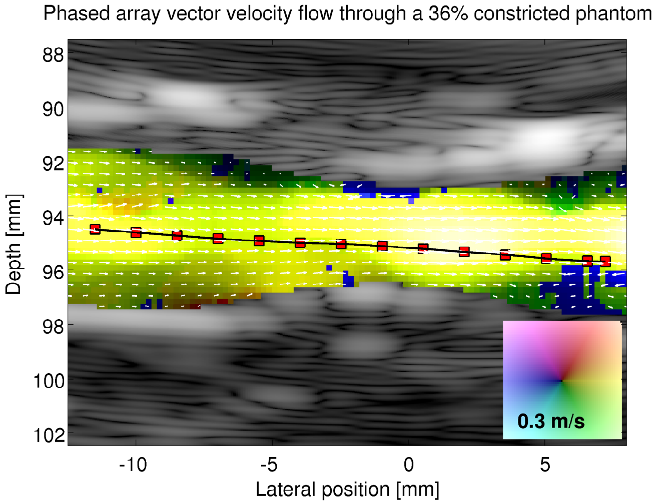

Figure 2. Vector velocity image at the constriction of the fabricated flow phantom. The image is captured during steady flow conditions. A black-dotted streamline passing through the center of the constriction is also displayed.

4. FINITE ELEMENT MODEL

The accuracy of the derived pressure is evaluated through comparison to a finite element (FE) model made in Comsol (Comsol v5.1, Comsol AB, Stockholm, Sweden). Flow parameters in the simulation model are set to mimic the actual flow conditions in the experimental set-up, with an input flow rate of 5 ml/s, and a simulated viscosity and density of $4.1 \cdot 10^{-3}$ Pa·s and 1,030 kg/m^3, respectively.

5. RESULTS

The method is tested for vector velocity flow data captured from the site of the 36% constriction. An example is displayed in Fig. 2. The image shows flow that accelerates toward the center of the constriction, producing a jet that then slowly decelerates as the lumen expands again. A black streamline following the vector field is also displayed. Throughout the study, changes in pressure are derived along this dotted line. A bias of -50% is observed in the measured flow data compared to the simulation model. This bias is used for compensating the velocity data, before inserting it in the pressure estimator.

For every position along the streamline, an individual pressure gradient is calculated using Eq. (2), relatively to its neighbouring estimates. Only spatial changes in velocity exist for steady flow, thus, the temporal acceleration in Eq. (2) is neglected. The spatial acceleration along the streamlines are found through polynomial filtering, using a window size of five data points and a polynomial order of two. Then, calculating the cumulative sum of the local pressure changes along the direction of the flow, gives the relative drop in pressure that exist between the start of the streamline to any position along the line. The result of doing this for every measured velocity frame is plotted in Fig. 3. The figure shows a relative drop in pressure as the fluid moves through the constricted part of the phantom. The shaded zone indicates a region of one standard deviation normalized to the number of frames recorded, which in this case is 264 frames. The dotted dark curve in Fig. 3 is the result of the simulation model.

6. DISCUSSION

A non-invasive method for detecting pressure changes in a deep positioned vessel using ultrasound vector velocity data has been presented. The method managed to produce pressures within a constriction with a standard

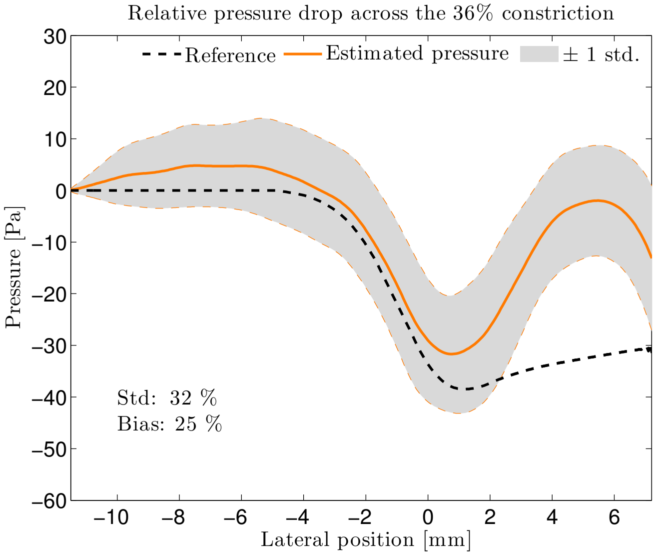

Figure 3. Constant flow: Estimated and simulated pressure drop through the center of a 36% constriction. The mean estimate is plotted together with ± 1 standard deviation, and the output from the FE models.

deviation of 32%, and a 25% bias compared to the FE simulation.

No previous studies on the subject have managed to estimate and validate pressure gradients from 2-D angle-independent vector velocity data obtained using a phased array and synthetic aperture. Every term in the estimator is calculated relative to neighboring velocity estimates, yielding pressure gradients that are independent of systemic flow factors, such as abnormalities in the cardiac output. The proposed method also offers the advantage of including temporal pressure changes, however, this was not considered in this paper as constant flow was studied. Yet, being able to include temporal changes is essential for studies on the cardiovascular system. A shortcoming of the proposed method is its lacking ability to estimate the out-of-plane velocity component v_y. This makes the estimator vulnerable in complex flow environments that has vector velocity components in all three spatial direction.

7. CONCLUSION

A non-invasive method for deriving pressure changes in a large field of view using ultrasound has been presented. Relative changes in pressure were derived using the Navier-Stokes equation for incompressible fluids. The vector velocities inserted into the equation were estimated using a directional synthetic aperture flow method yielding the two in-plane velocity components at a frame rate proportional to the pulse repetition frequency. The obtained pressure gradients were evaluated by comparison to a finite element simulation model. The result of this showed a standard deviation of 32% and a bias low of 25%. The abstract concludes that changes in pressure can be obtained to a depth of atleast 100 mm, thereby, allowing for the opportunity of performing cardiac scans.

REFERENCES

[1] Jensen, J. A. and Nikolov, S. I., “Directional synthetic aperture flow imaging,” *IEEE Trans. Ultrason., Ferroelec., Freq. Contr.* **51**, 1107–1118 (2004).

[2] Jensen, J. A. and Oddershede, N., “Estimation of velocity vectors in synthetic aperture ultrasound imaging.,” *IEEE Trans. Ultrason., Ferroelec., Freq. Contr.* **25**, 1637–1644 (2006).

Patent I

Non-invasive Estimation of Intravascular Pressure Changes using Vector Velocity Ultrasound (US)

Jacob Bjerring Olesen, Carlos Armando Villagomez-Hoyos, and
Jørgen Arendt Jensen

International Patent Application, filed on March 3, 2015.

Number: ANA1268-WO (BKM-10-7778-PCT).

Non-invasive Estimation of Intravascular Pressure Changes using Vector Velocity Ultrasound (US)

TECHNICAL FIELD

The following generally relates to ultrasound imaging and more particularly to non-invasively estimating intravascular pressure changes with velocity vector ultrasound (US).

BACKGROUND

Abnormal changes in intravascular blood pressure have been an indication of a diseased vessel. The literature indicates that measured pressure variations have been used clinically as a diagnostic marker in assessing the physiological state of a cardiovascular region. Intravascular pressure can be determined by inserting pressure sensing wires or catheters to the femoral artery and threading them to the region of interest. Such a procedure is invasive and has required the use of ionizing radiation for guidance of the pressure sensory device. Unfortunately, invasive procedures leave the patient susceptible to infection, bleeding, etc., and ionizing radiation can damage or kill cells. Furthermore, the literature has indicated that the accuracy of using catheters is greatly dependent on the physical size and shape of the catheter.

A less invasive approach estimates local pressure changes using microbubbles. This approach relies on injecting gas-filled bubbles into the circulatory system to measure the frequency shift that occurred in the scattered spectrum as ultrasonic waves were applied. Unfortunately, this approach requires the injection of microbubbles. A non-invasive approach is based on Doppler ultrasound. This approach includes analyzing audio signals of the frequency shifts received from the mitral jet, which reveals the peak systolic velocity. From this, local pressure gradients are calculated using an orifice equation. This approach is reliant on a single velocity estimate. Unfortunately, this renders the approach sensitive to hemodynamic factors unrelated to the constricted vessel's effect on the peak velocity, e.g. abnormal cardiac output. This approach has been considered in the literature as unreliable.

In view of at least the above, there is an unresolved need for another approach for measuring intravascular blood pressure.

SUMMARY

Aspects of the application address the above matters, and others.

In one aspect, a method for determining pressure gradients with ultrasound data includes acquiring ultrasound data of a vessel and generating a velocity vector profile for flow in the vessel with the ultrasound data. The method further includes computing an acceleration with the velocity vector profile. The acceleration includes at least a temporal acceleration, and computing the temporal acceleration includes reducing noise from the velocity vector profile and determining the temporal acceleration from the noise-reduced velocity data. The method further includes determining the pressure gradients with the computed acceleration. The method further includes displaying an ultrasound image of the vessel with indicia indicative of the pressure gradients superimposed thereover.

In another aspect, an apparatus includes a velocity estimator that processes ultrasound image data acquired by an ultrasound imaging system and generates velocity vector fields based thereon. The apparatus further includes a temporal acceleration processor that processes the velocity vector fields and generates a temporal acceleration, wherein the temporal acceleration processor filters the velocity vector fields while determining the temporal acceleration. The apparatus further includes a spatial acceleration processor that processes the velocity vector fields and generates a spatial acceleration. The apparatus further includes a pressure change estimator that estimates pressure gradients for the ultrasound data based on a model and the temporal and spatial accelerations. The apparatus further includes a display configured to display ultrasound image data and the pressure gradients estimates.

In another aspect a non-transitory computer readable storage medium is encoded with computer executable instructions which when executed by a processor of the computer causes the processor to: determine a spatial acceleration based on velocity vector fields, transform the velocity vector fields to the frequency domain, producing a sum of sinusoids, differentiate a sub-set of the sinusoids satisfying at least one of a predetermined energy of interest or a predetermine frequency range of interest, producing a sum of cosines, reconstruct the sum of cosines to determine a temporal acceleration, and determine a pressure change with the Navier-Stokes equation based on the spatial acceleration and the temporal acceleration.

Those skilled in the art will recognize still other aspects of the present application upon reading and understanding the attached description.

BRIEF DESCRIPTION OF THE DRAWINGS

The application is illustrated by way of example and not limited by the figures of the accompanying drawings, in which like references indicate similar elements and in which:

Figure 1 schematically illustrates an example ultrasound imaging system with an intravascular pressure determiner;

Figure 2 schematically illustrates an example of the intravascular pressure determiner;

Figure 3 shows an example inlet profile;

Figure 4 shows an ideal number of sinusoids needed to reconstruct the profile in Figure 3;

Figure 5 shows the approximated flow from the center of the constriction;

Figure 6 show results of mapping pressure gradients derived from the velocity data;

Figure 7 shows a plot of the temporal evolution of the pressure drop for the three measured cardiac cycles;

Figure 8 shows the mean of three measured pressure profiles plotted together with a simulated pressure drop from an FE model;

Figure 9 illustrates a method, and

Figure 10 shows an example display of 2-D pressure changes through a vessel.

DETAILED DESCRIPTION

The following generally describes a non-invasive approach for estimating intravascular pressure changes from ultrasound imaging data. In one instance, the approach estimates pressure gradients from 2-D or 3-D vector velocity fields. Changes in pressure are then derived using a model based on, e.g., the Navier-Stokes and/or other equations.

Initially referring to Figure 1, an example ultrasound imaging system 100 is illustrated.

A transducer array 102 includes a plurality of transducer elements, which are configured to transmit ultrasound signals and receive echo signals. Examples of suitable one-dimensional (1-D) arrays include arrays with 8, 16, 32, 64, 96, 128, 512, etc. transducer elements. Other numbers of elements and/or dimensions (e.g., two-dimensional, or 2-D) are also contemplated herein. The array 102 can be linear, curved, and/or otherwise shaped. The transducer array 102 can be fully populated or sparse and/or a combination thereof.

Transmit circuitry 104 generates a set of pulses that are conveyed to the transducer array 102. The set of pulses actuates a corresponding set of the transducer elements of the transducer array 102, causing the elements to transmit ultrasound signals into an examination or scan field of view. Receive circuitry 106 receives echoes generated in response to the transmitted ultrasound signals from the transducer 102. The echoes, generally, are a result of the interaction between the emitted ultrasound signals and the structure (e.g., flowing blood cells, organ cells, etc.) in the scan field of view.

A controller 108 controls the transmit circuitry 104 and/or receive circuitry 106. In one instance, the controller 108 controls the transmit circuitry 104 to emit waves (e.g., unfocused spherical, weakly focused, plane, etc.) from the aperture by placing virtual sources behind the transducer. A beamformer 112 processes the echoes and generates data at least for generating images and estimating velocity. In one non-limiting instance, this includes generating a sequence of focused, coherent echo samples along focused scanlines of a scanplane.

A velocity estimator 113 is configured to estimate 2-D and/or three-dimensional (3-D) vector velocity fields. For example, the velocity estimator 113 can be configured to estimate a 2-D in-plane vector velocity field $\vec{v}(\vec{r},t) = \big(v_x(t), v_z(t)\big)$. The out-of-plane velocity $v_y(t)$ can be set to zero. Alternatively, the out-of-plane velocity $v_y(t)$ is also determined to estimate a 3-D vector velocity field.

Examples of velocity estimators are described in Jensen et al., “Directional synthetic aperture flow imaging,” IEEE Trans. Ultrason., Ferroelec., Freq. Contr., 51:1107–1118, 2004, Jensen et al., “Estimation of velocity vectors in synthetic aperture ultrasound imaging,” IEEE Trans. Ultrason., Ferroelec., Freq. Contr., 25:1637–1644, 2006, and Jensen, “Vector velocity estimation using directional beam forming and cross-correlation,” US 6,725,076 B1, the entirety of which is incorporated herein by reference.

Other suitable velocity estimators can be based on Jensen, “A New Estimator for Vector Velocity Estimation,” *IEEE Trans. Ultrason., Ferroelec., Freq. Contr.*, 48(4):886–894, 2001, and Jensen, “Estimator for Vector Velocity,” US 6,859,659 B1, the entirety of which is incorporated herein by reference, and Jensen, “Apparatus and method for determining movements and velocities of moving objects,” US 6,148,224, the entirety of which is incorporated herein by reference.

An intravascular pressure estimator 114 is configured to process the velocity vector to estimate a change in intravascular pressure. As described in greater detail below, in one instance this includes smoothing the velocity vector profile, computing a temporal acceleration term from the smoothed velocity vector data, and determining a pressure gradient based on the temporal acceleration term, a spatial acceleration term, and the Navier-Stokes equation. The smoothing, in one instance, de-noises the velocity vector profile. Optionally, the intravascular pressure estimator 114 is further configured to determine pressure drops.

A scan converter 116 scan converts the scanlines for frames of data to generate data for display, for example, by converting the data to the coordinate system of the display. The scan converter 116 can employ analog and/or digital scan converting techniques. A display 118 is configured to display an ultrasound image, an intravascular pressure, a change in intravascular pressure, a pressure drop, etc. The pressure can be visually displayed with indicia (e.g., alphanumeric, graphical, etc.).

A user interface (UI) 110, which includes an input device (e.g., a button, a slider, a touch surface, etc.) and/or an output device (e.g., a visual and/or audible, etc.), provides an interface between the system 100 and a user of the system 100.

It is to be appreciated that the beamformer 112, the velocity estimator 113, the intravascular pressure estimator 114, and/or other components of the system 100 can be implemented via a processor (e.g., a microprocessor, central processing unit, a controller, etc.) executing one or more computer readable instructions encoded or embedded on a non-transitory computer readable storage medium such as physical memory. The processor can additionally or alternatively execute a computer readable instruction carried by a carrier wave, a signal, or other transitory medium.

Figure 2 illustrates an example of the intravascular pressure estimator 114.

The illustrated intravascular pressure estimator 114 includes a temporal acceleration processor 208. In this example, the temporal acceleration processor 208 approximates a temporal acceleration analytically by decomposing a measured flow profile into a series of sinusoids through a Fourier transform. These sinusoids oscillate at frequencies, such as those descriptive for the original profile. The temporal acceleration processor 208 identifies a sub-set of the sinusoids as sinusoids of interest. In one instance, the sub-set includes sinusoids that satisfy energy criterion of interest, e.g., a predetermined number of sinusoids with a highest energy, sinusoids with energy in a predetermined range, etc. In another instance, the sub-set includes sinusoids corresponding to a frequency below a cut-off frequency (e.g., 500 Hz, 1 kHz, etc.). In yet another instance, the sub-set is determined based on a combination of energy and frequency. Other criterion is also contemplated herein.

The temporal acceleration processor 208 differentiates the selected sinusoids. In this example, the temporal acceleration processor 208 computes a first order derivative as shown in Equation 1:

Equation 1:

$$\frac{d\vec{v}_m(i,j,t)}{dt} = \sum_{p=1}^{N} \left|\vec{v}_p(i,j)\right| 2\pi \vec{f}_p(i,j) \sin\left(2\pi \vec{f}_p(i,j)t - \vec{\varphi}_p(i,j)\right),$$

where *N* represents a number of sinusoids used in reconstructing the flow profile, V_p and φ_p represents an amplitude and a phase of the frequency component f_p, (i,j) represents a position within the each velocity field, and m a direction (e.g., either axial *z* or lateral *x*). Taking the derivative computes the temporal acceleration as a sum of cosines. The temporal acceleration processor 208 reconstructs the sum of cosines, e.g., using a trigonometric function, to transform the data back into the time domain. Reconstructing the flow profile as such in connection with cardiac data is possible as the flow is periodic over the cardiac cycle.

With this approach, the velocity profile at each position within the vector field is first transformed from the time domain to the frequency domain, e.g., through a Fourier transform to decompose the vector fields into the frequencies that make it up over a plurality of energy bins. A sub-set of the frequency components is then retained while others are discarded, ignored, etc. In one instance 4 to 12 frequency components, such as 6, 7, 8, 9, 10, etc. frequency components are retained. As discussed above, the selection can be based on energy, frequency, etc. such that a sub-set of the frequency bins are selected. An example where 8 frequency components or bins are selected is discussed below in connection with Figure 4 herein. The derivative shifts the phase of the selected frequencies by 90 degrees to produce the temporal acceleration profile. This process has the effect of smoothing the original vector velocity estimates, e.g., by removing higher frequency components, which results in higher precision of pressure gradient estimates. The differentiated data is then transformed back to the time domain and further processed as described herein.

The illustrated intravascular pressure estimator 114 further includes a spatial acceleration processor 210. In this example, the spatial acceleration processor 210 calculates a spatial acceleration using polynomial filtering of the measured velocity field. In one instance, the spatial acceleration processor 210 fits a second-order polynomial to a subset of adjacent data points by a linear least-squared approach and then calculates convolution coefficients from a least-squared model, which are used for finding the first-order derivatives. The spatial acceleration processor 210 calculates the axial and lateral derivatives discretely for each position in a scan plane at a given time *t*.

In one instance, the spatial acceleration processor 210 calculates the axial and lateral derivatives through Equations 2 and 3:

Equation 2:

$$\frac{d\vec{v}_m(i,j,t)}{di} \approx \frac{1}{\Delta m} \sum_{p=i-h_w}^{i+h_w} \vec{v}_m(p,j,t)\vec{B}(p-(i-h_w)+1),$$

and

Equation 3:

$$\frac{d\vec{v}_m(i,j,t)}{dj} \approx \frac{1}{\Delta m} \sum_{p=j-h_w}^{j+h_w} \vec{v}_m^T(p,i,t)\vec{B}(p-(j-h_w)+1),$$

where Δm represents a sampling interval of the velocity field in either the axial or lateral direction, p represents an index, $\vec{B}$ represents convolution coefficients, and $\vec{v}_m^T$ represents the transpose of $\vec{v}_m$. The index number p can be found from half a window size of the selected subset, which can be calculated by: $h_w = \frac{N_{set}+1}{2} - 1$, where N_{set} represents a number of samples in the subset. The convolution coefficients in $\vec{B}$ depend solely on the order of the fitted polynomial and the size of the selected window, which can be found in look-up tables. The multiplication of $\vec{v}_m$ and $\vec{B}$, in this example, is performed element by element.

The illustrated intravascular pressure estimator 114 further includes a pressure change estimator 202. The pressure change estimator 202 is configured to estimate at least an intravascular pressure with the 2-D or 3-D vector velocity fields based on a model. Model storage 204 stores such a model. In the following example, the model is used to determine, from the 2-D vector velocity, in-plane pressure gradients, using the temporal and spatial acceleration (i.e., the temporal and spatial derivatives), as shown in Equations 4A or 4B:

Equation 4A:

$$\begin{bmatrix} \frac{\partial p}{\partial x} \\ \\ \frac{\partial p}{\partial z} \end{bmatrix} = -\rho \begin{bmatrix} \frac{\partial v_x}{\partial t} + v_x \frac{\partial v_x}{\partial x} + v_z \frac{\partial v_x}{\partial z} \\ \\ \frac{\partial v_z}{\partial t} + v_x \frac{\partial v_z}{\partial x} + v_z \frac{\partial v_z}{\partial z} \end{bmatrix}, \text{and}$$

Equation 4B:

$$\begin{bmatrix} \frac{\partial p}{\partial x} \\ \frac{\partial p}{\partial z} \end{bmatrix} = -\rho \begin{bmatrix} \frac{\partial v_x}{\partial t} + v_x \frac{\partial v_x}{\partial x} + v_z \frac{\partial v_x}{\partial z} \\ \frac{\partial v_z}{\partial t} + v_x \frac{\partial v_z}{\partial x} + v_z \frac{\partial v_z}{\partial z} \end{bmatrix} + \mu \begin{bmatrix} \frac{\partial^2 v_x}{\partial x^2} + \frac{\partial^2 v_x}{\partial z^2} \\ \frac{\partial^2 v_z}{\partial x^2} + \frac{\partial^2 v_z}{\partial z^2} \end{bmatrix} + \begin{bmatrix} \rho g_x \\ \rho g_z \end{bmatrix}$$

where p represents the pressure, x represents the axial direction, z represents the lateral direction, *t* represents time, v_x represents the axial velocity component, v_z represents the lateral velocity component, ρ and μ represents density and viscosity, respectively, and g represents the gravitational force. In general, Equation 4B additionally includes viscous forces and the gravity terms. For Equations 4A and 4B, the out-of-plane velocity v_y and changes in this direction are zero. In a variation, the out-of-plane velocity v_y can be included in Equations 4A or 4B and/or otherwise considered in the determination of the pressure gradients.

Such a model can be based on the Navier-Stokes equation, which is shown in Equation 5:

Equation 5:

$$\rho\left[\frac{\partial\vec{v}}{\partial t}+\vec{v}\cdot\nabla\vec{v}\right]=-\nabla p+\rho\vec{g}+\mu\nabla^2\vec{v},$$

where ρ represents a density of the fluid, $\vec{v}$ represents a velocity vector, $\frac{\partial\vec{v}}{\partial t}$ represents a partial derivative of the velocity vector as a function of time, ∇ represents a spatial differential operator $\left(\frac{\partial}{\partial x},\frac{\partial}{\partial y},\frac{\partial}{\partial z}\right)$, $\vec{v}\cdot\nabla\vec{v}$ represents convective fluid acceleration, ∇p represents a pressure gradient, $\vec{g}$ represents a gravitational force, $\nabla^2\vec{v}$ a Laplacian of the velocity field, and $\mu\nabla^2\vec{v}$ represents a viscous drag caused by the viscosity of the fluid.

Equation 5 describes the development of a fluid's velocity field $\left(\vec{v}(\vec{r},t)=v_x(t),v_y(t),v_z(t)\right)$ by relating forces acting on an incompressible volume to acceleration and density at a position $\vec{r}$ and a time t. From Equation 5, the pressure gradient ∇p can be determined if the three spatial vector components of $\vec{v}$ are known. The gravitational term, in one instance, can be ignored, for example, as a patient undergoing a scan (e.g., ultrasound) is placed in a supine position. The viscous forces, in one instance, can be ignored, for example, when studying blood flow in larger arteries, for example, due to the forces small effect on the overall movement of flow.

A pressure drop determiner 206 determines one or more pressure drops based on the pressure gradients. In another embodiment, the pressure drop determiner 206 is omitted. Figure 6 below shows an image with pressure gradients (represented via the arrows) superimposed over a vessel in an image. In one instance, a user can identify (via a mouse, etc.) points of interest in the vessel, e.g., behind, within, and before the constriction. The pressure drop determiner 206 determines a pressure drop based on these three points. In another example using Figure 6, a user can draw a line along the long axis of the vessel running through the constriction. A pressure drop can be determined for a particular moment in time by integrating the pressure gradients along the line in the image. This can be repeated for multiple time points based on each corresponding image. In yet another example, pressure drops can be calculated for a plurality of such lines each time point.

The one or more pressure drops can be graphically and/or alpha-numerically presented or displayed via the display 118. For example, the three points and the pressure drop can be superimposed over the image. In another example, the pressure drops for the line can be shown as a plot as a function of time as shown below in Figure 7. In another example, the pressure drops for the plurality of lines can be shown as a pressure map, e.g., similar to weather map. Figure 10 shows an example display of 2-D pressure changes through a vessel. The pressure values are given in reference to the entrance of the vessel (left side), which is set to zero. In this case, pressure is derived using EQUATION 6A on multiple streamlines following the vector velocity field.

The following describes a non-limiting example that compares an accuracy of the pressure changes using the approach described herein with a simulation. The simulation includes a finite element (FE) model. The geometry of the model is built from segmented MRI data of the flow phantom obtained using a 3-T scanner. The flow parameters of the simulation model are set to mimic actual flow conditions in the experimental set-up. Figure 3 shows an example inlet profile equivalent to a one measured during experimental settings, which is applied to the entrance of the model. The viscosity (e.g., $4.1e^{-3}$ pascal-second, or Pa·s) and density (1,030 kilogram per cubic meter, or kg/m^3 are assigned values that match the properties of the blood-mimicking fluid. An example of such a model is discussed in Olesen et el., "Noninvasive estimation of 2-D pressure gradients in steady flow using ultrasound," *IEEE Transactions on Ultrasonics, Ferroelectrics and Frequency Control*, vol. 61, no. 8, pp. 1409-1418.

The experimental set-up and equipment are described next. Vector velocity data are acquired on a flow phantom mimicking the carotid bifurcation having a 70% constriction of the internal branch. Measurements are acquired using a linear array transducer such as the BK8670, a product of BK Medical, DK. The linear array transducer is connected to an experimental research scanner. A three-cycle pulse with a center frequency of 7 MHz is emitted at 12 kHz to a depth of 3 cm. Eight low-resolution images are summed for each high resolution image producing an effective frame-rate of 1,500 Hz. The ultrasound data can be processed on or off-line. The carotid phantom is connected to a flow system capable of generating customized flow waveforms.

The local acceleration is approximated by decomposing the measured waveform into a number of sinusoids each oscillating at different frequencies. This is done to express the derivatives for calculating the pressure gradients analytically. The number of sinusoids needed to make a realistic reconstruction of the original flow waveform depends on the complexity of the profile and the amount of noise present in the signal. Figure 4 shows an ideal number of sinusoids needed to reconstruct the profile in Figure 3 as a function of an increasing noise level in the measured signal. The system's inlet waveform can be more than 98% recovered from the sum of eight sinusoids, despite having a 20 dB level of white Gaussian noise. The approximated flow from the center of the constriction is plotted in Figure 5.

Maps of pressure gradients are derived from the velocity data, and a result is shown in Figure 6. The estimated gradients are plotted during the peak systolic phase of the cardiac cycle. Figure 6 is calculated using the estimator described in Equation 4A. The arrows and their background gray levels indicate a direction and a magnitude of the gradients, respectively. Figure 6 shows arrows that tend to point away from the center of the constriction, indicating that a low pressure is present here. The spatial derivatives used in Figure 6 are calculated using window sizes of 31 (3 mm) and 11 (2 mm) data points for the axial and lateral direction, respectively.

One way of displaying a pressure drop across a region is by using a streamline representation. For instance, adding vector components, v_x and v_z, which underlie the streamline, yields the velocity component tangent to the streamline, v_s. Re-writing the 2-D in-plane velocity components to a single component parallel to the streamline, means that pressure gradients along the line, can be derived using a 1-D representation of Equation 5, as shown in Equations 6A or 6B:

Equation 6A:

$$\frac{\partial p}{\partial s} = -\rho\left[\frac{\partial v_s}{\partial t} + v_s\frac{\partial v_s}{\partial s}\right]. \text{ and}$$

Equation 6B:

$$\frac{\partial p}{\partial s} = -\rho \left[\frac{\partial v_s}{\partial t} + v_s \frac{\partial v_s}{\partial s} \right] + \mu \left[\frac{\partial^2 v_{xs}}{\partial s^2} \right]$$

In general, Equation 6B additionally includes viscous forces and the gravity terms.

The total pressure drop that exists across the streamline is estimated as a function of time. The spatial derivatives, which go into the estimator, are calculated using polynomial filtering. A second-order polynomial is fitted to a subset of 71 adjacent velocity estimates covering a 1.4 mm line of the 10.7 mm long streamline. The window size and the order of the filter is selected to minimize the effect of estimator noise and under the assumption that flow within a 1.4 mm region can be approximated by a second-order polynomial. Each individual gradient gives an indication of how pressure at that particular position changes relative to neighboring pressure values. Summing the discrete contributions from each estimate along the line, the relative drop in pressure that exists between the two ends of the streamline is obtained.

The temporal evolution of the pressure drop for the three measured cardiac cycles is plotted in Figure 7. The figure shows the greatest pressure drop in the systolic phase of the cardiac cycle, and that the drop peaks just before the flow reaches its maximum velocity. The average standard deviation across the pulse is found to 4% in reference to the maximum pressure of 7 Pa. The mean of the three measured pressure profiles is plotted together with the simulated pressure drop from the FE model in Figure 8. A normalized root-mean-square error of 10% is found between the estimated data and the reference model.

In this example, non-invasive measurement of pressure changes has been calculated from vector velocity data. The intravascular pressure drop across the constricted phantom varied depending on when in the cardiac cycle it was measured. The largest drop was estimated just prior to the peak systolic phase, reaching 7 Pa with a standard deviation of 4%. A normalized error of 10% was seen between the estimated pressure and the results from the FE model. For this example, the approached described herein employs vector velocity data acquired to a depth of 3 cm using directional synthetic aperture flow imaging, producing 1,500 velocity frames a second.

Such techniques otherwise allow for averaging across estimates without compromising the peak of the profile. Averaging is beneficial as it essentially performs a low-pass filtering of the estimates, thus, avoiding the higher frequency content, which usually is associated with noise. Noise cancellation can be used for deriving proper derivatives, and can become important when moving into higher order derivatives. The effect of viscosity, which is related to second-order differentiation, gets introduced when studying flow in smaller vessel where the influence from the wall is more prominent. Therefore, pressure estimation by the Navier-Stokes equations should for those regions take the viscous forces into account.

The literature indicated a 24% overestimation of the peak systolic pressure from commonly employed catheters. The example herein showed results within 10% of the reference model and with a standard deviation of 4%, indicating that the approach described herein obtains pressure measurements that are more reliable than an invasive catheter. Superseding catheters in the clinic may eliminate the need for such invasive procedures and their appertaining X-ray radiation for guidance of the catheter.

Figure 9 illustrates a method.

It is to be understood that the following acts are provided for explanatory purposes and are not limiting. As such, one or more of the acts may be omitted, one or more acts may be added, one or more acts may occur in a different order (including simultaneously with another act), etc.

At 1402, ultrasound imaging data is acquired. It is to be appreciated that ultrasound imaging data can be acquired in near real-time and thus provides higher timer resolution data for superior filter, e.g., relative to MR and/or other imaging modalities, where data is averaged data over time due to slower acquisition capabilities.

At 1404, vector velocity fields are determined from the acquired ultrasound imaging data. As described herein, this includes 2-D and/or 3-D velocity vector fields determined using various approaches such a transverse oscillation, plane wave, synthetic aperture, etc.

At 1406, temporal and spatial acceleration components are determined based on the velocity vector fields, as described herein and/or otherwise.

At 1408, pressure gradients are estimated from the temporal and spatial acceleration components, as described herein and/or otherwise.

At 1410, the pressure gradients are presented, as described herein and/or otherwise.

At 1412, one or more pressure drops are determined based on the pressure gradients, as described herein and/or otherwise.

At 1414, the pressure drops are presented, as described herein and/or otherwise.

In another embodiment, acts 1410 and 1412 are omitted.

The pressure gradients and/or drops can be conveyed to another device. The other device can be a display, hardware memory, another device, etc. In one instance, a pressure gradient and/or drop that crosses a predetermined threshold level cause the other device to perform an act. For example, the drop may cause the other device to invoke an alarm, transmit a notification to a smartphone, page, or the like, sense another physiologic parameter, etc.

The methods described herein may be implemented via one or more processors executing one or more computer readable instructions encoded or embodied on computer readable storage medium such as physical memory which causes the one or more processors to carry out the various acts and/or other functions and/or acts. Additionally or alternatively, the one or more processors can execute instructions carried by transitory medium such as a signal or carrier wave.

The application has been described with reference to various embodiments. Modifications and alterations will occur to others upon reading the application. It is intended that the invention be construed as including all such modifications and alterations, including insofar as they come within the scope of the appended claims and the equivalents thereof.

CLAIMS

What is claimed is:

1. A method for determining pressure gradients with ultrasound data, the method comprising:

acquiring ultrasound data of a vessel;

generating a velocity vector profile for flow in the vessel with the ultrasound data;

computing an acceleration with the velocity vector profile, wherein the acceleration includes at least a temporal acceleration, and computing the temporal acceleration includes reducing noise from the velocity vector profile and determining the temporal acceleration from the noise-reduced velocity data;

determining the pressure gradients with the computed acceleration; and

displaying an ultrasound image of the vessel with indicia indicative of the pressure gradients superimposed thereover.

2. The method of claim 1, wherein the pressure gradients are generated using the Navier-Stokes equation.

3. The method of any of claims 1 to 2, wherein computing the temporal acceleration includes:

transforming the velocity vector profile from the time domain to the frequency domain;

selecting a sub-set of the frequency components;

processing the selected sub-set by differentiating the selected sub-set; and

transforming the differentiated selected sub-set back to the time domain.

4. The method of claim 3, wherein the transforming of the differentiated selected sub-set back to the time domain includes employing a trigonometric function that reconstructs the data back into the time domain.

5. The method of any of claims 3 to 4, wherein transforming the velocity vector profile to the frequency domain includes applying a Fourier transform to the velocity vector profile.

6. The method of any of claims 3 to 5, wherein selecting the sub-set of the frequency components includes selecting only 4 to 16 of the frequency components.

7. The method of any of claims 3 to 6, wherein selecting the sub-set of the frequency components include selecting a sub-set of the frequency components that satisfy predetermined energy criteria.

8. The method of any of claims 3 to 7, wherein selecting the sub-set of the frequency components include selecting a sub-set of the frequency components that satisfy predetermined frequency criteria.

9. The method of any of claims 1 to 8, wherein the acceleration further includes a spatial acceleration.

10. The method of any of claims 1 to 8, wherein determining the pressure drop includes:

receiving an identification of a plurality of points of interest on the ultrasound image, wherein the plurality of points of interest are respectively located behind a constriction of the vessel, within the constriction, and before the constriction;

determining a pressure drop based on the pressure gradients for the plurality of points of interest;

visually identifying the plurality of points of interest on the displayed ultrasound image; and

displaying the determined pressure drop.

11. The method of any of claims 1 to 8, wherein determining the pressure drop includes:

receiving a signal identifying a set of pixels in the image for a line along a long axis of the vessel;

determining a pressure drop by integrating over the pressure gradients corresponding to the identified set of pixels;

repeating the acts of receiving and determining for each image frame; and

visually presenting the pressure drops as a function of time.

12. The method of claim 11, further comprising:

repeating the acts of receiving, determining, repeating and presenting for a plurality of different lines along the long axis of the vessel each image frame; and

visually presenting the pressure drops as a pressure map.

13. The method of any of claims 1 to 12, wherein the velocity vector profile is one of a 2-D or 3-D velocity vector profile.

14. The method of any of claims 1 to 13, further comprising:

generating the velocity vector profile based on at least one of a transverse oscillation, a plan wave, or a synthetic aperture algorithm.

15. An apparatus, comprising:

a velocity estimator (113) that processes ultrasound image data acquired by an ultrasound imaging system and generates velocity vector fields based thereon;

a temporal acceleration processor (208) that processes the velocity vector fields and generates a temporal acceleration, wherein the temporal acceleration processor filters the velocity vector fields while determining the temporal acceleration;

a spatial acceleration processor (210) that processes the velocity vector fields and generates a spatial acceleration;

a pressure change estimator (202) that estimates pressure gradients for the ultrasound data based on a model and the temporal and spatial accelerations; and

a display configured to display ultrasound image data and the pressure gradients estimates.

16. The apparatus of claim 15, wherein the model is based on the Navier-Stokes equation.

17. The apparatus of any of claims 15 to 16, wherein the temporal acceleration processor generates the temporal acceleration by decomposing the velocity vector fields into a series of sinusoids, discarding a sub-set of the sinusoids that contribute to noise, differentiating the remaining sinusoids, and reconstructing the differentiated data back to the time domain.

18. The apparatus of any of claims 15 to 17, wherein the spatial acceleration processor fits a second-order polynomial to a subset of adjacent data points by a linear least-squared approach and then calculates convolution coefficients from a least-squared model to approximate first-order derivatives to generate the spatial acceleration.

19. The apparatus of any of claims 15 to 18, further comprising:

determining one or more pressure drop based on the pressure gradients.

20. A non-transitory computer readable storage medium encoded with computer executable instructions which when executed by a processor of the computer causes the processor to:

determine a spatial acceleration based on velocity vector fields;

transform the velocity vector fields to the frequency domain, producing a sum of sinusoids;

differentiate a sub-set of the sinusoids satisfying at least one of a predetermined energy of interest or a predetermine frequency range of interest, producing a sum of cosines;

reconstruct the sum of cosines to determine a temporal acceleration; and

determine a pressure change with the Navier-Stokes equation based on the spatial acceleration and the temporal acceleration.

ABSTRACT

A method for determining pressure gradients with ultrasound data includes acquiring ultrasound data of a vessel and generating a velocity vector profile for flow in the vessel with the ultrasound data. The method further includes computing an acceleration with the velocity vector profile. The acceleration includes at least a temporal acceleration, and computing the temporal acceleration includes reducing noise from the velocity vector profile and determining the temporal acceleration from the noise-reduced velocity data. The method further includes determining the pressure gradients with the computed acceleration. The method further includes displaying an ultrasound image of the vessel with indicia indicative of the pressure gradients superimposed thereover.

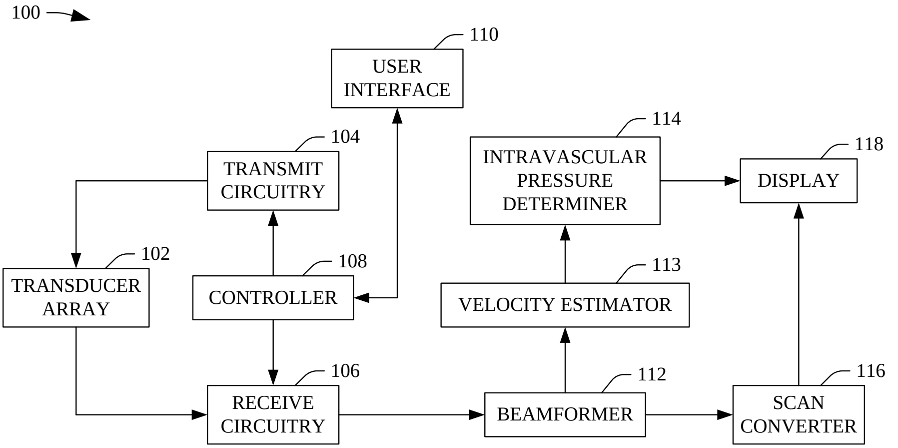
100
110
USER INTERFACE
114
INTRAVASCULAR PRESSURE DETERMINER
104
TRANSMIT CIRCUITRY
118
DISPLAY
102
TRANSDUCER ARRAY
108
CONTROLLER
113
VELOCITY ESTIMATOR
106
RECEIVE CIRCUITRY
112
BEAMFORMER
116
SCAN CONVERTER

FIGURE 1

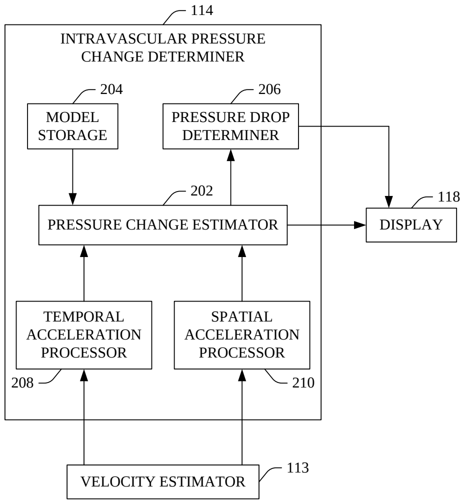
114
INTRAVASCULAR PRESSURE CHANGE DETERMINER
204
MODEL STORAGE
206
PRESSURE DROP DETERMINER
202
PRESSURE CHANGE ESTIMATOR
118
DISPLAY
TEMPORAL ACCELERATION PROCESSOR
SPATIAL ACCELERATION PROCESSOR
208
210
VELOCITY ESTIMATOR
113

FIGURE 2

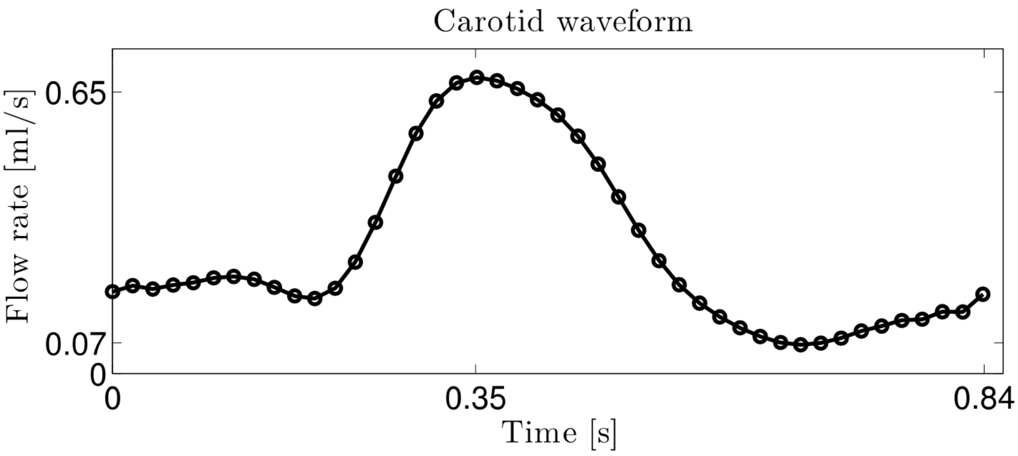

FIGURE 3

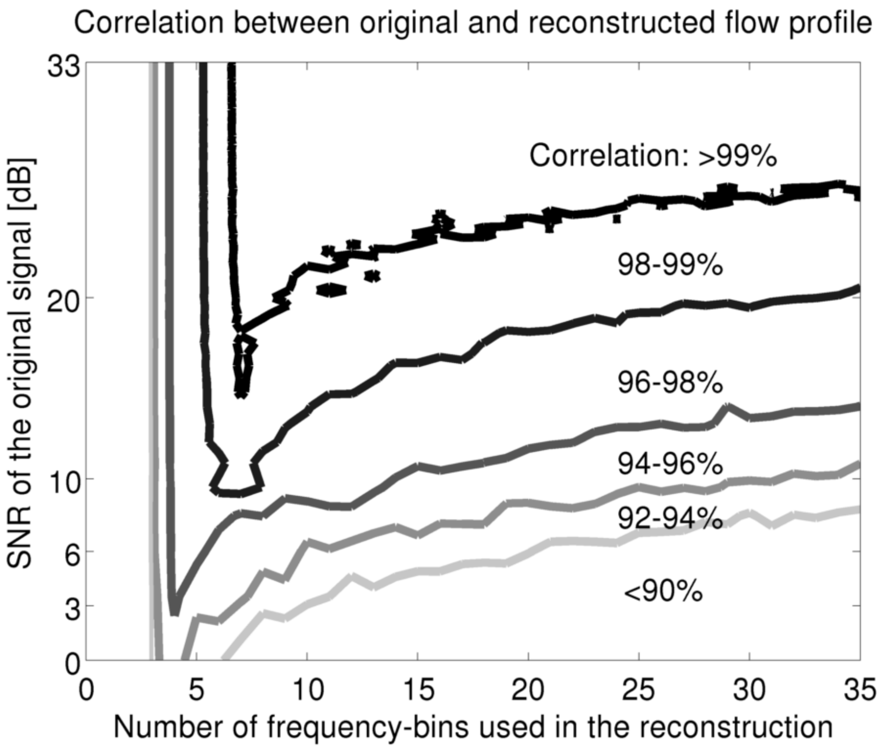
Correlation between original and reconstructed flow profile
SNR of the original signal [dB]
33
20
10
6
3
0
0
5
10
15
20
25
30
35
Number of frequency-bins used in the reconstruction
Correlation: >99%
98-99%
96-98%
94-96%
92-94%
<90%

FIGURE 4

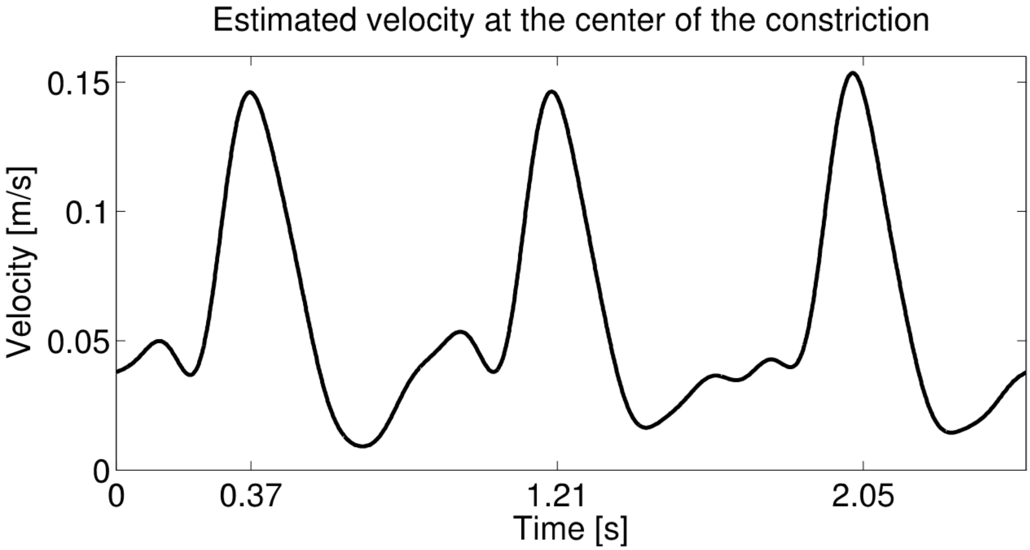
Estimated velocity at the center of the constriction
Velocity [m/s]
0.15
0.1
0.05
0
0
0.37
1.21
2.05
Time [s]

FIGURE 5

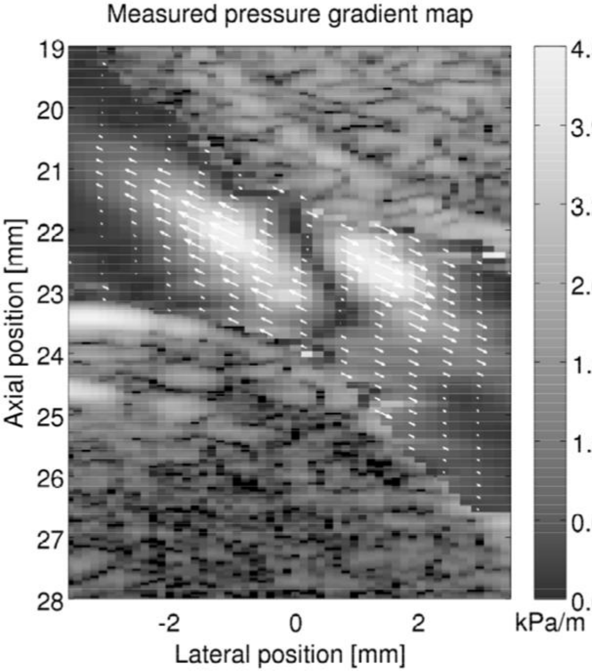
Measured pressure gradient map
19
20
21
22
23
24
25
26
27
28
Axial position [mm]
-2
0
2
Lateral position [mm]
4.5
3.9
3.2
2.6
1.9
1.3
0.6
0.0
kPa/m

FIGURE 6

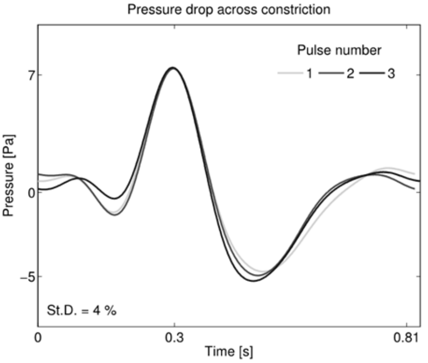

FIGURE 7

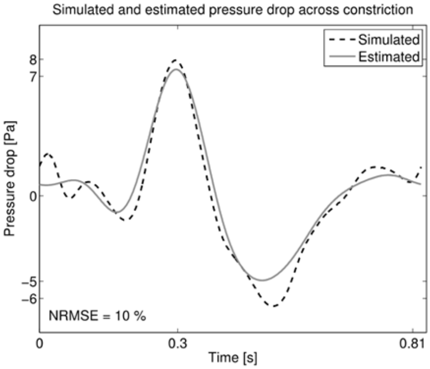

FIGURE 8

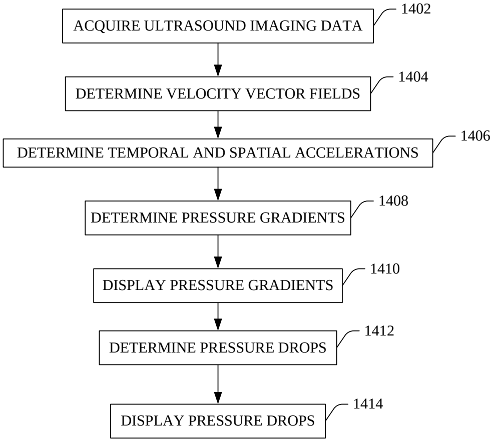

FIGURE 9

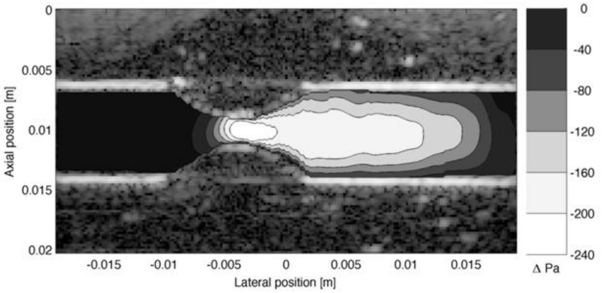

FIGURE 10

Patent II

Flow Acceleration Estimation Directly From Beamformed Ultrasound Data

Jacob Bjerring Olesen, Carlos Armando Villagomez-Hoyos, and Jørgen Arendt Jensen

International Patent Application, filed on September 23, 2015.

Number: ANA1282-WO-US (BKM-10-7837-US-PCT).

Flow Acceleration Estimation Directly From Beamformed Ultrasound data

TECHNICAL FIELD

The following generally relates to ultrasound imaging and more particularly to estimating temporal and/or spatial acceleration directly from beamformed ultrasound data.

BACKGROUND

An ultrasound imager can provide real-time structural images (e.g., a B-mode) of the interior of an object or a subject such as tissue, organs, etc. An ultrasound imager can also provide real-time images of flow (e.g., velocity) inside of a cavity such as the flow of blood cells in vascular tissue. In one instance, the flow image is super-imposed over the B-mode image, which provides a structural frame of reference for the flow image.

Flow acceleration has been used for clinical evaluation, including analyzing ventricular performance, studying hemodynamics, estimating pressure gradients in the circulatory system, etc. For example, Olesen et al., "Noninvasive estimation of 2-D pressure gradients in steady flow using ultrasound," IEEE Trans. Ultrason., Ferroelec., Freq. Contr., vol. 61, no. 8, pp. 1409–1418, 2014, discusses an approach to estimate pressure gradients from flow acceleration.

Flow acceleration estimation is especially used when deriving pressure through for instance the Navier-Stokes Equations. Spatial and temporal accelerations are calculated by differentiating velocity estimates. However, this approach is highly sensitive to the precision of the velocity estimates (and/or the velocity estimator estimating the velocity estimates), and the velocity estimates tend to be noisy.

Unfortunately, this leads to even higher noise levels of the derived acceleration as noise in the velocity field transfers directly to the acceleration estimate. The differential quotient increases the noise-level as the mathematical operator basically performs a high pass filtering of the velocity estimates, which primarily is governed by estimator noise. With these approaches, filtering (e.g., by means of Savitzky- Golay filters) and/or using a model and least squares analysis has been used to cope with the level of noise.

In view of at least the above, there is an unresolved need for another approach for estimating flow acceleration.

SUMMARY

Aspects of the application address the above matters, and others.

In one aspect, a method for determining a flow acceleration directly from beamformed ultrasound data includes extracting a sub-set of data from the beamformed ultrasound data, wherein the sub-set of data corresponds to predetermined times and predetermined positions of interest, determining the flow acceleration directly from the extracted sub-set of data, and generating a signal indicative of the determined flow acceleration.

In another aspect, an apparatus includes a beamformer configured to processes electrical signals indicative of received echoes produced in response to an interaction of a transmitted ultrasound signal with tissue and generate RF data, and an acceleration flow processor configured to directly process the RF data and generate a flow acceleration therefrom.

In another aspect a non-transitory computer readable storage medium is encoded with computer executable instructions which when executed by a processor of the computer causes the processor to: beamform ultrasound data acquired with an ultrasound imaging system producing RF ultrasound data, determine a double cross-correlation between a first sub-set of data from the RF ultrasound data and a second different sub-set of data from the RF ultrasound data, and determine a flow acceleration directly from the double cross-correlation.

Those skilled in the art will recognize still other aspects of the present application upon reading and understanding the attached description.

BRIEF DESCRIPTION OF THE DRAWINGS

The application is illustrated by way of example and not limited by the figures of the accompanying drawings, in which like references indicate similar elements and in which:

Figure 1 schematically illustrates an example ultrasound imaging system with a flow acceleration processor.

Figure 2 schematically illustrates an example of the flow acceleration processor.

Figure 3 illustrates an example method for determining a temporal acceleration directly from beamformed ultrasound data.

Figure 4 illustrates an example method for determining a temporal acceleration directly from beamformed ultrasound data.

DETAILED DESCRIPTION

The following generally describes a non-invasive approach for estimating flow acceleration (temporal and/or spatial) directly from ultrasound imaging measurements, i.e., independent of velocity estimates.

Initially referring to Figure 1, an example ultrasound imaging system 100 is illustrated.

A transducer array 102 includes one or more transducer elements, which are configured to transmit ultrasound signals and receive echo signals. Examples of suitable arrays include arrays with 1, 8, 16, 32, 64, 96, 128, 512, etc. transducer elements. The array 102 can be linear, curved, and/or otherwise shaped, fully populated or sparse and/or a combination thereof.

Transmit circuitry 104 generates a set of pulses that are conveyed to the transducer array 102. The set of pulses actuates a corresponding set of the transducer elements of the transducer array 102, causing the elements to transmit ultrasound signals into an examination or scan field of view.

Receive circuitry 106 receives echoes generated in response to the transmitted ultrasound signals from the transducer 102 and producing an electrical signal indicative thereof. The echoes, generally, are a result of the interaction between the emitted ultrasound signals and the structure (e.g., flowing blood cells, organ cells, etc.) in the scan field of view.

A controller 108 controls the transmit circuitry 104 and/or receive circuitry 106.

A user interface (UI) 110, which includes an input device (e.g., a button, a slider, a touch surface, etc.) and/or an output device (e.g., a visual and/or audible, etc.), provides an interface between the system 100 and a user of the system 100.

A beamformer 112 processes the electrical signal and generates beamformed or RF data at least for estimating a flow acceleration. In one instance, the beamformer 112 generates a sequence of focused, coherent echo samples along focused scanlines of a scanplane. In general, the beamformer 112 can generate 1-D, 2-D, 3-D, synthetic aperture, etc. and/or other ultrasound data. The beamformer 112 may also be configured to process the scanlines to lower speckle and/or improve specular reflector delineation via spatial compounding and/or perform other processing such as FIR filtering, IIR filtering, etc.

A flow acceleration processor 114 processes the RF data and determines. As described in greater detail below, the flow acceleration processor 114 is configured to process the RF data and estimate a flow acceleration (temporal and/or spatial) directly from the RF data, independent of velocity estimates. In one instance, this approach mitigates transferring noise from velocity estimates into the flow acceleration estimate relative to a configuration which derives the flow acceleration estimate from velocity estimates. In another instance, this approach could use another configuration which is not linked to the one used for the velocity estimates. Therefore, the acceleration range of estimates could be selected independently of the velocities and estimated more accurately. The resulting data is a more robust acceleration estimate and may mitigate a need for invasive catheters, thereby creating a safer and more problem-free work environment for the physician performing the estimate.

An acceleration evaluation processor 116 processes the flow acceleration estimate. This includes processing the flow acceleration estimate to analyze ventricular performance, study hemodynamics, estimate pressure gradients, etc. An example of computing intravascular pressure changes from temporal and spatial flow acceleration estimates is described in PCT/IB2015/054246, filed June 4, 2015, and entitled "Non-invasive Estimation of Intravascular Pressure Changes using Vector Velocity Ultrasound (US)," the entirety of which is incorporated herein by reference.

An image processor 118 processes the beamformed data and generates one or more ultrasound images.

A rendering engine 120 visually presents an ultrasound image, the flow acceleration estimate, and/or information derived from the flow acceleration estimate.

A display 122 is configured to display the ultrasound image, the flow acceleration estimate (e.g., via numerical and/or graphical data).

In a variation, the ultrasound imaging system 100 further includes a velocity estimator configured to computer velocity and/or vector velocity information from the beamformed data. In this instance, the flow acceleration processor 114 can additionally be configured to estimate acceleration from the velocity and/or vector velocity information.

It is to be appreciated that the beamformer 112, the flow acceleration processor 114, the acceleration evaluation processor 116, and/or one or more other components of the system 100 can be implemented via a processor (e.g., a microprocessor, central processing unit, a controller, etc.) executing one or more computer readable instructions encoded or embedded on a non-transitory computer readable storage medium such as physical memory. The processor can additionally or alternatively execute a computer readable instruction carried by a carrier wave, a signal, or other transitory medium.

Figure 2 illustrates an example of the flow acceleration processor 114.

The illustrated flow acceleration processor 114 includes a temporal data extractor 202. The temporal data extractor 202 extracts data based on time for computing a temporal acceleration. For example, the temporal data extractor 202 can extract data for different times and a same position.

The illustrated flow acceleration processor 114 further includes a spatial data extractor 204. The spatial data extractor 204 extracts data based on position for computing a spatial acceleration. For example, the spatial data extractor 204 can extract data for different positions and a same time.

In a variation, the spatial data extractor 204 is omitted. In another variation, the temporal data extractor 202 is omitted.

A cross-correlation processor 206 computes a cross-correlation between the data extracted at different times and at the same position and/or the data extracted at different positions and the same time. An example of a suitable cross-correlation approach is a double cross-correlation approach, such as the one described in Equation 1:

Equation 1:

$$R_x(\tau) = \frac{1}{2L}\sum_{l=-L}^{L} R^{(1)}(l)\, R^{(1+K)}(l-\tau)$$

where $R_x(\tau)$ is the double cross-correlation, $R^{(1)}$ and $R^{(1+K)}$ are cross-correlation functions, L is a length of the correlation function, l is an index, K is the indication of temporal or spatial distance between the correlation functions, and τ is the lag. In general, $2L$ is the length of the segment of the cross-correlation functions. Examples of suitable lengths include, but are not limited to, two (2) to five (5) wavelengths, or less or more, as data is available for all time and all space.

The cross-correlation functions $R^{(1)}$ and $R^{(1+K)}$ can be computed as described in US 6,725,076 B1, filed May 10, 2000, and entitled "Vector velocity estimation using directional beam forming and cross-correlation," and EP 1 300 690 A1, filed October 2, 2001, and entitled "Apparatus and method for velocity estimation in synthetic aperture imaging," the entirety of which is incorporated herein by reference, and Jensen, "Directional Synthetic Aperture Flow imaging," IEEE Trans. Ultrason., Ferroelec., Freq. Contr., Vol. 51, NO. 9, September 2004. Other approaches are also contemplated herein.

In one instance, $R^{(1)}$ and $R^{(1+K)}$ are adjacent cross-correlation functions. For example, $R^{(1)}$ and $R^{(1+K)}$ can be the first and second (or next) time instances. However, $R^{(1)}$ and $R^{(1+K)}$ do not have to be adjacent cross-correlation functions. For example, $R^{(1)}$ and $R^{(1+K)}$ can be the first and third time instance, the first and fourth time instance, etc. This may be well-suited for an instance where there is low acceleration such that there is small shift between adjacent signals. In general, $R^{(1)}$ and $R^{(1+K)}$ can be the Nth and Kth time instance, since data for all time and all space is available if a synthetic aperture or plane wave sequence is used. Examples of such approaches are described in Villagomez-Hoyos et al., "Adaptive multi-lag for synthetic aperture vector flow imaging," in Proc. IEEE Ultrason. Symp., 2014, pp. 1722-1725, and Udesen et al., "High Frame-Rate Blood Vector Velocity Imaging Using Plane Waves: Simulations and Preliminary Experiments" IEEE Transactions on Ultrasonics Ferroelectrics and Frequency Control, Vol. 55, No. 8, 2008, p. 1729-1743.

An acceleration estimator 208 is configured to generate a flow acceleration estimate based on the cross-correlation estimate. For this, the acceleration estimator 208 processes the cross-correlation value for the different times and same position for the temporal acceleration, and process the cross-correlation value for the different positions and same times for the spatial acceleration. In the illustrated embodiment, the acceleration estimator 208 is configured to generate a temporal flow acceleration estimate (Acc_t) with an acceleration algorithm 210 such as the one described in Equation 2:

Equation 2:

$$Acc_t = \frac{\tau_{max}\, c\, f_{prf}^2}{2K f_s}$$

where c is the speed of sound, f_{prf} is a pulse-repetition frequency, K/f_{prf} is a temporal distance between the correlation functions $R^{(1)}$ and $R^{(1+K)}$, f_s is a sampling frequency and τ_{max} is a lag value where $R_x(\tau)$ has its maximum value.

In the illustrated embodiment, the acceleration estimator 208 is configured to generate a spatial flow acceleration estimate (Acc_s) with an acceleration algorithm 210 such as the one described in Equation 3:

Equation 3:

$$Acc_s = \frac{\tau_{max}\, c\, f_{prf}}{2K\Delta r f_s}$$

where c is the speed of sound, f_{prf} is a pulse-repetition frequency, $K\Delta r$ is a spatial distance between the two correlation functions $R^{(1)}$ and $R^{(1+K)}$, and f_s is a sampling frequency and τ_{max} is a lag value where $R_x(\tau)$ has its maximum value.

An increased accuracy in the output of the flow acceleration processor 114 is obtained if a polynomial is fitted to the discrete cross-correlation function $R_x(\tau)$ around its maximum. An example of a fitted polynomial is found at Foster et al., "Flow velocity profile via time-domain correlation: Error analysis and computer simulation." IEEE Transactions on Ultrasonics Ferroelectrics and Frequency Control, Vol. 37, 1990, p. 164-175.

The output of the flow acceleration processor 114 is the temporal and/or spatial acceleration estimates.

Figure 3 illustrates an example method for determining a temporal acceleration directly from beamformed ultrasound data.

It is to be understood that the following acts are provided for explanatory purposes and are not limiting. As such, one or more of the acts may be omitted, one or more acts may be added, one or more acts may occur in a different order (including simultaneously with another act), etc.

At 302, electrical signals, generated in response to the transducer array 102 receiving and detecting echoes produced in response to an interaction of a transmitted ultrasound signal and tissue, are beamformed producing beamformed RF ultrasound data.

At 304, first ultrasound data for a first time and a first position is extracted from the beamformed ultrasound data.

At 306, second ultrasound data for a second time and the first position is extracted from the beamformed ultrasound data, where the first and second times are different times.

At 308, a double cross-correlation between the first and second ultrasound data is computed, as described herein (e.g., Equation 1) and/or otherwise, producing cross-correlation data.

At 310, an acceleration is estimated, as described herein (e.g., Equation 2) and/or otherwise, from the double cross-correlation data producing a temporal acceleration estimate.

The temporal acceleration estimate can be processed to derive information therefrom, which can be utilized for analyzing ventricular performance, studying hemodynamics, estimating pressure gradients in the circulatory system for diagnosing various cardiovascular diseases, etc.

Figure 4 illustrates an example method for determining a temporal acceleration directly from beamformed ultrasound data.

It is to be understood that the following acts are provided for explanatory purposes and are not limiting. As such, one or more of the acts may be omitted, one or more acts may be added, one or more acts may occur in a different order (including simultaneously with another act), etc.

At 402, electrical signals, generated in response to the transducer array 102 receiving and detecting echoes produced in response to an interaction of a transmitted ultrasound signal and tissue, are beamformed producing beamformed RF ultrasound data.

At 404, first ultrasound data for a first position and a first time is extracted from the beamformed ultrasound data.

At 406, second ultrasound data for a second position and the first time is extracted from the beamformed ultrasound data, where the first and second positions are different positions.

At 408, a double cross-correlation between the first and second ultrasound data is computed, as described herein (e.g., Equation 1) and/or otherwise, producing cross-correlation data.

At 410, an acceleration is estimated, as described herein (e.g., Equation 2 or 3) and/or otherwise, from the double cross-correlation data producing a spatial acceleration estimate.

The spatial acceleration estimate can be processed to derive information therefrom, which can be utilized for analyzing ventricular performance, studying hemodynamics, estimating pressure gradients in the circulatory system for diagnosing various cardiovascular diseases, etc.

Another method combines (in part, in full, and/or with additional and/or different acts) Figure 3 and Figure 4. In this instance, one or both of the temporal and spatial acceleration estimates can be processed to derive further information that can be utilized for analyzing ventricular performance, studying hemodynamics, estimating pressure gradients in the circulatory system for diagnosing various cardiovascular diseases, etc.

The methods described herein may be implemented via one or more processors executing one or more computer readable instructions encoded or embodied on computer readable storage medium such as physical memory which causes the one or more processors to carry out the various acts and/or other functions and/or acts. Additionally or alternatively, the one or more processors can execute instructions carried by transitory medium such as a signal or carrier wave.

The application has been described with reference to various embodiments. Modifications and alterations will occur to others upon reading the application. It is intended that the invention be construed as including all such modifications and alterations, including insofar as they come within the scope of the appended claims and the equivalents thereof.

CLAIMS

What is claimed is:

1. A method for determining a flow acceleration directly from beamformed ultrasound data, the method comprising:

extracting a sub-set of data from the beamformed ultrasound data, wherein the sub-set of data corresponds to a predetermined time and a predetermined position of interest;

determining the flow acceleration directly from the extracted sub-set of data; and

generating a signal indicative of the determined flow acceleration.

2. The method of claim 1, further comprising:

generating an image with the beamformed ultrasound data;

generating indicia indicative of the determined flow acceleration; and

visually presenting the image with the indicia superimposed over the image.

3. The method of any of claims 1 to 2, further comprising:

deriving clinical information from the determined flow acceleration.

4. The method of any of claims 1 to 3, wherein determining the flow acceleration includes determining a temporal flow acceleration from extracted data from two different times and a same position.

5. The method of any of claims 1 to 4, wherein determining the flow acceleration includes determining a spatial flow acceleration from extracted data from two different positions and a same time.

6. The method of any of claims 1 to 5, wherein determining the flow acceleration includes determining a double cross-correlation and determining the flow acceleration from the double cross-correlation.

7. The method of claim 6, wherein the double cross-correlation is determined based on:

$$R_x(\tau) = \frac{1}{2L}\sum_{l=-L}^{L} R^{(1)}(l)\, R^{(1+K)}(l-\tau)$$

where $R_x(\tau)$ is the double cross-correlation, $R^{(1)}$ and $R^{(1+K)}$ are cross-correlation functions, L is a length of the correlation function, K is an indication of temporal or spatial distance between the correlation functions, l is an index, and τ is a lag.

8. The method of claim 7, wherein $R^{(1)}$ and $R^{(1+K)}$ are adjacent cross-correlation functions.

9. The method of claim 7, wherein $R^{(1)}$ and $R^{(1+K)}$ are non-adjacent cross-correlation functions.

10. The method of any of claims 7 to 9, wherein the temporal flow acceleration is determined based on:

$$Acc_t = \frac{\tau_{max}\, c\, f_{prf}^2}{2K f_s}$$

where Acc is the temporal flow acceleration, c is the speed of sound, f_{prf} is a pulse-repetition frequency, K/f_{prf} is a temporal distance between the correlation functions $R^{(1)}$ and $R^{(1+K)}$, f_s is a sampling frequency and τ_{max} is a lag value where $R_x(\tau)$ has a maximum value.

11. The method of any of claims 7 to 9, wherein the spatial flow acceleration is determined based on:

$$Acc_s = \frac{\tau_{max}\, c\, f_{prf}}{2K\Delta r f_s}$$

where c is the speed of sound, f_{prf} is a pulse-repetition frequency, $K\Delta r$ is a spatial distance between the two correlation functions $R^{(1)}$ and $R^{(1+K)}$, and f_s is a sampling frequency and τ_{max} is a lag value where $R_x(\tau)$ has a maximum value.

12. The method of any of claims 1 to 11, wherein the beamformed ultrasound data includes 1-D ultrasound data, and the determining of the flow acceleration includes determining of the flow acceleration directly from the 1-D ultrasound data.

13. The method of any of claims 1 to 11, wherein the beamformed ultrasound data includes 2-D ultrasound data, and the determining of the flow acceleration includes determining of the flow acceleration directly from the 2-D ultrasound data.

14. The method of any of claims 1 to 11, wherein the beamformed ultrasound data includes 3-D ultrasound data, and the determining of the flow acceleration includes determining of the flow acceleration directly from the 3-D ultrasound data.

15. The method of any of claims 1 to 11, wherein the beamformed ultrasound data includes synthetic aperture ultrasound data, and the determining of the flow acceleration includes determining of the flow acceleration directly from the synthetic aperture ultrasound data.

16. An apparatus, comprising:

a beamformer (112) configured to processes electrical signals indicative of received echoes produced in response to an interaction of a transmitted ultrasound signal with tissue and generate RF data; and

an acceleration flow processor (114) configured to directly process the RF data and generate a flow acceleration therefrom.

17. The apparatus of claim 16, further comprising:

an image processor (118) that generates an image with the RF data; and

a rendering engine (120) that visually presents the image and the flow acceleration.

18. The apparatus of any of claims 16 to 17, further comprising:

an acceleration evaluation processor (116) that derives clinical information from the flow acceleration.

19. The apparatus of any of claims 16 to 18, wherein the acceleration flow processor determines a temporal flow acceleration from data of the RF data from two different times and a same position.

20. The apparatus of any of claims 16 to 19, wherein the acceleration flow processor determines the flow acceleration by determining a double cross-correlation and determining the flow acceleration from the double cross-correlation.

21. The apparatus of claim 16 to 19 wherein the double cross-correlation is determined based on:

$$R_x(\tau) = \frac{1}{2L}\sum_{l=-L}^{L} R^{(1)}(l)\, R^{(1+K)}(l-\tau)$$

where $R_x(\tau)$ is the double cross-correlation, $R^{(1)}$ and $R^{(1+K)}$ are cross-correlation functions, L is a length of the correlation function, K is an indication of temporal or spatial distance between the correlation functions, l is an index, and τ is a lag.

22. The apparatus of claim 21, wherein the acceleration flow processor determines temporal flow acceleration based on:

$$Acc_t = \frac{\tau_{max}\, c\, f_{prf}^2}{2Kf_s}$$

where Acc is the flow acceleration, c is the speed of sound, f_{prf} is a pulse-repetition frequency, K is an intermediate step of correlation functions, f_s is a sampling frequency and τ_{max} is a lag value where $R_x(\tau)$ has a maximum value.

23. The apparatus of claim 21, wherein the spatial flow acceleration is determined based on:

$$Acc_s = \frac{\tau_{max}\, c\, f_{prf}}{2K\Delta r f_s}$$

where c is the speed of sound, f_{prf} is a pulse-repetition frequency, $K\Delta r$ is a spatial distance between the two correlation functions $R^{(1)}$ and $R^{(1+K)}$, and f_s is a sampling frequency and τ_{max} is a lag value where $R_x(\tau)$ has a maximum value.

24. A non-transitory computer readable storage medium encoded with computer executable instructions which when executed by a processor of the computer causes the processor to:

beamform ultrasound data acquired with an ultrasound imaging system producing RF ultrasound data;

determine a double cross-correlation between a first sub-set of data from the RF ultrasound data and a second different sub-set of data from the RF ultrasound data; and

determine a flow acceleration directly from the double cross-correlation.

ABSTRACT

A method for determining a flow acceleration directly from beamformed ultrasound data includes extracting a sub-set of data from the beamformed ultrasound data, wherein the sub-set of data corresponds to predetermined times and predetermined positions of interest, determining the flow acceleration directly from the extracted sub-set of data, and generating a signal indicative of the determined flow acceleration. An apparatus includes a beamformer (112) configured to processes electrical signals indicative of received echoes produced in response to an interaction of a transmitted ultrasound signal with tissue and generate RF data, and an acceleration flow processor (114) configured to directly process the RF data and generate a flow acceleration therefrom.

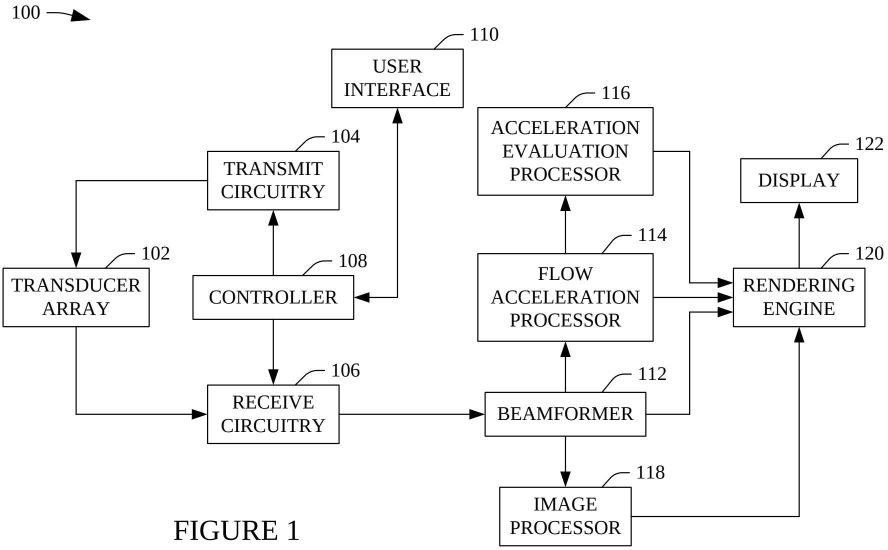
100
110
USER INTERFACE
116
ACCELERATION EVALUATION PROCESSOR
104
TRANSMIT CIRCUITRY
122
DISPLAY
102
TRANSDUCER ARRAY
108
CONTROLLER
114
FLOW ACCELERATION PROCESSOR
120
RENDERING ENGINE
106
RECEIVE CIRCUITRY
112
BEAMFORMER
118
IMAGE PROCESSOR

FIGURE 1

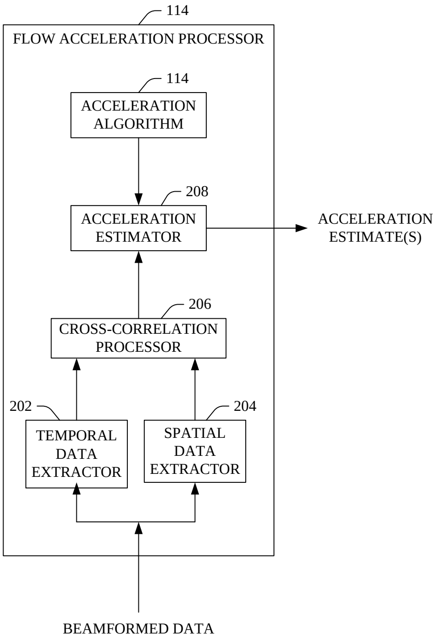
114
FLOW ACCELERATION PROCESSOR
114
ACCELERATION ALGORITHM
208
ACCELERATION ESTIMATOR
ACCELERATION ESTIMATE(S)
206
CROSS-CORRELATION PROCESSOR
202
TEMPORAL DATA EXTRACTOR
204
SPATIAL DATA EXTRACTOR
BEAMFORMED DATA

FIGURE 2

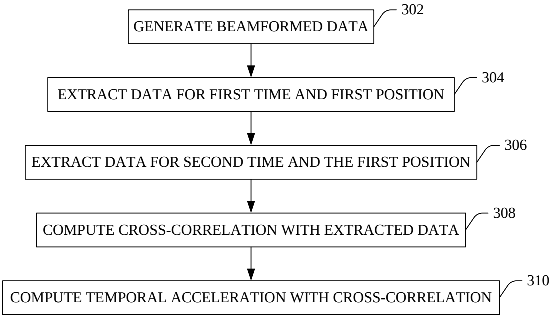

FIGURE 3

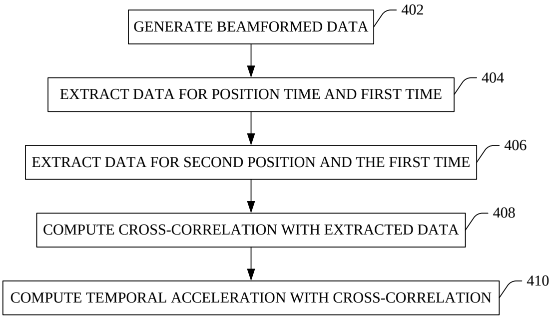

FIGURE 4